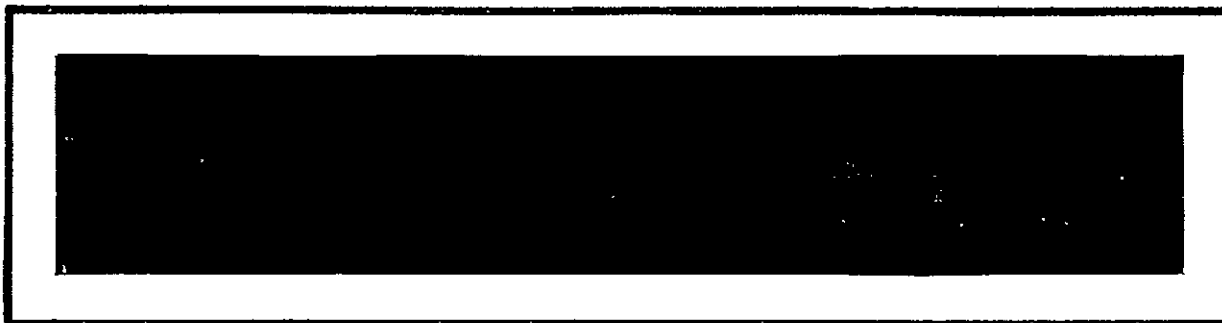


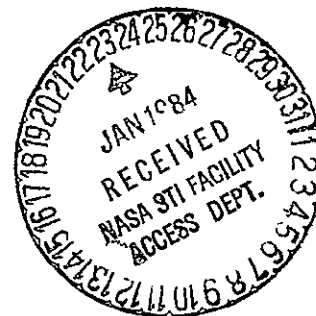
CR-171 726

C.1



Axiomatix

(NASA-CR-171726) ENGINEERING EVALUATIONS AND STUDIES. / VOLUME 2: EXHIBIT B, PART 2
Final Report (Axiomatix, Los Angeles, Calif.) 343 p HC A15/MF A01 CSCI 22B
N84-15176
Unclas
G3/16 43327



ENGINEERING EVALUATIONS AND STUDIES
FINAL REPORT FOR CONTRACT NAS 9-16067
VOLUME II, EXHIBIT B *Part 2*
Part 2

Technical Monitor: William Teasdale

Prepared for

NASA Lyndon B. Johnson Space Center
Houston, Texas 77058

Prepared by

Unjeng Cheng
James G. Dodds
Jack K. Holmes
Gaylord K. Huth
Richard S. Iwasaki
Robert G. Maronde
Peter W. Nilsen
Andreas Polydoros
Don Roberts
Sergei Udalov
Charles L. Weber

Axiomatix
9841 Airport Blvd., Suite 912
Los Angeles, California 90045

Axiomatix Report No. R8310-6
October 31, 1983

TABLE OF CONTENTS

Page

Volume I, Exhibit A

1.0	EXECUTIVE SUMMARY	1
1.1	Contract Tasks	2
1.1.1	Exhibit A Contract Tasks	2
1.1.2	Exhibit B Contract Tasks	7
1.1.3	Exhibit C Contract Tasks	11
1.2	Performance of the Contract Tasks	12
2.0	ORBITER INERTIAL UPPER-STAGE STUDIES	16
3.0	KU-BAND HARDWARE STUDIES	19
4.0	S-BAND HARDWARE INVESTIGATIONS	21
5.0	SHUTTLE/CENTAUR COMMUNICATION SYSTEM ENGINEERING INVESTIGATIONS.	22

Volume II, Exhibit B, Part 1

6.0	KU-BAND COMMUNICATION SYSTEM ANALYSIS	23
6.1	Shuttle/TDRSS Sidelobe Avoidance	25
6.1.1	Introduction	25
6.1.2	Derivation of Sidelobe Discrimination Budgets	26
6.1.3	Conclusions	26
6.2	Shuttle/TDRSS Acquisition and Tracking Performance	30
6.2.1	Introduction	30
6.2.2	Dynamic-Rate Limitations	30
6.2.3	Flux-Density Specification Considerations	31
6.2.4	Summary and Conclusions	32
7.0	S-BAND SYSTEM INVESTIGATIONS	33
8.0	ORBITER ANTENNA STUDIES AND INVESTIGATIONS	34
9.0	PAYLOAD COMMUNICATION INVESTIGATIONS	36
10.0	SHUTTLE/TDRSS AND GSTDN COMPATIBILITY ANALYSIS	37
10.1	TDRSS Antenna Scan for Shuttle Acquisition	37
10.2	PSD of Staggered Quadrature PN with Identical Sequences	38

TABLE OF CONTENTS (CONTINUED)

		<u>Page</u>
<u>Volume II, Exhibit B, Part 2</u>		
11.0	PRELIMINARY SHUTTLE/CENTAUR COMMUNICATION SYSTEM ANALYSIS . . .	39
12.0	SHUTTLE GLOBAL-POSITIONING SYSTEM INVESTIGATIONS	40
13.0	TELEVISION DIGITIZER DEVELOPMENT	41
13.1	Background	43
13.2	Principles of Delta Modulation	44
13.2.1	Conventional Bistate Delta Modulation	44
13.2.2	Tri-State Delta Modulation	47
13.2.3	Application of TSDM to NTSC Color TV	50
13.3	Breadboard System Description	52
13.3.1	Overall Test Setup	52
13.3.2	Transmitter Functional Block Diagram Description	55
13.3.3	Receiver Functional Block Diagram Discussion	57
13.3.4	TSDM Digitizer/Reconstructor Implementation	59
13.3.5	Run-Length Encoder Implementation	63
13.3.6	Implementation of the Run-Length Decoder	66
13.4	Summary and Conclusions	66

Volume III, Exhibit C

14.0	ORBITER/PAYLOAD INTERFACE INVESTIGATIONS	69
14.1	Spacelab ICD Revision	70
14.1.1	HRM Asymmetry and Jitter	70
14.1.2	Data-Dependent Amplitude Variations	76
14.1.3	Transition Density	76
15.0	PAYLOAD/SHUTTLE DATA-COMMUNICATION-LINK HANDBOOK	77
REFERENCES	78

APPENDIX A - MONTHLY PROGRESS REPORTS

11.0 PRELIMINARY SHUTTLE/CENTAUR COMMUNICATION SYSTEM ANALYSIS

In response to technical direction given on June 1, 1981, Axiomatix began the preliminary Centaur system analysis. This analysis was performed under the broad scope of Tasks 2 - 5 and is presented in this section. The preliminary effort was concluded toward the end of 1981 when the Centaur development was not funded by Congress as part of the Shuttle effort. However, in October 1982, Congress reestablished the Centaur as part of the Shuttle project. Because the Centaur communication system was now on a tight schedule, system implementation became the most important task. Therefore, further analysis of the Centaur communication system was performed under Task 15 of Exhibit A and is presented in Section 5.

The results of the Shuttle/Centaur investigations are presented in Axiomatix Report No. R8112-2, "Preliminary Shuttle/Centaur System Analysis," dated December 10, 1981. There are five major areas of analysis, as follows:

- (1) initial acquisition of the transponder by the Shuttle
- (2) potential loss of lock due to antenna transitions
- (3) Centaur antenna-design approaches
- (4) interface circuits between the Centaur and the payload recorder and payload data interleaver
- (5) the hardline Interface Control Document (ICD).

PRELIMINARY CENTAUR SYSTEMS ANALYSIS

FINAL REPORT

Contract No. NAS9-16067, Exhibit B

Technical Monitor: William Teasdale

Prepared for

NASA Lyndon B. Johnson Space Center
Houston, Texas 77058

Prepared by

Robert G. Maronde
Dr. Jack K. Holmes
Dr. Richard S. Iwasaki

Axiomatix
9841 Airport Blvd., Suite 912
Los Angeles, California 90045

Axiomatix Report No. R8112-2
December 10, 1981

TABLE OF CONTENTS

	Page
1.0 INTRODUCTION	1
2.0 BACKGROUND	1
3.0 FINDINGS	4
3.1 Problem 1	4
3.1.1 Solution to Problem 1	4
3.2 Problem 2	4
3.2.1 Solution to Problem 2	6
3.3 Problem 3	6
3.3.1 Solution to Problem 3	7
3.4 Additional Tasks	7
3.5 Conclusions	7

APPENDICES

A	Motorola Transponder Response to One-to-40-ms Transients
A.1	Frequency Drift of Centaur Transponder VCO Frequency due to Antenna Switching
A.2	Potential Centaur Carrier-Loop False-Lock Problem due to Antenna Switching
A.3	Shuttle/Centaur TDRSS User Transponder Response to Antenna-Switching Transients
A.4	Motorola Viewgraphs
A.5	Antenna-Switching Transient Tests on the NASA Standard TDRSS User Transponder
B	Centaur Antenna Approaches
B.1	Shuttle Centaur TT&C Link Margin Trade Study
B.2	A Candidate Centaur Switched-Beam High-Gain Antenna Study
B.3	Configuration Modification of the Preliminary Biconical/Conical Log Spiral Antennas and Phase Synchronization Technique for the Centaur Vehicle
C	Centaur Hardline ICD

1.0 INTRODUCTION

The purpose of this report is to summarize the Axiomatix activities to date on the Shuttle/Centaur program. This document contains both new findings and those previously discussed in Axiomatix Interim Report No. R8109-2, dated September 15, 1981.

2.0 BACKGROUND

The Centaur is stored in the Orbiter payload bay on the Centaur Integrated Support System (CISS), as shown in Figure 2.1. The CISS not only cradles the Centaur prior to deployment but also provides any signal conditioning required to make the Centaur/Orbiter hardware interfaces compatible. In addition, the CISS provides other Centaur functions such as controlling all the avionics safety features and providing all the helium supplies for tank pressurizations.

Upon deployment, the Centaur is raised up and mechanically spring ejected from the CISS which returns with the Orbiter for future use. After arming the reaction control motors, the Centaur is stabilized and, for thermal reasons, has a roll imparted to it. Sometime prior to Centaur/payload separation, the initial roll is significantly increased. The roll rates are still under discussion but, originally, the initial roll rate was 1 RPM at Centaur/Orbiter separation. Just prior to Centaur/payload separation, the 1-RPM rate was to have been increased to 2.9 RPM. Currently, General Dynamics (GD) feels that the initial roll rate will be 0.1 RPM and will be increased to 0.33 RPM prior to Centaur/payload separation.

Once separated from the Orbiter, the Centaur RF links will be either between the Centaur and the Orbiter utilizing the Orbiter Payload Interrogator (PI) or between the Centaur and the ground stations via the TDRSS. The Centaur transponder under consideration by GD is a NASA standard transponder manufactured by Motorola which was previously used by the Goddard Spaceflight Center. Since this particular transponder possesses no false-lock discrimination circuits, the payload specialist aboard the Orbiter must employ a manual acquisition process, as illustrated in Figure 2.2

Briefly, the payload specialist must transmit an unmodulated carrier to the Centaur, achieve return link lock and modulate the carrier. In order to verify proper lock, the operator should also examine the

ORIGINAL PAGE IS
OF POOR QUALITY.

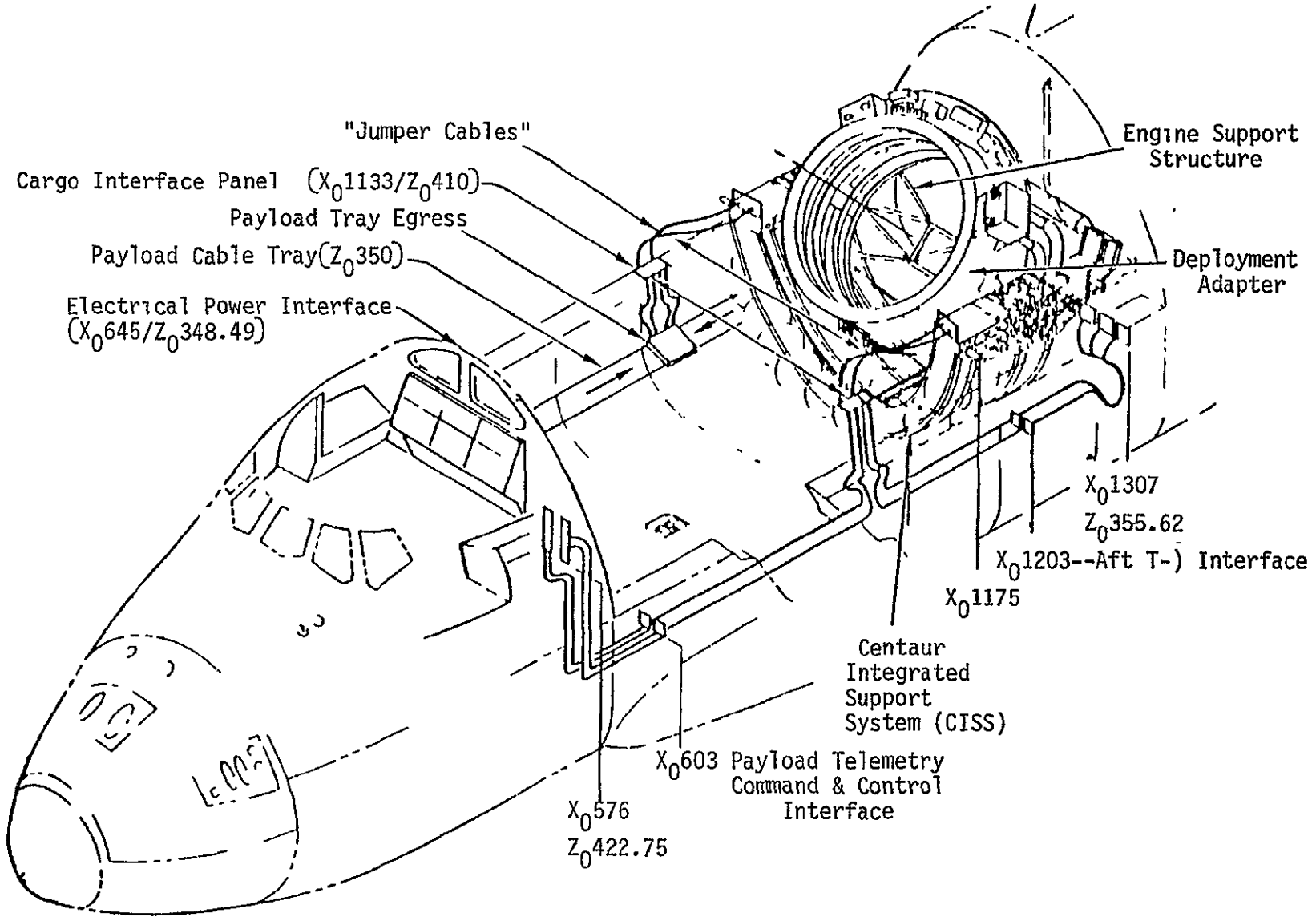
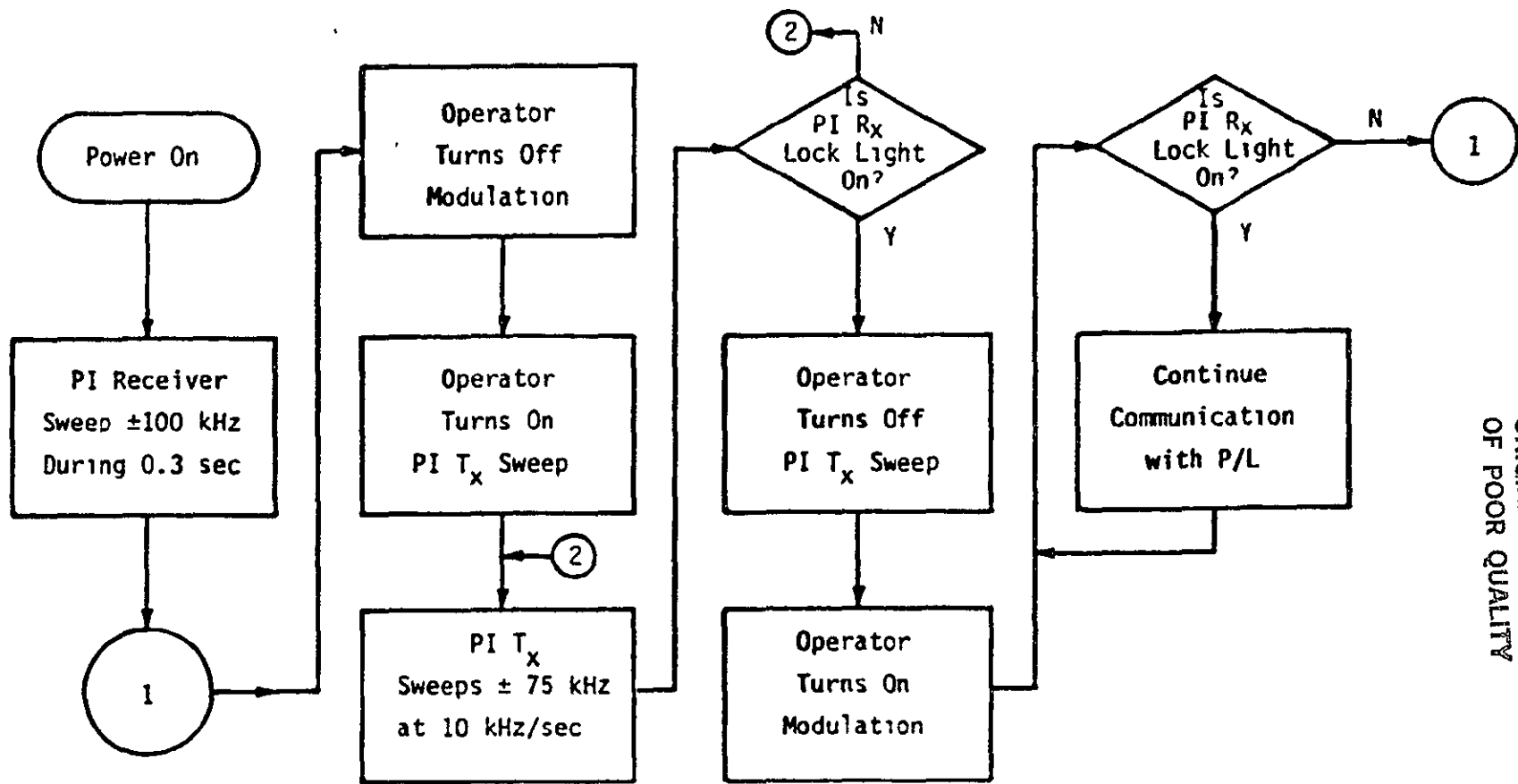


Figure 2.1. Centaur/Payload Bay Interface Overview



ORIGINAL PAGE IS
OF POOR QUALITY

Note 1. PI Receiver can tolerate 50-ms signal dropout without reinitiating the sweep

Note 2. Standard transponder's receiver has ±1400-Hz instantaneous acquisition range

Figure 2.2. Orbiter Payload Interrogator/Payload Transponder Link Acquisition Sequence

return link telemetry. It has been estimated that this manual acquisition procedure could take as long as 30 seconds.

In order to provide full spherical RF coverage for the Centaur, the initial antenna concept was to employ two S-band switchable hemispherical antennas on 1-to-2-foot booms, as shown in Figure 2.3. Since each antenna provides hemispherical coverage, the antennas will switch from one to another and back every Centaur revolution. For example, each antenna will switch every 300 seconds for a roll rate of 0.1 RPM, every 30 seconds for a roll rate of 1 RPM and every 10 seconds for a roll rate of 3 RPM.

3.0 FINDINGS

There are a number of very serious potential problems associated with a Centaur design concept using the Motorola transponder and the two switchable-hemispherical antennas.

3.1 Problem 1

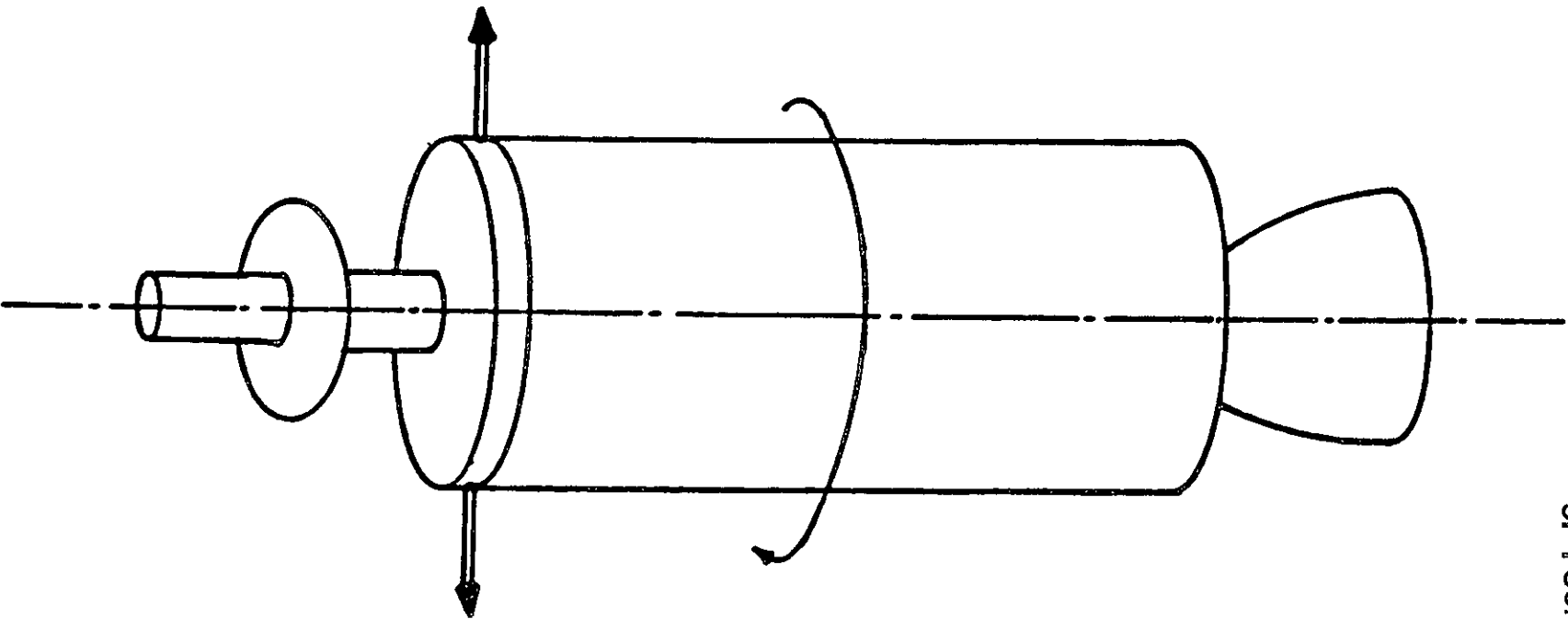
The first problem is the manual acquisition sequence previously described. At the present time, the Orbiter software does not display the Centaur telemetry on the crew CRT to determine if the telemetry is valid. Without verifying the telemetry, it is possible to be false locked on a sideband and not be aware of the situation. It is also possible for the Shuttle/Centaur link to be in the noncoherent mode, i.e., the return link locked on the Centaur TCXO instead of the VCXO, and have no indication of the problem.

3.1.1 Solution to Problem 1

One possible solution is to implement in the Orbiter software the ability to display the Centaur telemetry for the payload specialist on the crew CRT. A second possible solution is to design antifalse-lock circuits into the Motorola transponder.

3.2 Problem 2

The second potential problem dealt with is the ability of the transponder to hold lock in the presence of transients. The GD Functional



ORIGINAL PAGE IS
OF POOR QUALITY

Figure 2.3. Initially Proposed GD Centaur Antenna System

Requirements Document (FRD) 65-03001, Specification for Transponder-Shuttle/Centaur states in paragraph 3.2.1.3.1.8 that antenna-switching transients of 1 to 40 ms shall be accommodated without loss of lock.

3.2.1 Solution to Problem 2

When Axiomatix initially examined the transponder FRD, it appeared that the transponder would lose lock in the presence of transients. After a detailed analysis by Axiomatix with follow-up testing verification by Motorola, however, Axiomatix now feels that the transponder can tolerate 40-ms transients.

Appendix A, Sections 1 and 2, are the results of the Axiomatix transponder analysis. Appendix A, Section 3, is a Motorola analysis, while Sections 4 and 5 are the TDRS mode and STDN mode, respectively, Motorola test results.

The conclusion reached is that, in the presence of 1-to-40-ms transients, the transponder will not lose lock but, of course, any data acquired during the transient will be lost.

3.3 Problem 3

The third problem concerns the phase transients produced when switching from one antenna to another and the low gain of the hemispherical antennas which contribute to a marginal RF link. Since both antennas are many wavelengths apart from each other physically, the geometric differences between the two phase centers will produce a phase transient when the antennas are switched.

Depending on the Centaur roll rate, a very serious potential problem may occur. Consider the magnitude of the impact upon the Shuttle/Centaur RF link should loss of lock occur with the Centaur rolling at a rate of 1 to 3 RPM, which means that the antennas switch every 30 to 10 seconds, respectively. The time for the manual acquisition sequence to establish lock between the Orbiter and Centaur is 30 seconds maximum. The worst-case situation is that, with the long acquisition sequence and the relatively fast antenna switching, the phase transients may be such that Shuttle/Orbiter lock may never be established or, if it is, the payload specialist has no real method with which to determine if true lock has occurred since there is no telemetry to analyze.

3.3.1 Solution to Problem 3

It can easily be seen that, should the roll rates be decreased to the order of 0.1 to 0.33 RPM, the potential problem of not being able to establish lock is resolved. If the roll rates are sufficiently high, however, another antenna concept may be used--not only to minimize switching--but to improve the antenna gain as well.

Appendix B, Section 1, discusses the various GD antenna approaches. Appendix B, Section 2, describes an initial concept which Axiomatix presented at the Centaur Communications Panel meeting at Lewis Research Center, held September 30 to October 1, 1981. After addressing a number of criticisms, Axiomatix presents a second approach for consideration which is discussed in Appendix B, Section 3.

3.4 Additional Tasks

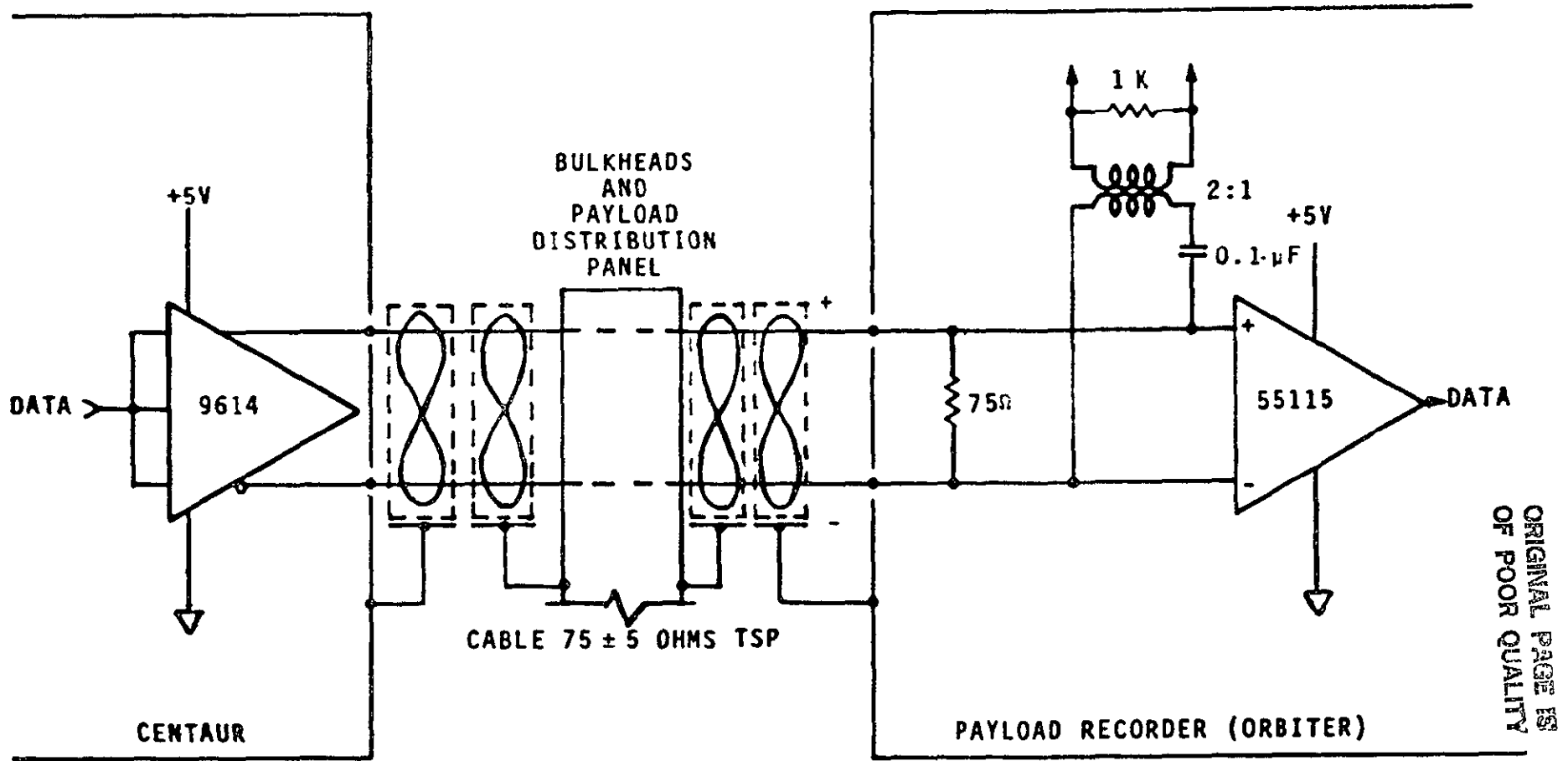
Additional tasks performed by Axiomatix included determining acceptable interface circuits between the Centaur and the payload recorder and the Payload Data Interleaver (PDI). Figures 3.1 and 3.2 show interface circuits that are being used successfully by Boeing for the Inertial Upper Stage (IUS) program, and these circuits should be adaptable for Centaur use.

Also, generation of a hardware Interface Control Document (ICD) was required. Rockwell, working with Axiomatix, produced the hardline ICD shown in Appendix C.

3.5 Conclusions

Axiomatix feels that the Orbiter crew needs some indication that the Centaur/Orbiter link is coherent and, therefore, recommends that the Orbiter software be modified to display Centaur telemetry. Axiomatix has concluded that 1-to-40-ms transients will not cause the transponder to lose lock but, of course, any data during the transient will be lost.

Lastly, Axiomatix is very concerned about the impact that high Centaur roll rates will have on the ability to maintain the Centaur link. Axiomatix has proposed an antenna approach to minimize this problem but also recommends that the required roll rates be established as soon as possible in order to study their effects on link integrity.



ORIGINAL PAGE IS
OF POOR QUALITY

Figure 3.1. Centaur/Payload Recorder Hardline Interface

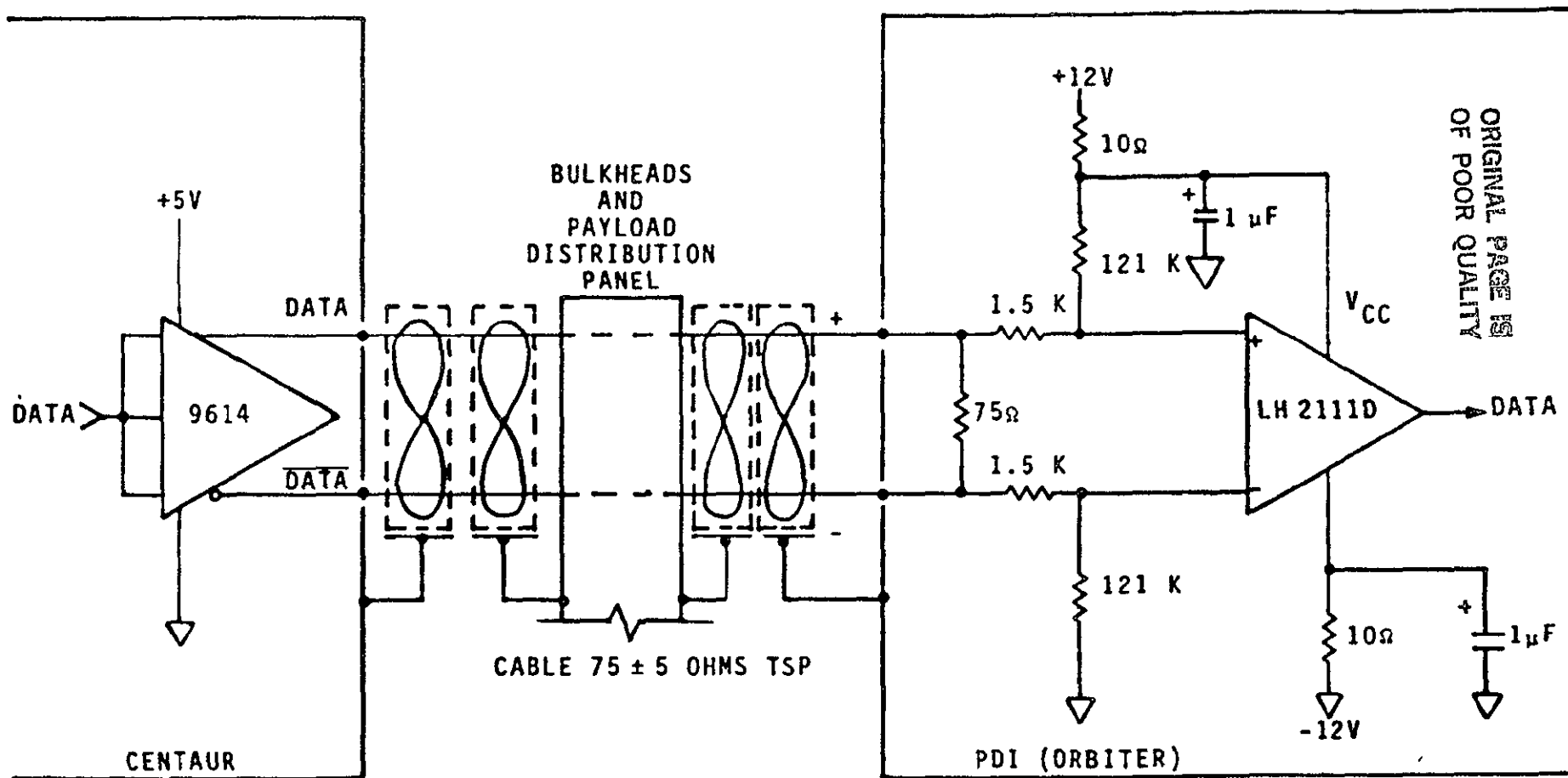


Figure 3.2. Centaur/PDI Hardline Interface

APPENDIX A

MOTOROLA TRANSPONDER RESPONSE TO

ONE-TO-40-MS TRANSIENTS

APPENDIX A.1

FREQUENCY DRIFT OF CENTAUR TRANSPONDER VCO FREQUENCY
DUE TO ANTENNA SWITCHING

Just after dropout, the noise-only input is given by

$$y(t) = \sqrt{2} N_c(t) \cos(\omega_0 t + \theta) + \sqrt{2} N_s(t) \sin(\omega_0 t + \theta) \quad (1)$$

which is an in-phase and quadrature noise representation of bandpass noise centered at angular frequency ω_0 . After heterodyning by the VCO frequency, the error signal is of the form

$$\epsilon(t) = N_c(t) \cos\phi + N_s(t) \sin\phi + V_{dc} \quad (2)$$

where ϕ is the phase difference between the VCO frequency and the reference phase angle of the noise process. The multiplier offset bias is denoted by V_{dc} . It can be shown that $\epsilon(t)$ has the statistics of $N_c(t)$ or $N_s(t)$, i.e., bandlimited white Gaussian noise. Therefore, we model the error signal by

$$\epsilon(t) = N'(t) + V_{dc} \quad (3)$$

where $N'(t)$ has the same statistics as $N_c(t)$. Using Heaviside operator notation in the variable s , for the VCO phase estimate, we have

$$\hat{\theta}(t) = \frac{K_m K_{VCO} F(s)}{s} (N'(t) + V_{dc}) \quad (4)$$

where K_m is the multiplier gain and K_{VCO} is the VCO gain constant having units of radians per second per volt. Since the Centaur transponder loop is specified as a second-order loop, we can model the loop filter as a passive second-order loop filter

$$F(s) = \frac{1 + \tau_2 s}{1 + \tau_1 s} \quad (5)$$

where τ_1 and τ_2 are the time constants of the loop filter. This can be rewritten as

$$F(s) = F_0 \left[1 + \frac{\frac{1}{\tau_2} - \frac{1}{\tau_1}}{s + \frac{1}{\tau_1}} \right] \quad (6)$$

where

$$F_0 = \frac{\tau_2}{\tau_1} \quad (7)$$

Denoting $K_m K_{VCO}$ by K and using (6) in (4) yields

$$\dot{\hat{e}}(t) = \left\{ KF_0 + KF_0 \left[\frac{\frac{1}{\tau_2} - \frac{1}{\tau_1}}{s + \frac{1}{\tau_1}} \right] \right\} \{ v_{dc} + N'(t) \} \quad (8)$$

Now since

$$\frac{1}{s + \frac{1}{\tau_1}} g(t) \leftrightarrow \int_0^t e^{-(t-\tau)/\tau_1} g(\tau) d\tau + C_0 e^{-t/\tau_1} \quad (9)$$

where the third term is due to the homogeneous solution associated with the differential equation

$$e_i(t) = \dot{e}_0(t) + \frac{1}{\tau_1} e_0(t) \quad (10)$$

We have that

$$\dot{\hat{e}}(t) = \left\{ KF_0 v_{dc} + KF_0 N'(t) + KF_0 \int_0^t e^{-(t-\tau)/\tau_1} (v_{dc} + N'(\tau)) d\tau + C_0 e^{-t/\tau_1} \right\} \quad (11)$$

Since v_{dc} is unknown, we will assume that it is negligible*, thus allowing us to approximate (10) by

*This assumption minimizes the worst-case out-of-lock VCO drift rate

$$\dot{\hat{\theta}}(t) = KF_0 N'(t) + KF_0 \frac{\frac{1}{\tau_2} - \frac{1}{\tau_1}}{s + \frac{1}{\tau_1}} \int_0^t e^{-(t-\tau)/\tau_1} N'(\tau) d\tau + C_0 e^{-t/\tau_1} \quad (12)$$

implied by (9).

From (12), we see that the value of $\dot{\hat{\theta}}(t)$ at any time t is composed of the original noise process $N'(t)$ plus a filtered version of the noise process. Consequently, the noise is large compared to the dc loop control voltage (nominally zero in lock). Furthermore, it appears that the VCO noise voltage changes appreciably with time, whereas the dc component of the VCO voltage changes slowly, with a time constant τ_1 . When the loop is in lock (signal is present), the thermal noise is again quite large; however, the loop can tolerate this condition since phase tracking "sees" one more integration than frequency tracking. Therefore, we consider the dc voltage on the VCO as the important parameter in reacquisition. At $t=0$, the dc value of the VCO frequency is $\Delta\omega_0$ (relative to the rest VCO frequency) so that, at $t=0$,

$$C_0 = \Delta\omega_0 \quad (13)$$

and the change, or error, in the VCO frequency is given by

$$\delta\omega(t) = \Delta\omega_0 - \Delta\omega_0 e^{-t/\tau_1} \quad (14)$$

In order to estimate the parameter τ_1 , we must estimate* some loop parameters. First, since $B_L = 500$ Hz, we can determine the value of ω_n via

$$\omega_n = \frac{2B_L}{\left(\zeta + \frac{1}{4\zeta}\right)} \text{ rad/sec} \quad (15)$$

*The parameters were unknown at the time of this writing.

Using $\zeta = 0.707$ in (15) yields

$$\omega_n = 942.9 \text{ rad/sec} \quad (16)$$

From [1], we have that

$$\omega_n = \sqrt{\frac{AK}{\tau_1}} \text{ rad/sec} \quad (17)$$

A typical value of AK , the open-loop gain, is 3.25×10^5 , so that τ_1 can be solved to be

$$\tau_1 = \frac{\sqrt{AK}}{\omega_n} \quad (18)$$

or

$$\tau_1 = 0.367 \text{ sec} \quad (19)$$

Now, if the VCO swing is ± 100 kHz (from [1], subsection 3 2.1.3 2.9) and the frequency offset is one-half the maximum, or 50 kHz, then $\Delta\omega_0 = 2\pi$ (50 kHz) From (14), we can write

$$\delta f(t) = \Delta f_0 - \Delta f_0 e^{-t/\tau_1} \quad \left(\Delta f_0 = \frac{\Delta\omega_0}{2\pi} \right) \quad (20)$$

Hence, at time t , we have

$$\delta f(t) = 50 \text{ kHz} \left[1 - e^{-2.72t} \right] \quad (21)$$

For various values of t , $\delta f(t)$ is tabulated in Table 1.

We see from Table 1 that, at 40 ms, the frequency generated with a 50-kHz off-rest frequency is 5,155 Hz, or over 10 loop bandwidths. It is very improbable that a phase-lock-loop will reacquire when it drifts 10 loop bandwidths away from the carrier since the practical limit is something like one loop bandwidth away. However, a few millisecond dropout would probably not cause loss of lock.

Table 1. Mean Frequency Offsets as a Function of Dropout Time

t (ms)	δf (Hz)
1	135.3
2	271.3
3	406.3
4	675.4
10	1,341.7
20	2,647.3
30	3,918
40	5,154.5

It is to be noted that, under large dropout time conditions (40 ms), the carrier phase shift due to switching Centaur antennas is not an additional concern since the frequency drift is about 5000 Hz!

Also note that, if the frequency drift is 5155 Hz in 0.04 seconds, the drift rate is $\dot{f} \approx 129,000$ Hz/s. Therefore, the phase change assuming a linear drift rate is

$$\Delta\theta(t) = \int_0^t 129000u \, du = 64500t^2 \text{ cycles}$$

so that, after about 4 ms, the carrier phase has drifted by one cycle. Hence, the phase shift due to the VCO drift during dropout is as important as the antenna-induced phase shifts for dropouts greater than 4 ms. Furthermore, only phase shifts of modulo-one cycle are important.

REFERENCES

1. W. C. Lindsey, Synchronization Systems in Communication and Control, Chapter 4, Prentice-Hall, 1972

APPENDIX A.2

POTENTIAL CENTAUR CARRIER-LOOP FALSE-LOCK PROBLEM
DUE TO ANTENNA SWITCHING

ORIGINAL PAGE IS
OF POOR QUALITY

Note that

$$\cos \left[\theta \sin \omega_2 t \right] = J_0(\theta) + \sum_{\substack{n=2 \\ n \text{ even}}}^{\infty} J_n(\theta) \cos(n \omega_2 t) \quad (3)$$

$$\sin \left[\theta \sin \omega_2 t \right] = \sum_{\substack{n=1 \\ n \text{ odd}}}^{\infty} 2 J_n(\theta) \sin(n \omega_2 t) \quad (4)$$

$$\text{sq}(\omega_1 t) = \frac{4}{\pi} \cos \omega_1 t - \frac{4}{3\pi} \cos 3 \omega_1 t + \frac{4}{5\pi} \cos 5 \omega_1 t + \dots \quad (5)$$

Using (3), (4) and (5) in (2) yields

$$\begin{aligned} y(t) = & \sqrt{2}A \sin \omega_0 t \left\{ J_0(\theta) + \sum_{\substack{n=2 \\ n \text{ even}}}^{\infty} J_n(\theta) \cos n \omega_2 t \right\} + \sqrt{2}A \cos \omega_0 t \\ & \times \left\{ \frac{4}{\pi} J_1(\theta) \sin \left[(\omega_1 + \omega_2) t \right] - \frac{4}{\pi} J_1(\theta) \sin \left[(\omega_1 - \omega_2) t \right] \right. \\ & - \frac{4}{3\pi} J_1(\theta) \sin \left[(\omega_1 + 3\omega_2) t \right] + \frac{4}{3\pi} J_1(\theta) \sin \left[(\omega_1 - 3\omega_2) t \right] \\ & \left. + \frac{4}{5\pi} J_1(\theta) \sin \left[(\omega_1 + 5\omega_2) t \right] + \frac{4}{5\pi} J_1(\theta) \sin \left[(\omega_1 - 5\omega_2) t \right] + \dots \right\} \quad (6) \end{aligned}$$

In (6), we have indicated only the significant terms between the carrier frequency and the 16-kHz subcarrier frequency. Figure 1 illustrates the spectral distribution of the Shuttle-to-Centaur link when the data is on the idle pattern (which is a square wave of 500 Hz).

Using a nominal value of θ of 1 radian yields

$$\frac{P_{f_0 - f_1}}{P_c} = -8.7 \text{ dB} \quad \frac{P_{f_0 - 3f_1}}{P_c} = -18.2 \text{ dB} \quad , \quad \frac{P_{f_0 - 5f_1}}{P_c} = -22.7 \text{ dB} \quad (7)$$

Thus, we see that the sideband power diminishes quite rapidly as we approach the carrier from the upper 16-kHz subcarrier, but the main sidebands are down only 8.7 dB from the carrier.

ORIGINAL PAGE IS
OF POOR QUALITY

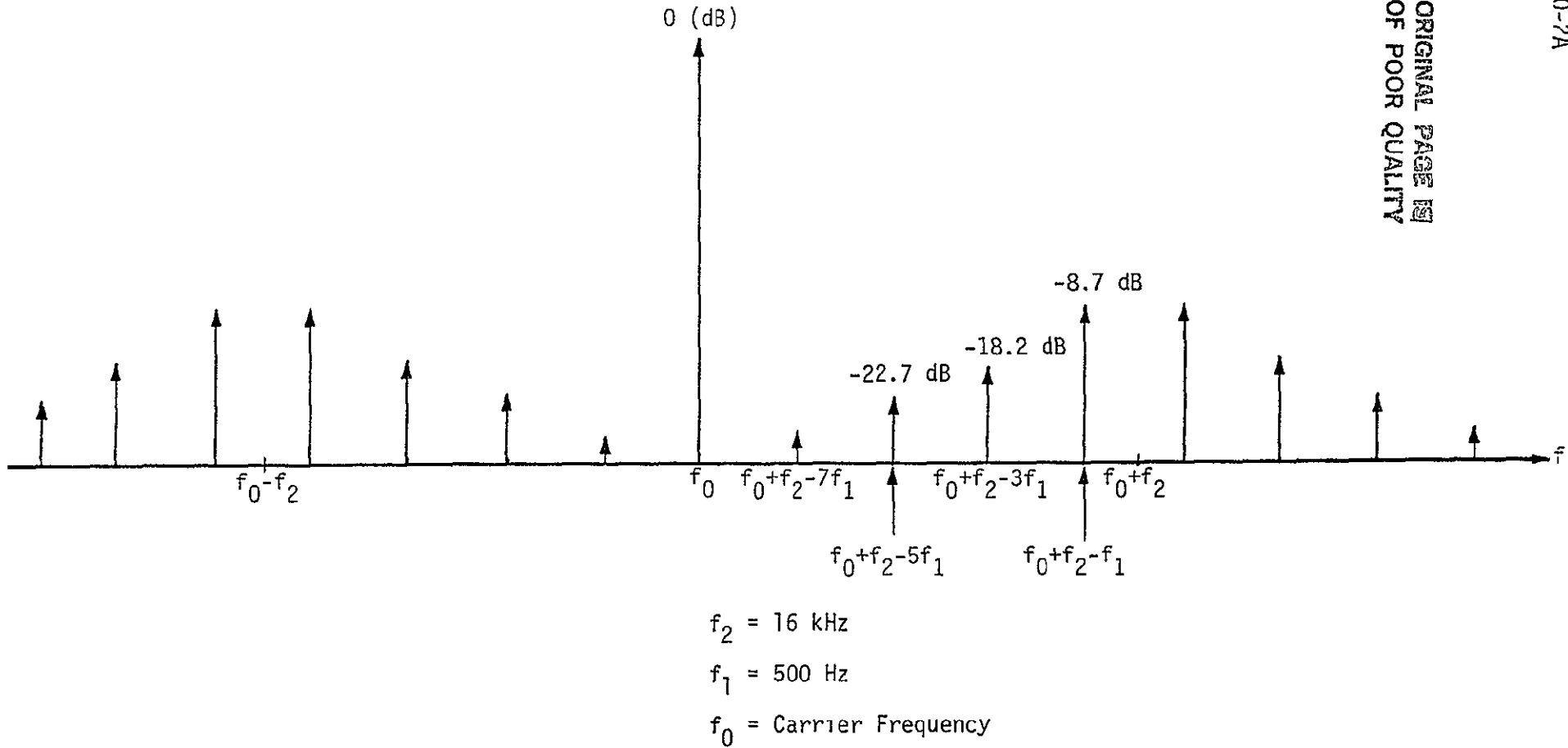


Figure 1. Spectral Distribution Near f_0 in the Idle Pattern (relative levels)

3.0 ANALYSIS--VCO DRIFT

We can now determine how far the Centaur loop VCXO can drift during a 40-ms dropout. Using the method discussed in [1] and the actual* closed-loop parameter values of [2], we can determine the VCXO frequency drift during the (maximum time) 40-ms dropout due to antenna switching. Consider the assumed second-order passive loop filter of the form

$$F(s) = G \frac{1 + \tau_2 s}{1 + \tau_1 s} \quad (8)$$

which is illustrated in Figure 2. For this loop filter, when the input e_1 was nonzero and constant for a long time, then suddenly drops to zero, the output voltage drops quickly to $(R_3)/(R_2+R_3) V_0$, where V_0 is the previous (before dropout) voltage, then decays from $(R_3)/(R_2+R_3) V_0$ to zero, as shown in Figure 3.

For the Centaur loop, we have the following loop parameters [2]:

$$\begin{array}{ll} B_L = 500 \text{ Hz} & K_{DC} = 69.1 \\ \zeta = 0.707 & \tau_1 = 16.2 \text{ sec} \\ \omega_n = 943 \text{ rad/sec} & \text{Loop gain} = 1.44 \times 10^7 \end{array}$$

By calculation,

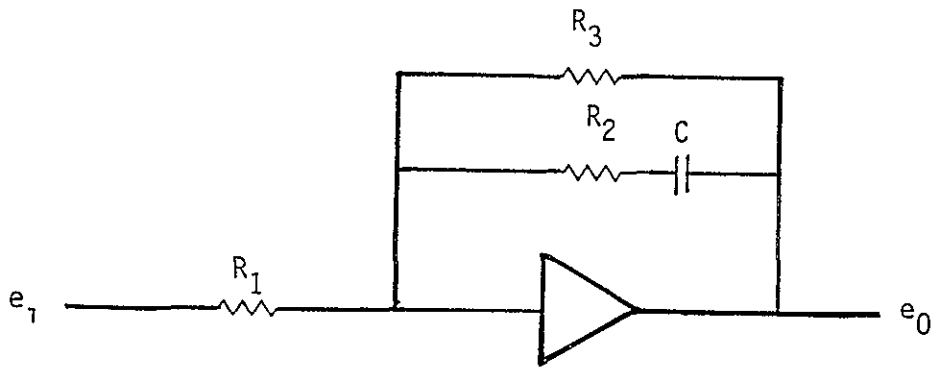
$$\frac{\tau_2}{\tau_3} \ll 1 \implies \frac{R_2}{R_2 + R_3} \cong 0 \quad (9)$$

therefore, the frequency decays in the form

$$\delta f(t) = \Delta f \left[1 - e^{-t/\tau_1} \right] \quad (10)$$

Using 100 kHz as the nominal maximum value of Δf along with $\tau_1 = 16.2$ seconds yields, after 40 ms,

* As opposed to the estimated time constant values of [1].



$$F(s) = \frac{R_3}{R_1} \frac{(1 + \tau_2 s)}{1 + \tau_1 s}$$

$$\tau_2 = R_2 C$$

$$\tau_1 = (R_3 + R_2) C$$

Figure 2. Passive Second-Order Loop Filter Model

ORIGINAL PAGE IS
OF POOR QUALITY

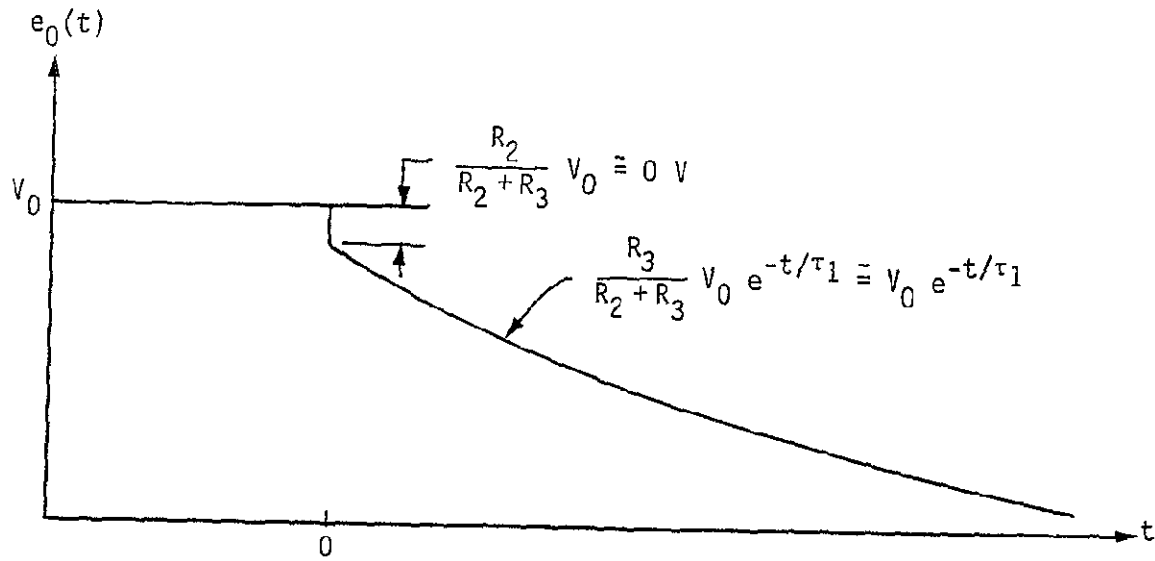


Figure 3. Output Loop Filter Response Due to a Sudden Zeroing of the Input

$$\delta f(0.04) = 100 \times 10^3 \left[1 - e^{-(0.04)/16.2} \right] = 246.6 \text{ Hz} \quad (11)$$

Since this value is about one-half the loop bandwidth, it is very likely that the loop will acquire in a few milliseconds after the signal reappears. Also, since the nearest significant spectral line is at 13.5 kHz from the center frequency, false lock is quite unlikely.

4.0 CONCLUSION

Although the false-lock potential exists (see Figure 1), the loop should drift only about 250 Hz in the worst-case 40-ms outage during the antenna switching. Since this frequency offset (247 Hz) is only one-half the loop bandwidth, and far from any potential false-lock points, the loop should reacquire in a few milliseconds.

References

1. J. K. Holmes, "Frequency Drift of Centaur Transponder VCO Frequency Due to Antenna Switching," Axiomatic Technical Memo No. M8109-2, September 25, 1981.
2. J. R. Nelson, "Shuttle/Centaur TDRSS User Transponder Response To Antenna Switching Transients," Motorola Report No. PIA 3123-700, September 22, 1981.

APPENDIX A.3

SHUTTLE/CENTAUR TDRSS USER TRANSPONDER RESPONSE
TO ANTENNA-SWITCHING TRANSIENTS



22 September 1981

PIA 3123-700

SHUTTLE/CENTAUR TDRSS USER TRANSPONDER
RESPONSE TO ANTENNA SWITCHING TRANSIENTS

Prepared for
GENERAL DYNAMICS/CONVAIR

Prepared by
John R. Nelson

SHUTTLE/CENTAUR
TDRSS USER TRANSPONDER
RESPONSE TO ANTENNA SWITCHING TRANSIENTS

The TDRSS User Transponder will accommodate antenna switching transients of up to 40 milliseconds duration without indicating loss-of-lock and without requiring initiation of the receiver acquisition sequence. A transient is considered to be a momentary loss of forward link signal where the phase of the re-established signal is random (0° - 360°) relative to the previously received signal.

The antenna switching transient will cause the receiver tracking phase-locked loop (PLL) to drop lock. When the signal is re-established after 40 msec or less, the PLL will relock within milliseconds (as detailed in the appendix). The RECEIVER LOCK telemetry signal has an out-of-lock sensor time constant of approximately two seconds. The 40 msec transient will therefore not cause an out-of-lock indication and will not re-initiate the receiver acquisition sequence.

The forward link command data will, of course, be lost during the switching transient. Depending on the duration of the transient, the command detector unit (CDU) LOCK INDICATOR may or may not indicate loss of CDU lock for STDN mode operation. In the TDRSS mode the CDU will remain locked to the internally generated 16 kHz command subcarrier and the CDU LOCK INDICATOR will not indicate loss of lock. In either mode, however, the CDU may not be able to maintain internal bit synchronization during the transient drop-out period. It will therefore be necessary to supply the 132 bit minimum alternate one/zero command acquisition sequence following the antenna switching transient.

APPENDIX

ANALYSIS OF RECEIVER TRACKING LOOP RELOCK FOLLOWING ANTENNA SWITCHING TRANSIENTS

The accommodation of antenna switching transients of up to 40 msec duration is based on the fact that the receiver tracking phase-locked loop (PLL) will immediately relock after the switching transient. The PLL will relock if the frequency error is within the pull-in range of the loop, regardless of the phase relationship between the pre-transient and post-transient signals. Since the received signal frequency is the same before and after the transient*, the only potential source for frequency error is receiver VCXO frequency drift during the switching transient. These parameters must be examined separately for the STDN and TDRSS modes.

* If the forward link signal is changing frequency (sweeping) at the time of the antenna switching transient, then the post-transient frequency will actually be different from the pre-transient frequency. For TDRSS mode operation, the maximum sweep rate is only 70 Hz/sec and the PLL will still relock practically instantaneously following the transient. In the STDN mode, however, the analysis becomes quite complicated because the PLL must pull in and lock to a signal which is sweeping farther away in frequency. It is estimated that the 40 msec antenna switching transients can be accommodated for STDN sweep rates up to approximately 13 kHz/sec.

STDN MODE

The STDN mode tracking loop parameters are as follows:

Bandwidth (β_L)	= 500 Hz
Damping factor (ζ)	= .707
Natural frequency (ω_n)	= 943 rad/sec
Loop filter DC gain (K_{DC})	= 69.1
Loop filter pole time constant (τ_p)	= 16.2 sec
VCXO gain constant (K_v)	= 66300 Hz/v at 22F1F
Loop gain (A)	= 1.44×10^7

Worst case frequency drift during the antenna switching transient will take place when the forward link frequency is at a tracking range extreme (± 150 kHz). If the VCXO exhibits worst case temperature stability (± 14 ppm), the static phase error (SPE) to the VCXO under quiescent conditions would be

$$(150000 \text{ Hz} + 29650 \text{ Hz}) / (66300 \text{ Hz/V}) = 2.710 \text{ Vdc}$$

and the input to the loop filter amplifier would be

$$2.710 \text{ Vdc} / 69.1 = 39.2 \text{ mVdc}$$

If the loop filter input voltage takes a step from V_1 to V_2 , the output (V_{SPE}) responds as follows:

$$\Delta V_{SPE}(t) = K_{DC} (V_2 - V_1) (1 - e^{-t/\tau_p})$$

As indicated above, worst case V_1 is 39.2 mVdc. Worst case V_2 would be an input offset voltage of -20 mVdc. Therefore,

$$\begin{aligned} \Delta V_{SPE} &= 69.1 (.020 + .0392)(1 - e^{-.040/16.2}) \\ &= 4.09 (1 - .9975) \\ &= .010 \text{ Vdc} \end{aligned}$$

STDN MODE—Continued

This ΔV_{SPE} will produce a frequency drift in the loop of $(.010 \text{ Vdc})(66300 \text{ Hz/V}) = 663 \text{ Hz}$. The loop will relock practically instantaneously for frequency offsets less than $2\zeta f_n = 212 \text{ Hz}$. The loop will pull in to lock for offsets within $\left[\frac{2}{\pi}\zeta f_n A\right]^2 = 31180 \text{ Hz}$, and will pull into lock from 663 Hz with pull-in time

$\frac{(\Delta f)^2}{4\pi\zeta f_n^3} = 14.7 \text{ msec}$. The time for the PLL to relock is therefore much less than the lock detector time constant of two seconds and the receiver will not give an out-of-lock indication.

TDRSS MODE

The TDRSS mode tracking loop parameters at or above the nominal 1000 bps command threshold (-126 dBm) are as follows:

Bandwidth (β_L)	= 42 Hz
Damping factor (ζ)	= .90
Natural frequency (ω_n)	= 77 rad/sec
Loop filter integrator time constant (τ)	= 24.3 sec
VCXO gain constant (K_V)	6300 Hz/V at 221F1
Loop gain (A)	= 1.42×10^5

Worse case frequency drift during the antenna switching transient corresponds to worst case dc offset voltages in the dc-coupled loop filter circuits. For a net dc offset voltage V_1 at the loop filter input, the output (V_{SPE}) responds as follows:

$$\Delta V_{SPE}(t) = \frac{V_1 t}{\tau}$$

The worst case dc offset voltage is expected to be 20 mVdc, so

$$\Delta V_{SPE}(.040) = \frac{(20\text{mVdc})(.040)}{24.3} = .04 \text{ mVdc}$$

This ΔV_{SPE} will produce a frequency drift in the loop of $(.04 \text{ mV})(66300 \text{ Hz/V}) = 26 \text{ Hz}$. The loop will relock practically instantaneously for frequency offsets less than $2\zeta f_n = 22 \text{ Hz}$. The time for the PLL to relock is therefore much less than the lock detector time constant of two seconds and the receiver will not give an out-of-lock indication.

APPENDIX A.4

‡

MOTOROLA VIEWGRAPHS



SHUTTLE/CENTAUR TDRSS USER TRANSPONDER
RESPONSE TO ANTENNA-SWITCHING TRANSIENTS

- ANTENNA-SWITCHING TRANSIENTS (SIGNAL DROPOUTS)
OF UP TO 40 MSEC DURATION SHALL BE ACCOMMODATED
- RECEIVER LOCK TELEMETRY SHALL NOT INDICATE LOSS OF LOCK
- INITIATION OF ACQUISITION SEQUENCE SHALL NOT BE REQUIRED



ANALYSIS

- TRACKING LOOP WILL DROP LOCK AND THEN WILL RELOCK WITHIN A FEW MSEC OF END OF TRANSIENT, EVEN UNDER WORST-CASE CONDITIONS (STDN OR TDRSS MODE)
- OUT-OF-LOCK SENSOR TIME CONSTANT IS APPROXIMATELY 2 SEC AND WILL NOT INDICATE OUT-OF-LOCK
- COMMAND DATA WILL BE LOST DURING TRANSIENT AND RELOCK TIME, CDU MAY OR MAY NOT INDICATE OUT-OF-LOCK. COMMAND BIT SYNC MUST BE RE-ESTABLISHED (132 BITS OF 1/0).



DATA (TDRSS MODE)

<u>FORWARD LINK LEVEL</u>	<u>DATA RATE</u>	<u>TRANSIENT DURATION REQUIRED FOR OUT-OF-LOCK INDICATION</u>
-120 dBm	LOW	2.2 SEC
-135 dBm	LOW	0.7 SEC
-138 dBm	LOW	0.2 SEC
-126 dBm	HIGH	1.6 SEC

NOTES:

1. TRACKING THRESHOLD WAS -139 dBm
2. FORWARD LINK SWEEPING ± 700 Hz AT 70 Hz/SEC

APPENDIX A.5

ANTENNA-SWITCHING TRANSIENT TESTS ON THE
NASA STANDARD TDRSS USER TRANSPONDER



27 OCTOBER 1981

PIA 3123-700

ANTENNA SWITCHING TRANSIENT TESTS
ON THE
NASA STANDARD TDRSS USER TRANSPONDER

Prepared for
GENERAL DYNAMICS/CONVAIR

Prepared by
John R. Nelson

Antenna Switching Transient Tests
on the

NASA Standard TDRSS User Transponder

Shuttle/Centaur antenna switching will cause level and phase transients in the received signal supplied to the transponder. These transients are estimated to be less than 5 msec in duration when "make-before-break" antenna switches are employed.

Previous test data and analysis have shown conclusively that these antenna switching transients will cause no loss-of-lock indication or reacquisition sequence for the TDRSS mode of operation. Motorola has now also conducted a series of tests wherein these transient conditions were simulated for the STDN mode of operation and the transponder behavior was characterized. The transponder under test was a flight model NASA Standard TDRSS User Transponder which was configured for a STDN mode command data rate of 2 kbps and a TDRSS mode command data rate of 1 kbps.

The tests described herein were performed under the worst-case conditions for the STDN-ONLY mode of operation. The forward link signal level was -112 dBm and the command data was alternate 1/0 at 2 kbps. Tests were conducted at various forward link frequencies, command modulation indices, and transient durations. At least 25 test trials were conducted for each test condition. The test conditions and test results are summarized in Table 1.

The test data shows that the transponder will accommodate antenna switching transients of more than 50 msec duration (10 times the specified duration) without indicating loss-of-lock and without requiring initiation of the receiver acquisition sequence.

TABLE 1
Antenna Swtiching Transient Test Results

TEST CONDITIONS ¹

<u>Frequency</u>	<u>Command Mod. Index</u>	<u>Transient Duration</u>	<u>Results</u>
f_c ²	1.0 rad	50 msec	No out-of-lock or false lock.
		100 msec	No out-of-lock or false lock
		200 msec	Drop lock and relock to lower 16 kHz sideband.
f_c	1.3 rad	50 msec	No out-of-lock or false lock.
		100 msec	No out-of-lock or false lock
		200 msec	Drop lock and relock to lower 16 kHz sideband
f_c+150 kHz	1.0 rad	50 msec	No out-of-lock or false lock
		100 msec	Dropped lock and went to center rest frequency without reacquisition once out of 50 trials. No out-of-lock or false lock for 49 out of 50 trials.
		200 msec	Drop lock and relock to lower 16 kHz sideband
f_c+150 kHz	1.3 rad	50 msec	No out-of-lock or false lock
		100 msec	Dropped lock and went to center rest frequency without reacquisition for 12 out of 25 trials.
		200 msec	Drop lock and relock to lower 16 kHz sideband
f_c-150 kHz	1.0 rad	50 msec	No out-of-lock or false lock
		100 msec	No out-of-lock or false lock
		200 msec	Drop lock and relock to lower 16 kHz sideband
f_c-150 kHz	1.3 rad	50 msec	No out-of-lock or false lock
		100 msec	No out-of-lock or false lock
		200 msec	Drop lock and relock to lower 16 kHz sideband 1 out of 10 trials.

NOTES:

1. For all tests, forward link signal is -112 dBm with alternate 1/0 command data at 2 kbps.
2. f_c = design center frequency.

APPENDIX B

CENTAUR ANTENNA APPROACHES

APPENDIX B.1

SHUTTLE/CENTAUR TT&C LINK MARGIN TRADE STUDY

SHUTTLE/CENTAUR TT&C LINK MARGIN TRADE STUDY

GENERAL DYNAMICS
Convair Division

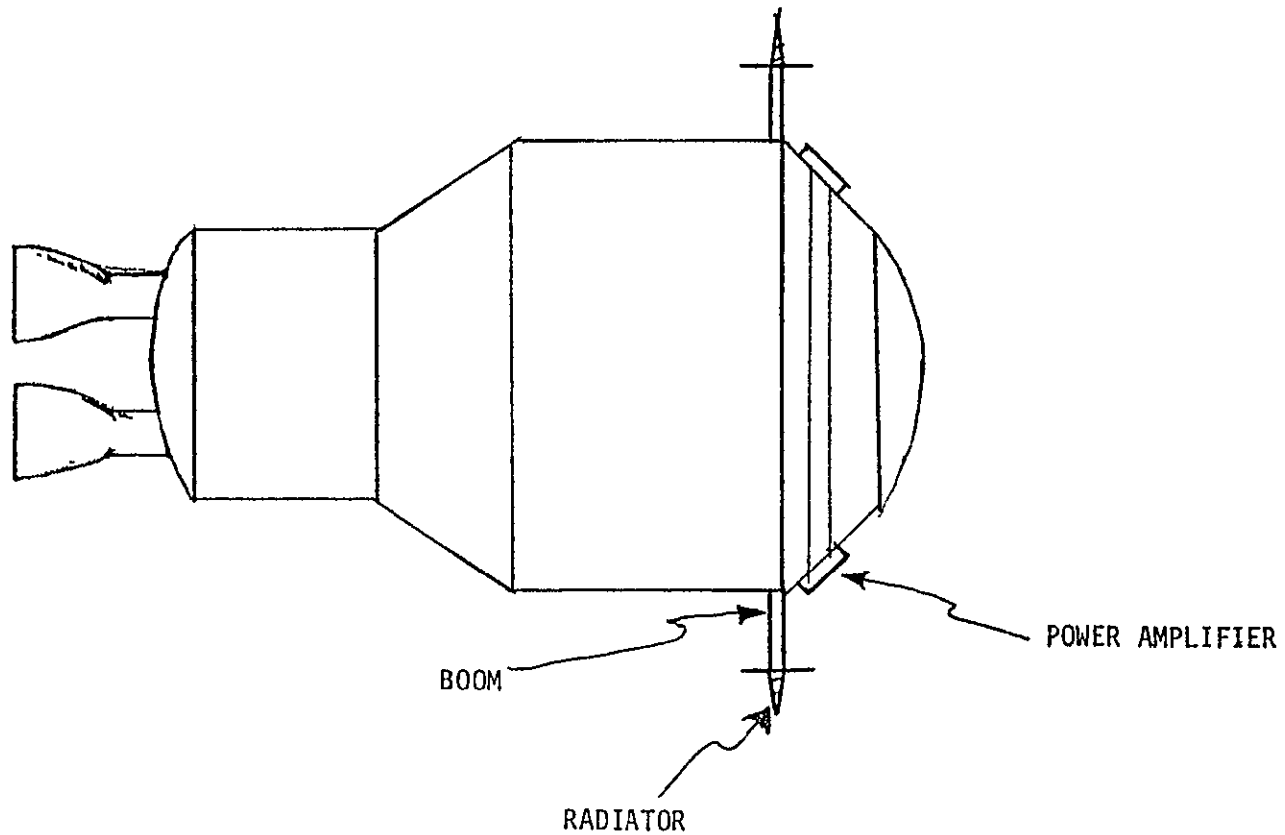
ANTENNAS	SWITCHING ANTENNA	STEERABLE ANTENNA	COMBINATION ANTENNA
TYPE	CIRCUMFERENTIAL ARRAY	HELICAL ANTENNA W/2 AXIS DRIVE	AUTONOMOUS OMNI-DIRECTIONAL ANTENNA
DESCRIPTION	SERIES OF RADIATORS AROUND CIRCUMFERENCE OF VEHICLE SWITCHED TO ESTABLISH AND MAINTAIN LINK.	HIGH GAIN HELIX POINTED BY MEANS OF TWO AXIS DRIVE CONTROLLED BY DCU.	30 MICROSTRIP RADIATORS USED WITH SWITCHING POWER DIVIDERS TO PRODUCE STEERABLE BEAM. MICROPROCESSOR CONTROLLED.
PARTS	SERIES OF CIRCUMFERENTIAL RADIATORS RF SWITCHES AS REQUIRED 1 SWITCHING INTERFACE BOX	2 HELICAL RADIATORS 2 TWO-AXIS MOTOR DRIVES 1 DRIVE INTERFACE BOX	2 TRUNCATED SPHERE RADIATOR ARRAYS 1 MICROPROCESSOR CONTROLLER
DEVELOPMENT STATUS	CONCEPT PROVEN. HARDWARE NOT YET DEVELOPED. SWITCHING ALGORITHM NOT DEVELOPED.	HARDWARE DESIGN PARTIALLY ACCOMPLISHED. INTERFACE BOX DESIGN REQUIRED.	HARDWARE DESIGN PRIMARILY ACCOMPLISHED. SOFTWARE DESIGN REQUIRED.
ADVANTAGES	LOW PROFILE NO LARGE RF AMPLIFIER REQUIRED. SIMPLE HARDWARE.	+13 dBi GAIN OVER 27° BEAMWIDTH	+7 dBi GAIN OVER 47° BEAMWIDTH. MINIMAL PHASE DISTORTION WITH MOVING BEAM.
DISADVANTAGES	SPECIFIC HARDWARE UNDEVELOPED DEVELOPMENT, QUALIFICATION AND SWITCHING ALGORITHM REQUIRED	MECHANICAL STEERING UNIT MORE PRONE TO FAILURE THAN ELECTRONIC STEERING UNIT.	HEAVY (10#/ARRAY) ANTENNA WOULD REQUIRE STRONGER SUPPORT BOOM.
ESTIMATED DELIVERY DATE	LATE '83 TO EARLY '84	EARLY TO MID '83	MID '83 TO EARLY '84

SHUTTLE/CENTAUR TT&C LINK MARGIN TRADE STUDY

AMPLIFIERS	SOLID-STATE AMPS		TWT AMPS
TYPE	DUAL 20 WATT AMPS	GANGED 20 WATT AMPS	130 WATT TWT
DESCRIPTION	AN AMP AT THE BASE OF EACH ANTENNA BOOM THIS MINIMIZES CABLE LOSS	TWO OR MORE AMPLIFIERS WITH OUTPUTS PARALLELED TO INCREASE EFFECTIVE OUTPUT PWR	DERIVATIVE OF SHUTTLE/ ORBITER POWER AMPLIFIER
PARTS	2 - 20 WATT RF POWER AMPLIFIERS	2 OR MORE 20 WATT POWER AMPLIFIERS	1 - 130 WATT NON-REDUNDANT TWT.
DEVELOPMENT STATUS	CURRENTLY AVAILABLE FROM SEVERAL VENDORS. FURTHER QUALIFICATION MAY BE REQUIRED.		RECONFIGURING AND REQUALIFICATION REQUIRED.
ADVANTAGES	DRASTICALLY REDUCES CABLE LOSSES	INCREASE IN POWER LIMITED ONLY TO SPACE AVAILABLE.	MAKES LINK WITH POWER TO SPARE. POTENTIAL ABILITY TO INCREASE DATA RATE.
DISADVANTAGES	LINK STILL MARGINAL ADDITIONAL GAIN REQUIRED.	INCREASE IN POWER NOT DIRECTLY ADDITIVE. (20 + 20 < 40) WEIGHT AND HEAT GO UP AS A PERFECT SUM	WILL NEED HIGH POWER ANTENNA AND SWITCHES. LARGE HEAT DISSIPATION PROBLEM.
ESTIMATED DELIVERY DATE	LATE '83, EARLY '84	LATE '83, EARLY '84	LATE '83, EARLY '84

ANTENNA LINK MARGIN TRADE STUDY

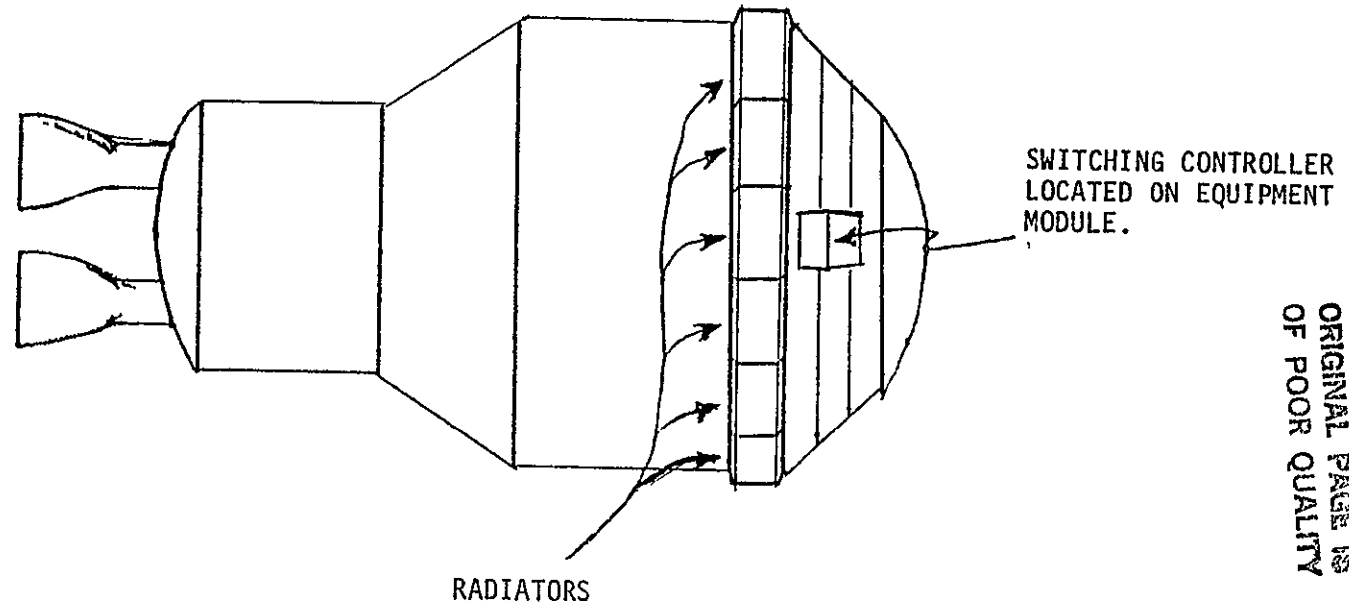
PLACEMENT OF RADIATORS AND AMPLIFIERS
FOR DUAL 20-WATT CONFIGURATION.



ORIGINAL PAGE IS
OF POOR QUALITY

ANTENNA LINK MARGIN TRADE STUDY

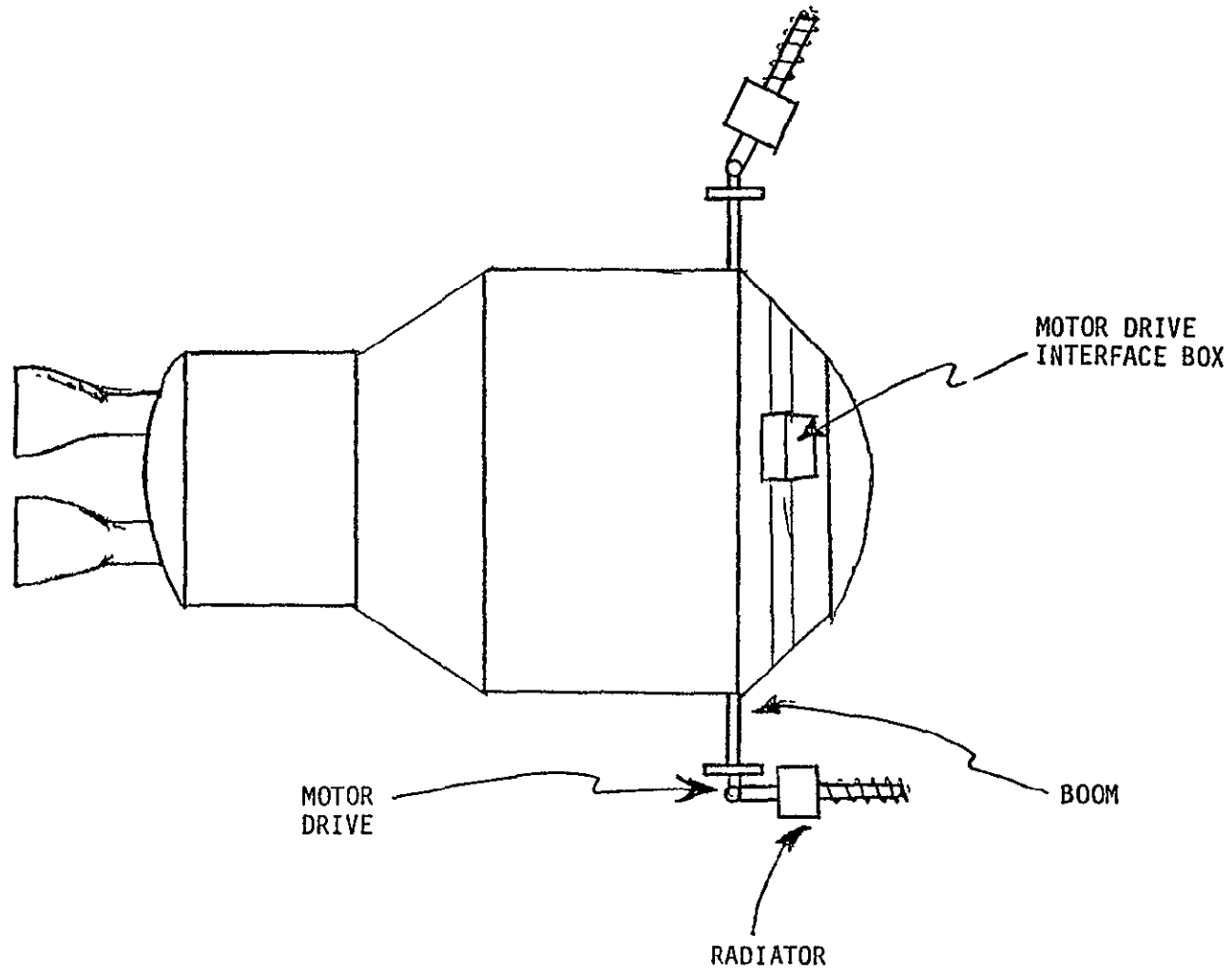
PLACEMENT OF RADIATOR BAND FOR
SWITCHING ANTENNA CONFIGURATION.



ORIGINAL PAGE IS
OF POOR QUALITY

ANTENNA LINK MARGIN TRADE STUDY

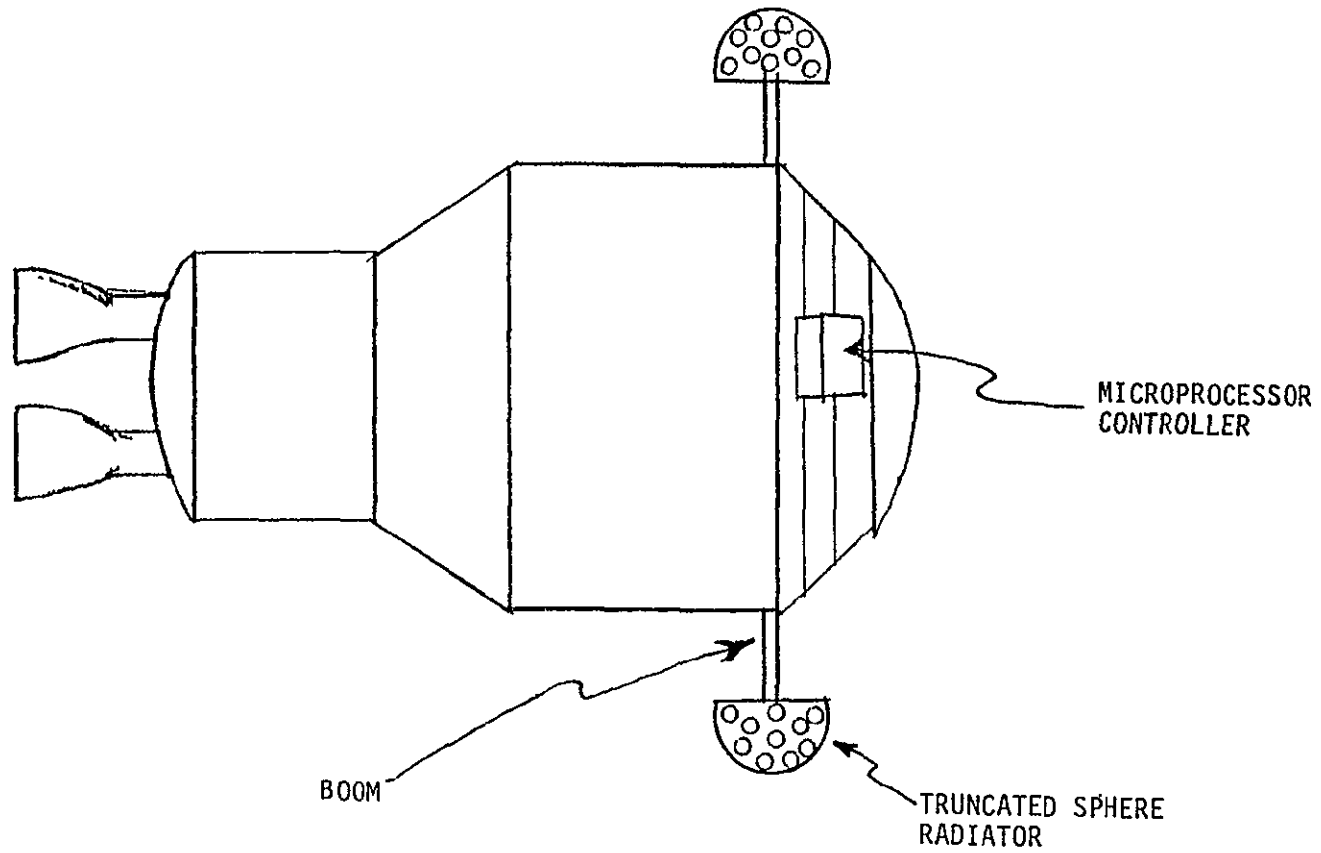
PLACEMENT OF RADIATING AND MOTOR DRIVE
ELEMENTS FOR STEERABLE ANTENNA CONFIGURATION



ORIGINAL PAGE IS
OF POOR QUALITY

ANTENNA LINK MARGIN TRADE STUDY

PLACEMENT OF RADIATORS FOR COMBINATION
ANTENNA CONFIGURATION



ORIGINAL PAGE IS
OF POOR QUALITY

APPENDIX B.2

A CANDIDATE CENTAUR SWITCHED-BEAM HIGH-GAIN ANTENNA SYSTEM

A CANDIDATE CENTAUR SWITCHED-BEAM
HIGH-GAIN ANTENNA SYSTEM
NAS 9-16067, EXHIBIT B

Interim Report

Technical Monitor
William Teasdale

Prepared for
NASA Lyndon B. Johnson Space Center
Houston, Texas 77058

Prepared by
Dr. Richard Iwasaki
Axiomatix
9841 Airport Blvd, Suite 912
Los Angeles, California 90045

Axiomatix Report No. R8109-1
September 10, 1981

1.0 INTRODUCTION

The selection of a suitable antenna configuration for a spacecraft is always a critical factor in achieving the communications systems requirements. Many conflicting design parameters must be considered to select a reasonable assortment of suitable antenna configuration candidates and then judiciously arrive at a final recommended choice.

The purpose of this study will be to first examine the existing IUS antenna system and the proposed Centaur antenna system and then gradually develop an alternate scheme which should be considered for possible implementation if the basis for the development appears warranted by the arguments introduced. Since some of the communication link margin budgets have not been firmly established, some flexibility in design exists and various alternatives are discussed.

In order to increase the acceptance of these proposed concepts, the study will concentrate heavily on existing spacecraft antenna systems which have been space-qualified by actual operation and then introduce a means for improving the antenna system performance by adapting a switched-beam concept which is currently being implemented on the Shuttle Orbiter S-band quad antenna system. Therefore, using the existing technology with little modification, a high-gain spherical-coverage switched-beam antenna system is developed for the particular system constraints of the Centaur vehicle.

2.0 GENERAL DYNAMICS CENTAUR ANTENNA CONFIGURATION

During the system formulation phase for the Centaur vehicle development, Axionix was asked to evaluate the antenna configuration tentatively, proposed by General Dynamics. The design proposed is very basic, being two log conical spiral antennas extending outwardly on opposite sides of the Centaur vehicle on pods, as shown in Figure 1. Having hemispherical coverage, the two log conical spiral antennas would provide spherical coverage by appropriately switching while the Centaur vehicle was rotated for thermal equalization reasons.

There are two problem areas that must be directly addressed with the General Dynamics antenna approach because of the communications system constraints. First, it has been established by analysis that reacquiring a communications link is estimated to require a maximum time of 17 seconds

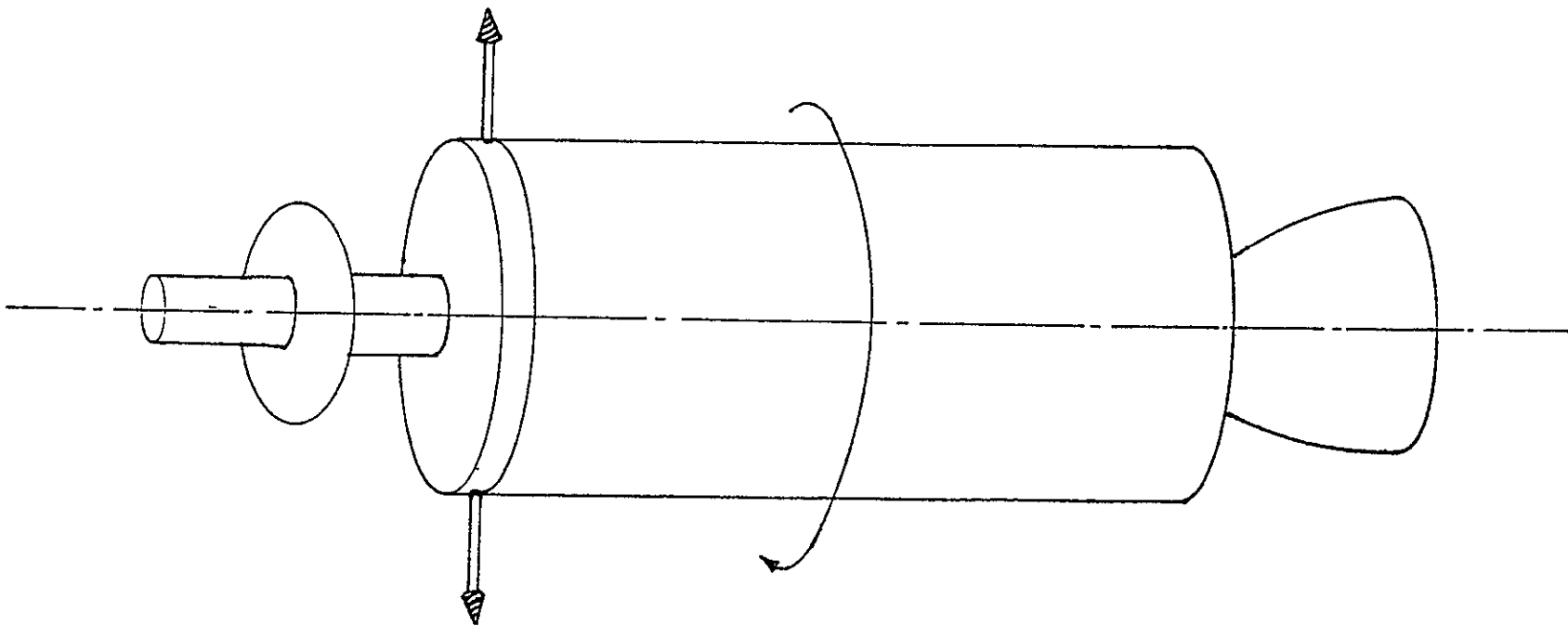
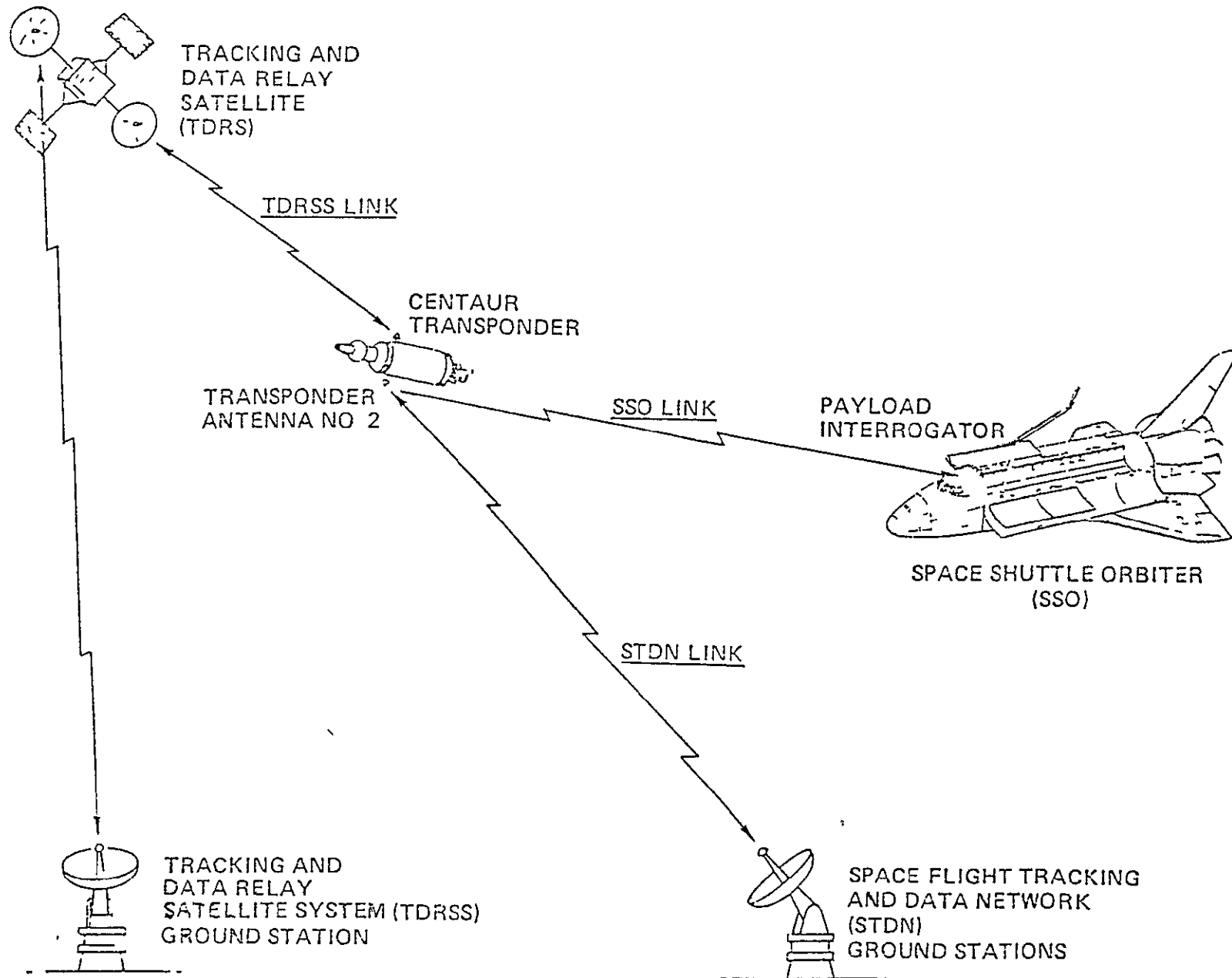


Figure 1a. Proposed General Dynamics Centaur Antenna System

DETACHED MODE S-BAND RF LINKS



ORIGINAL PAGE IS
OF POOR QUALITY

Figure 1b Centaur Vehicle Communication Links

automatically and 30 seconds manually if a link is disrupted and the phase-locked loop synchronization is lost. In the case of the Shuttle Orbiter/Centaur link, an astronaut must be dedicated to maintaining this link since the manual reacquisition process of the NASA/Motorola transponder requires the switching off and on of the data and carrier channels. Since the Centaur vehicle rotates at one revolution per minute, if lock is indeed lost by either phase or amplitude transients, then the astronaut will be continuously trying to reacquire, and much essential data will be lost in the process during the constant interruptions.

The other problem that must be considered is the gain and orientation of the antenna patterns with respect to the Centaur vehicle itself. The proposed log conical spiral antennas could be reasonably expected to have a peak gain of 5 dB with broad coverage, with lower values of 0 dB or less at the extremes of the hemisphere. The antenna coverage along the longitudinal axis of the Centaur vehicle is therefore greatly restricted. In addition, since the two hemispherical coverages are on the opposite sides of the vehicle in the roll-plane, switching between antennas is necessary for continuous coverage, with the attendant phase transient difficulties. The preliminary link budgets indicate a negative margin of -4 to -5 dB in the critical Centaur/TDRS link, and, although these margins can theoretically be reduced by further refinements in the approximations used in determining the losses attributed to link performance, it might be prudent to consider long range goals of having sufficient gain to provide positive link margins, especially during the initial system design rather than as an expensive retrofit which cannot be later considered because of the cost and schedule impacts.

3.0 BOEING INERTIAL UPPER STAGE (IUS) ANTENNA CONFIGURATION

The Boeing ISU system has been retained for military operations and still might be considered for NASA applications. Basically, the IUS antenna configuration utilizes clusters of five log conical spirals, as sketched in Figure 2, mounted on pods to extend the clusters outwardly from the vehicle. Four clusters are used, as shown in Figure 3, to obtain full spherical coverage about the vehicle, as indicated in Figure 4. The main purpose in having so many log conical spiral antennas is that each optimizes the gain obtainable for a specific coverage region so that, by multiplicity, optimum high-gain percentage coverage is achieved at the expense of complexity.

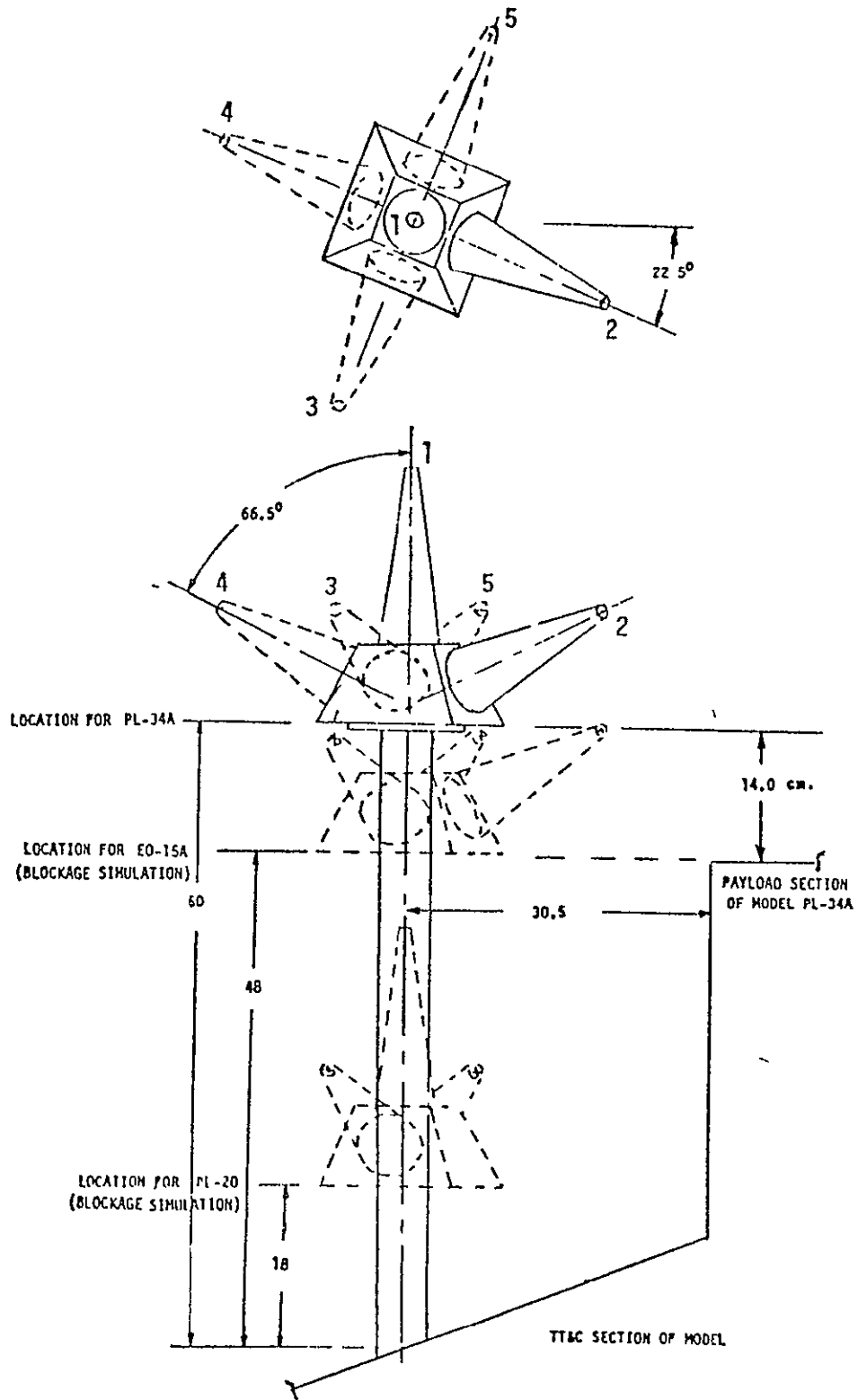


Figure 2. Antenna Assembly Positions

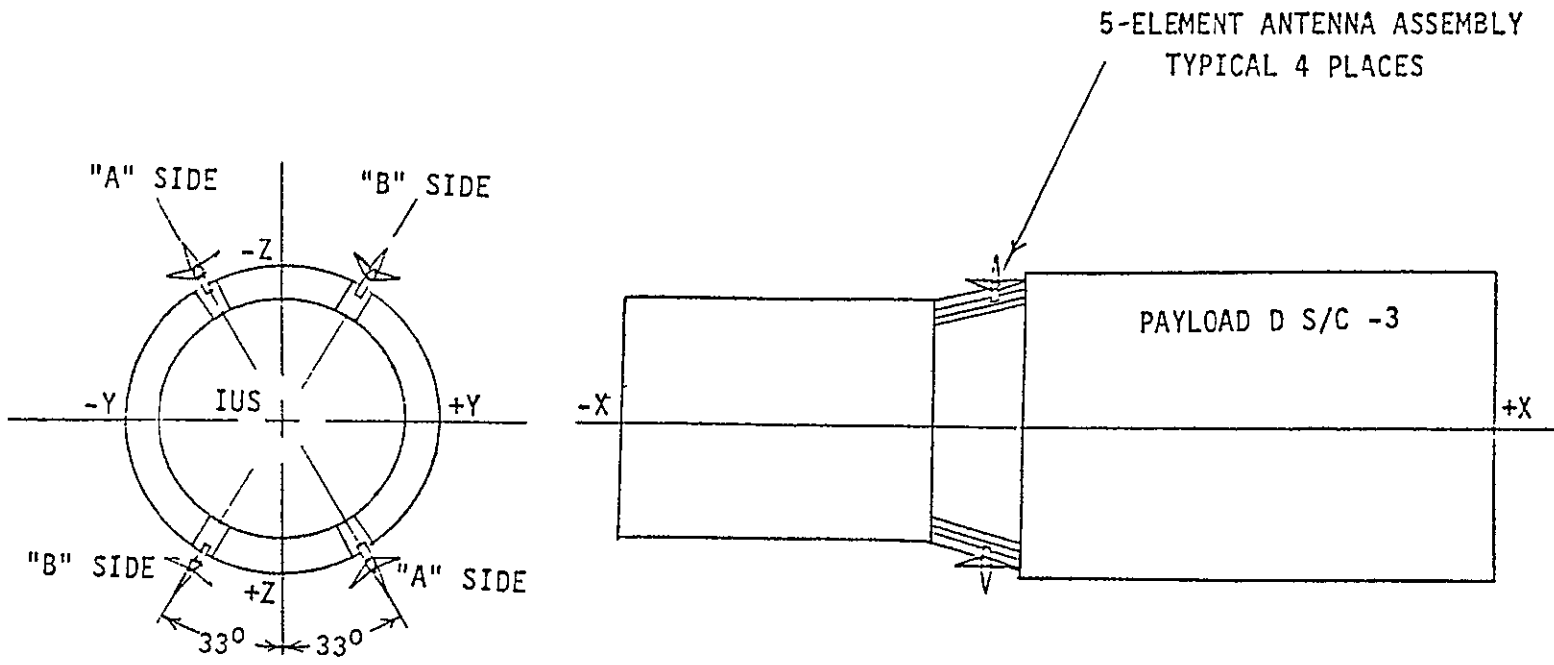
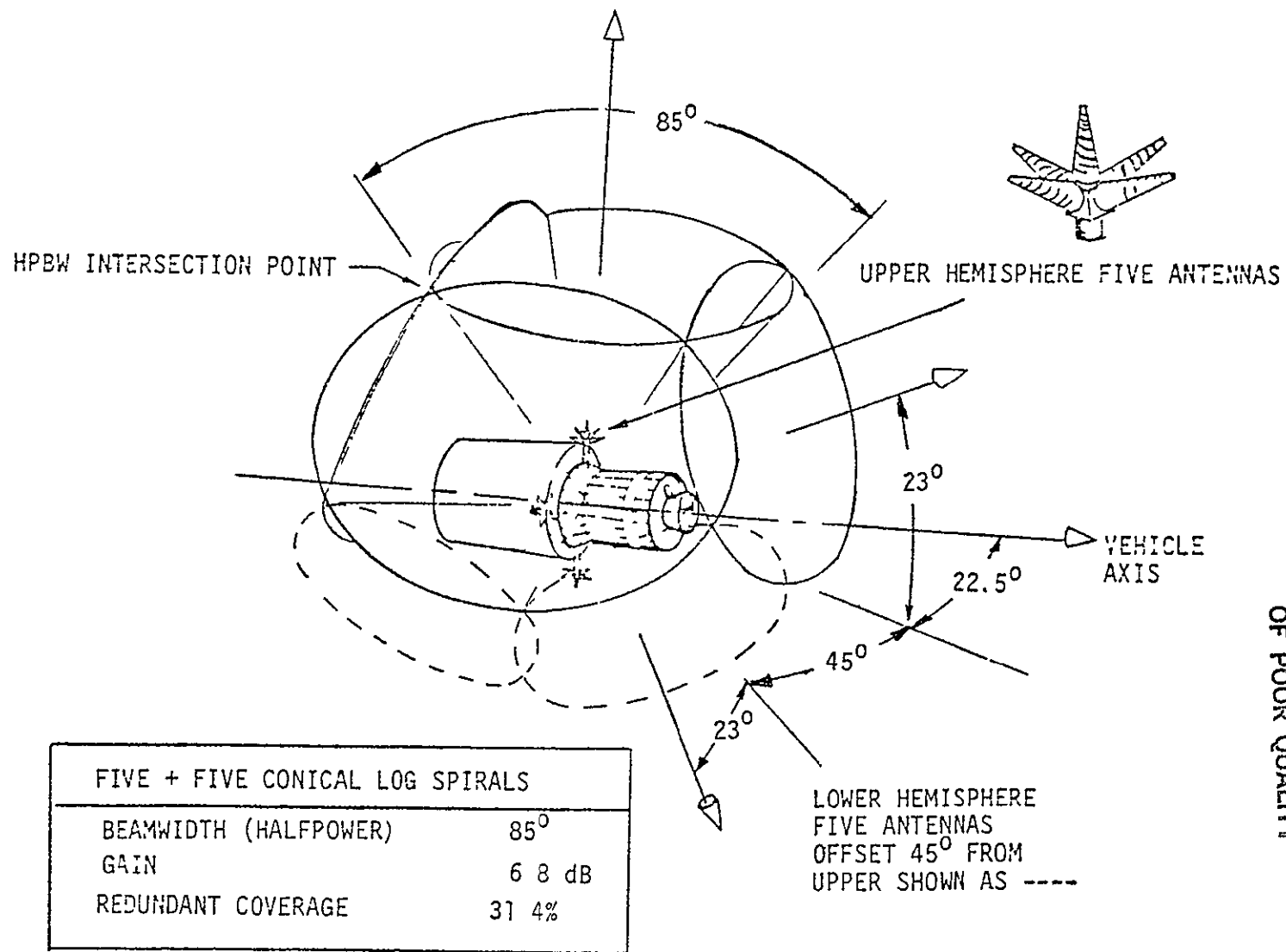


Figure 3. Five-Element Antenna Assembly Positions

ORIGINAL PAGE IS
OF POOR QUALITY



ORIGINAL PAGE IS
OF POOR QUALITY

Figure 4. NASA IUS TT&C Antenna Assembly Meets TDRSS Requirements

Although the IUS antenna system satisfies the gain requirements of the Centaur/IUS vehicles, there is a definite phase transient problem which arises from two sources from the IUS configuration since it also rotates about its longitudinal axis and, therefore, requires switching between antennas and clusters to maintain proper antenna pointing. As Boeing noted in its phase transient analysis, the switching of patterns from one antenna to another can result in a phase discontinuity of up to 90°. This phase shift is caused by the abrupt change in effective phase centers which cannot be physically collocated in the cluster of five log conical spiral antennas. This physical phase center displacement can be geometrically described, as shown in Figure 5, and is a potential source of the loss of lock of synchronization of the link.

An even more drastic phase shift can arise from the switching between antenna clusters as the vehicle rotates. It is obvious that the phase centers of the two antennas on the extending pods, as in the presently proposed Centaur configuration, will be physically separated by many meters since they are located on opposite sides of the Centaur vehicle, as was depicted earlier in Figure 1. As the vehicle rotates, these phase centers also rotate. The major concern is then the phase relationship between these two phase centers during switching. Ideally, they would be identical so that phase continuity exists. The best position for antenna switching might be when the two antennas are equidistant from the target antenna. Other positions are located at specific orientations of the vehicle during rotation wherever the differential distances to the target antenna are an integral number of wavelengths apart. In summary, it is possible to switch between antennas without causing phase transients that would create loss of lock of the communications link, but the switching must be precisely temporally controlled by a computer. Identical conditions apply to the Boeing IUS configuration, which is even more complicated because it has four asymmetrically located antennas.

Rather than pursuing this approach, which is susceptible to error, Axionix proposes another approach which will not rely on antenna switching, yet will provide high gain to increase the link margin.

ORIGINAL PAGE IS
OF POOR QUALITY

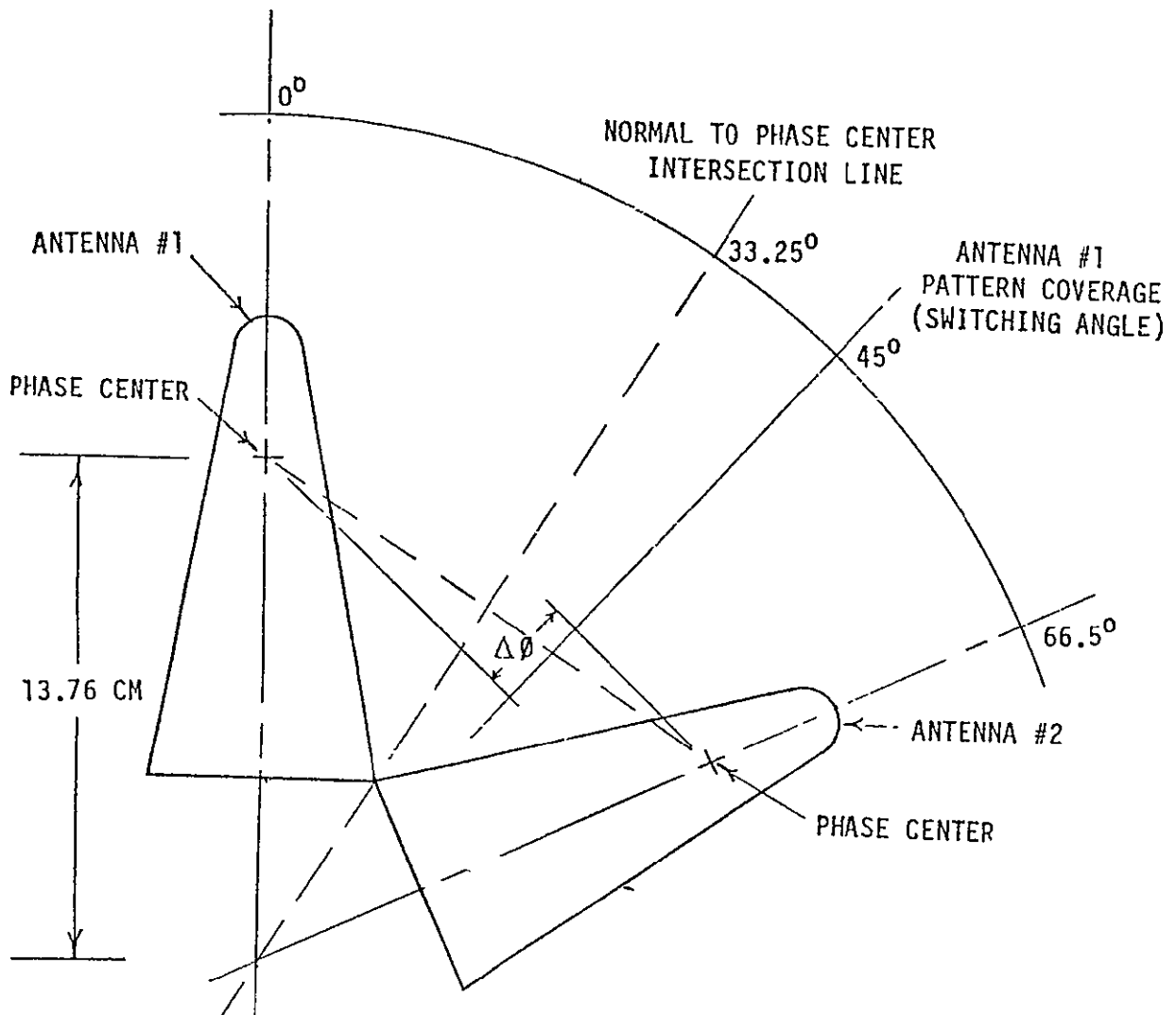


Figure 5. Phase Shift due to NASA Antenna Switching

4.0 AXIOMATIX CENTAUR ANTENNA CONFIGURATION PROPOSAL

Axiomatix proposes a switched-beam system which is compatible with the operational requirements of the Centaur vehicle. The primary concern is the presence of phase discontinuity when antennas are switched, thereby causing a loss of lock of synchronization in the communications link. As discussed earlier, the Centaur vehicle rotates at a rate between 1 and 3 RPM to more uniformly distribute solar irradiance. This requires that antennas be switched to avoid vehicle blockage if the antennas are radially extended, as in the case of both present IUS and Centaur configurations.

The Axiomatix approach attempts to avoid this switching requirement by utilizing a toroidal antenna pattern in the roll plane. Using this configuration allows continuous coverage in the roll plane to a target without the need for switching, thereby eliminating phase transients. The circular symmetry of the Centaur vehicle rotation is ideally suited to this toroidal pattern, which can also be tilted to accommodate targets which are not exactly perpendicular to the longitudinal roll axis. This tilting will be accomplished by a switched-beam technique similar to that being employed by the Shuttle Orbiter switched-beam quad antenna system, as will be discussed in more detail later.

Fore and aft coverage will be provided by log conical spiral antennas which have been used extensively in the other proposed configurations. Figure 6 shows such a log conical spiral antenna configured with a biconical antenna, which will provide the toroidal pattern discussed earlier. This dual-antenna configuration has been used previously on other space programs, e.g., the Global-Positioning Satellite (GPS) shown in Figure 7.

The main problem with the biconical antenna toroidal coverage is that very little gain is achievable in the roll plane, being of the order of 0-1 dBC. Although this can be used for broad coverage in the roll plane, it is not suitable for high-gain requirements which may arise from a realistic assessment of the communication link budgets presently being evaluated, especially concerning the Centaur/TDRS link. The Axiomatix adaptation to this concept is to develop a collinear array of three biconical antennas, as sketched in Figure 8. These three biconical antennas now constitute a three-element array similar to the switched-beam antennas

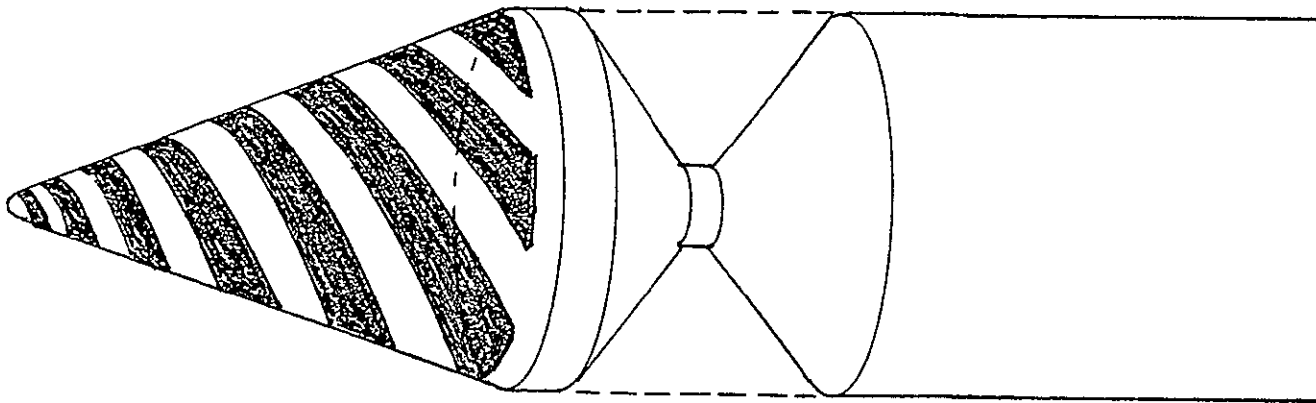
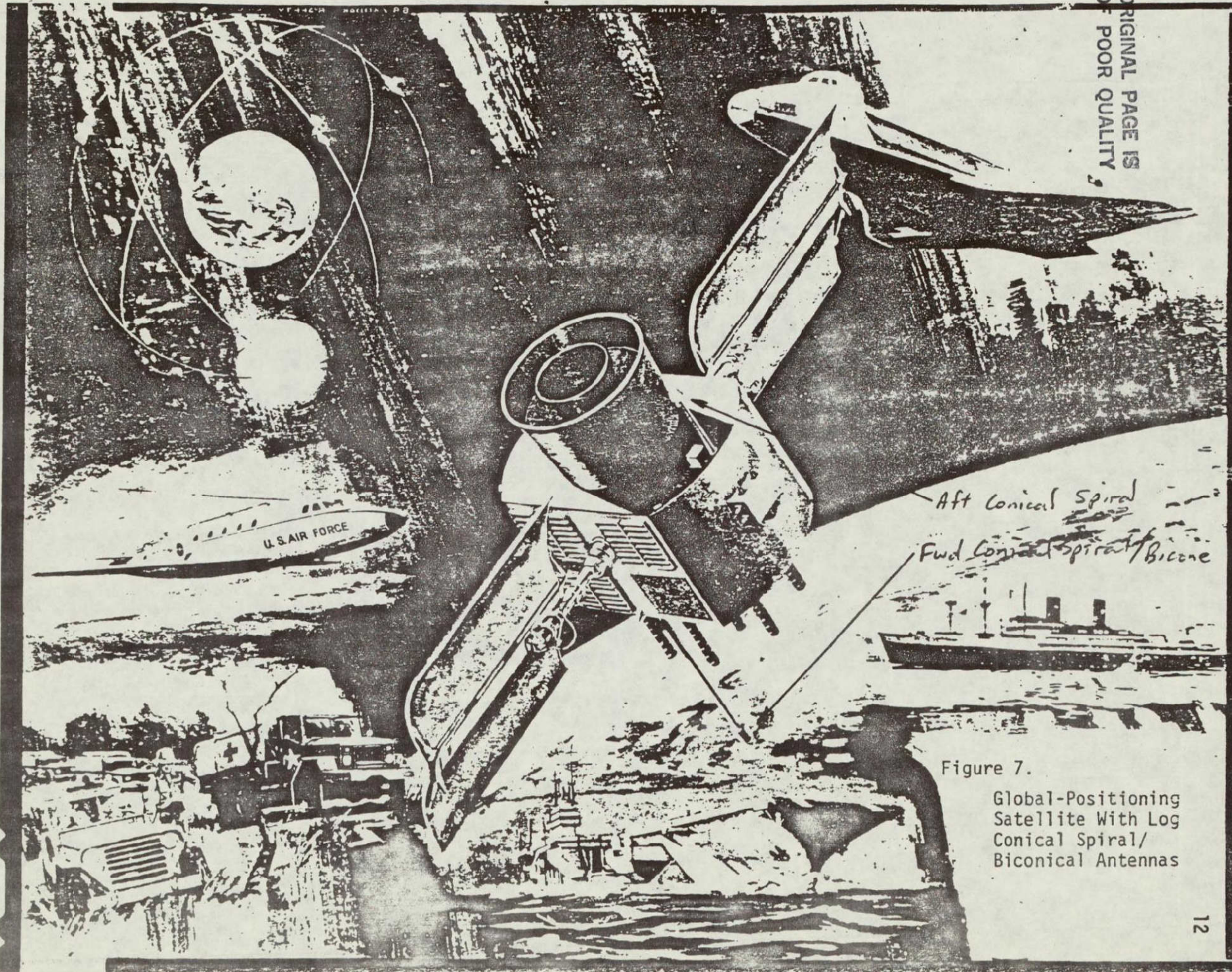


Figure 6. Log Conical Spiral/Biconical Antenna Combination

ORIGINAL PAGE IS
OF POOR QUALITY

ORIGINAL PAGE IS
OF POOR QUALITY



Aft Conical Spiral
Fwd Conical Spiral/Bicone

Figure 7.
Global-Positioning
Satellite With Log
Conical Spiral/
Biconical Antennas

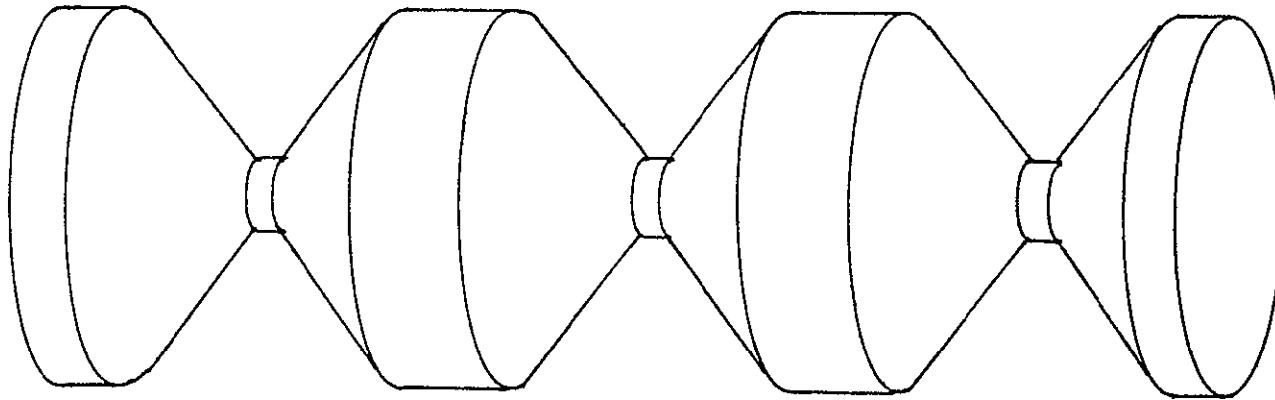


Figure 8. Collinear Array of Three Biconical Antennas

of the Shuttle Orbiter switched-beam quad antenna system. The center element is directly fed with a voltage amplitude ratio of 1.0, and the two outer biconical antennas have a relative voltage amplitude ratio of 0.6. Beam-orientation switching is attained by mechanically switching discrete phase shifts. The three-element array achieves higher gain, "guesstimated" in the range of 4-5 dBCi, in the roll plane.

The log conical spiral antenna/biconical antenna array combination now looks like the configuration shown in Figure 9. Note that the two antenna systems are independently operated in that, with one setting the log conical spiral antenna is employed and, with the other, the high-gain biconical antenna array is operational.

The other major obstacle to the antenna design is vehicle obscuration effects on the pattern. This difficulty has been surmounted in the past by extending long pods (or booms) past the vehicle and its payload. In this particular case, the antenna configuration might take the appearance shown in Figure 10, where pods fore and aft position the antennas clear of the obstructing vehicle. Note that the roll plane clearance is essential for proper operation of this biconical antenna and array concept since this is the only means to avoid antenna switching. If only one roll plane antenna is necessary (i.e., low-gain biconical or high-gain biconical array), then only one long pod is required since the fore and aft log conical spirals do not need the extension. As for the antennas located adjacent to the nozzle of the Centaur vehicle, high-temperature quartz radomes have been successfully implemented in previous programs to avoid the thermal problems associated with the rocket plume.

And finally, the main justification for considering the biconical antenna array is the multiple high-gain switched-beam patterns available in the roll plane, as shown in Figures 11 and 12. For simplicity, consider the two-switched-beam case, forward (Figure 11) and aft (Figure 12). The switching concept is identical to that used in the Shuttle Orbiter S-band quad antenna except that higher gain and less effective loss is attained by using a directly fed center element in a three-element array rather than the quad two-element array. Further, the number of possible switched beams is related to the number of switches n used in series in the feed line, with the appropriate phase shifts. The number of possible switched beams is determined by 2^n so that, if one switch is used, two switched beams are possible, and four beams arise from two switches. The

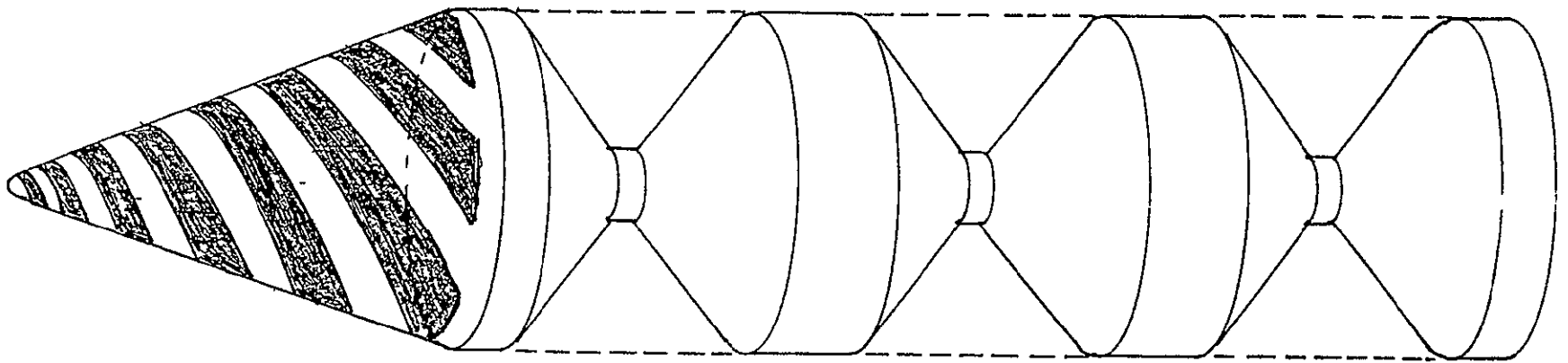


Figure 9 Log Conical Spiral/Biconical Array Combination

ORIGINAL PAGE IS
OF POOR QUALITY

ORIGINAL PAGE IS
OF POOR QUALITY

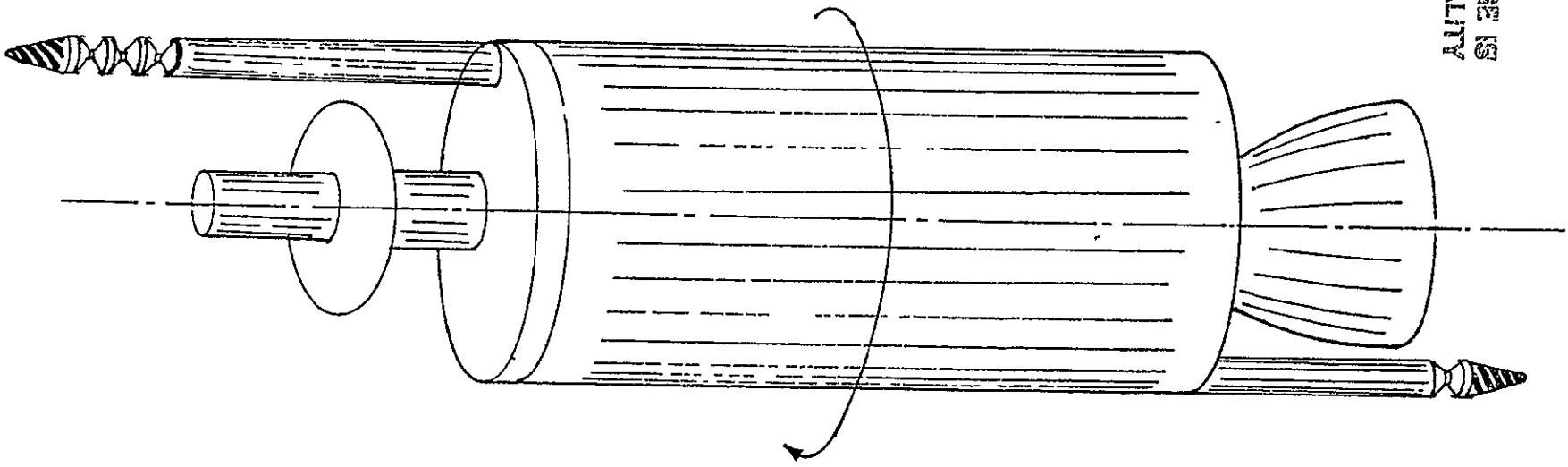


Figure 10. Proposed Aximatic Log Conical Spiral/Biconical Array Antenna Configuration

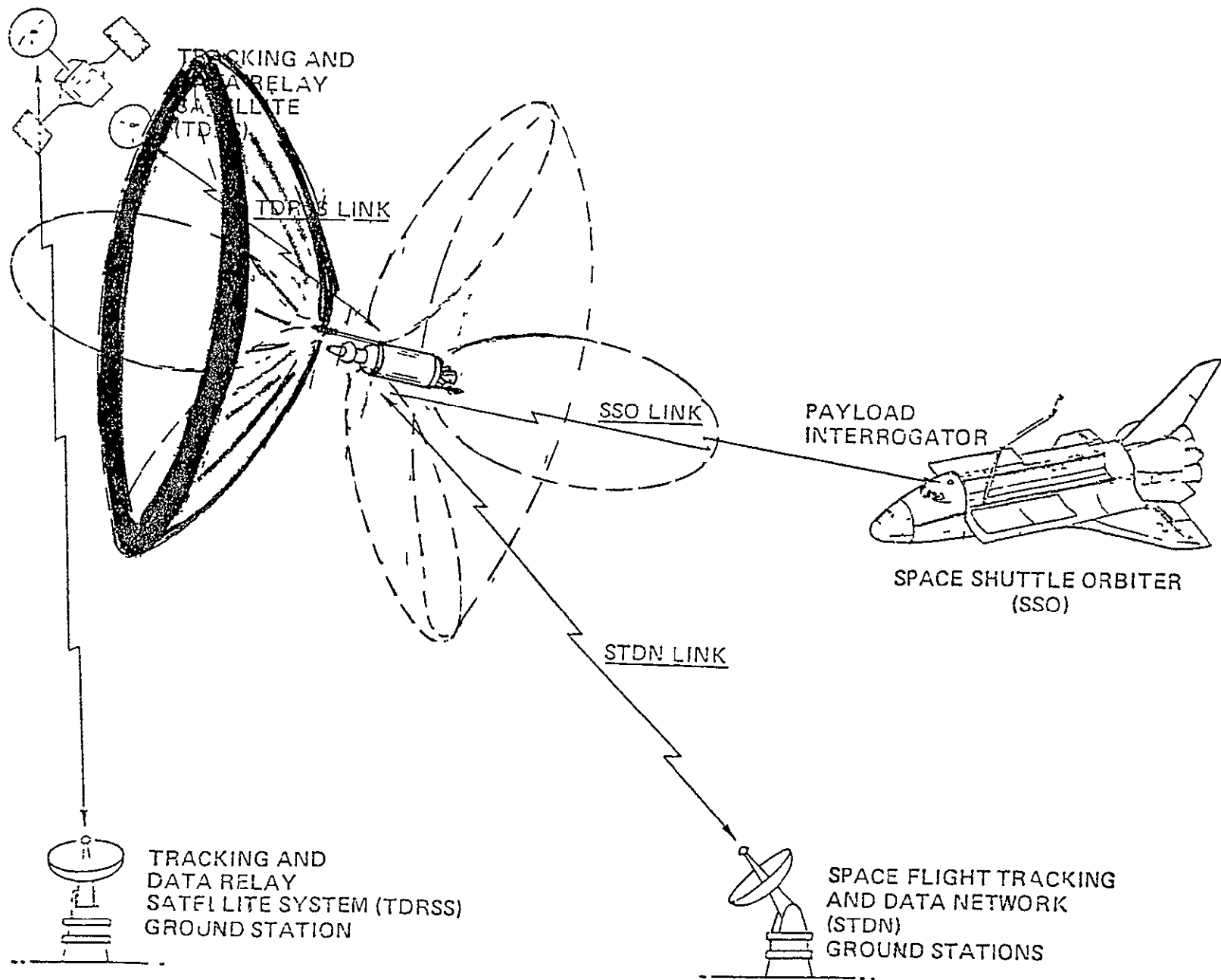
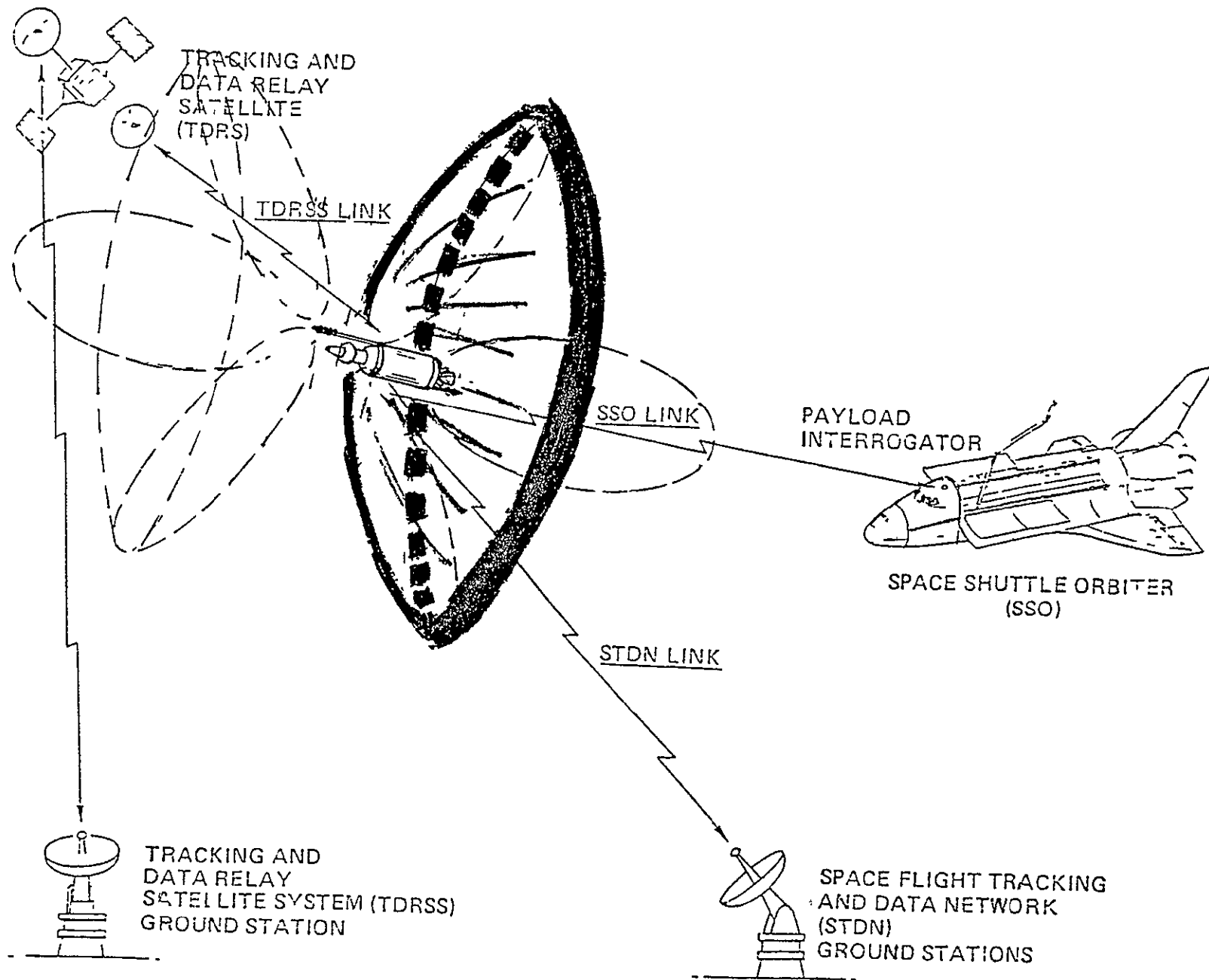


Figure 11 Forward-Looking Switched High-Gain Biconical Array Antenna Pattern

ORIGINAL PAGE IS
OF POOR QUALITY



ORIGINAL PAGE IS
OF POOR QUALITY

Figure 12. Aft-Looking Switched High-Gain Biconical Array Antenna Pattern

use of three switches enables the antenna system to have eight beam positions, which greatly enhances the antenna capabilities because the high gain of the three-element array can be selectively positioned for optimal performance. These mechanical latching switches require no electrical holding power and add, with the discrete phase-shift circuit, only 0.2 dB per switch. The center element, which is directly fed, carries the majority of the radiated power so that the effective antenna loss is less than that of the additive switch losses.

The final proposed Centaur antenna configuration then consists of either a forward-looking or aft-looking log conical spiral or, in the roll plane, any of the multiple biconical antenna array switched beams. It is anticipated that full +4 dBci gain coverage is achievable about the Centaur vehicle with no antenna switching phase or power transients since, once the proper mode of operation is selected, no further switching is required.

APPENDIX B.3

CONFIGURATION MODIFICATION
OF THE
PRELIMINARY BICONICAL/CONICAL LOG SPIRAL ANTENNAS
AND PHASE SYNCHRONIZATION TECHNIQUE
FOR THE CENTAUR VEHICLE

CONFIGURATION MODIFICATION
OF THE
PRELIMINARY BICONICAL/CONICAL LOG SPIRAL ANTENNAS
AND PHASE SYNCHRONICATION TECHNIQUE
FOR THE CENTAUR VEHICLE

Interim Report

Contract No. NAS9-16067, Exhibit B

Technical Monitor: William Teasdale

Prepared for

NASA Lyndon B. Johnson Space Center
Houston, Texas 77058

Prepared by

Dr. Richard Iwasaki

Axiomatix
9841 Airport Blvd., Suite 912
Los Angeles, California 90045

Axiomatix Report No. R8111-6
November 20, 1981

1.0 INTRODUCTION

The two primary objections to the initial antenna design concept involved the extended protrusion of the forward antenna past the payload and the protrusion of the aft-looking conical log spiral antenna adjacent to the Centaur rocket nozzle which would be affected by the thermal and RF blockage effects of the plume during transfer. The objections were well taken if, indeed, the envelope restrictions do not allow antennas extended in such a manner although, ideally, a biconical array is most suitable along the longitudinal axis in front of the payload, where it would have an unobstructed view of a large portion of space. But, if the payload envelope does not allow this configuration, modifications are obviously required.

The biconical-array configuration has been modified to change its proposed location to deploy radially outward from the Centaur vehicle similar to the other boom-mounted antenna configurations proposed by General Dynamics (GD). Two biconical arrays are now required because of pattern blockage by the body of the vehicle itself, and the switching requirements have been reduced to switching between the two sides of the vehicle only.

To avoid the loss of data during this unavoidable switching between arrays, a simple detection scheme has been developed to switch during a period of phase synchronization using the constructive interference pattern of the overlap region between the two arrays. Even though the onboard computer knows the geometric relationship of the communicator with respect to the Centaur, the technique electronically determines the optimum switching time to maintain phase coherence by actually sampling the received signals using the dual-antenna scheme.

2.0 PRESENT GENERAL DYNAMICS CENTAUR ANTENNA CONSIDERATIONS

Two design criteria were changed substantially. One was the roll about the longitudinal axis for thermal equalization reasons which was reduced to 0.1 RPM versus the earlier 1-RPM roll rate. The maximum roll rate prior to payload separation was also reduced from the earlier 2.9 RPM to 0.67 RPM. Therefore, the loss-of-lock conditions on which the earlier design was based was minimized significantly. Similarly, it was

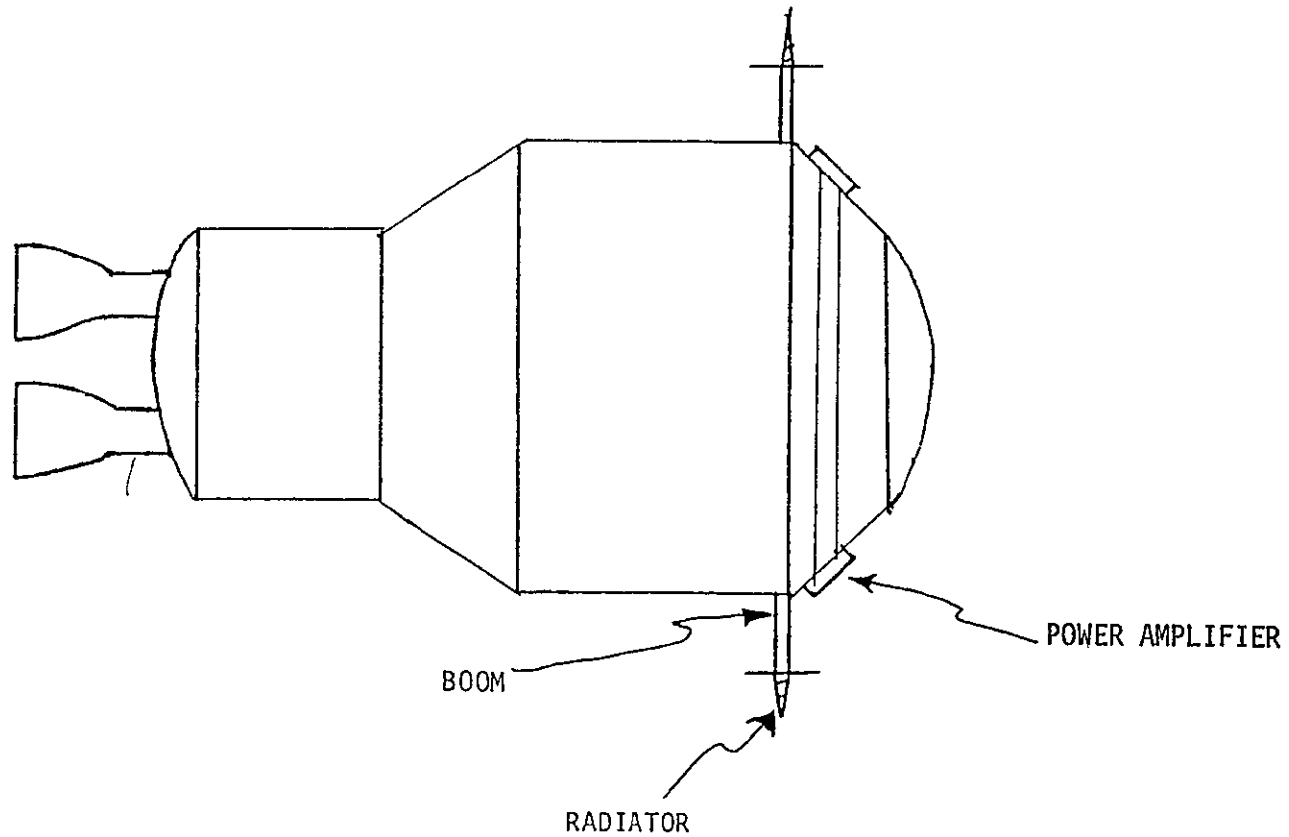
noted that the Motorola transponder does not initiate frequency sweep immediately upon loss of synchronization; rather, it simply "holds" momentarily until the signal is reacquired if there is an abrupt loss of received power. Synchronization is then automatically reacquired; however, data loss occurs during this procedure until the phase-locked-loop is again synchronized. Thus, this condition is to be avoided if possible. Under this new operating environment, the candidate antenna configuration will then be modified to attempt to alleviate objectionable features of the initial preliminary baseline design and, hopefully, thus exploit the advantageous features of the earlier configuration which will then add the alternatives being proposed by GD to the antenna system.

It should be reemphasized that the stated purpose of this study is to explore other possible approaches to the antenna problem besides the IUS approach and those being proposed by GD. This report is then an attempt to develop some new ideas for the Centaur antennas in addition to evaluating the existing candidate configurations by outlining inherent advantages and disadvantages independently from the GD system engineers. By using this process, which is, by definition, an iterative procedure that is continuously refined, some insight into an optimal antenna configuration for this application will arise. This antenna configuration evaluation is especially critical for the Centaur vehicle since it is not obvious that any of the existing proposed systems is suitable for the operational requirements of the mission; therefore, the problem should be approached openly in a constructive manner so that no possible satisfactory solution is overlooked.

Before continuing a more detailed description of the biconical array, it would be worthwhile to quickly reexamine the other alternative antenna candidates proposed by General Dynamics and describe specific features for comparison purposes. First, the two conical log spirals extending out radially on booms, as illustrated in Figure 1, does not provide adequate gain in all directions, especially along the longitudinal axis of the Centaur vehicle. This low-gain fore-and-aft coverage deficiency also exists for the circumferential array, shown in Figure 2, which consists of flush-mounted radiators around the Centaur vehicle, with the appropriate hemispherical coverage array facing the target switched into operation as the vehicle rotates. Another candidate antenna system

ANTENNA LINK MARGIN TRADE STUDY

PLACEMENT OF RADIATORS AND AMPLIFIERS FOR DUAL 20-WATT CONFIGURATION

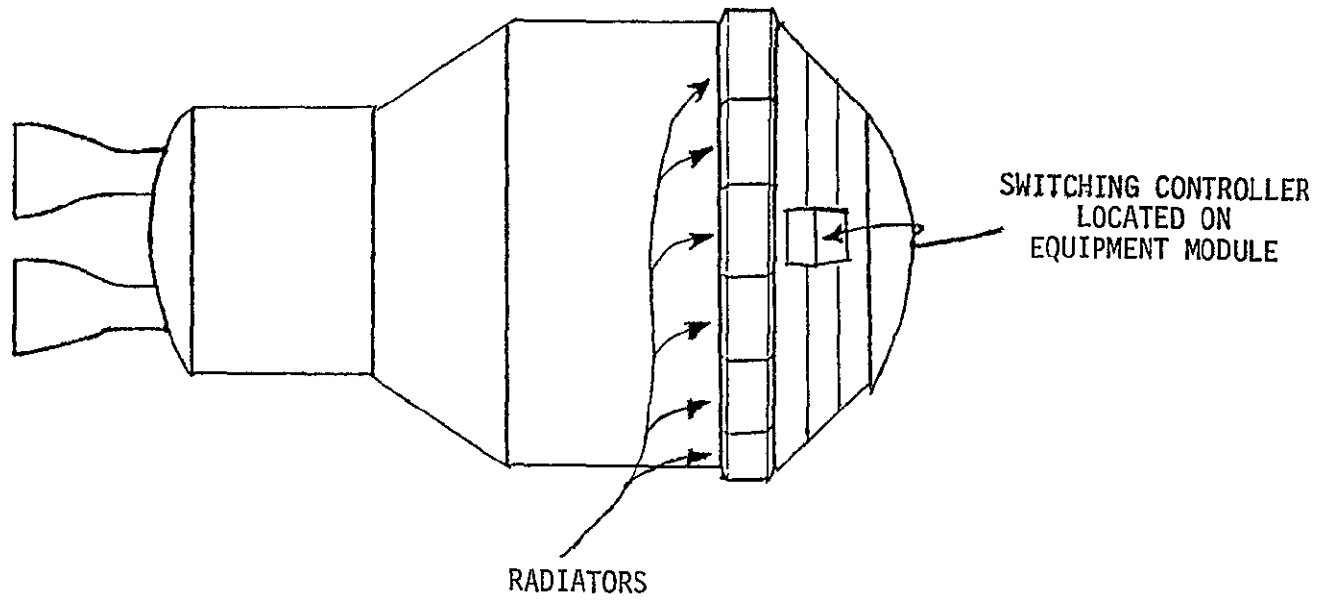


ORIGINAL PAGE IS
OF POOR QUALITY

Figure 1. General Dynamics Log Conical Spiral Antenna Configuration

ANTENNA LINK MARGIN TRADE STUDY

PLACEMENT OF RADIATOR BAND FOR ANTENNA-SWITCHING CONFIGURATION



ORIGINAL PAGE IS
OF POOR QUALITY

Figure 2. General Dynamics Circumferential Array

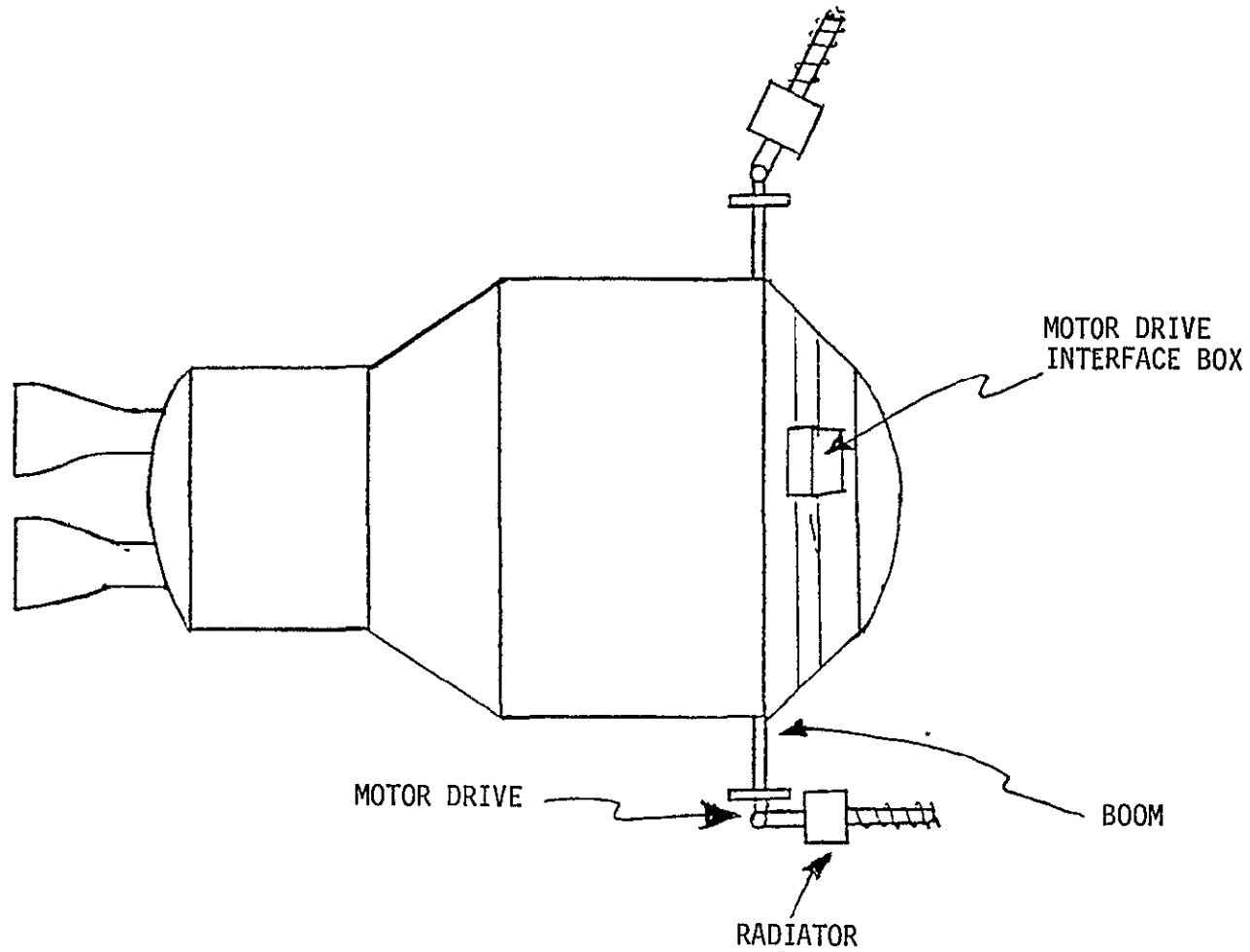
recently discussed was two motor-driven two-axis steerable helical antennas located on booms, as sketched in Figure 3, which are pointed at the target by a computer since it would not have tracking capabilities. The obvious problem with this approach is the uncertainty in the reliability of the motor-driven platform, which is greatly complicated by the revolution rate of the vehicle. The difficulties encountered by the scanning Ku-band rendezvous radar/communication antenna preclude ready acceptance of a similar configuration. Another attempt to solve the spherical high-gain coverage problem uses two truncated sphere radiators extended radially out on booms, as depicted in Figure 4. This novel concept most closely satisfies the antenna system requirements, so it will be described in more detail and compared to the biconical array.

2.1 Truncated Sphere Antenna

The truncated sphere radiator is a clever means of obtaining spot-beam coverage over a hemisphere with good axial ratios for circularly polarized radiation. This coverage is achieved by using many circular radiating discs mounted on a hemispherical ground plane for proper pointing attitudes for hemispherical coverage. The circular polarization is obtained by proper positioning of the RF cable connection such that the proper radiation mode is set up. Individually, these circular discs have a relatively wide beam, so a cluster array of four adjacent discs is used as a three-dimensional array to create a high-gain narrow spot beam. The selection of the appropriate cluster of four elements is determined by a computer which, for the smaller 15-inch-diameter model, can select one of 128 separate beams with 8-dB gain and 47° beamwidth. Electronic switching of the radiating discs is achieved by PIN diode switches placed at the hub of a centralized distributing network not unlike the spokes of a wheel. The PIN diode, which can be switched from "off" to "on" in less than $1 \mu\text{s}$, is reverse biased for the "off" condition and forward biased for the "on" condition. Since only four diodes are "on" at any time, the electrical holding power requirements are small because the reversed-biased diode state requires very little power. The virtual phase centers of these radiating discs on the hemisphere are relatively close together, so switching adjacent beams on the same truncated sphere causes very little phase shift (estimated at 4° to 10°). However, the differential phase shift

ANTENNA LINK MARGIN TRADE STUDY

PLACEMENT OF RADIATING AND MOTOR DRIVE ELEMENTS FOR STEERABLE ANTENNA CONFIGURATION

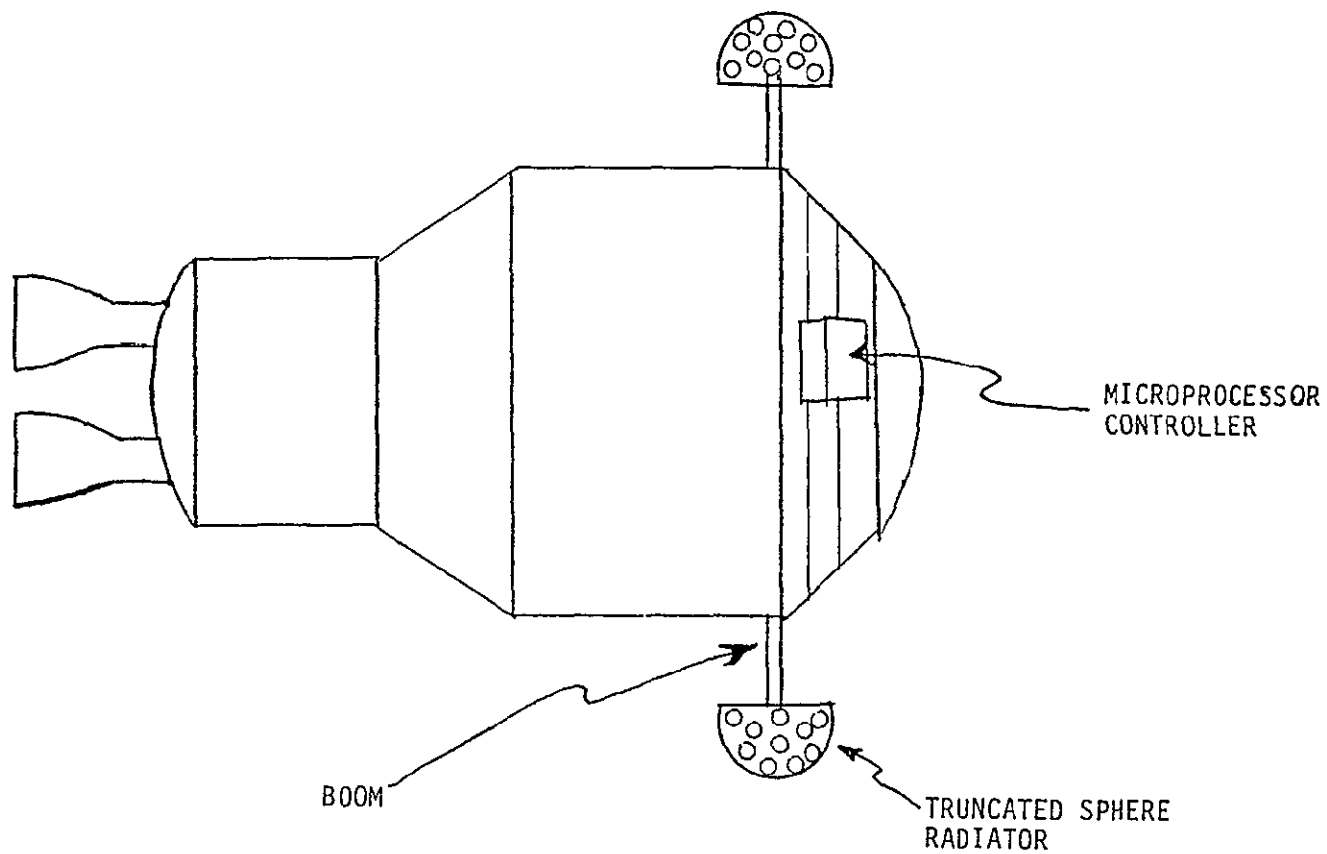


ORIGINAL PAGE IS
OF POOR QUALITY

Figure 3. General Dynamics Steerable Helical Antennas

ANTENNA LINK MARGIN TRADE STUDY

PLACEMENT OF RADIATORS FOR COMBINATION ANTENNA CONFIGURATION



ORIGINAL PAGE IS
OF POOR QUALITY

Figure 4. Truncated-Sphere Antennas

between the two truncated sphere antennas on opposite sides of the vehicle suffer the same problem as all other similar configurations since the virtual phase centers are located a substantial distance apart. The fore-and-aft coverage is adequately satisfied, however, with the same limitations as any of the extended-boom configurations.

Ideally, this truncated sphere antenna is suited for a stable platform since the spot-beam orientation for a stationary target is a simple problem. The rotation of the Centaur vehicle, however, creates a degree of complexity since the spot beam must now be continuously switched to follow the target about the axis of rotation, which is equivalent to electronic conical scanning. By viewing the photograph of the prototype model and assuming that only two elements are switched in a serially progressive manner, it is estimated that there would be eight switched spot beams per hemisphere in the broadside case, for a total of 16 switched spot beams per revolution in the worst case. This necessity to continuously switch is one of the disadvantages of this system, but it is shared in the similar arrangement used for the IUS cluster approach using five conical log spiral antennas.

3.0 MODIFIED BICONICAL-ARRAY CONFIGURATION

The objections voiced at the Centaur meeting are readily corrected by simply repositioning the placement of the boom and slightly modifying the configuration to accommodate the new requirements. Instead of forward-and-aft booms, if two booms are extended radially outward from the vehicle, as proposed by IUS/Boeing and Centaur/General Dynamics, the configuration then becomes compatible with the current system plan for deployed antennas. Two separate antenna systems are now required on opposite sides of the vehicle rather than the main one extending past the payload, as originally proposed. The proposed modified configuration is sketched in Figure 5. It should be noted that this sketch is not to scale. Dimensionally, the actual cylindrical antennas themselves should be approximately six inches in diameter and less than two feet long. The deployment feature, as in the case of the other candidate configurations, is to physically separate the antennas from the spacecraft body for improved performance by minimizing blockage and ground plane effects.

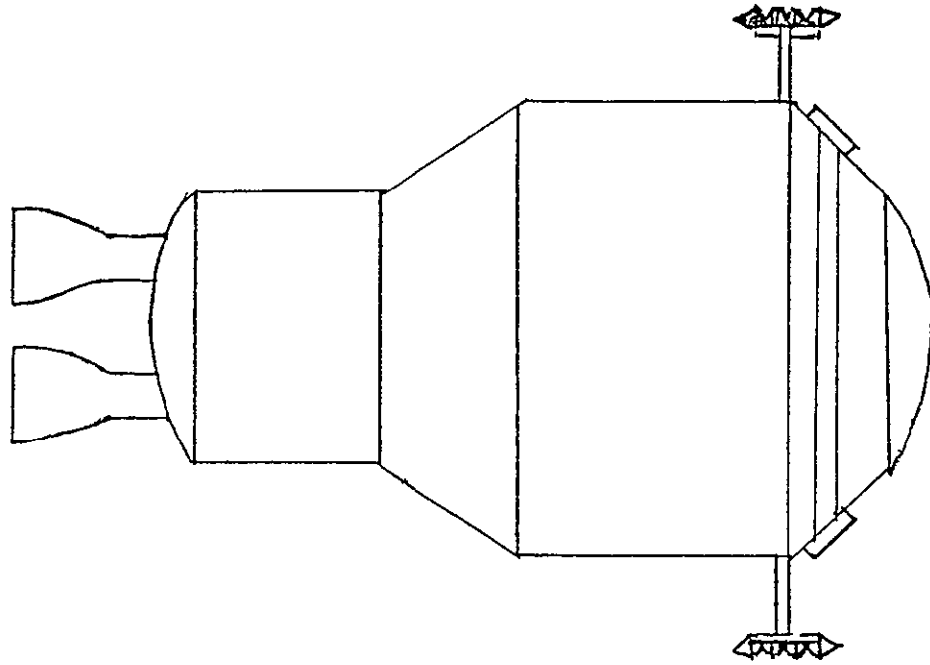
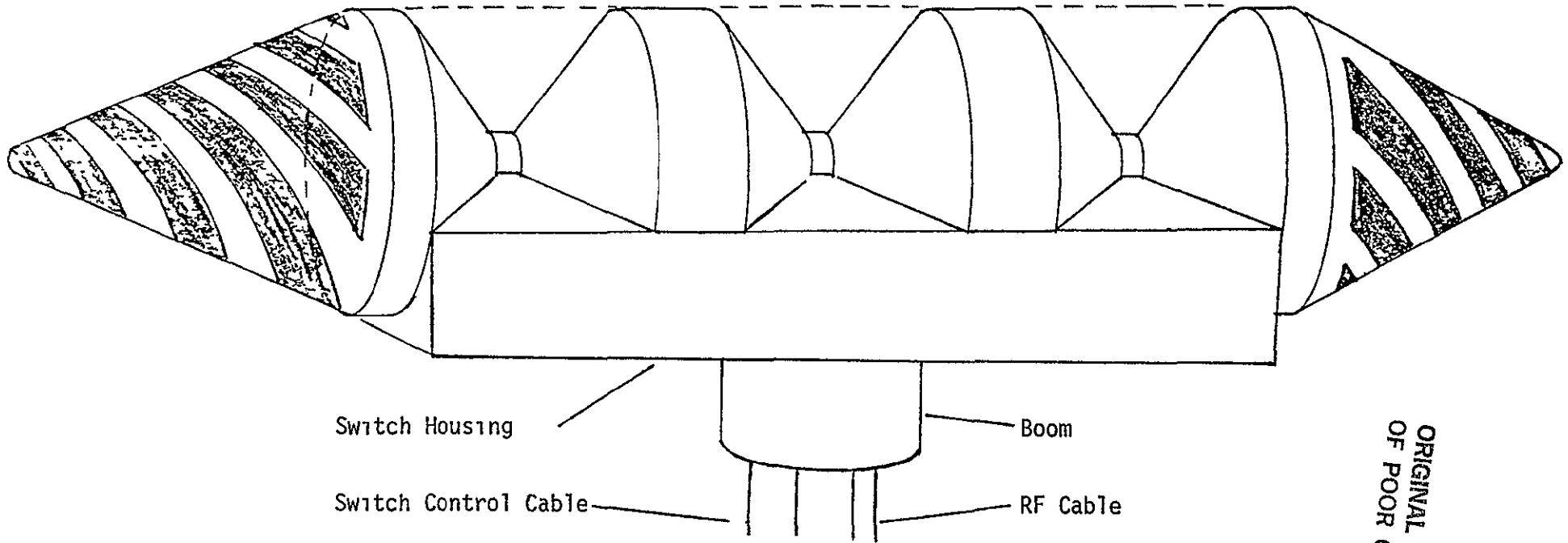


Figure 5. Modified Compound Log-Conical-Spiral/Biconical-Array Antenna

3.1 Circular Symmetry

The primary advantage of the biconical array is that the antenna pattern is a conical toroid which, since the target remains at a constant conical angle, would not normally be switched at all. The restriction that longitudinally extended booms are not permitted, however, has compromised this concept but, by using the same radially extended boom concept, it is possible to recreate this pattern using two truncated biconical arrays, each radiating half the required toroid since the vehicle blockage effects cannot be avoided. Only two antenna switches per revolution are now necessary, which is a definite advantage, depending on the final rate of revolution of the vehicle, which seems somewhat uncertain.

Each compound antenna consists of a forward-looking and an aft-looking log conical spiral antenna which are separated by the biconical array described earlier, as shown in Figure 6. But, since the Centaur vehicle now obstructs the circularly symmetric biconical antenna pattern, the biconical element is truncated so that the sector facing the Centaur vehicle is removed and serves instead as a supporting structure which also houses the electromechanical switches that select the operational modes of the antenna. Therefore, two biconical arrays on opposite sides of the vehicle provide broadside coverage about the Centaur vehicle, and the conical log spiral antennas cover the region in front of and behind the vehicle, as sketched in Figure 7. Basically, the IUS system uses the same concept for fore-and-aft coverage; however, the biconical array provides flexibility for multiple switched-beam performance with high gain and circular symmetry, which is important when accounting for the Centaur revolving slowly about its longitudinal axis. The obvious advantage of the circular symmetry is, of course, to reduce pointing and tracking requirements since a target remains relatively stationary with respect to the conical angle to the rolling Centaur vehicle. Since two compound antennas exist on opposite sides of the vehicle, each revolution requires only two switching procedures, greatly reducing the possibility of losing data. Since the two opposite semicircular beams overlap and make-before-break electromechanical switches are recommended, the signal dropout will momentarily occur only if lobing of the antenna pattern exists from the two widely separated radiating elements during the period of transition, i.e., 40 ms. The amount of phase shift during the compound antenna switching may be



ORIGINAL PAGE IS
OF POOR QUALITY

Figure 6. Compound Log-Conical-Spiral/Biconical-Array Antenna

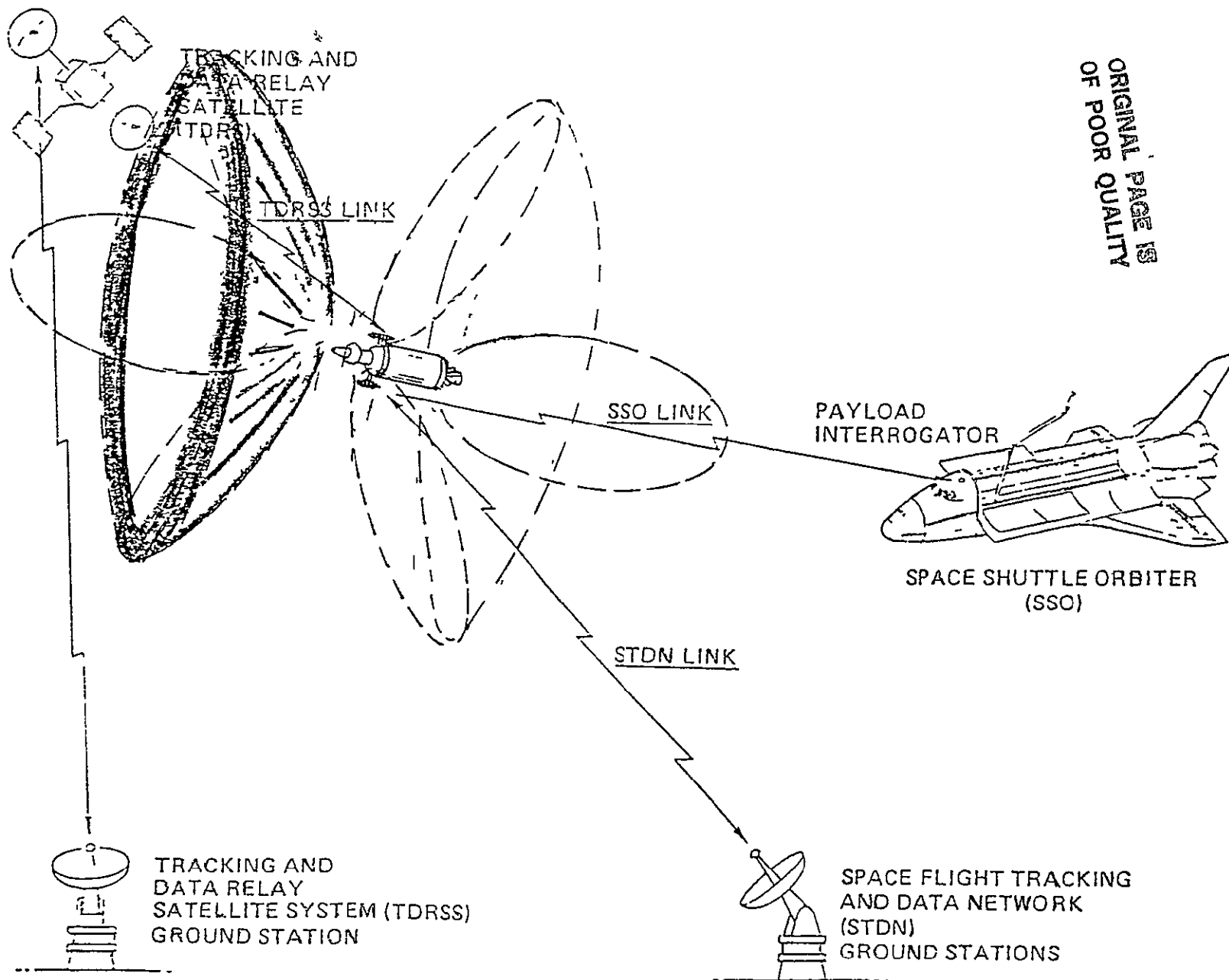


Figure 7. Toroidal Coverage Provided by the Switched-Beam Biconical Array

substantial since the phase centers are widely separated, but all the candidate antenna systems proposed to date suffer from this possible problem. The only real solution is to have only one biconical array which, as has been determined, is not feasible because of payload envelope requirement limitations.

The operation of the biconical array needs further explanation since it is a relatively new idea for this type of application. First, the idea is to create a conical toroidal pattern which has the desirable characteristics of circular symmetry, since the Centaur vehicle revolves and the target, therefore, is always at a constant conical angle with respect to the Centaur, except for the fore-and-aft coverage case which is obviously accommodated by the conical log spiral antennas pointed in those directions. An array of three individual biconical antennas is used to achieve higher gain, which is one of the essential requirements of the Centaur antenna system since the Centaur/TDRS link is marginal, at best. The choice of only three biconical antennas for the array is based on simplicity since electromechanical switching is envisioned. Of course, this method is not absolutely necessary, and situations may arise where PIN diode phase shifters and more than three biconical elements are needed to provide higher gain but, for the moment, this baseline configuration can be used to justify the feasibility of this approach. The PIN diode phase shifters require costly electrical holding power and are lossy, but the use of more biconical elements with PIN diode phase shifters should be studied if this configuration is seriously considered since higher gain might be a critical mission requirement.

3.2 Switched-Beam Concept

The Shuttle Orbiter S-band quad-antenna program uses a two-element switched two-beam configuration with one electromechanical switch to transpose discrete phase shifts of the two radiating elements, thereby creating two selectable switched beams. Since there are four quad antennas composed of two switched beams about the Orbiter, a total of eight switched beams are possible. This Centaur biconical-array configuration, on the other hand, would have two clusters of three biconical elements which can have, for example, 32 "half"-toroidal beam positions (for a total of 16 toroidal beam positions), which covers most of the surrounding space except for the

fore-and-aft coverage provided by the conical log spiral antennas. Once the particular toroidal beam is selected and concurrently set by the switch position of both clusters, only one switch is activated to direct power to the appropriate side of the vehicle, which greatly simplifies acquisition, tracking and reliability considerations.

3.3 Power-Handling Capability

Electromechanical latching switches on the Orbiter S-band quad antennas were used primarily because of the high power of the transmitter, which is of the order to 50 watts. Since the Centaur vehicle TWTA might be similar to the Hughes 40-W version, this high-power switch requirement must also be evaluated seriously for this application because PIN diode switches cannot handle much power. This consideration must also be taken into account, for example, when studying the feasibility of the truncated sphere antenna concept since the four activated PIN diode switches must be capable of handling 40 W of power. The high switching rate of PIN diodes is desirable, of course, but, for the Centaur application, it does not appear to be a critical design parameter since, once the beam position is selected, the switches do not have to be activated. The only switch to be activated during operation is that which directs power alternately from one side of the vehicle to the other. High-power PIN diode SPDT switches have recently been developed, but their insertion loss of 0.7 dB is substantially higher than the 0.1-dB loss of the electromechanical switches.

3.4 Multiple-Beam Switching Configurations

The beam-pointing mechanism of a linear phased array is used to point the toroidal beam. Three biconical elements were chosen for the array because this is the most basic phased array for the electromechanical high-power switches. The center element is directly fed with a voltage ratio of 1.0; the two outer elements are then fed with a voltage ratio of 0.6 to provide illumination taper. Introducing discrete phase shifts to the two outer elements then causes the beam position to shift, thereby creating the necessary pointing capability. For example, Figure 8 shows the tilting of the radiated phase front by adjusting the phase at the two outer elements. Figure 9 shows the two-beam configuration, Figure 10

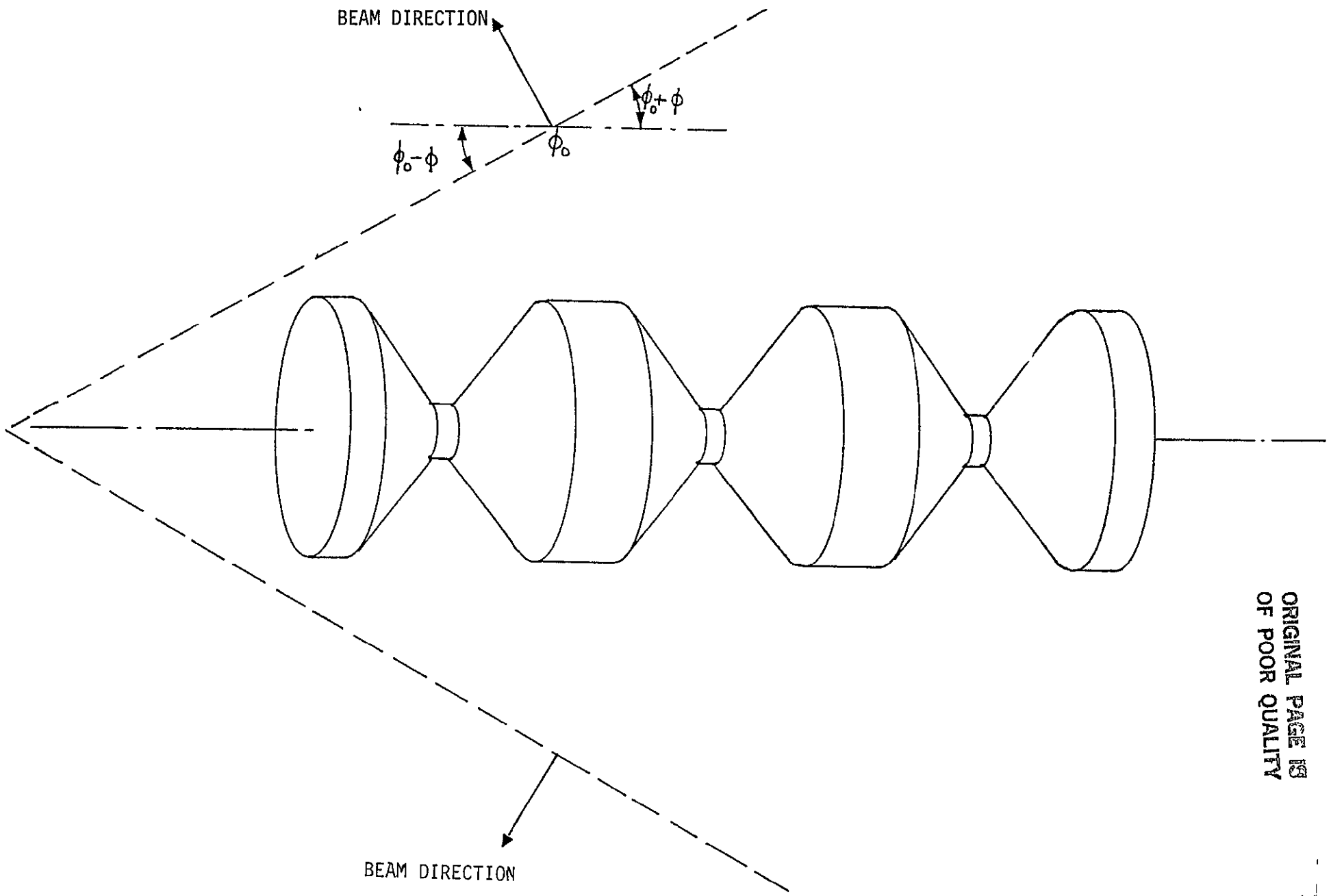


Figure 8. Beam Tilting by Phase Shifting

ORIGINAL PAGE IS
OF POOR QUALITY

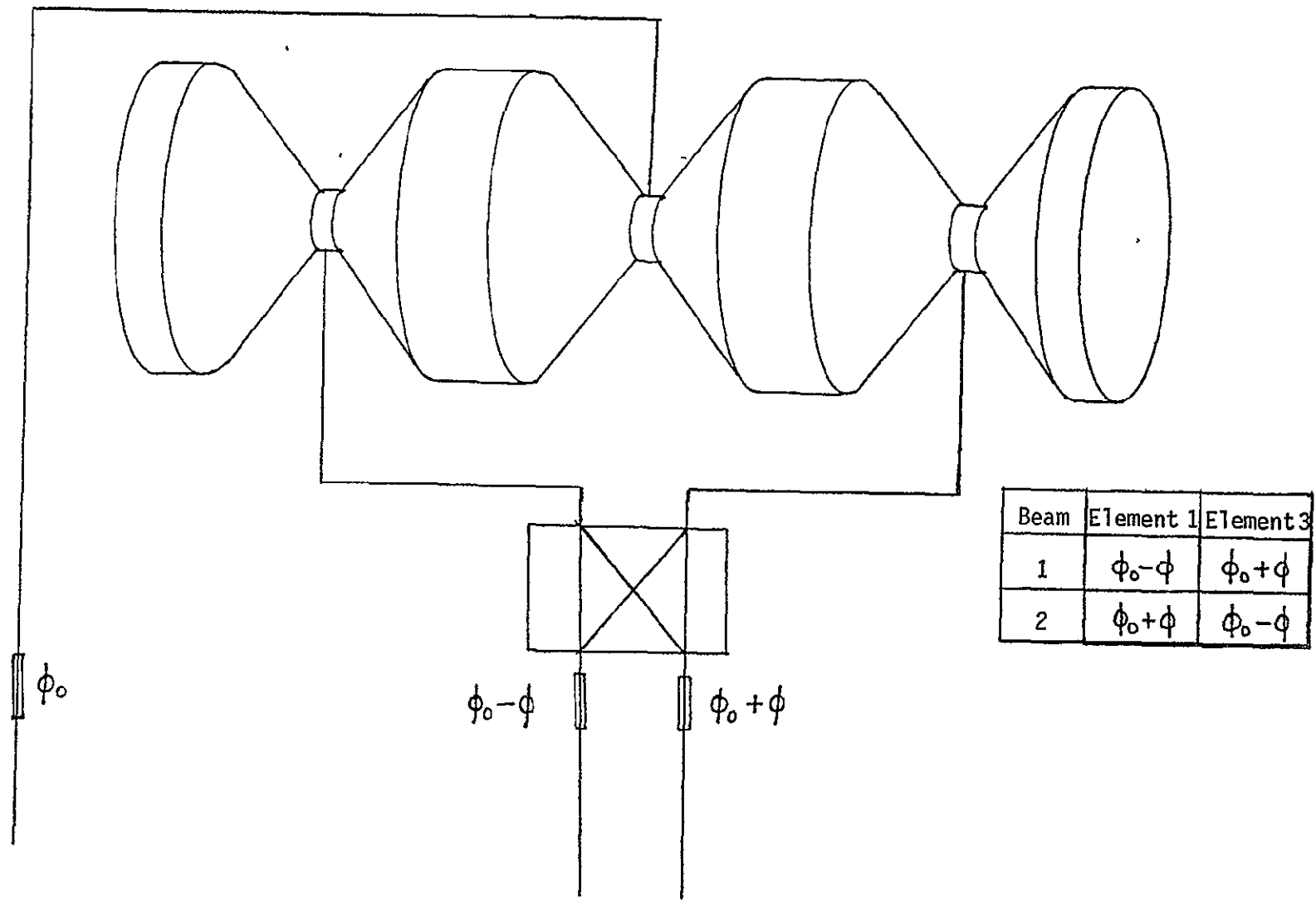


Figure 9 Two-Beam Switching Scheme

ORIGINAL PAGE IS
OF POOR QUALITY

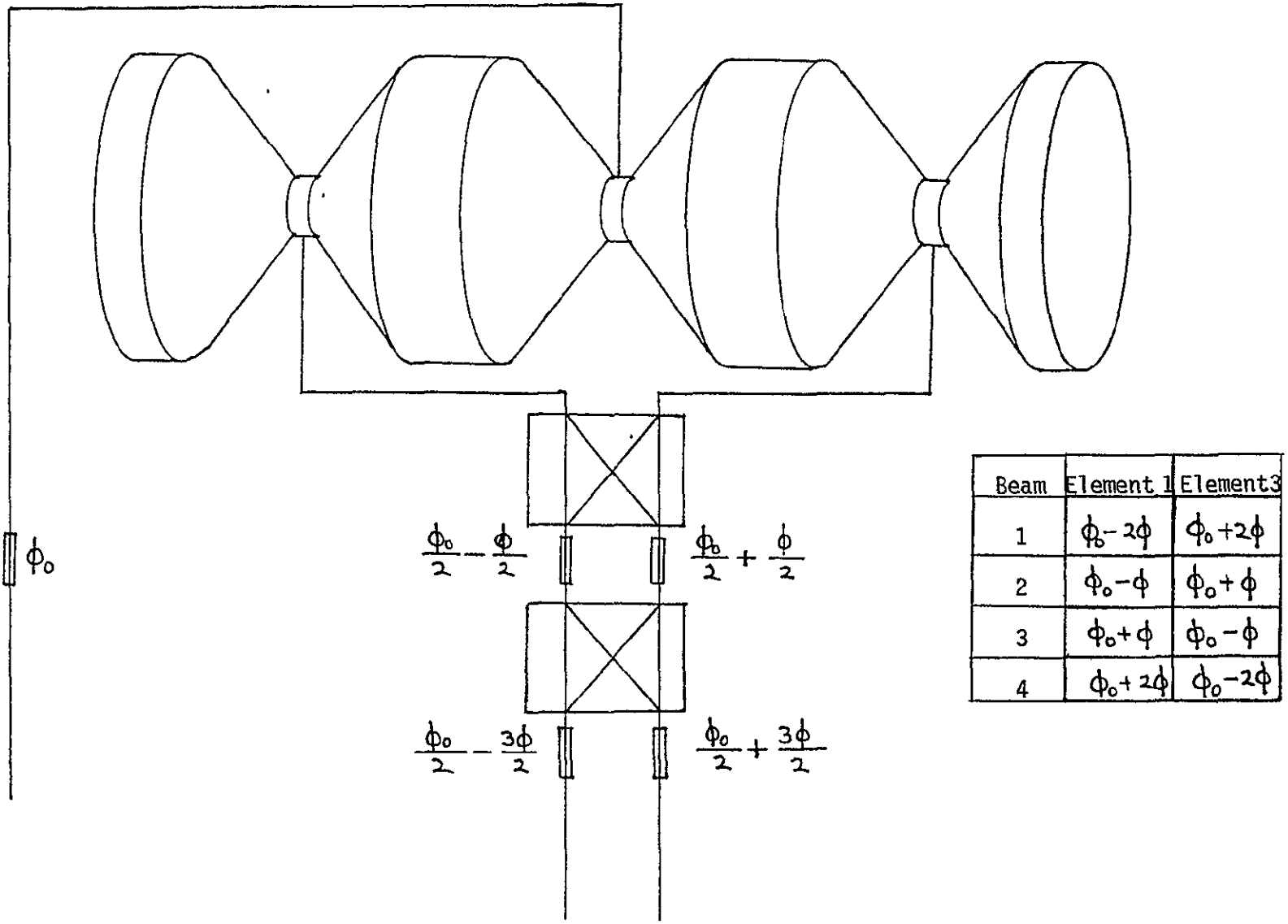


Figure 10. Four-Beam Switching Scheme

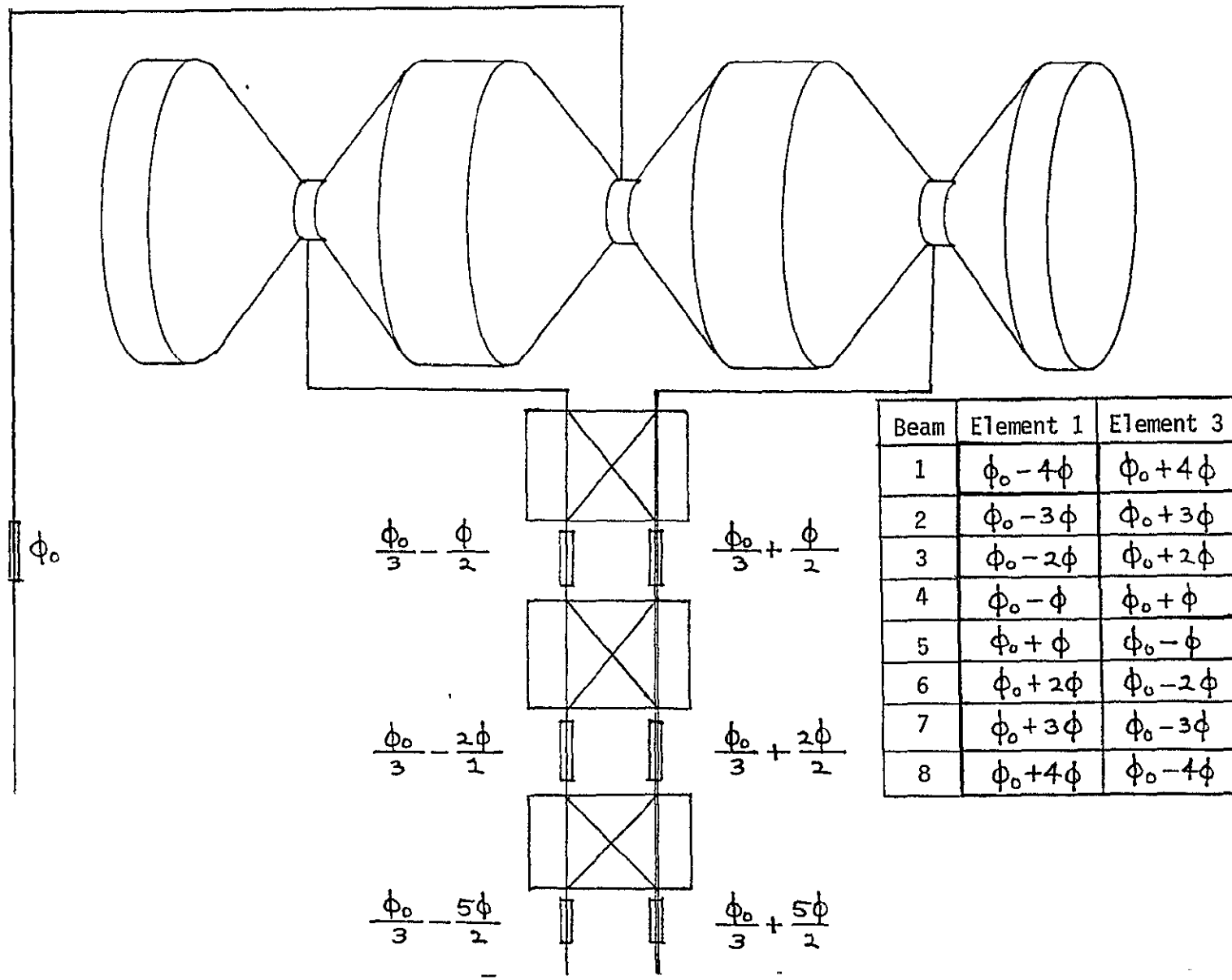
ORIGINAL PAGE IS
OF POOR QUALITY

depicts the four-beam configuration, Figure 11 illustrates the eight-beam configuration and, finally, Figure 12 gives the 16-beam configuration. Note that the addition of each switch and discrete phase shift adds only 0.2 dB of additional loss so that four electromechanical switches in a series is not unreasonable. Also, since the center element which carries most of the power is directly fed, the use of multiple switches does not significantly degrade performance in the normal additive manner. These switches can readily be housed in the base of the truncated biconical array so that only one RF cable is required to carry the power along the boom to the compound antenna. The switching arrangement might appear as shown in Figure 13, where switch A determines which side of the Centaur is activated, switch B determines if the biconical array or conical log spiral antennas are used, and switch C determines the fore-or-aft conical log spiral antenna. For the sake of illustration, the beam-switching switches are not emphasized here. Note that these electromechanical latching switches can be characterized by binary numbers to describe the switch state. For example, if the "straight-through" state is defined as "0," the "cross-over" state is then "1." Thus, a given beam position can be adequately described by a series of binary numbers. If switch A is "1," switch B is "0," etc., then a specific beam position has a uniquely defined code. Thus, each beam position can be obtained by switch drivers being controlled by this code, and switching between the two opposite sides of the Centaur requires the switch A position to switch alternately from "1" to "0" and back cyclically, depending only on the roll rate of the vehicle. Since the beam position code on both compound antennas can be made identical, the specific beam position code remains the same and only switch A operates, greatly minimizing the software requirements. Similarly, an electromechanical switch (not included here) can switch functions from the transmitter and receiver modes. Although the electromechanical switch provides a high degree (>40 dB) of isolation, a duplexer might be required to further protect the receiver, especially since the "half"-toroidal patterns overlap.

3.5 Broadside-Beam Coverage

At this time, it would be appropriate to discuss the problem associated with beam symmetry, which may be apparent by close examination of Figure 10, where the broadside beams are separated by 2θ (i.e., $\theta_0 + \theta$

C-2



ORIGINAL PAGE IS
OF POOR QUALITY

Figure 11. Eight-Beam Switching Scheme

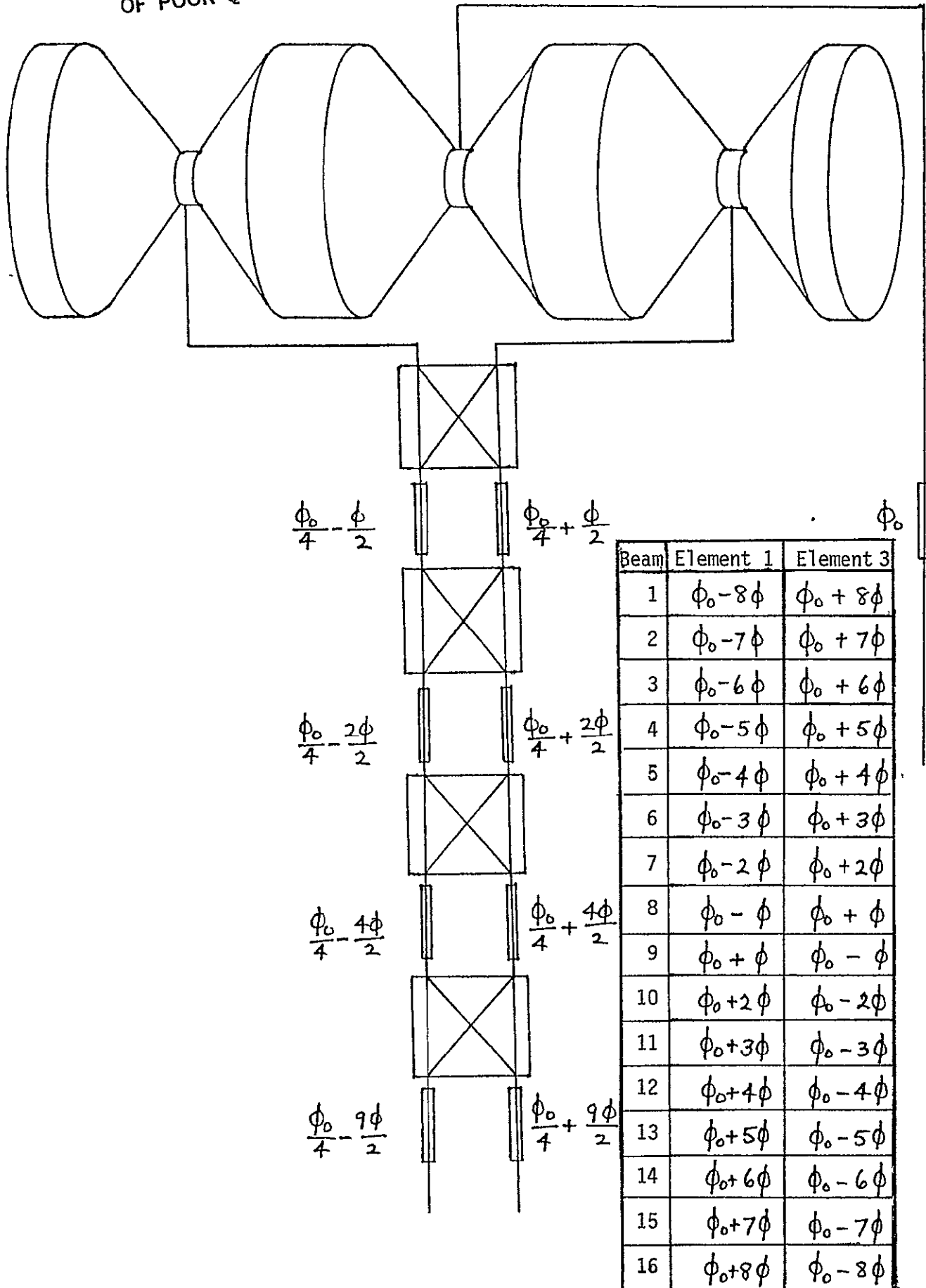
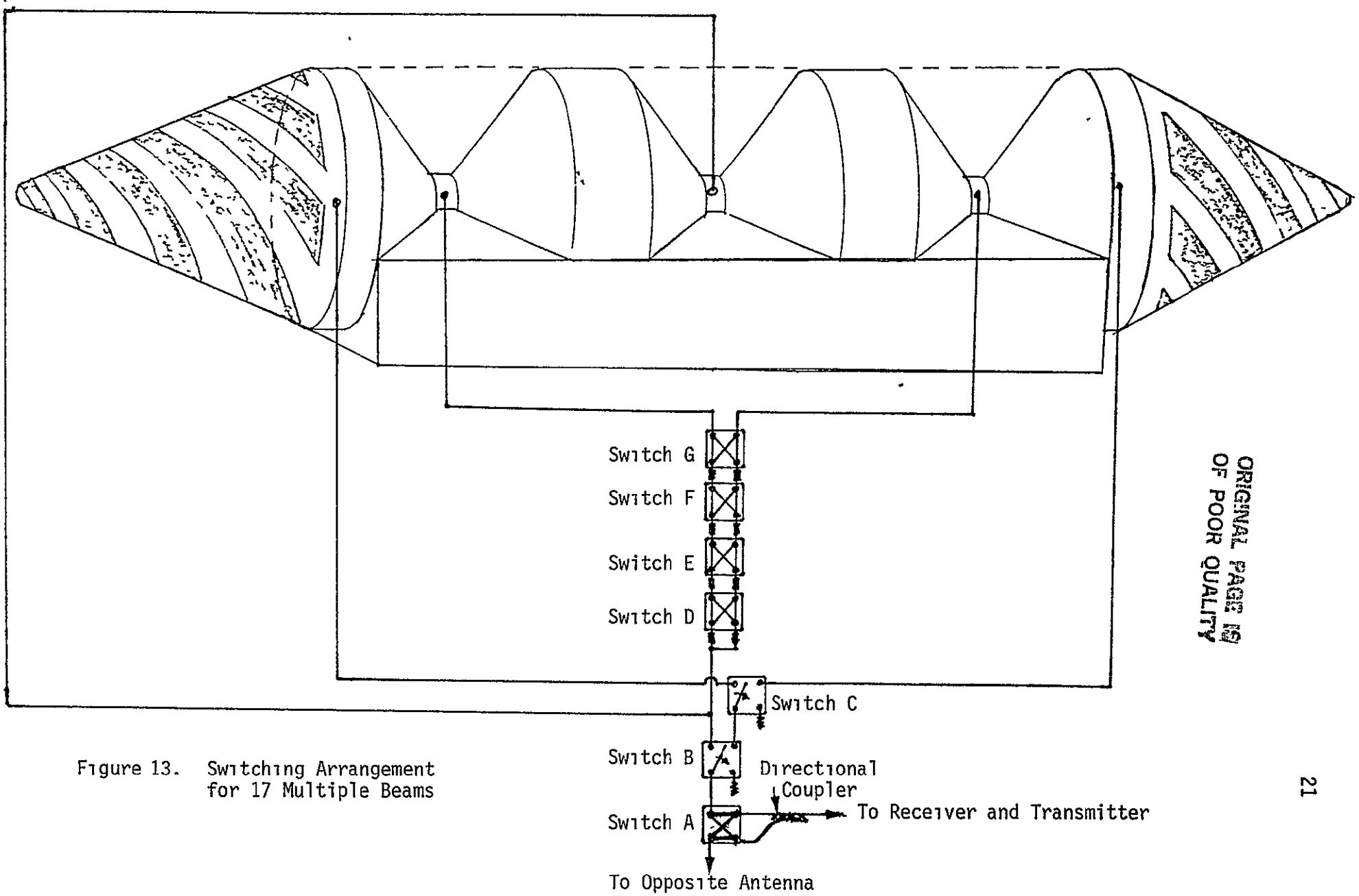


Figure 12. 16-Beam Switching Scheme



ORIGINAL PAGE IS
OF POOR QUALITY

Figure 13. Switching Arrangement for 17 Multiple Beams

and $\theta_0 - \theta$). The exact broadside beam requires equal phase angles at all three elements (θ_0). This condition is attainable, but only at the expense of one beam position since the broadside beam is double redundant; therefore, two switch settings comprise the broadside case. For a large number of beam positions, this consideration is not important. For example instead of 16 beams, 15 beam positions are used. The necessary phase shift changes to effect this change are listed in Figures 14 through 16 for the three-, seven- and 15-beam configurations, respectively. Incidentally, a 31-beam configuration should at least be evaluated since the additional pointing flexibility justifies the additional switch if obtaining the peak biconical array gain is important.

3.6 Circular Polarization

The biconical antenna is usually associated with linear polarization since it is readily envisioned with a radiating probe feed at the intersecting apex of the two conical sections comprising the impedance-matching taper of the antenna. However, a number of methods may be employed to generate circular polarization and these different techniques must be evaluated further to determine their feasibility for this particular application. The intent of this discussion is to indicate that circular polarization is readily achievable, although the best-type of transducer is not specified. The simplest and probably most efficient transducer would consist of the probe feed used for linear polarization, combined with an orthogonal probe with the appropriate phase-shifting network to create circular polarization. This orthogonal probe would not necessarily be located at the apex of the cones, but might be located at a position that is radially outward from the conical axis, as sketched in Figure 17, such that the orthogonal mode can readily propagate outward. Because of the conical tapering effect, this probe would be reactively terminated and the radial distance can be usefully employed to contribute to the necessary phase shift needed to generate circular polarization. The phase relationship of this orthogonal probe (with respect to the original probe at the apex of the conical antenna) then determines whether the transducer is right-hand circularly polarized (RHCP) or left-hand circularly polarized (LHCP). Since the biconical element is truncated, the orthogonal probe feed is only a section of the circular loop, and the gain is accordingly higher.

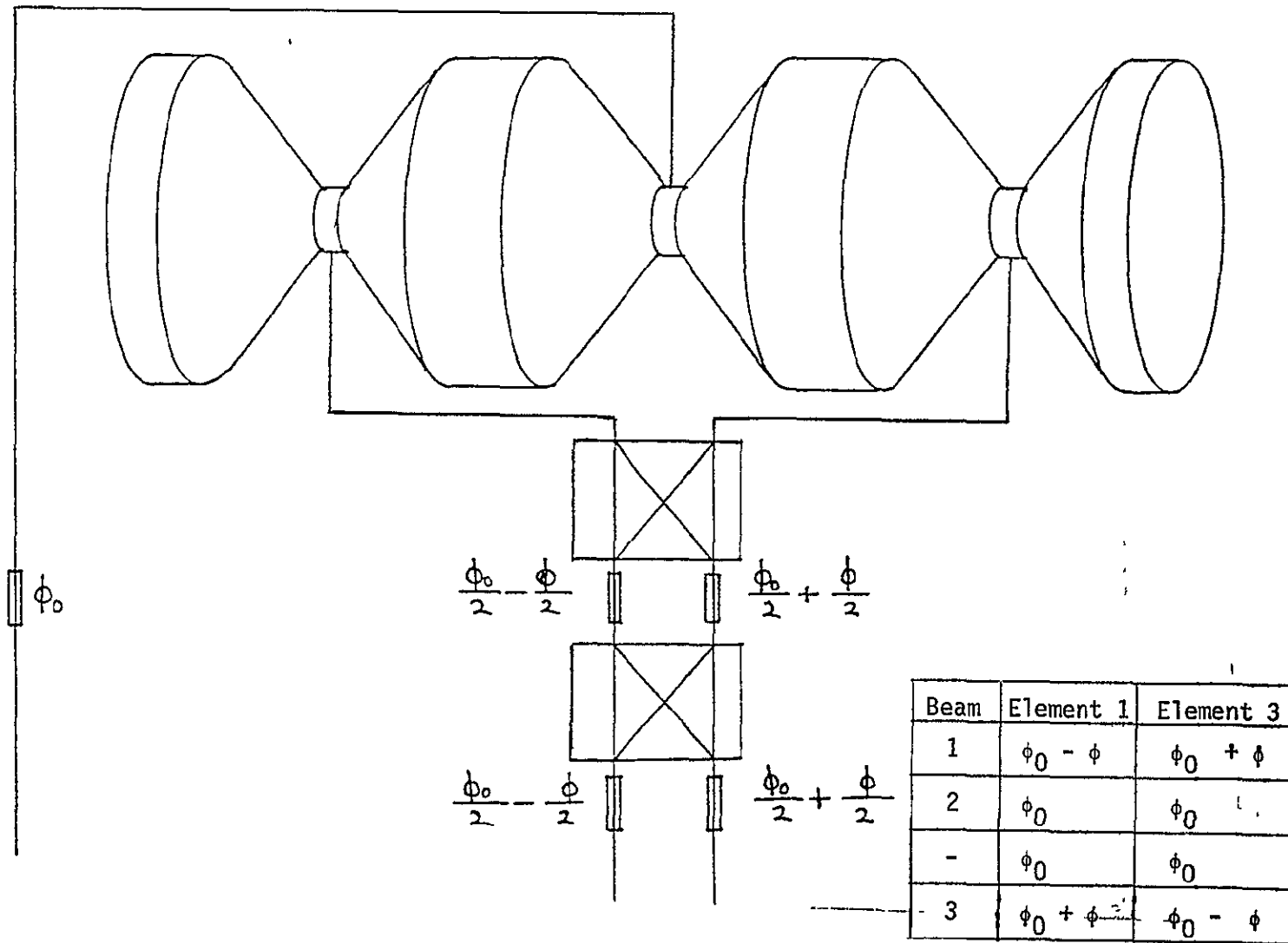


Figure 14. Three-Beam Switching Scheme

ORIGINAL PAGE IS
OF POOR QUALITY

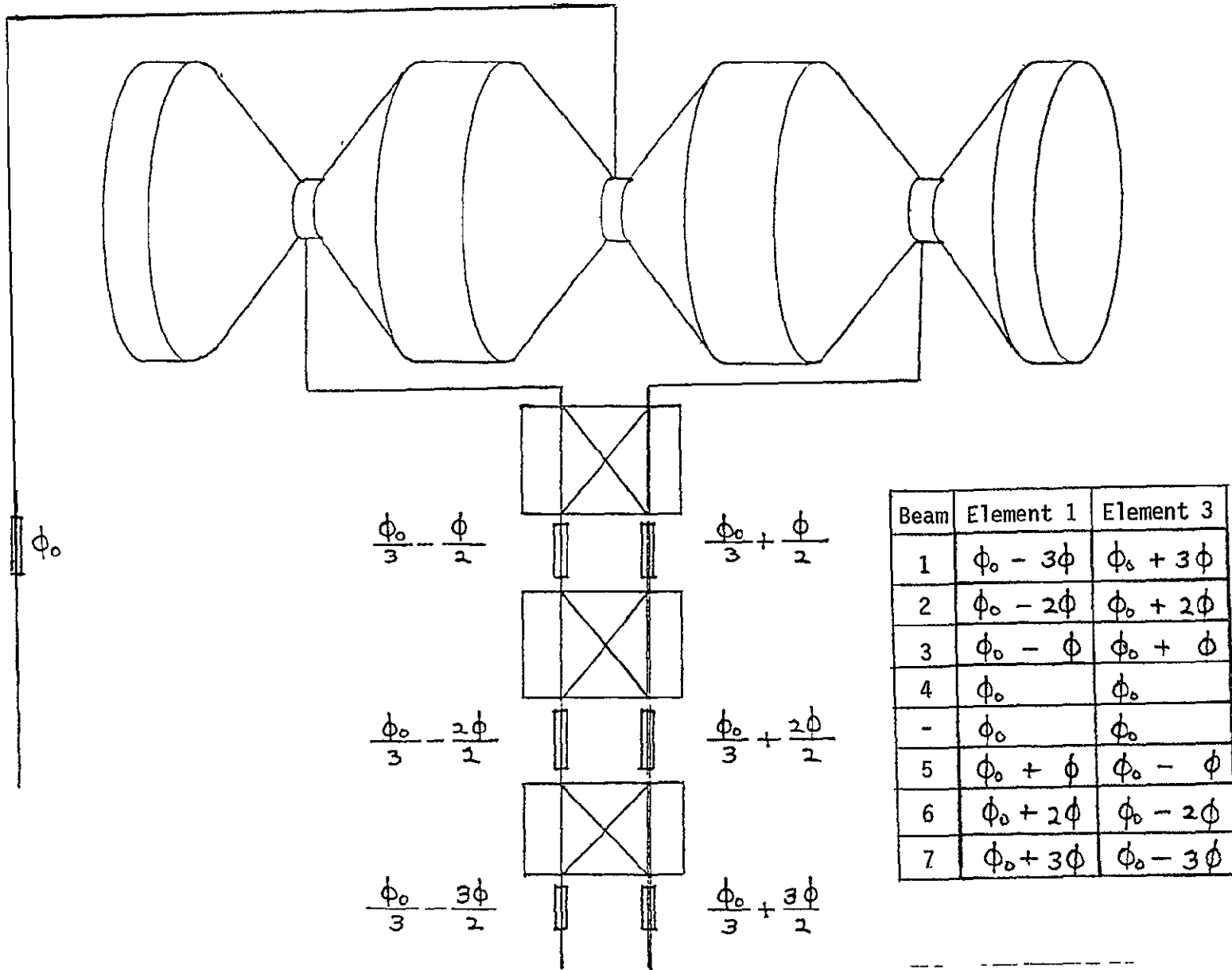
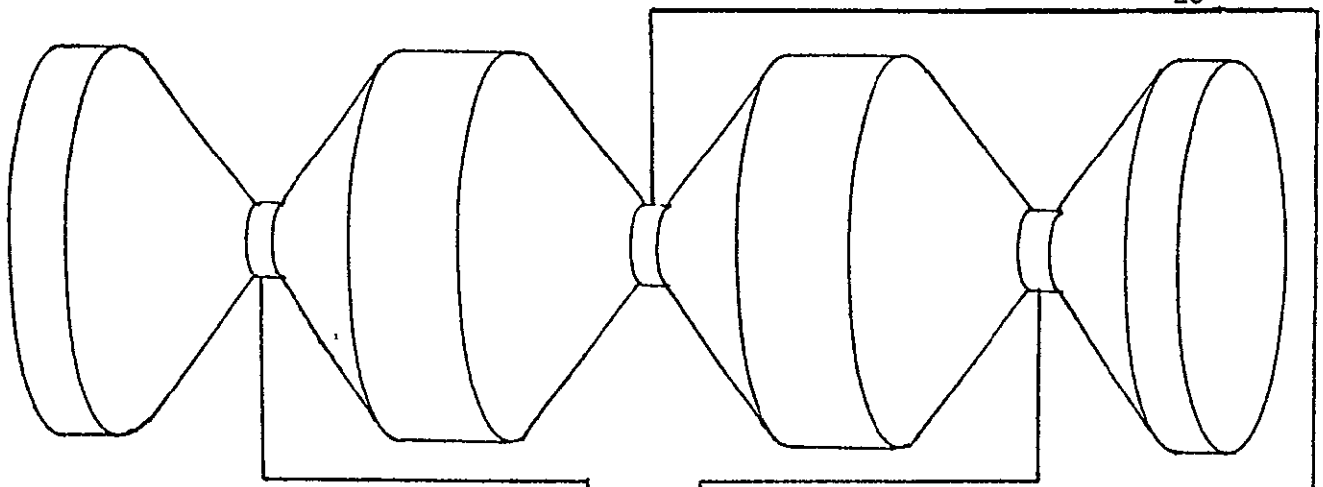
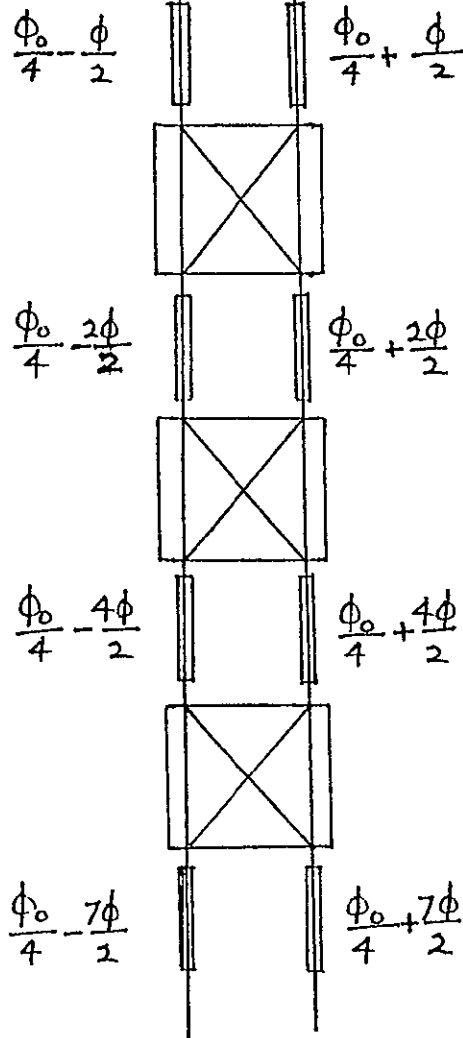


Figure 15. Seven-Beam Switching Scheme



ORIGINAL PAGE IS
OF POOR QUALITY



Beam	Element 1	Element 3
1	$\phi_0 - 7\phi$	$\phi_0 + 7\phi$
2	$\phi_0 - 6\phi$	$\phi_0 + 6\phi$
3	$\phi_0 - 5\phi$	$\phi_0 + 5\phi$
4	$\phi_0 - 4\phi$	$\phi_0 + 4\phi$
5	$\phi_0 - 3\phi$	$\phi_0 + 3\phi$
6	$\phi_0 - 2\phi$	$\phi_0 + 2\phi$
7	$\phi_0 - \phi$	$\phi_0 + \phi$
8	ϕ_0	ϕ_0
-	ϕ_0	ϕ_0
9	$\phi_0 + \phi$	$\phi_0 - \phi$
10	$\phi_0 + 2\phi$	$\phi_0 - 2\phi$
11	$\phi_0 + 3\phi$	$\phi_0 - 3\phi$
12	$\phi_0 + 4\phi$	$\phi_0 - 4\phi$
13	$\phi_0 + 5\phi$	$\phi_0 - 5\phi$
14	$\phi_0 + 6\phi$	$\phi_0 - 6\phi$
15	$\phi_0 + 7\phi$	$\phi_0 - 7\phi$

Figure 16. 15-Beam Switching Scheme (With Redundant Broadside Beams)

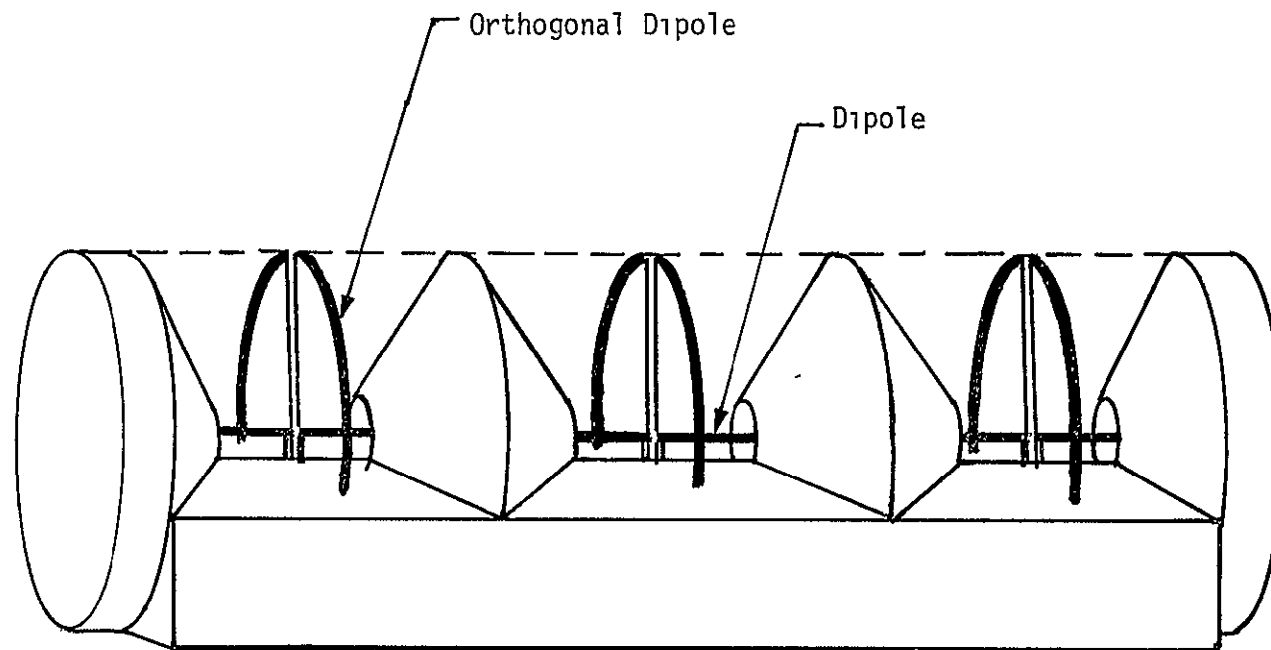


Figure 17. Circular Polarization Transducers for Biconical Antennas

Mounting of the orthogonal probe feed can be on a dielectric circular wedge for mechanical stability and increasing the effective taper of the biconical element. Since the biconical elements will be spaced so that their phase centers are less than a half wavelength apart, the effective taper of the bicone is increased by the factor $\sqrt{\epsilon_r}$, where ϵ_r is the relative permittivity of the dielectric. Use of the dielectric thus effectively shortens the physical wavelength and gives greater flexibility in design considerations.

The design criteria for these orthogonal probes are basically those of two crossed half-wavelength dipoles (or monopoles), separated by $\pi/2$ to provide the quadrature phase relationship. This phase shift can also be achieved by phase shifters, but an intrinsic physical design relationship exists with the biconical element which can be readily exploited. Since the biconical element is circularly symmetric and the orthogonal dipole is curved accordingly, the off-axis axial ratio degradation is decreased substantially.

Other techniques used to obtain circular polarization from a biconical element are more complex and therefore require more study. However, the basic operating principles can be discussed. Jasik [1] discusses the use of inclined slots as a feed for a biconical element which utilizes the differential propagation delay of the horizontal and vertical polarization modes to create the phase quadrature relationship, where the slant length of the biconical horn is experimentally adjusted to achieve the $\pi/2$ phase shift at the aperture. The inclined-slot arrangement simply provides both polarizations with equal amplitudes and the horn slant length then creates the differential delay.

4.0 ANTENNA SWITCHING WITH PHASE CONTINUITY

The phase discontinuity arising from switching between the two antennas on opposite sides of the vehicle appears to be an insurmountable problem unless very sophisticated phase detection circuitry is incorporated into the system, thereby increasing complexity and cost. Even the conceptual development of such a system is difficult. Although this time period may be very short (of the order of the switching time of 40 ms), the importance of this data must be weighed in terms of the difficulties required to attempt to rectify the problem.

The IUS system for minimizing phase and amplitude transients appears to be based on an onboard computer which switches at the 45° position of the 85° HPBW. The computer knows the direction of the appropriate TDRSS and the center of the earth and can therefore switch when the theoretical pattern overlap occurs. The computer algorithm is said to be developed and system is therefore operational. A close examination of this antenna switching is warranted, however, since there may be another solution to the problem.

First, minimization of the phase transient relies on maintaining the phase centers of each antenna on the two clusters close together. Ideally, these phase centers are coincident and the phase shifts due to the feed lines have to be matched. These conditions can be accomplished, especially since the apparent phase centers of the log conical spiral antenna can be adjusted. Note that the actual phase center is difficult to determine without very accurate phase pattern measurements, but it is possible. The only real problem then is switching between clusters since, by definition, the phase centers cannot be coincident on opposite sides of the vehicle. It is this aspect of the problem that should be studied in a little more detail and, using the biconical-array configuration, a possible approach is outlined.

First, recall that the biconical array has higher gain and a circularly symmetric pattern with overlap, and requires only two switching procedures per revolution. The main consideration now is to minimize the phase transient problem switching from one antenna to the other on the opposite side of the vehicle. The easiest solution is to switch when the phase centers are exactly equidistant from the target (i.e., when the antennas form an isosceles triangle with the target). This is probably the condition employed by the IUS antenna switch scheme but, because of the large physical leverage arms of the antennas extended out on booms, the exact switching position is difficult to ascertain. The antenna-switching scheme to be discussed here is an attempt to solve this problem by using a modified monopulse sum pattern technique to determine the optimum switching position.

The optimum switching position occurs when the phases of two simultaneous signals from both antennas on opposite sides of the Centaur vehicle are identical. This condition can be described as a constructive interference pattern when the phases of the two signals reinforce each

other to create a higher gain sidelobe, which is the mechanism by which phased arrays and monopulse tracking circuits operate. Therefore, if this constructive interference pattern exists at the point where the antennas are switched, phase continuity is maintained. Again, although this condition exists cyclically since it causes lobing phenomena, the optimum switching position is where the antennas are equidistant to the target; the on-board computer should know this approximately. This position must be known exactly, however, if it is determined that no data loss is acceptable. A phase synchronization scheme has therefore been devised to determine the optimum switching point.

If a double-pole/double-throw (DPDT) electromechanical switch is used to switch power between the two arrays, the introduction of a directional coupler to split the power unequally will create a modified phased array situation where an asymmetrical toroidal pattern exists. The region of concern is then the beam overlap region where pattern interference occurs. This pattern interference is characterized by lobing, where both constructive and destructive interference exists. If both biconical arrays received equal power, serious lobing with deep nulls develop in the main antenna pattern when destructive interference conditions are satisfied and undesirable amplitude signal loss would occur. However, if unequal power distribution is employed, the effects of constructive and destructive interferences are reduced accordingly. For example, if a 10-dB coupler is used, 10% of the power is diverted to the other (secondary) antenna, with the operational or primary antenna receiving 90% of the power. This power division ratio is somewhat arbitrary now for explanatory purposes and can be determined later by system analysis if such a scheme is considered seriously. Also, it is emphasized that the only reason that power division is feasible is that the higher gain of the biconical array compensates for the apparent power loss.

As a result of the power division, the beam overlap region now develops sidelobes by constructive and destructive interference in the main antenna pattern, as shown in Figure 18. The cyclical fluctuations arise from the additional radiation from the secondary antenna. The condition for phase concurrence is constructive interference, where the newly developed sidelobe is at its peak and, if the antenna can be switched at this position, phase continuity is maintained. In essence, this is a modified monopulse-tracking scheme where the sum pattern is used to detect a relative maximum whose amplitude is related to the power division ratio.

ORIGINAL PAGE IS
OF POOR QUALITY

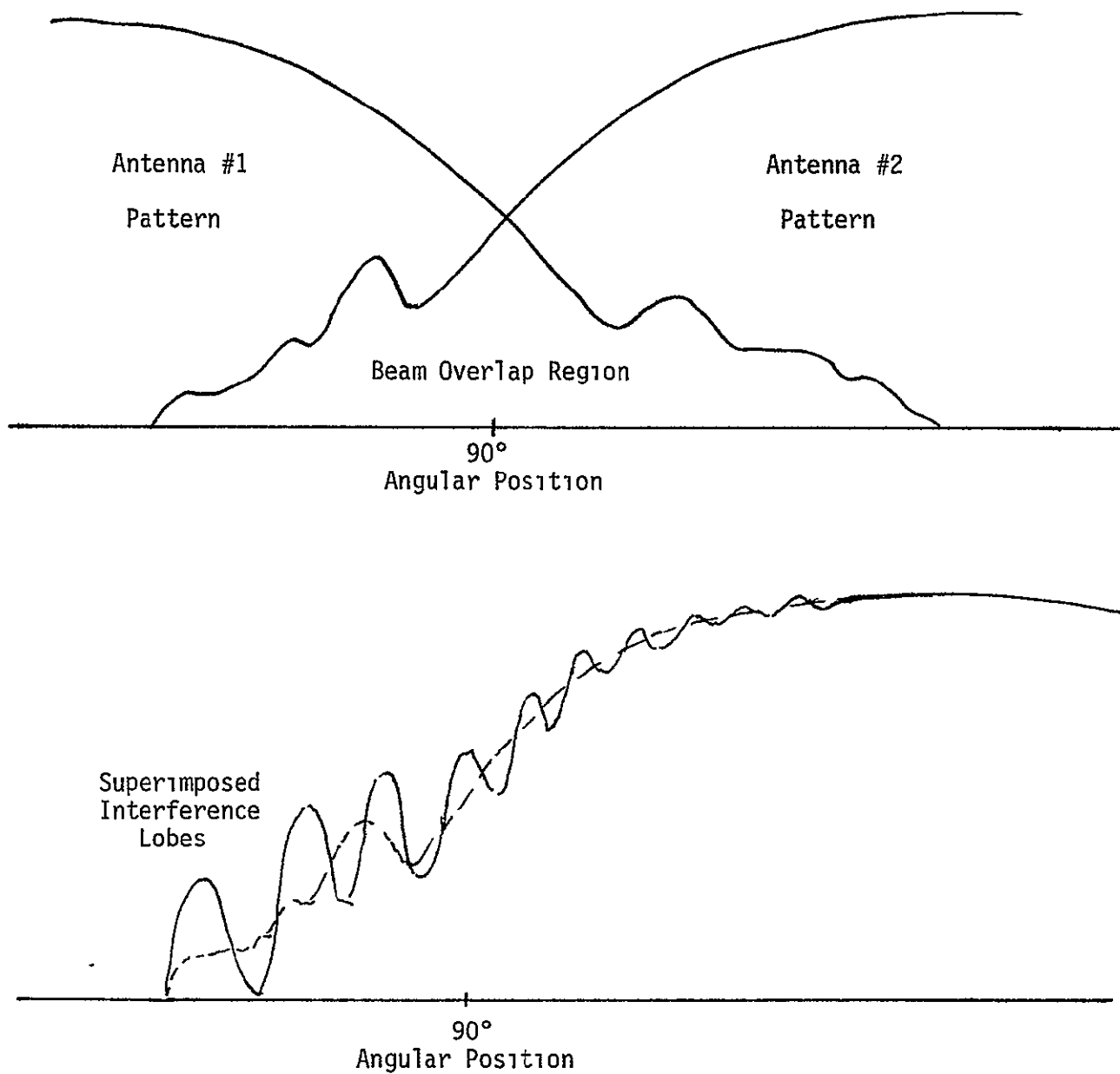


Figure 18. Interference Lobes Superimposed on Primary Antenna Patterns

The simplest method of implementing this phase continuity switching scheme is to use the automatic gain control (AGC) voltage as a basic power-level detector. This power-level detector then monitors the receiving antenna pattern in the beam overlap position and actually measures the antenna-switching position, which can then be stored for use during the transmission mode also. At the present time, determination of the optimum switching points can be made in the receive mode only when a distant source, such as the TDRSS, transmits.

The detected power-level voltage at the transition point should consist of a periodic series of lobes varying $\pm 10\%$ if a 10-dB directional coupler is used as a power divider. The phase concurrence position will be at the peak voltage, where the maximum lobe exists, since constructive phase interference occurs there. It is desirable to have some beam overlap between antennas so that approximately equal signal levels exist when the antennas are switched to the opposite side. Although the optimum switching point on a system basis has not been established, this phase synchronization concept can be used as a basis for further development of a scheme to maintain a continuous communication link for rotating space vehicles.

5.0 SWITCHABLE PREAMPLIFIER

It is obviously advantageous to operate in a mode where the signal-to-noise ratio (SNR) is high. One possible means of improving this condition in the "receive" mode is to employ preamplifiers close to the antennas, especially since very low noise figure FET preamplifiers exist at S-band. This can be feasible if, during the "transmit" mode, the preamplifiers can be switched out of the circuit. One means that might be considered is to again use the double-pole/double-throw (DPDT) electromechanical switch in a novel manner and turn the preamplifier off during transmission. Figure 19 shows a possible scheme which, in the "0" state, allows transmission by bypassing the preamplifier and incorporating the preamplifier in the "1" state. The isolation between connectors is critical, but 30 dB should not be unreasonable. If the preamplifier is de-energized during transmission, no damage due to leakage currents should occur. Since the preamplifier is located at the antenna, the noise figure of the receiver is greatly enhanced and the link margin is substantially improved.

The preamplifier also serves to simplify the phase synchronization scheme since it permits the equalization of received signal amplitude levels by amplifying the signal from the secondary antenna to the receiver to compensate for the loss imposed by the directional coupler. Since the contributions from both the primary and secondary antennas would then be equal, the constructive and destructive interference patterns will consist of lobes with well-defined peaks and nulls. Therefore, determination of the optimum switching-level detection circuitry problem might be reduced to a basic threshold detection problem. The preamplifier can remain on after the antenna-switching procedure, thereby substantially lowering the receiver system noise temperature.

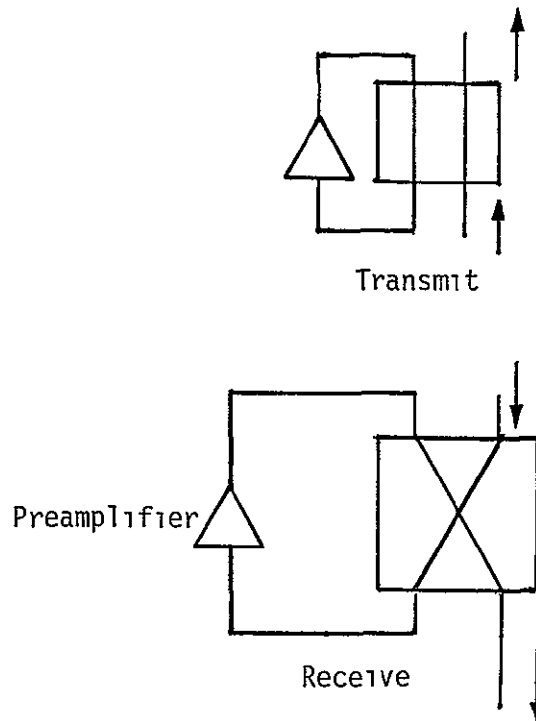


Figure 19. Candidate Switchable Preamplifier

APPENDIX C

CENTAUR HARDLINE ICD

8.4 Instrumentation & Command Data Links.

8.4.1 Instrumentation Data Links. The Orbiter shall provide the capability to transmit selected data from four PCM digital data streams (CISS, Centaur, and two S/C) from the CCE to the ground.

During prelaunch checkout, the only two PCM streams (CISS and Centaur) will be hardwired from the CCE, through the Orbiter, to the Ground Computer Controlled Launch Set (CCLS). CCLS access will be required until T-0 (Note: at SRB ignition) in the countdown.

During the final countdown and ascent mission phases the CCE will provide the four data streams (max. 64 Kbps each) to the Orbiter and the Orbiter will select and interleave 6.4 Kbps (max) of data from the four PCM streams and transmit this information to the ground for real-time systems evaluation. In addition, two of the four CCE data streams shall be recorded by the Orbiter for transmission to the ground after achieving orbit. Each data stream to recorder and orbiter telemetry system shall be isolated from each other at the orbiter interface.

During on-orbit operations, prior to Centaur stage deployment, the Orbiter will select, interleave, and transmit a maximum of 34.4 Kbps of the CCE data. The Orbiter shall continue to record one of the CCE data streams for delayed transmission to the ground. After Centaur stage deployment, only one PCM stream (CISS) will continue to be supplied directly to the Orbiter via an RF link. This data will be interleaved with the orbiter operational PCM data for transmission to the ground.

8.4.1.1 Payload Data Interleaves Interface. The Orbiter shall provide for the acquisition of asynchronous PCM data via the Payload Data Interleaver (PDI) from the four (1 CISS, 1 Centaur stage, and 2 spacecraft) CCE channels and from the Payload Signal Processor for the deployed Centaur. The PDI has a maximum composite throughput on-orbit of 64 kbps, See Figure 1 for Payload Data Interleaver data flow. However, ascent downlink CCE data shall be limited to that specified in paragraph 8.3.1.1.3.1.

8.4.1.1.1 PDI Input Data Format Characteristics.

8.4.1.1.1.1 CISS Data Format Characteristics. The PDI shall accept one data stream from the CISS. The CISS Data Format is defined as a format containing master frames and minor frames. Refer to Figure 2. Every minor frame shall be identified by a minor frame sync pattern which occurs once each minor frame, and shall be the same for all minor frames. A master frame shall contain TBD minor frames. Additionally, every minor frame shall contain an eight bit minor frame count word. The start of the master frame shall be identified as the minor frame which contains the initial value of the minor frame count word. The CISS data format characteristics shall be as shown in Table 1.

INTERFACE CONTROL DOCUMENT

ORBITER VEHICLE/CENTAUR

SIZE
A

ICD NO
ICD-2-1F001

REV
SHEET 45
OF

8.4.1.1.1.2 Centaur Data Format Characteristics. The PDI shall accept one data stream from the centaur. The Centaur Data Format is defined as a format containing master frames and minor frames. Refer to Figure 2.

Every minor frame shall be identified by a minor frame sync pattern which occurs once each minor frame, and shall be the same for all minor frames. A master frame shall contain TBD minor frames. Additionally, every minor frame shall contain an eight bit minor frame count word. The start of the master frame shall be identified as the minor frame which contains the initial value of the minor frame count word. The Centaur data format characteristics shall be as shown in Table 2.

8.4.1.1.1.3 Centaur Payload Data Format Characteristics. The PDI shall accept two redundant NRZ-L data streams and associated clock with each stream from the Centaur Payload. The data format is identical for both data streams and each is defined as a format containing master frames and minor frames. Refer to Figure 2.

Every minor frame shall be identified by a minor frame sync pattern which occurs once each minor frame, and shall be the same for all minor frames. A master frame shall contain TBD minor frames. Additionally, every minor frame shall contain an eight bit minor frame count word. The start of the master frame shall be identified as the minor frame which contains the initial value of the minor frame count word. The Centaur Payload data format characteristics shall be as shown in Table 3.

8.4.1.1.1.4 Detached Centaur Data Format Characteristics. In the detached mode, the Centaur will transmit a data stream via an RF link to the Orbiter Payload Signal Processor (PSP) via the Payload Interrogator. The PDI shall accept the data stream from the PSP. The detached Centaur data format is defined as a format containing master frames and minor frames. Refer to Figure 2.

Every minor frame shall be identified by a minor frame sync pattern which occurs once each minor frame, and shall be the same for all minor frames. A master frame shall contain TBD minor frames. Additionally, every minor frame shall contain an eight bit minor frame count word. The start of the master frame shall be identified as the minor frame which contains the initial value of the minor frame count word. The Detached Centaur data format characteristics shall be as shown in Table 4.

8.4.1.1.2 PDI Electrical Interface Characteristics.

8.4.1.1.2.1 CCE/PDI Data Electrical Interface Characteristics. The electrical interface characteristics of each of the CCE data streams interfacing with the orbiter PDI shall be as shown in Table 5.

INTERFACE CONTROL DOCUMENT

ORBITER VEHICLE/CENTAUR

SIZE

A

ICD NO

ICD-2-1F001

REV

SHEET 46

OF

8.4.1.1.2.2 CCE/PDI Clock Electrical Interface Characteristics. The electrical interface characteristics of each of the Centaur Payload clocks interfacing with the Orbiter PDI shall be as shown in Table 6.

8.4.1.1.2.3 Grounding and Shielding. Grounding and shielding for the PDI Data and clock interfaces shall be as shown in Figure 6.

8.4.1.1.3 Orbiter PCM TLM Downlink Service. Throughputting CCE data to the ground via the Orbiter's PCM downlink is implemented via the PDI's data RAM. Before individual measurements within the minor frame can be transferred to the PDI's data RAM, valid recognition of two successive minor frame sync patterns and their corresponding minor frame count patterns must first occur. When this has happened, Data RAM storage for each CCE measurement shall proceed as follows:

- a. Within each minor frame word column of a master frame, those eight bit words containing data samples for a payload measurement, which are to be accessed by the PCM Master Unit (PCMMU) shall be stored within a unique PDI data RAM address. Each word stored in the PDI data RAM is accessed by the PCMMU at a uniform rate of 5 times per second and placed into a unique location in the PCMMU data RAM. Those words required for PCM downlink are formatted by the PCMMU into unique locations within the PCM downlink format.
- b. A multisyllable CCE measurement shall have its constituent eight bit bytes independently stored within a separate PDI data RAM byte address whenever its word position within the appropriate minor frame is processed.
- c. Maintaining the time homogeneity for both individual and multisyllable CCE measurements and CCE measurement word sets cannot be guaranteed.

8.4.1.1.3.1 CCE and Detached Centaur PCM Downlink Measurements. Measurements and their format locations for CISS, attached Centaur, detached Centaur and Centaur Payload, required for PCM downlink are identified in Appendix A.

8.4.1.1.3.1.1 CCE Ascent Downlink Data. Total combined CISS, Centaur and Centaur Payload downlink data shall be limited to 6.4 KBPS during the ascent phase.

8.4.1.1.3.1.2 CCE On Orbit Downlink Data. Total combined CISS, Centaur and Centaur Payload downlink PCM data shall be limited to 34.4 KBPS during on orbit prelaunch checkout.

8.4.1.1.3.1.3 Detached Centaur PCM Downlink Data. The Payload Signal Processor (PSP) receives Centaur telemetry data via the Payload Interrogator and routes the telemetry data to the PDI. Total data on this link is limited to 16 KBPS.

INTERFACE CONTROL DOCUMENT

ORBITER VEHICLE/CENTAUR

SIZE
A

ICD NO
ICD-2-1F001

REV
SHEET 47
OF

8.4.1.1.4 Orbiter GPC Software Service. Transferring individual CCE or detached Centaur measurements to the GPC Software Services is implemented via the PCMMU data RAM. Individual measurements are accessed by the PCMMU as specified in paragraph 8.4.1.1.3.

Measurements and their format locations for CISS, attached Centaur, Detached Centaur and Centaur Payload required for GPC software service are identified in Appendix A.

8.4.1.2 Detached Centaur/Payload Interrogator Interface. The characteristics for the telemetry link from the detached centaur to Shuttle Orbiter are defined in ICD 2-TBD.

8.4.1.3 CCE PCM Recording. The orbiter shall provide the capability to record biphase-level digital data from two sources. Additionally the orbiter operational recorders will record all data included in the PCM downlink data stream. Payload recorder data flow is shown in Figure 12.

8.4.1.3.1 CISS PCM Recording. The orbiter shall provide the capability to record biphase-level digital data from the CISS for a period of 64 minutes. The electrical interface characteristics at the orbiter /CISS interface shall be as shown in Table 7.

8.4.1.3.2 Centaur PCM Recording. The orbiter shall provide the capability to record biphase-level digital data from the centaur for a period of 13 hours, 52 minutes. The electrical interface characteristics at the orbiter/Centaur interface shall be as shown in Table 7.

8.4.1.3.3 Grounding and Shielding. Grounding and shielding for the CCE data recording shall be as shown in Figure 7.

8.4.1.3.4 Centaur Payload PCM Recording. No direct recording capability will be provided for the recording of Centaur Payload PCM data. However, those parameters in the PCM data downlink will be recorded on the operational recorder.

8.4.1.3.5 Recorder Playback. In flight playback of CCE digital data is via the orbiter KU-Band transmitter to ground. Playback of data to GSE is via the orbiter T-0 umbilical.

8.4.1.4 Multiplexer/Demultiplexer (MDM) Signal Acquisition Interface. The orbiter shall provide data channels for the acquisition of data parameters through MDM's which are under control of the on-board computers. MDM signal transfer capabilities at the orbiter/CCE interface are TBD.

Processing requirements to activate these interfaces are specified in Section 9.0 of this ICD.

8.4.1.4.1 MDM/CCE Electrical Interfaces. TBD.

INTERFACE CONTROL DOCUMENT

ORBITER VEHICLE/CENTAUR

SIZE

A

ICD NO

ICD-2-1F001

REV

SHEET 48

OF

8.4.2 Command Data Link.

8.4.2.1 Payload Signal Processor (PSP). The PSP receives command data from the GPC via the payload MDM. The PSP rate buffers the data and sends it to the Payload Interrogator (detached Centaur), payload umbilical (attached CCE) or GSE. A functional block diagram of the PSP command portion is shown in Figure 3. PSP command data flow is shown in Figure 11.

Configuration Message Control - The PSP receives a configuration message from the GPC (via the payload MDM) consisting of five 16-bit words and configures the PSP to the proper command and telemetry rates. The bit assignment of the PSP configuration message is shown in Figure 4.

Message Validation Logic - The message validation logic performs data validation on each word in the configuration and command messages from the MDM. When one of the words of the configuration message fails to conform to the data validation criteria, the word shall be considered invalid and shall be rejected. If any word is rejected by the validation logic, the entire configuration and command message shall be rejected. The PSP shall then reconfigure according to the instructions in a new configuration message within one millisecond after receipt of the message. If the configuration message is different from the previous configuration message while the command data is being transmitted, the validation logic shall reject both the configuration message and the command data message.

Status Message Assembler - Provide five 16-bit status messages to the GPC (via payload MDM up to once every 80 milliseconds) for verification of the PSP configuration. The bit assignment of the PSP status message is shown in Figure 5.

Initial Configuration and Status - The PSP shall assume a known initial configuration within 30 seconds after the application of prime power and shall remain in the initial configuration until the reception and execution of the first configuration message. The PSP shall also assume the initial configuration within 1 msec when power interruption from 24 vdc to 0 back to 24 vdc is experienced and/or when the "Re-Initialize bit of configuration message is at logic 1". The following is the initial configuration:

- | | | |
|----|----------------------------------|--|
| a. | Command Rate | 2 kbps |
| b. | Command Data Type | NRZ-L |
| c. | Command Data Subcarrier | 16 khz sine wave with
no modulation |
| d. | Idle Pattern | off |
| e. | Telemetry Rate | 16 kbps |
| f. | Telemetry Type | Bi-Phase-L |
| g. | Telemetry Frame Length | Sixty-four 8-bit words |
| h. | Telemetry Frame Sync Word Length | 32 bits |
| i. | Telemetry Frame Sync Word | All "one's" |

INTERFACE CONTROL DOCUMENT

ORBITER VEHICLE/CENTAUR

SIZE
A

ICD NO

ICD-2-1F001

REV

SHEET 49

OF

j. Subcarrier Output

Output to P/L
umbilical, P/I, or GSE
umbilical is inhibited

k. Subcarrier Input

Input from PLI or GSE
umbilical is inhibited.

Idle Pattern Generation - PSP can output an unmodulated or modulated 16 khz subcarrier to allow a payload to maintain command receiver lock. The idle pattern modulation consist of alternating "ones" and "zeros". The rate of the idle pattern is the same as the last "real" command data transmission, and always begins with a logic "one." The idle pattern begins in the first bit period following the last bit of the last "real" command data word transmission if the idle pattern enable bit in the previous PSP configuration word has been set. Likewise, the idle pattern will end with the last bit period prior to transmission of the first bit of the next "real" command message.

8.4.2.1.1 PSP/CCE Command Interface. The PSP shall provide command data on two redundant paths to the CCE while operating in the attached Centaur mode, and on an RF link via the Payload Interrogator while operating in the detached Centaur mode. Only one of the redundant paths shall be active at one time when operating in the attached mode. The CCE shall select the active path for receiving the command data. The PSP data output characteristics at the PSP/CCE interface shall be as shown in Table 8. The Centaur command format is shown in Figure 10.

8.4.2.1.2 Grounding and Shielding. Grounding and shielding for the PSP/CCE interfaces shall be as shown in Figure 7.

8.4.2.2 MDM/CCE Command Interface. TBD.

8.4.2.3 Detached Centaur Command Data Link. The characteristics for the command link from the orbiter to the detached Centaur are defined in ICD 2 - TBD.

INTERFACE CONTROL DOCUMENT

ORBITER VEHICLE/CENTAUR

SIZE
A

ICD NO

ICD-2-1F001

REV

SHEET 50

OF

TABLE 1

Payload Data Interleaver Input Data Format Characteristics-CISS

Parameter	Dimension	PDI Tolerance	Payload Characteristic	Notes
Bit rate	KPBS	64	64	
Code		Bi \emptyset -L	Bi \emptyset -L	
Word Length	Bits	8 or multiples of 8	TBD	
Minor Frame Length	Words	8 to 1024	TBD	
Minor Frame Rate	Frames/Sec	200 Max	TBD	
Master Frame Length	Minor Frames	1-256	TBD	
Minor Frame Sync		8, 16, 24 or 32 bits any pattern Contiguous locations at start of minor frame	TBD	
Master Frame Sync		8, 16, 24 or 32 bits any pattern Contiguous locations at start of minor frame	TBD	
Master Frame Sync		8 bit minor frame counter	TBD	
Format Sample Rates		One equal to minor frame rate. Five equal to interger submultiple of Minor Frame Rate.	TBD	

INTERFACE CONTROL DOCUMENT

ORBITER VEHICLE/CENTAUR

SIZE
A

ICD NO

ICD-2-1F001

REV

SHEET 51

OF

TABLE 2

Payload Data Interleaver Input Data Format Characteristics-CENTAUR

Parameter	Dimension	PDI Tolerance	Payload Characteristic	Notes
Bit rate	KPBS	64	64	
Code		Bi ϕ -L	Bi ϕ -L	
Word Length	Bits	8 or multiples of 8	TBD	
Minor Frame Length	Words	8 to 1024	TBD	
Minor Frame Rate	Frames/Sec	200 Max	TBD	
Master Frame Length	Minor Frames	1-256	TBD	
Minor Frame Sync		8, 16, 24 or 32 bits any pattern Contiguous locations at start of minor frame	TBD	
Master Frame Sync		8, 16, 24 or 32 bits any pattern Contiguous locations at start of minor frame	TBD	
Master Frame Sync		8 bit minor frame counter	TBD	
Format Sample Rates		One equal to minor frame rate. Five equal to interger submultiple of Minor Frame Rate.	TBD	

INTERFACE CONTROL DOCUMENT

ORBITER VEHICLE/CENTAUR

SIZE

A

ICD NO

ICD-2-1F001

REV

SHEET 52

OF

TABLE 3

Payload Data Interleaver Input Data Format Characteristics-
CENTAUR Payload

Parameter	Dimension	PDI Tolerance	Payload Characteristic	Notes
Bit rate	KPBS	9.6	9.6	
Code		NRZ-L	NRZ-L	
Word Length	Bits	8 or multiples of 8	TBD	
Minor Frame Length	Words	8 to 1024	TBD	
Minor Frame Rate	Frames/Sec	200 Max	TBD	
Master Frame Length	Minor Frames	1-256	TBD	
Minor Frame Sync		8, 16, 24 or 32 bits any pattern Contiguous locations at start of minor frame	TBD	
Master Frame Sync		8, 16, 24 or 32 bits any pattern Contiguous locations at start of minor frame	TBD	
Master Frame Sync		8 bit minor frame counter	TBD	
Format Sample Rates		One equal to minor frame rate. Five equal to interger submultiple of Minor Frame Rate.	TBD	

INTERFACE CONTROL DOCUMENT

ORBITER VEHICLE/CENTAUR

SIZE
A

ICD NO

ICD-2-1F001

REV

SHEET 53

OF

TABLE 4

Payload Data Interleaver Input Data Format Characteristics
Detached CENTAUR

Parameter	Dimension	PDI Tolerance	Payload Characteristic	Notes
Bit rate	KPBS	16	16	
Code		NRZ-L	NRZ-L	
Word Length	Bits	8 or multiples of 8	TBD	
Minor Frame Length	Words	8 to 1024	TBD	
Minor Frame Rate	Frames/Sec	200 Max	TBD	
Master Frame Length	Minor Frames	1-256	TBD	
Minor Frame Sync		8, 16, 24 or 32 bits any pattern Contiguous locations at start of minor frame	TBD	
Master Frame Sync		8, 16, 24 or 32 bits any pattern Contiguous locations at start of minor frame	TBD	
Master Frame Sync		8 bit minor frame counter	TBD	
Format Sample Rates		One equal to minor frame rate. Five equal to interger submultiple of Minor Frame Rate.	TBD	

INTERFACE CONTROL DOCUMENT

ORBITER VEHICLE/CENTAUR

SIZE
A

ICD NO

ICD-2-1F001

REV

SHEET 54

OF _____

TABLE 5

PDI DATA INPUT/CCE TO ORBITER ELECTRICAL INTERFACE CHARACTERISTICS
ALL PARAMETERS REFERENCED TO CISS INTERFACE

Parameter	Dimension	Characteristics Orbiter/CCE Interface	Notes
Signal Type		Differential-Balanced	Refer to Figures 5-1 and 5-2
Amplitude	Volts pk-pk	Min: 2.5 Max: 9.0	Measured line-to-line AT CISS interface
Duty Cycle	Percent	50 ± 1	(1) (2)
Bit-Rate Accuracy	Percent	± 3.25	(3)
Stability		< 1 part in 10 ⁵ over 60 sec period	
Waveform Distortion		Overshoot and under- shoot less than 20% of peak amplitude level	
Noise	Milivolts	100 pk-pk, differential line-to-line, DC to 100 KHz	CCE transmitting, not transmitting, or failed
Cable		2 conductor twisted, shielded, jacketed, controlled impedance	Rockwell design standard MP572-0328- 0102
Cable Impedance	Ohm	75 ± 5	Characteristic Impedance
Cable Capacitance	Picofarads	2900 max	Capacitance across differential line pair from CISS inter- face to PDI (18 to 23 pf/ft)
Load Impedance	Ohm	74 min 91 max	DC resistance line- to-line at interface includes cable resistance

INTERFACE CONTROL DOCUMENT

ORBITER VEHICLE/CENTAUR

SIZE
A

ICD NO

ICD-2-1F001

REV

SHEET 55

OF

TABLE 5

PDI DATA INPUT CCE TO ORBITER ELECTRICAL INTERFACE CHARACTERISTICS
ALL PARAMETERS REFERENCED TO CISS INTERFACE (Continued)

Parameter	Dimension	Characteristics Orbiter/CCE Interface	Notes
Cable Resistance	Ohm	4.4 per conductor max	Based on 126 foot cable length from CISS interface to PDI input
Cable Length	Feet	126 (max)	From CISS interface to PDI input
Rise/Fall Time		Max: Refer to Differential Phase Skew	(4) RT/FT are independent of bit rate and data code type (BiØ or NRZ)
Skew-Differential Phase	Nanosecond to Millisecond depending on PL bit rate		(5) (7)
For BiØ data:		Max: $0.159 T_p - 1 \times 10^{-6} - 2NT_p - (R/(R+1)) T_p - T_{lr} (\text{Loge}(V_{lpk}-100\text{mv}) / (V_{lpk}-300\text{mv})) - T_{tr} (\text{Loge}(V_{tpk}+300\text{mv}) / (V_{tpk}+100\text{mv}))$	
		Where: N = Payload Duty Cycle Offset $0 \leq N \leq 0.05$ R = PDI Programmed Bit Rate Offset with respect to Payload Bit Rate (Refer to Figures 5-4 and 5-5.	

INTERFACE CONTROL DOCUMENT

ORBITER VEHICLE/CENTAUR	SIZE A	ICD NO ICD-2-1F001	REV	SHEET 56 OF
-------------------------	-----------	-----------------------	-----	----------------

TABLE 5

PDI DATA INPUT CCE TO ORBITER ELECTRICAL INTERFACE CHARACTERISTICS
 ALL PARAMETERS REFERENCED TO CISS INTERFACE (Continued)

Parameter	Dimension	Characteristics Orbiter/CCE Interface	Notes
Skew-Differential Phase (Cont.) For NRZ data:		V _l pk = Peak amplitude level of Bi \emptyset waveform leading edge. V _t pk = Peak amplitude level of Bi \emptyset waveform trailing edge. T _p - Reciprocal of CCE bit rate (center frequency) T _l r = Max. rise time of Bi \emptyset waveform leading edge measured between 10% & 90% points. T _t r = Max. fall time of Bi \emptyset waveform trailing edge measured between 10% and 90% points Max: $0.309 T_p - NT_p -$ $T_{cr}(\text{LOGe}(V_{cpk}-100\text{mv})/(V_{cpk}-300\text{mv})) -$ $T_{dr}(\text{LOGe}(V_{dpk} + 300\text{mv})/(V_{dpk} + 100\text{mv}))$ Where: N = Clock Duty Cycle Offset $0 \leq N \leq 0.05$ V _{cpk} = Peak amplitude level of CCE Clock signal.	

INTERFACE CONTROL DOCUMENT

ORBITER VEHICLE/CENTAUR	SIZE A	ICD NO ICD-2-1F001	REV	SHEET <u>57</u> OF _____
-------------------------	------------------	-----------------------	-----	-----------------------------

TABLE 5

PDI DATA INPUT/CCE TO ORBITER ELECTRICAL INTERFACE CHARACTERISTICS
ALL PARAMETERS REFERENCED TO CISS INTERFACE (Continued)

Parameter	Dimension	Characteristics Orbiter/CCE Interface	Notes
		<p>V_{dpk} = Peak amplitude level of CCE NRZ Data signal.</p> <p>T_p - Reciprocal of CCE bit rate (center frequency)</p> <p>T_{cr} = Max. transition time (rise or fall time) of CCE Clock signal measured between 10% and 90% points.</p> <p>T_{dr} = Maximum transition time (rise or fall time) of CCE NRZ DATA signal measured between 10% and 90% points.</p>	
Common Mode	Volt	+3 pk-pk continuous or -60 pk-pk for 10 μ sec for damage level	(6) + 3 volts from EMI, negligible from CCE or PDI. (6)

- (1) Relative position of Bi \emptyset -L mid bit transition at interface
- (2) Any bit or clock transition point occurs in time at the 50% pk-pk amplitude point.
- (3) The PDI shall set an error flag within its BITE Status Register whenever the Payload bit rate exceeds \pm 3.25% of its specified center frequency.
- (4) The maximum limit for CCE signal Rise/Fall time is not to be determined independently, but instead is to be determined as part of a tradeoff with other related offsets. In order to make that tradeoff, the appropriate general case equation for Differential Phase Skew shall be utilized.
- (5) These two general case equations for Bi \emptyset data and NRZ data are an expression of how the CCE bit period is partitioned between the PDI's Bit Lock Range, CCE Duty Cycle Offset, PDI Programmed Bit Rate Offset (for Bi \emptyset data only), and CCE maximum Rise and

INTERFACE CONTROL DOCUMENT

ORBITER VEHICLE/CENTAUR	SIZE	ICD NO	REV	SHEET	58
	A	ICD-2-1F001		OF	

TABLE 5

PDI DATA INPUT/CCE TO ORBITER ELECTRICAL INTERFACE CHARACTERISTICS
 ALL PARAMETERS REFERENCED TO CISS INTERFACE (Continued)

Parameter	Dimension	Characteristics Orbiter/CCE Interface	Notes														
<p>Fall time. The solution for each of these two general case equations indicates that amount of the CCE bit period which remains (CCE bit period minus PDI Bit Lock Range minus appropriate Offsets) for partitioning between the CCE signal Differential Phase Skew and/or Phase Shift. A solution for either of these two general case equations which produces a negative result indicates that the appropriate offset themselves have utilized all the remaining CCE bit period such that none is available for Differential Phase Skew and/or Phase Shift. <u>PDI Bit Lock Range</u> identifies the absolute minimum amount of the CCE bit period required for the PDI's Bit Synchronizer to achieve and maintain bit lock.</p> <table border="1"> <thead> <tr> <th>Date Type</th> <th>Bit Lock Range</th> </tr> </thead> <tbody> <tr> <td>BiØ</td> <td>0.159 T_p -1 x 10⁻⁶</td> </tr> <tr> <td>NRZ</td> <td>0.309 T_p</td> </tr> </tbody> </table> <p><u>CCE Signal Differential Phase Skew</u>, as defined here, shall consist of the absolute value of the difference between the Leading Edge Phase Shift and the Trailing Edge Phase Shift (refer to Figure 5-3 and is independent of Payload amplitude level.</p> <p><u>CCE Signal Phase Shift</u> is the time differential between the 50% points of associated amplitude transitions of the two CCE differential inputs.</p> <p>(6) Volts over frequency spectrum from DC to 100 KHz.</p> <p>(7) This example illustrates how the BiØ Data general case equation for Differential Phase Skew shall be utilized by the CCE. The following interface characteristics are utilized as part of the <u>first tradeoff</u> for determining the upper limit for each of the <u>Offsets</u> applicable to the CCE.</p> <table border="1"> <tbody> <tr> <td>Bit Rate (Center Frequency):</td> <td>64 KBPS</td> </tr> <tr> <td>BiØ Data Duty Cycle:</td> <td>50 + 1%</td> </tr> <tr> <td>BiØ Data Peak Amplitude</td> <td>1.25 volts</td> </tr> <tr> <td>Maximum Transition Time: (Rise and Fall Time)</td> <td>1 µ sec</td> </tr> </tbody> </table>				Date Type	Bit Lock Range	BiØ	0.159 T _p -1 x 10 ⁻⁶	NRZ	0.309 T _p	Bit Rate (Center Frequency):	64 KBPS	BiØ Data Duty Cycle:	50 + 1%	BiØ Data Peak Amplitude	1.25 volts	Maximum Transition Time: (Rise and Fall Time)	1 µ sec
Date Type	Bit Lock Range																
BiØ	0.159 T _p -1 x 10 ⁻⁶																
NRZ	0.309 T _p																
Bit Rate (Center Frequency):	64 KBPS																
BiØ Data Duty Cycle:	50 + 1%																
BiØ Data Peak Amplitude	1.25 volts																
Maximum Transition Time: (Rise and Fall Time)	1 µ sec																

INTERFACE CONTROL DOCUMENT

ORBITER VEHICLE/CENTAUR	SIZE	ICD NO	REV	SHEET 59
	A	ICD-2-1F001		OF _____

TABLE 5

PDI DATA INPUT/CCE TO ORBITER ELECTRICAL INTERFACE CHARACTERISTICS
 ALL PARAMETERS REFERENCED TO CISS INTERFACE (Continued)

Parameter	Dimension	Characteristics Orbiter/CCE Interface	Notes
<p>For the specified center frequency of 64 KBPS, the corresponding amount of time for one bit period is: $T_p = 1/64 \text{ KBPS} = 15.6 \mu \text{ seconds}$.</p> <p>Within each CCE bit period (T_p), the general case equation for BiØ Data Differential Phase Skew provides for the following amounts of T_p time to be dedicated to:</p>			
<p>1) PDI's Bit Lock Range:</p> $0.159 T_p - 1 \times 10^{-6} = 0.159 (15.6 \mu \text{ sec}) - 1 \mu \text{ sec} = 1.48 \mu \text{ sec}$ <p>PDI's Bit Synchronizer to achieve and maintain bit lock.</p>			
<p>2) Payload BiØ Data Duty Cycle Offset:</p> $2 N T_p = 2 (0.01) (15.6) \mu \text{ sec} = 0.31 \mu \text{ sec with}$ <p>$N = 0.01$ corresponding to a 1% Duty Cycle Shift.</p>			
<p>3) PDI Programmed Bit Rate Offset: -</p> $(R/(R+1))T_p = (0.008/(0.008+1))(15.6 \mu \text{ sec}) = 0.123 \mu \text{ sec}$ <p>with $R = 0.8 \%$ as obtained from Figure 5-5 for a Payload bit rate of 64 KBPS.</p>			
<p>4) Ambiguity in Change of PDI Receiver Output Due to Slow Transition Time of CCE Data Differential Inputs:</p> $T_{lr}(\text{LOGe}(V_{lpk}-100\text{mv})/(V_{lpk}-300\text{mv})) + T_{tr}(\text{LOGe}(V_{tpk}+300\text{mv})/(V_{tpk}+100\text{mv})) =$ $1\mu \text{ sec}(\text{LOGe}(1.25-0.10)/(1.25-0.30)) + 1\mu \text{ sec}(\text{LOGe}(1.25+0.30)/(1.25+0.10)) = 1\mu \text{ sec}(\text{LOGe } 1.21) + 1\mu \text{ sec}(\text{LOGe } 1.15) = 0.3 \mu \text{ sec}$			
<p>The remaining amount of T_p time which is available to the CCE user for partitioning between CCE BiØ Data Differential Phase Skew and/or Phase Shift is:</p>			

INTERFACE CONTROL DOCUMENT

ORBITER VEHICLE/CENTAUR	SIZE	ICD NO	REV	SHEET 60
	A	ICD-2-1F001		OF

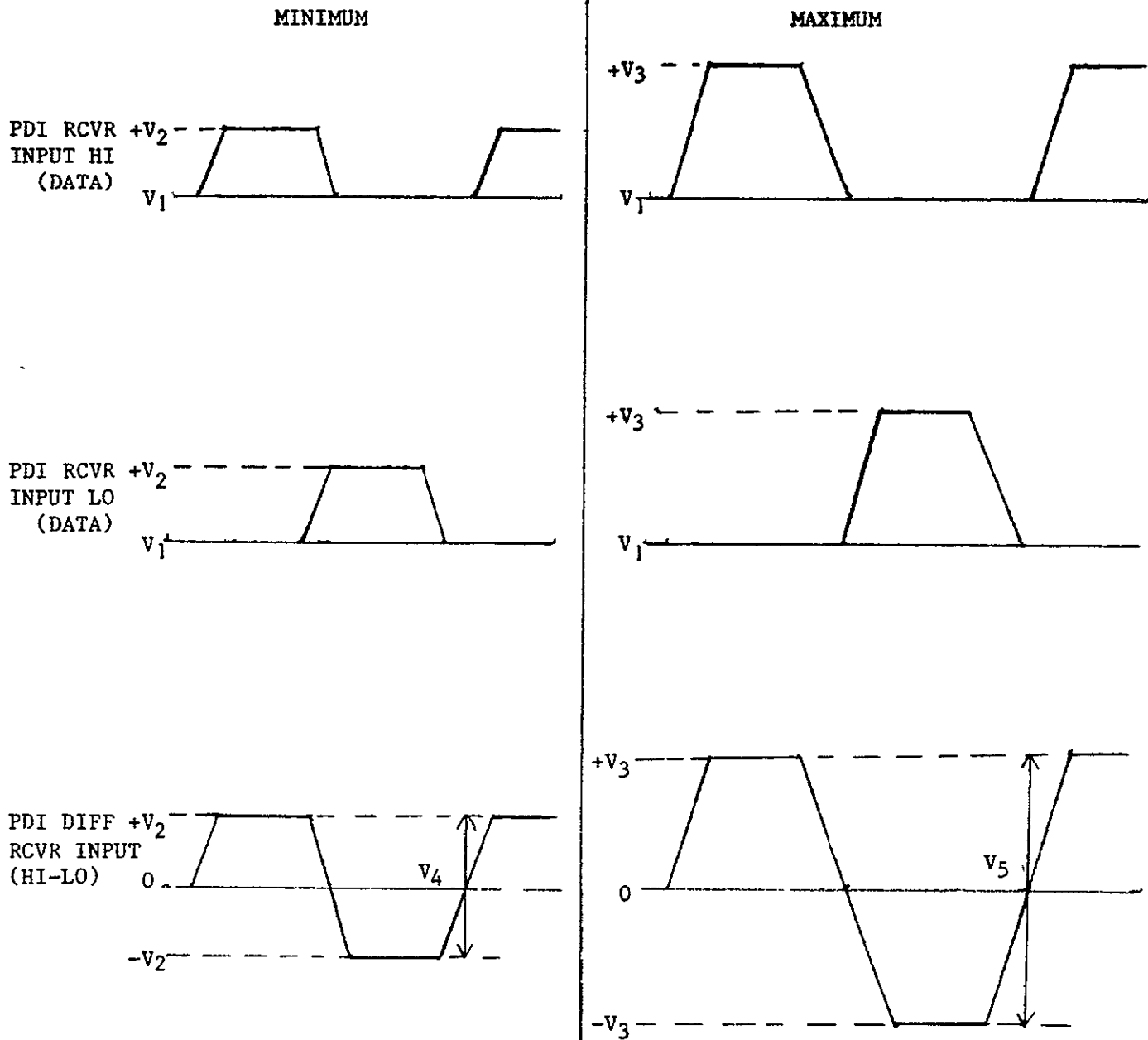
TABLE 5

PDI DATA INPUT/CCE TO ORBITER ELECTRICAL INTERFACE CHARACTERISTICS
ALL PARAMETERS REFERENCED TO CISS INTERFACE (Continued)

Parameter	Dimension	Characteristics Orbiter/CCE Interface	Notes
<p>Diff. Phase Skew/Phase Shift = $1.48 \mu \text{ sec} - 0.31 \mu \text{ sec} - 0.123 \mu \text{ sec}$ $- 0.3 \mu \text{ sec} = 0.747 \mu \text{ sec}$</p> <p>This completes the first tradeoff such that the general case equation for BiØ Data Differential Phase Skew has enabled the user to dedicate the following amounts of time as upper limits for:</p> <ul style="list-style-type: none"> $0 \leq \text{Duty Cycle Offset} \leq 0.31 \mu \text{ seconds}$ $0 \leq \text{Transition Time Ambiguity} \leq 0.30 \mu \text{ seconds}$ $0 \leq \text{Diff. Phase Skew/Phase Shift} \leq 0.747 \mu \text{ seconds}$ <p>If these upper limits are acceptable, then the CCE user shall determine the actual amounts of time to be allocated to each appropriate Offset. These "Actual Values" shall be specified within this ICD so as to characterize the Payload-to-PDI interface. If these upper limits are not acceptable, then the Payload user shall have to develop a <u>second tradeoff</u> with an appropriate change in either the Duty Cycle Shift, <u>Maximum Transition Time</u>, or <u>Peak Amplitude</u>. It should be noted that a Payload user can only change PDI Bit Lock Range and PDI Programmed Bit Lock Range and PDI Programmed Bit Rate Offset by choosing a different Payload Bit Rate.</p> <p>The general case equation for NRZ Data Differential Phase Skew is utilized in a manner identical to its BiØ Data counterpart with the exception that PDI Programmed Bit Rate Offset is not included.</p>			

INTERFACE CONTROL DOCUMENT

ORBITER VEHICLE/CENTAUR	SIZE A	ICD NO ICD-2-1F001	REV	SHEET <u>61</u> OF _____
-------------------------	------------------	-----------------------	-----	-----------------------------



- V_1 = SIGNAL GROUND
- V_2 = 1.25 VOLTS LINE TO SIG. GND.
- V_3 = 4.5 VOLTS LINE TO SIG. GND.
- V_4 = 2.5 VOLTS P -P LINE TO LINE DIFFERENTIAL BALANCED
- V_5 = 9.0 VOLTS P -P LINE TO LINE DIFFERENTIAL BALANCED

FIGURE 5-1 Data/Data - Diferential Transmission

INTERFACE CONTROL DOCUMENT

ORBITER VEHICLE/CENTAUR

SIZE
A

ICD NO

ICD-2-1F001

REV

SHEET 62

OF

ORIGINAL PAGE IS
OF POOR QUALITY

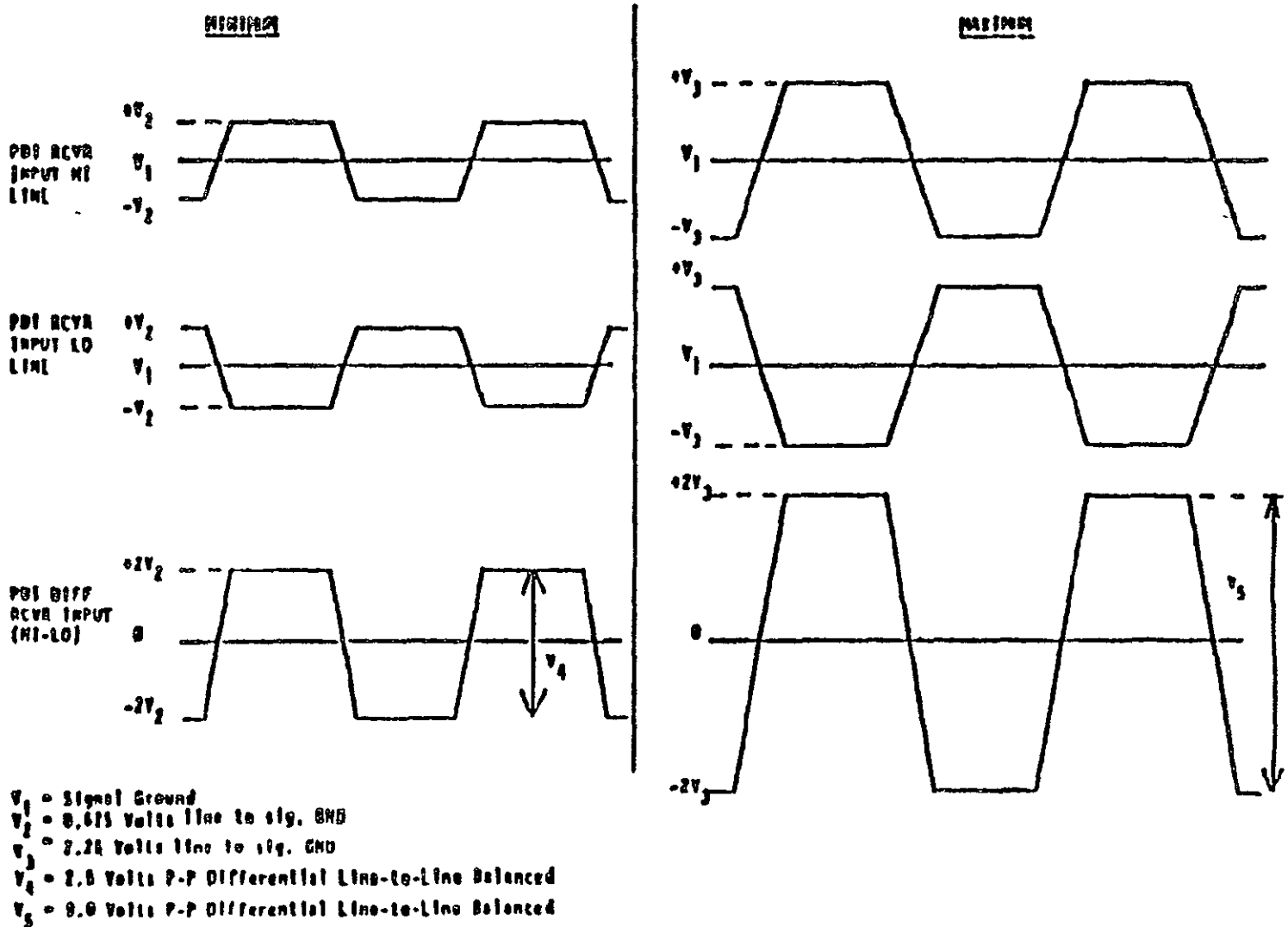


FIGURE 5-2 Bi-Polar Lines - Differential Transmission

INTERFACE CONTROL DOCUMENT

ORBITER VEHICLE/CENTAUR

SIZE
A

ICD NO

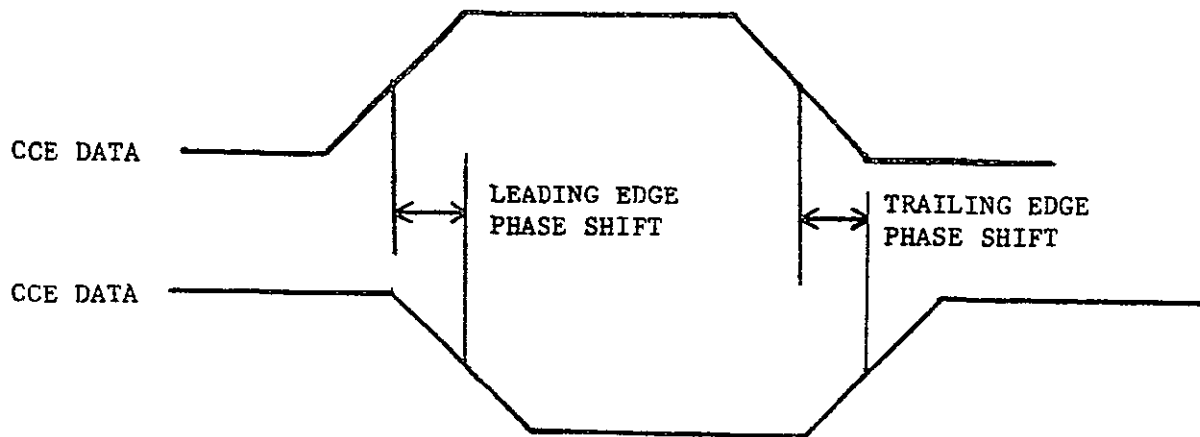
ICD-2-1F001

REV

SHEET 63

OF

ORIGINAL PAGE IS
OF POOR QUALITY



$$\text{Differential Phase Skew} = \left| \text{Leading Edge Phase Shift} - \text{Trailing Edge Phase Shift} \right|$$

Where:

Leading/Trailing Edge Phase Shift is the time differential between the 50% points of associated amplitude transitions of the two differential inputs.

FIGURE 5-3 Differential Phase Skew

INTERFACE CONTROL DOCUMENT

ORBITER VEHICLE/CENTAUR

SIZE
A

ICD NO

ICD-2-1FU01

REV

SHEET 64
OF

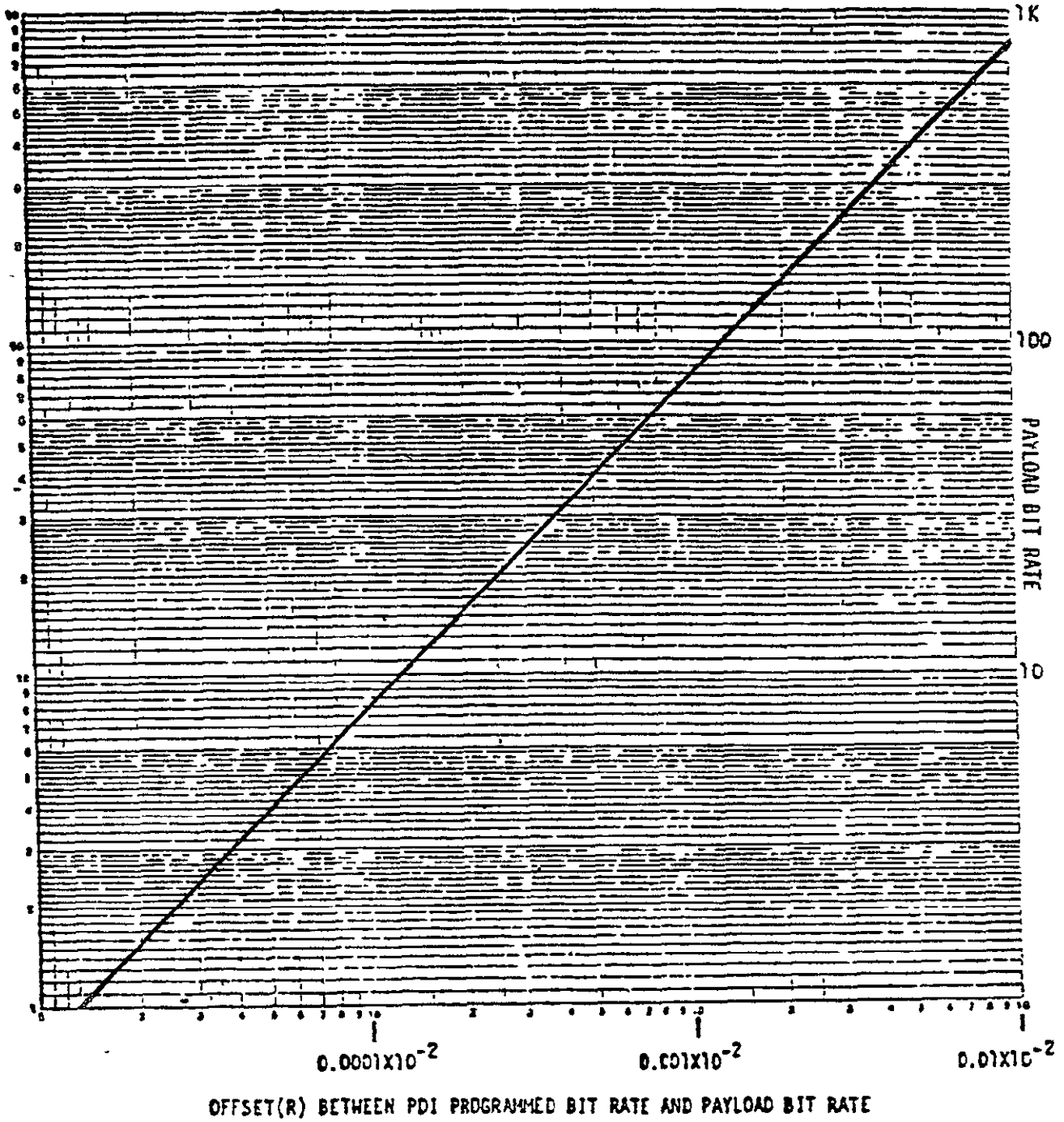


Figure 5-4 10 BPS Payload Bit Rate 500 BPS

INTERFACE CONTROL DOCUMENT

ORBITER VEHICLE/CENTAUR

SIZE
A

ICD NO

ICD-2-1F001

REV

SHEET 65

OF

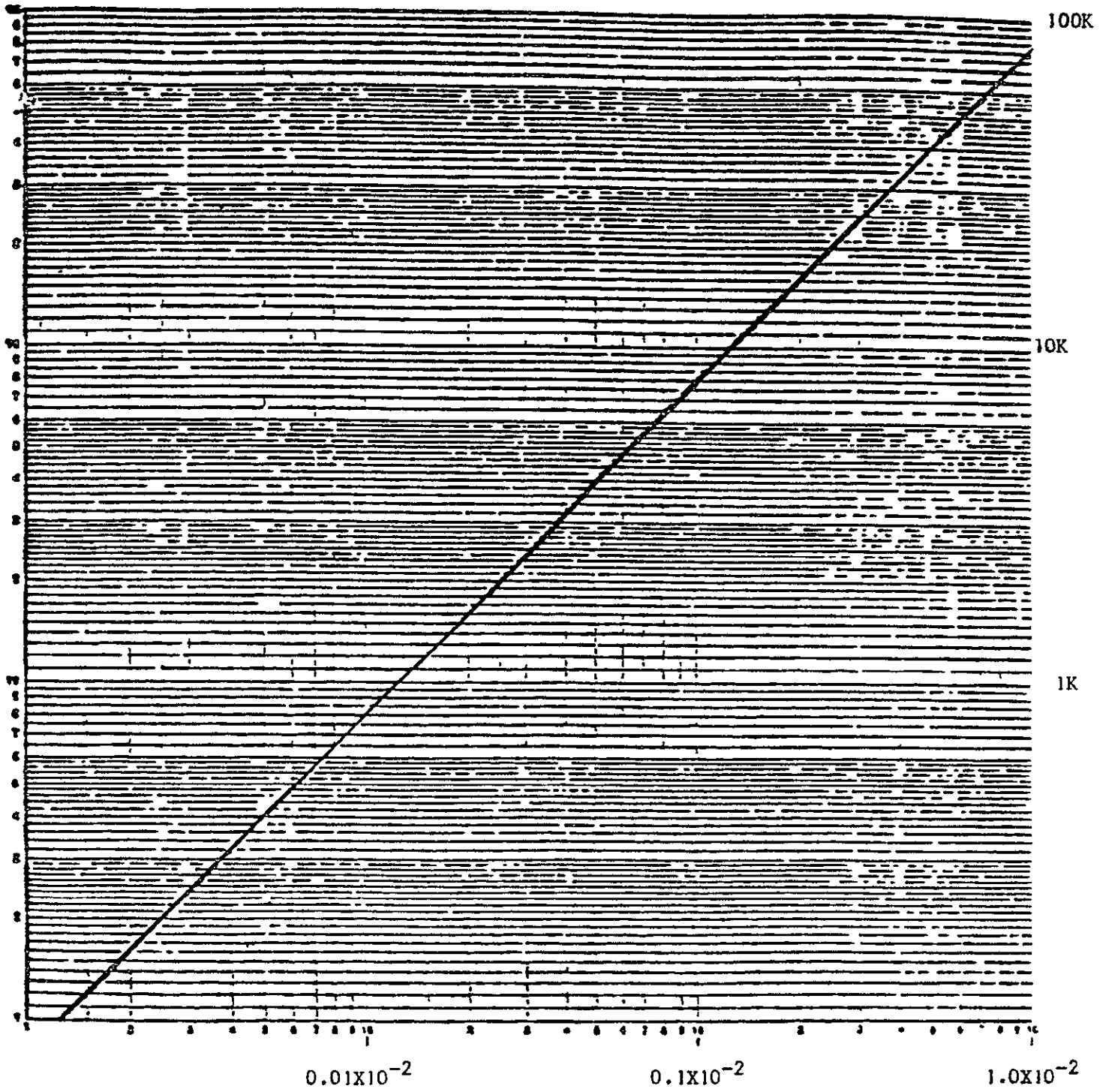


Figure 5-5 500 BPS Payload Bit Rate 64 KBPS

INTERFACE CONTROL DOCUMENT

ORBITER VEHICLE/CENTAUR

SIZE
A

ICD NO

ICD-2-1F001

REV

SHEET 6b

OF

TABLE 6

PDI CLOCK INPUT/CCE TO ORBITER ELECTRICAL INTERFACE CHARACTERISTICS
ALL PARAMETERS REFERENCED TO CISS INTERFACE

Parameter	Dimension	Characteristics Orbiter/CCE Interface	Notes
Signal Type		Differential-Balanced	Refer to Figures 5-1 and 5-2
Amplitude	Volts pk-pk	Min: 2.5 Max: 9.0	Measured line-to-line
Duty Cycle	Percent	50 ± 5	NRZ bit rate clock
Skew - Data to Clock (NRZ)		Max: + 10% of clock period	Bit rate clock to NRZ bit start (1). See Figure 2.10.2.3.2-1
Stability		< 1 part in 10 ⁵ over 60 sec period	
Clock Accuracy	Percent	+ 3.25	(2)
Waveform Distortion		Overshoot and under- shoot less than 20% of peak amplitude level	
Noise	Milivolts	100 pk-pk, differential line-to-line, DC to 100 KHz	CCE transmitting, not transmitting, or failed
Cable		2 conductor twisted, shielded, jacketed, controlled impedance	Rockwell design standard MP572-0328- 0002
Cable Impedance	Ohm	75 ± 5	Characteristic Impedance
Cable Capacitance	Picofarads	2900 max	Capacitance across differential line pair from CISS inter- face to PDI (18 to 23 pf/ft)
Load Impedance	Ohm	74 min 91 max	DC resistance line- to-line at interface includes cable resistance

INTERFACE CONTROL DOCUMENT

ORBITER VEHICLE/CENTAUR

SIZE
A

ICD NO

ICD-2-1F001

REV

SHEET 67

OF

TABLE 6

PDI CLOCK INPUT/CCE TO ORBITER ELECTRICAL INTERFACE CHARACTERISTICS
 ALL PARAMETERS REFERENCED TO CISS INTERFACE (Continued)

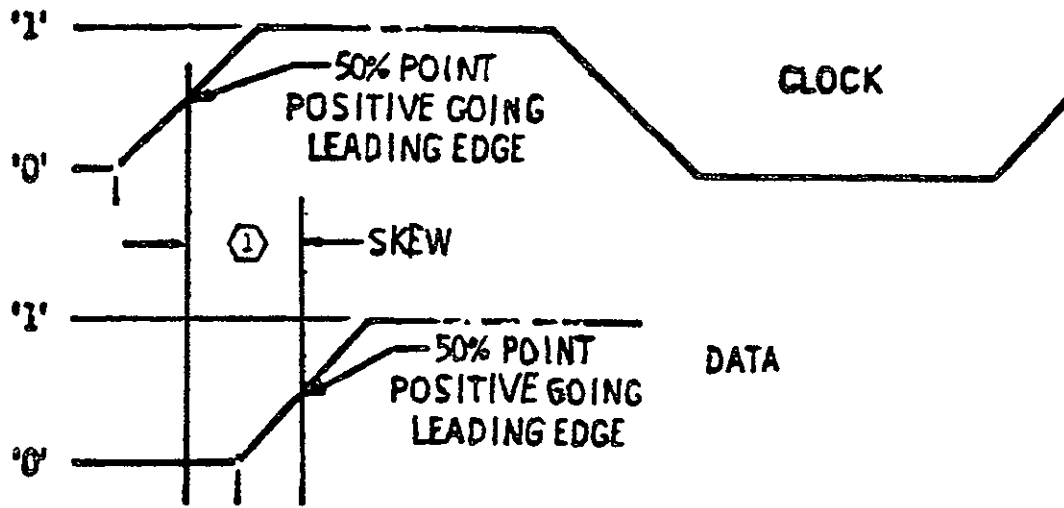
Parameter	Dimension	Characteristics Orbiter/CCE Interface	Notes
Cable Resistance	Ohm	4.4 per conductor (max)	Based on 126 ft. cable length
Cable Length	Feet	126 max	From CISS interface to PDI input
Rise/Fall Time		Max: Refer to Differential Phase Skew	RT/FT are independent of bit rate and data code type (Bi \emptyset or NRZ)
Skew-Differential Phase	Nanosecond to Millisecond depending on bit rate	Maximum value shall be the same as that specified for associated NRZ data	
Common Mode	Volt	Min: +3 pk-pk continuous or +60 pk-pk for 10 μ sec for damage level	+ 3V from EMI, negligible from payload or PDI (3)

- (1) Any bit or clock transition point occurs in time at the 50% pk-pk amplitude point.
- (2) The PDI shall set an error flag within its BITE Status Register whenever the Payload bit rate exceeds \pm 3.25% of its specified center frequency.
- (3) Volts across frequency spectrum from DC to 100 KHz.

INTERFACE CONTROL DOCUMENT

ORBITER VEHICLE/CENTAUR	SIZE	ICD NO	REV	SHEET
	A			ICD-2-1F001
			OF	

ORIGINAL PAGE IS
OF POOR QUALITY



① The rising edge of each clock signal shall be coincident with the starting edge of the corresponding data bit period within plus or minus 10 percent of the clock period maximum.

Figure 6-1 Skew

INTERFACE CONTROL DOCUMENT

ORBITER VEHICLE/CENTAUR

SIZE
A

ICD NO
ICD-2-1F001

REV

SHEET 69
OF

TABLE 7

DIGITAL DATA RECORDING ELECTRICAL INTERFACE CHARACTERISTICS
ALL PARAMETERS REFERENCED TO CISS INTERFACE

Parameter	Dimension	Characteristics Orbiter/CCE Interface	Notes
Bit Rate	kbps	64	
Signal Type		Differential	
Data Type		Bi ϕ -L	
Rise & Fall Time	Percent Bit Cell Time (BCT)	10 Max	
Signal Amplitude	V, P-P	3.7 Min 9 Max	(3)
Jitter & Assymetry	Percent of BCI	± 2	
Input Impedance (Recorder)	Ohms, L-L	75 \pm 10%	
Source Impedance (Payload)	Ohms, L-L	TTI Compatible (4)	
Common-mode Rejection	volts	± 15	(1)
Cable Type		Twisted Shielded Pair	(2)
Cable Impedance (Orbiter)	Ohms	75 \pm 5	
Cable Capacitance (Orbiter)	Picofarads	2900 Max (3)	18 to 23 pf per foot
Cable Resistance (Orbiter)	ohms	4.4 per conductor(max) (3)	

INTERFACE CONTROL DOCUMENT

ORBITER VEHICLE/CENTAUR

SIZE
A

ICD NO

ICD-2-1F001

REV

SHEET 70
OF

- (1) Referenced to Signal Ground
- (2) FMI class 'RF'. Refer to Table 10.7.1-1
- (3) Eased on 126-ft cable length from CISS interface to payload recorder input
- (4) such as TI SN55114, or equivalent

INTERFACE CONTROL DOCUMENT

ORBITER VEHICLE/CENTAUR

SIZE

A

ICD NO

ICD-2-1F001

REV

SHEET 71

OF

TABLE 8

ORIGINAL PAGE IS
OF POOR QUALITYPSP COMMAND DATA OUTPUT, ELECTRICAL INTERFACE CHARACTERISTICS
ALL PARAMETERS REFERENCED AT CISS INTERFACE

Parameter	Dimension	Value	Notes
Subcarrier Frequency	KHz	$16 \pm 0.001\%$ (long term) (1)	Sine wave
Subcarrier Harmonic Distortion	Percent	Less than 2% of the power in the subcarrier	Total harmonic distortion
Subcarrier Frequency Stability		$< 10^{-7}$ of the sub-carrier frequency over a 10 second period (short term) (1)	
Subcarrier Modulation		PSK	
Data Rate	bps	$1000 \pm 0.001\%$ (long term) (1)	
Data Rate Stability		10^{-7} over a 10 second period (short term) (1)	
Data Types		NRZ-L	
Frequency-to-Bit Rate Ratio		Multiple of data rate	Data waveform shall conform to S/C zero crossings within \pm degrees
Data Transition		Data shall alter S/C phase by $\pm 90^\circ \pm 10\%$	
Amplitude	volts p-p	3.0 to 4.4, line-to-line	Voltage at CISS interface includes orbiter cable losses
Phase Jitter	Percent of bit period	3 max	
Data Asymetry	Percent of bit period	2 max over a 300 bit period	See Fig 9
Channel-to-Channel Isolation	dB	40 min	Between-channel isolation when each channel is terminated with 75 ohms

INTERFACE CONTROL DOCUMENT

ORBITER VEHICLE/CENTAUR

SIZE
A

ICD NO

ICD-2-1F001

REV

SHEET 72
OF

TABLE 8

PSP COMMAND DATA OUTPUT, ELECTRICAL INTERFACE CHARACTERISTICS
 ALL PARAMETERS REFERENCED TO CISS INTERFACE (Continued)

Parameter	Dimension	Value	Notes
Source Impedance	Ohms	< 15	
Load Impedance	ohms	75 ± 10%	
Output Type		Differential	
Load Termination		Differential, Direct Coupled	
Offset	volts	0.0 ± 0.5 either line-to-ground	
Cable Type		Twisted Shielded Pair	EMI class 'RF' refer to Table TBD
Cable Impedance (Orbiter)	Ohms	75 ± 5	
Cable Capacitance (Orbiter)	Picofarads	2900 max (2)	18 to 23 pf per foot
Cable Resistance (Orbiter)	Ohms	4.4 maximum per conductor (2)	
Cable Length (Orbiter)	Feet	126 (max)	From PSP to CISS interface

- (1) Based on MTU accuracy and stability
- (2) Based on 126 foot cable length from PSP output to CISS interface

INTERFACE CONTROL DOCUMENT

ORBITER VEHICLE/CENTAUR	SIZE	ICD NO	REV	SHEET
	A			ICD-2-1F001
			OF	

ORIGINAL PAGE IS
OF POOR QUALITY

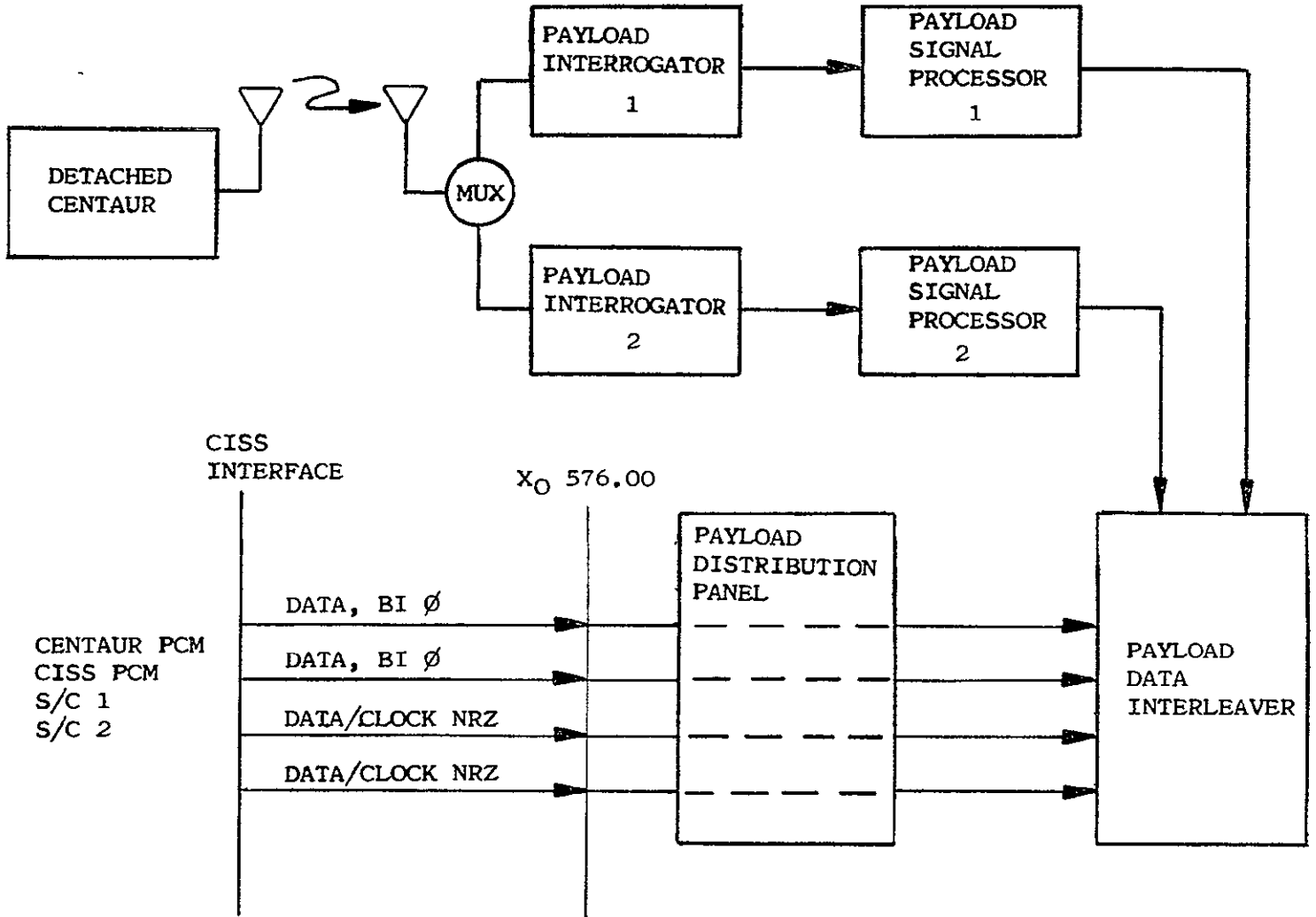


FIGURE 1 PAYLOAD DATA INTERLEAVER DATA FLOW

INTERFACE CONTROL DOCUMENT

ORBITER VEHICLE/CENTAUR

SIZE
A

ICD NO

ICD-2-1F001

REV

SHEET 74
OF

	N WORDS PER FRAME	
	SYNC	COUNTER
M FRAMES PER DATA CYCLE	"	"
	"	"
	"	"
	"	"
	"	"
	"	"
	"	"
	"	"
	"	"
	"	"
	"	"
	"	"

- . CENTAUR USES A SHUTTLE STANDARD TYPE 3 FORMAT
- . WORD LENGTH IS 8 BITS.
- . DCU DIGITAL DATA OCCUPIES 3 WORDS (24 BITS).
- . SYNC PATTERN IS 01147537 OCTAL - PROGRAMMED BY SOFTWARE.
- . FRAME COUNTER COUNTS FROM 1 TO M (COUNTER IS 8 BITS).
- . M, N ARE TBD, BUT BOTH WILL BE EVEN.
- . DATA CYCLE WILL BE APPROXIMATELY 1 SECOND LONG.

Figure 2 Type 3 Shuttle Standard Format

INTERFACE CONTROL DOCUMENT

ORBITER VEHICLE/CENTAUR	SIZE	ICD NO	REV	SHEET
	A	ICD-2-1F001		75
				OF

INTERFACE CONTROL DOCUMENT

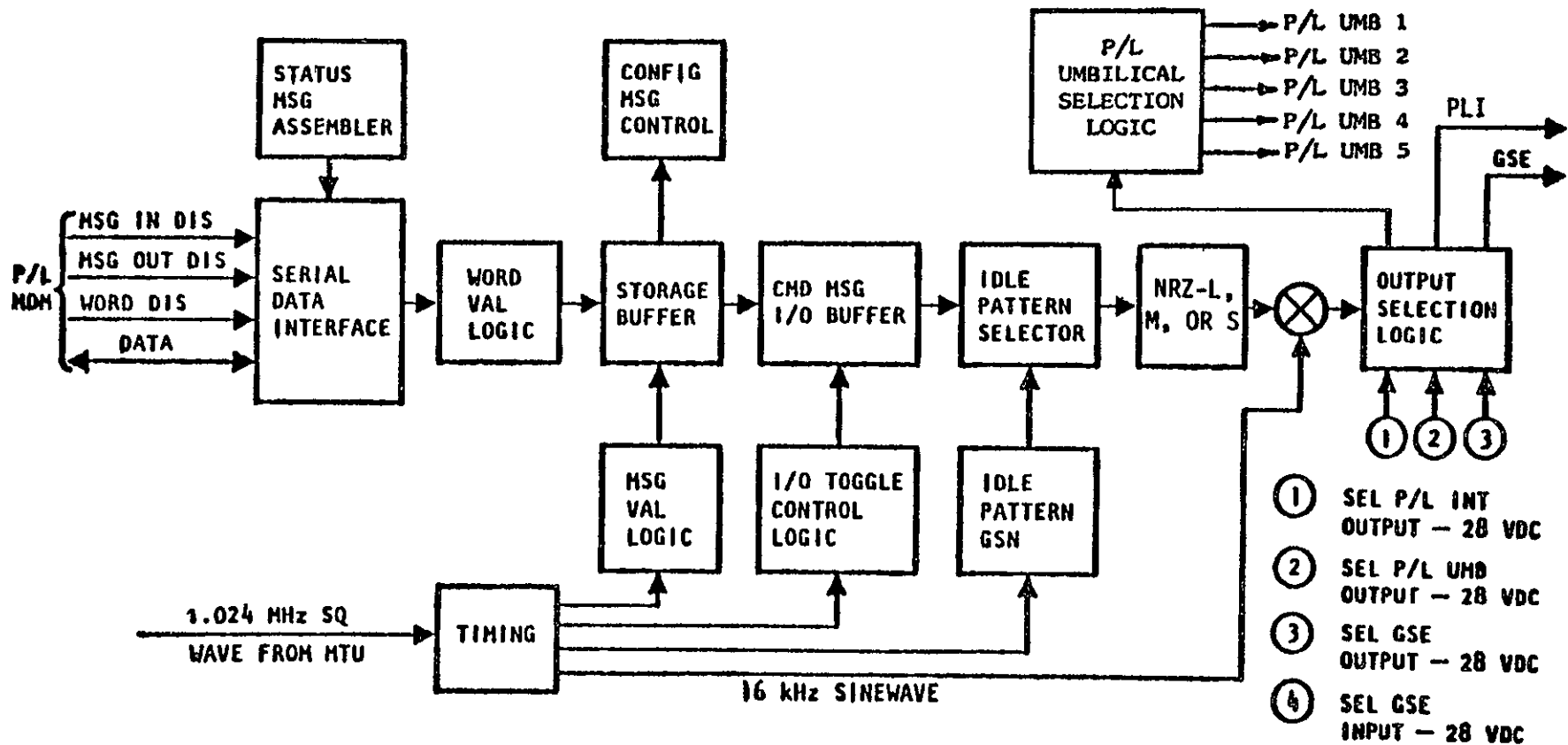


Figure 3 Functional Block Diagram (Command Portion)

ORIGINAL PAGE IS
OF POOR QUALITY

ORIGINAL PAGE IS
OF POOR QUALITY

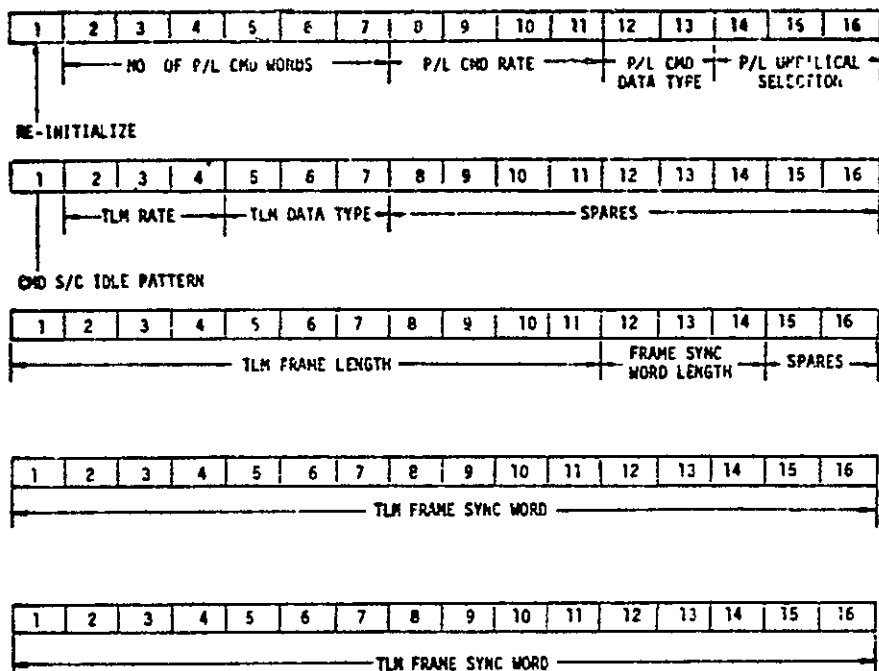


Figure 4 PSP Configuration Message

INTERFACE CONTROL DOCUMENT

ORBITER VEHICLE/CENTAUR

SIZE
A

ICD NO

ICD-2-1F001

REV

SHEET 77

OF

ORIGINAL PAGE IS
OF POOR QUALITY

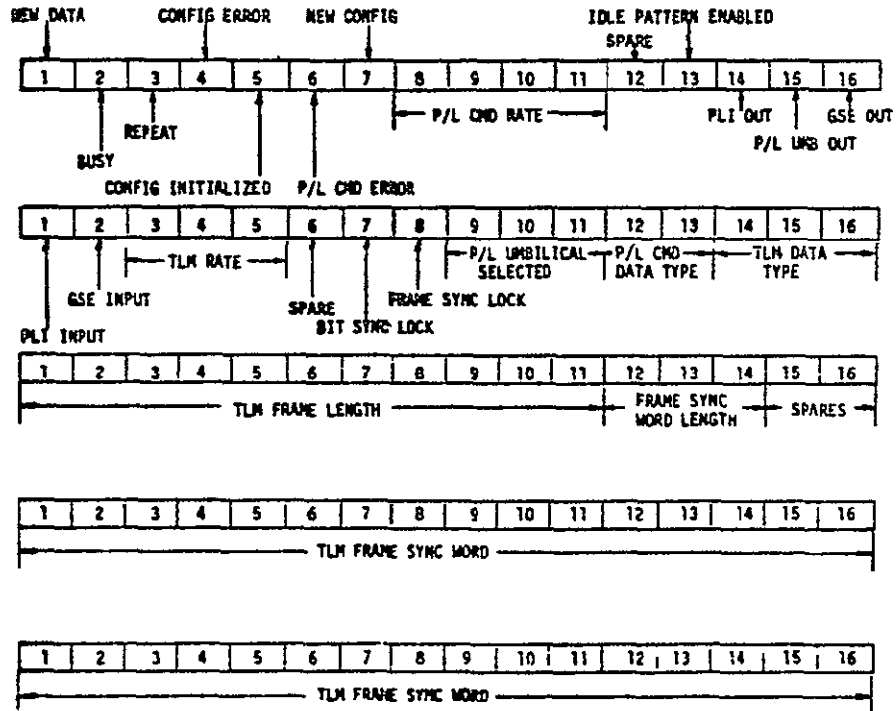


Figure 5 PSP Status Message

INTERFACE CONTROL DOCUMENT

ORBITER VEHICLE/CENTAUR

SIZE
A

ICD NO

ICD-2-1F001

REV

SHEET **78**

OF

GROUNDING AND SHIELDING TERMINATION

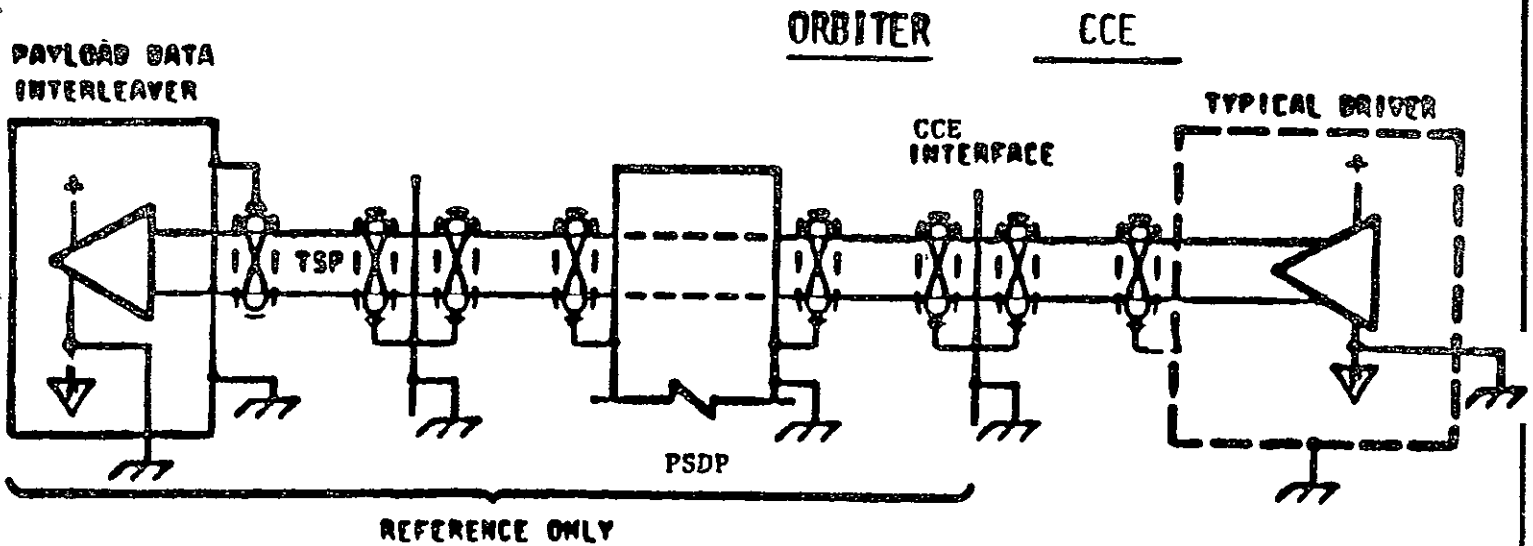


Figure 6 Payload Data Interleaver Grounding and Shielding
Interface Data & Clock

INTERFACE CONTROL DOCUMENT

ORBITER VEHICLE/CENTAUR

SIZE
A

ICD NO

ICD-2-1F001

REV

SHEET 79
OF

ORIGINAL PAGE IS
OF POOR QUALITY

GROUNDING AND SHIELDING TERMINATIONS

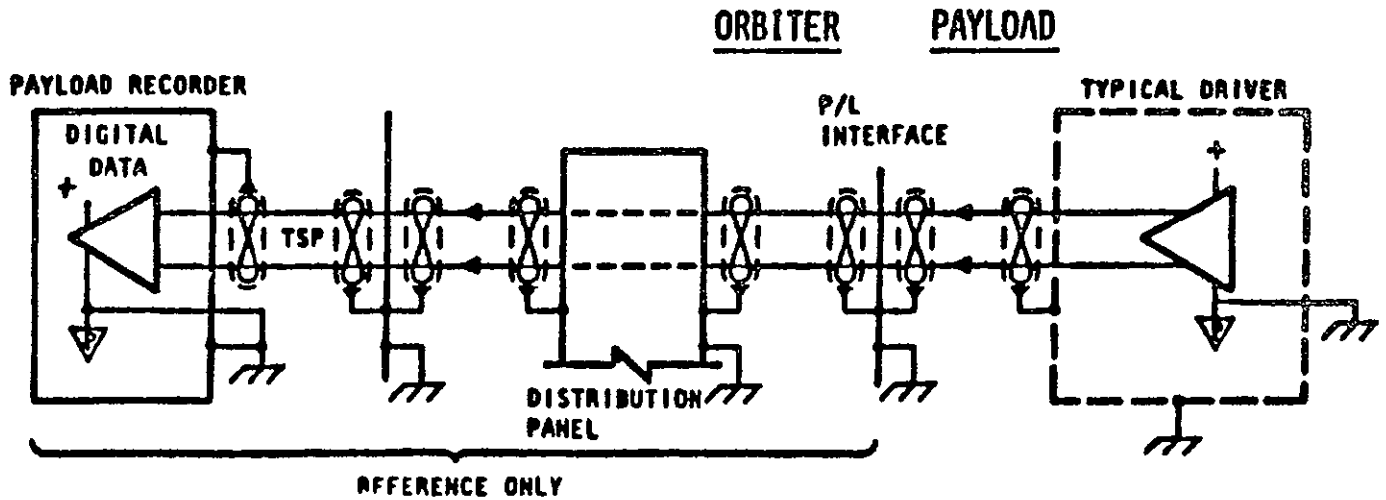


Figure 7 Data Recorder Grounding and Shielding

INTERFACE CONTROL DOCUMENT

ORBITER VEHICLE/CENTAUR

SIZE
A

ICD NO

ICD-2-1F001

REV

SHEET 80

OF

ORIGINAL PAGE IS
OF POOR QUALITY

GROUNDING AND SHIELDING TERMINATION

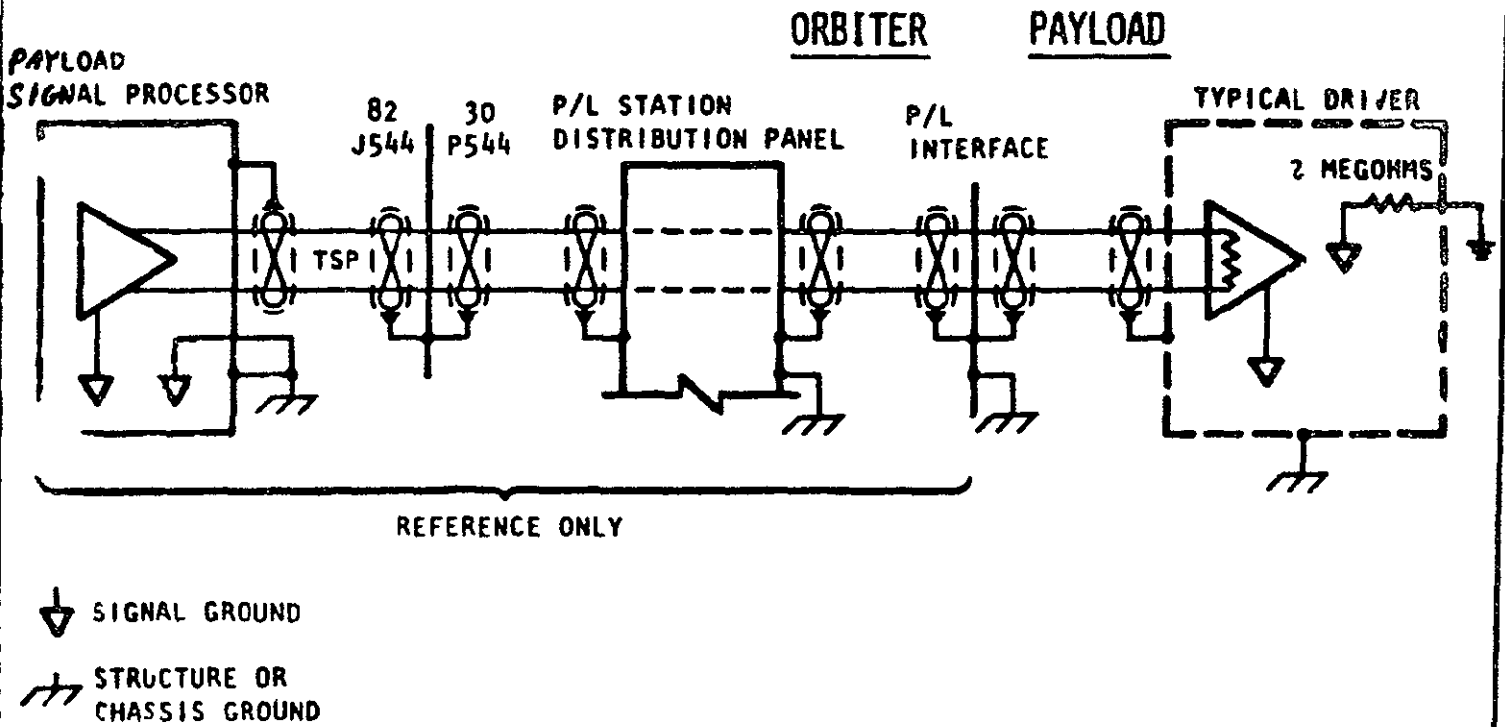


Figure 8 Payload Signal Processor Grounding and Shielding

INTERFACE CONTROL DOCUMENT

ORBITER VEHICLE/CENTAUR

SIZE
A

ICD NO

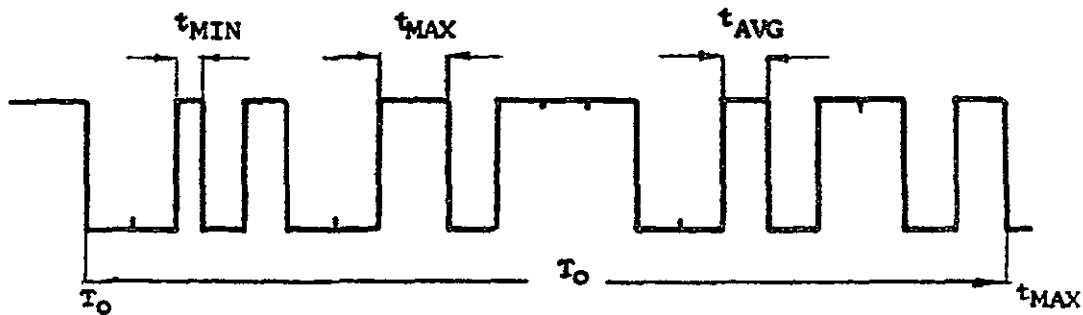
ICD-2-1F001

REV

SHEET 81

OF

ORIGINAL PAGE IS
OF POOR QUALITY



NOTES:

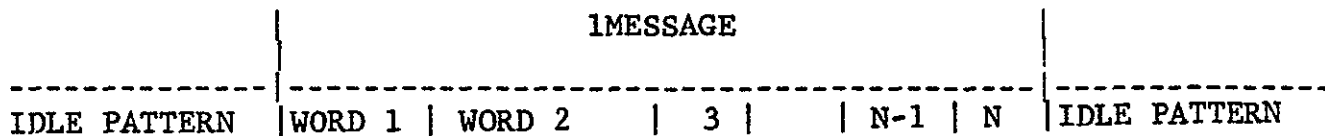
1. t_{MAX} - MAXIMUM SYMBOL PERIOD
2. t_{MIN} - MINIMUM SYMBOL PERIOD
3. t_{AVG} - IS THE AVERAGE SYMBOL PERIOD
4. T_0 - IS THE OBSERVATION TIME
5. ASYMMETRY DOES NOT ACCUMULATE (i.e., $t_{AVG} = \frac{1}{R}$ WHERE R IS THE DATA RATE)

$$\text{ASYMMETRY \%} = \frac{t_{MAX} - t_{MIN}}{t_{MAX} + t_{MIN}} \times 100\%$$

Figure 9 Digital Data Asymmetry

INTERFACE CONTROL DOCUMENT

ORBITER VEHICLE/CENTAUR	SIZE	ICD NO	REV	SHEET 82
	A	ICD-2-1F001		OF



- IDLE PATTERN IS 101010 .. - MINIMUM OF 132 BITS PRECEEDING EACH MESSAGE
- ALL WORDS ARE 16 BITS. THERE ARE NO START OR STOP BITS BETWEEN WORDS.
- WORD 1 IS A FIXED SYNCHRONIZATION PATTERN, REGARDLESS OF THE MESSAGE TYPE. THE SPECIFIC PATTERN IS TBD.
- WORD 2 DEFINES THE MESSAGE TYPE (I.E., COMMAND OR NAVIGATION UPDATE) AND MESSAGE LENGTH (NUMBER OF WORDS).
- WORD N IS A CHECKSUM OF THE PREVIOUS WORDS FOR ERROR DETECTION PURPOSES. THERE IS NO ERROR CORRECTION CAPABILITY.
- THE TOTAL MESSAGE LENGTH IS VARIABLE.
- A CONTINUOUS IDLE PATTERN IS DESIRED BETWEEN MESSAGES TO MAINTAIN SYNCHRONIZATION OF THE COMMAND DETECTOR UNIT IN THE CENTAUR TRANSPONDER.

Figure 10 Preliminary Centaur Command Format

INTERFACE CONTROL DOCUMENT

ORBITER VEHICLE/CENTAUR	SIZE	ICD NO	REV	SHEET 83
	A	ICD-2-1F001		OF

ORIGINAL PAGE IS
OF POOR QUALITY

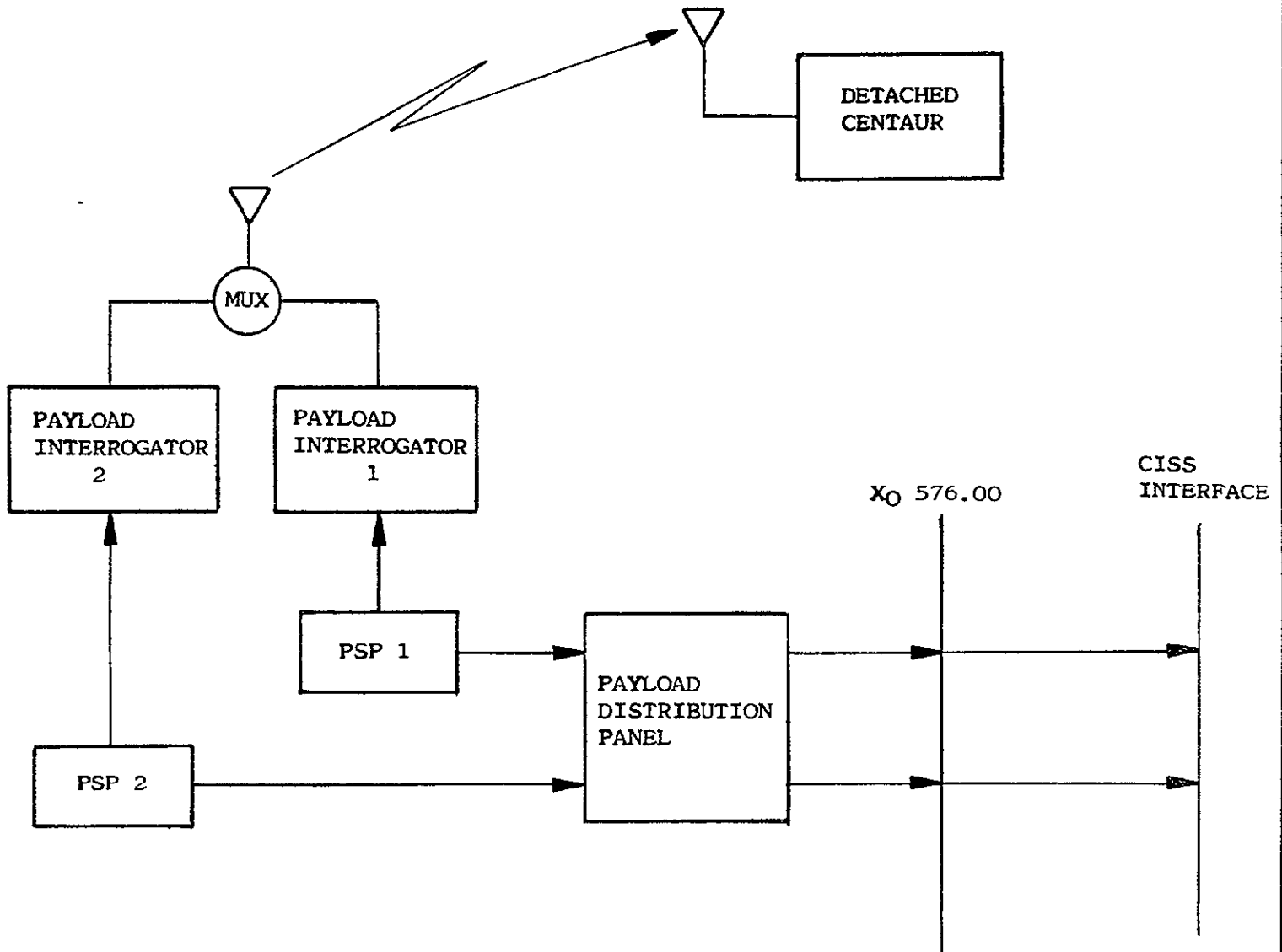


FIGURE 11 PAYLOAD SIGNAL PROCESSOR COMMAND DATA FLOW

INTERFACE CONTROL DOCUMENT

ORBITER VEHICLE/CENTAUR

SIZE
A

ICD NO

ICD-2-1F001

REV

SHEET 84
OF

ORIGINAL PAGE IS
OF POOR QUALITY

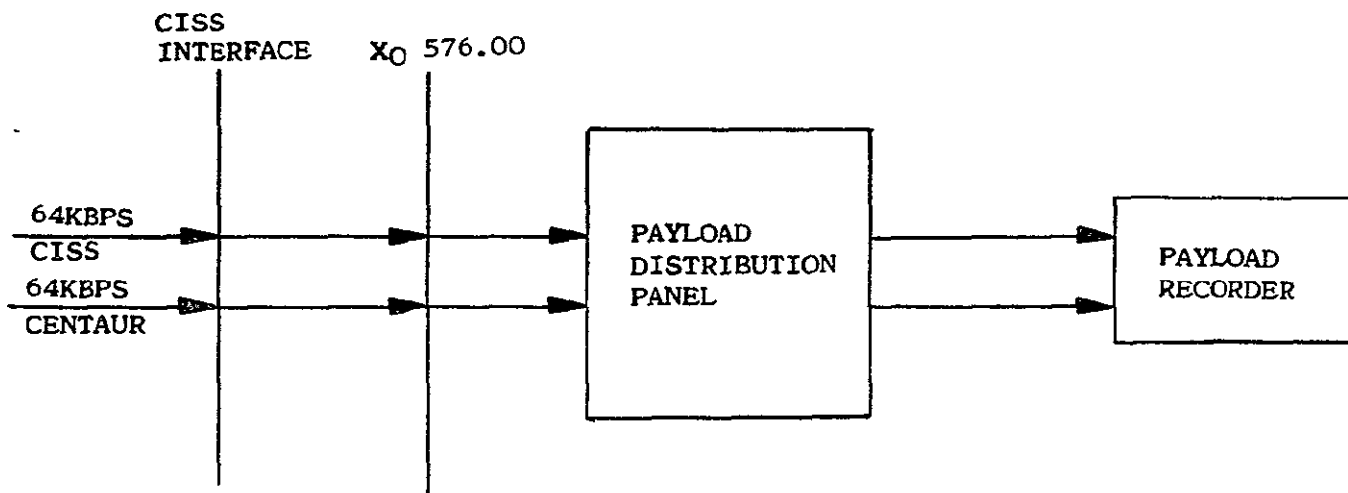


FIGURE 12 PAYLOAD RECORDER DATA FLOW

Figure 12 Payload Recorder Data Flow

INTERFACE CONTROL DOCUMENT

ORBITER VEHICLE/CENTAUR

SIZE
A

ICD NO

ICD-2-1F001

REV

SHEET 85

OF

9.0 SOFTWARE REQUIREMENTS

9.1 Software Overview. TBD.

9.2 Orbiter General Purpose Computer Standard Software Service. TBD.

9.3 Mission Phase Applicability. TBD.

9.4 Software Constraints. TBD.

INTERFACE CONTROL DOCUMENT

ORBITER VEHICLE/CENTAUR	SIZE A	ICD NO ICD-2-1F001	REV	SHEET 86 OF
-------------------------	-----------	-----------------------	-----	----------------

12.0 SHUTTLE GLOBAL-POSITIONING SYSTEM INVESTIGATIONS

The analyses and investigations of the Global-Positioning System (GPS) centered on the Texas Instruments (TI) digital multiplex receiver since it was a potential candidate receiver for the Shuttle GPS navigation system. Furthermore, this TI receiver utilizes a unique design approach which has not heretofore been seen or reviewed by NASA or Axiomatix.

In Axiomatix Report No. R8111-2, "Shuttle Global Positioning System (GPS) Design Study," dated November 5, 1981, the multiplex code-tracking performance, multiplex carrier-tracking performance and multiplex code-acquisition performance are analyzed. The carrier-loop time-sharing loss analysis shows that the loop threshold increases by $-10 \log (d_F)$, where d_F is the duty factor due to time-sharing among multiple satellites. However, the receiver also multiplexes between L_1 and L_2 frequencies, so there is also some time-sharing loss due to L_1/L_2 sharing. It is shown in the report that the TI implementation avoids most of this loss and that the actual loss due to L_1/L_2 sharing is between 0.4 and 1.0 dB. The report also explains how the TI tracking discriminator functions for L_1 and L_2 code tracking. The time-sharing loss due to code-tracking-loop multiplexing among satellites is shown to be $L = 10 \log (d_F)$, where d_F is the on-time duty factor of the code loop.

The report discusses acquisition strategies for single- and dual-RF channel receivers as well as dedicated versus multiplexing receiver channels. It is shown that, for a single receiver, dedicated pseudochannel or multiple channels acquire four times slower than a continuous receiver, and dividing the uncertainty among the channels results in acquisition times which are five times longer. Finally, some actual C/A code-acquisition times are calculated for a Shuttle scenario, it is found that a four-channel receiver can acquire with a probability of 0.999 in approximately 60 seconds.

The unique frequency plan and processing-gain preservation scheme used in the TI receiver is also discussed in the report. In order to derive the receiver threshold for the GPS/Shuttle link, the error response of a third-order carrier loop to a step in jerk is analyzed. From the receiver threshold results, the GPS/Shuttle link budget is calculated. Finally, the report documents the update on TACAN interference analysis.

SHUTTLE GLOBAL POSITIONING SYSTEM (GPS)

DESIGN STUDY

ANNUAL REPORT

Contract No. NAS 9-16067, Exhibit B

Technical Monitor: J. Pawlowski

Prepared for

NASA Lyndon B. Johnson Space Center
Houston, Texas 77058

Prepared by

Jack Holmes
Peter Nilsen

Axiomatix
9841 Airport Blvd, Suite 912
Los Angeles, California 90045

Axiomatix Report No. R8111-2
November 5, 1981

TABLE OF CONTENTS

	Page
LIST OF TABLES	iii
LIST OF FIGURES	iv
1.0 INTRODUCTION AND SUMMARY	1
2.0 OVERVIEW OF TEXAS INSTRUMENTS' MULTIPLEX RECEIVER	2
3.0 GPS CARRIER-LOOP TIME-SHARING LOSS.	8
3.1 Analysis	8
3.2 Carrier-Loop Time-Sharing Loss	8
4.0 PERFORMANCE OF THE TEXAS INSTRUMENTS' CARRIER-LOOP SCHEME FOR AVOIDING THE L_1/L_2 TIME-SHARING LOSSES	14
4.1 Executive Summary	14
4.2 L_1/L_2 Carrier-Loop System	18
4.3 Analysis of the L_1/L_2 Carrier System	22
4.4 Response to Dynamics	43
4.5 Delay Effects on the Carrier Loop	45
4.6 Conclusions	56
5.0 TEXAS INSTRUMENTS' GPS TRACKING DISCRIMINATOR FOR L_1 AND L_2 CODE TRACKING	57
6.0 GPS TIME-SHARING CODE-TRACKING PERFORMANCE LOSSES	61
6.1 Analysis	61
6.2 Conclusions	72
7.0 COMPARISON OF SINGLE/DUAL RECEIVER SCHEMES TO ACHIEVE FAST PN CODE ACQUISITION TIMES	73
7.1 Summary	73
7.2 Preliminary Discussion	73
7.3 Single-Receiver Acquisition	74
7.3.1 Four-Dedicated-Pseudochannel Approach, Single Receiver	74
7.3.2 Divide-Down Strategy for Four Satellites, Single Receiver	79
7.4 Dual-Receiver Acquisition	81
7.4.1 Eight-Dedicated-Pseudochannel Approach, Dual Receiver	81
7.4.2 Divide-Down Strategy for Four Satellites with Two Receivers	85

	Page
7.5 Single-Receiver Acquisition--Refined Model	86
7.5.1 Four-Dedicated-Pseudochannel Approach	86
7.5.2 Divide-Down Strategy for One Receiver	88
7.6 Conclusions	91
8.0 PRELIMINARY C/A CODE ACQUISITION TIME ESTIMATES	92
8.1 Summary	92
8.2 Analysis	92
8.3 Conclusions	100
9.0 PRESERVATION OF THE PROCESSING GAIN FOR THE TI GPS RECEIVER L ₁ /L ₂ AND DISCUSSION OF THE RECEIVER FREQUENCY PLAN	101
9.1 Summary	101
9.2 L ₁ Frequency Plan	101
9.3 Processing Gain	106
9.4 L ₂ Frequency Plan	107
9.5 Conclusions	110
10.0 RESPONSE OF THIRD-ORDER PLL TO STEP IN JERK	111
11.0 SHUTTLE GPS RECEIVER MINIMUM REQUIRED SNR	113
12.0 SHUTTLE/GPS LINK BUDGET	116
12.1 GPS/Shuttle Link Budgets	116
12.1.1 Satellite EIRP	116
12.1.2 Space Loss	116
12.1.3 Pointing Loss	119
12.1.4 Polarization Loss	119
12.1.5 Antenna Gain	121
12.1.6 Circuit Loss	121
12.1.7 System Noise Temperature	121

APPENDICES

- A Review of TACAN/GPS Interference
- B Review of GPS Phase IIB Program Testing

LIST OF TABLES

	Page
4.1 Degradation from Ideal Nontime-Shared Loop	40
4.2 Results for $B_{L\Sigma}/B_{L\Delta} = 1 + 4\zeta^2/3$	44
7.1 Single-Receiver Relative Acquisition Time Comparison	91
7.2 Dual-Receiver Relative Acquisition Time Comparison	91
8.1 Summary of Acquisition Times and Probabilities for a Two-Doppler 1023-Chip Search	92
8.2 Acquisition Probability versus Number of Sweeps	96
12.1 Shuttle/GPS Link Budget Update	117
12.2 RF Circuit Loss	121

LIST OF FIGURES

		Page
2.1	Comparison of Sequential and Multiplex Receiver Timing	3
2.2	Multichannel Receiver Timing	4
2.3	Multiplex Receiver Functional Block Diagram	5
2.4	Hardware/Software Interfaces for Multiplex Carrier and Code Tracking	6
2.5	Simplified Functional Block Diagram of TI Carrier Loop	7
3.1	Phase-Locked-Loop Model	9
3.2	Multiplexing Function Where the Value 1 Implies On and 0 Implies Off	9
3.3	Autocorrelation of $g(t)$ for $ \tau \leq d_F T_0$	13
4.1	Simplified Functional Block Diagram of TI Carrier Loop	15
4.2	L_1/L_2 Time/Multiplex Carrier-Loop Performance Degradation as a function of SNR	17
4.3	Carrier-Loop L_1/L_2 Time-Sharing for Tracking One Satellite Channel [4,5]	19
4.4	L_1/L_2 Time-Sharing Function	20
4.5	Carrier Loop L_1/L_2 Time-Sharing Model Configured for One Satellite Tracking	23
4.6	Autocorrelation Function for $N_2(t)$	35
4.7	Cross-Correlation Function $R_{N_1 N_2}(\tau)$	39
4.8	Costas Loop Model with I&D Arm Filters	46
4.9	Closed-Loop Bandwidth Expansion with Delay, $\zeta = 0.707$	50
4.10	Closed-Loop Bandwidth Expansion with Delay, $\zeta = 1.0$	51
4.11	Closed-Loop Bandwidth Expansion with Delay, $\zeta = 3.0$	52
4.12	Closed-Loop Bandwidth Expansion with Delay, $\zeta = 5.0$	53
5.1	Code Sum and Difference Tracking Loops	58

	Page
6.1 Gating Function and its Autocorrelation Function	62
6.2 Time-Gated Code-Tracking Loop with Arm Filters having Bandwidth $B[\text{Hz}]$	64
7.1 Satellite Multiplexing Pattern for a Single Receiver with Four Dedicated Channels	74
7.2 One Possible Satellite Acquisition Sequence for the Dedicated-Pseudochannel Approach	76
7.3 Models of the Acquisition Time Probability Density Function	77
7.4 One Possible Satellite Acquisition Sequence for the Divide-Down Strategy	80
7.5 Satellite Multiplexing Pattern for a Dual-Receiver with Eight Dedicated Channels	82
7.6 Typical Acquisition Scenario for the Dedicated-Pseudochannel Case	83
7.7 Distribution Function of Acquisition Time When $P_D < 1$. . .	87
7.8 Distribution Function of Acquisition Time for the Case When $P_D < 1$ and the Uncertainty per Pseudochannel is $N\tau_D/4$. . .	89
8.1 PN Code Sequential Detector	94
8.2 Noise-Only and Signal-Plus-Noise Realization	95
8.3 Acquisition Probability versus Acquisition Time Indexed by the Number of Complete Sweeps of the Code Uncertainty . .	97
8.4 Doppler Uncertainty and the Associated Doppler Bins	99
9.1 Equivalent Frequency Plan Model for the TI GPS Receiver . .	102
9.2 Interference Model and Signals	106
10.1 Plot of Normalized Loop-Tracking Error for Third-Order Phase-Lock-Loop with Jerk Step Input	112
11.1 Probability of Not Losing Lock	115
12.1 Geometry for Shuttle/GPS Link Space-Loss Calculation . . .	118
12.2 Derivation of Off-Axis Pointing Error for Orbiter in 200-Mile Orbit	120

	Page
12.3 System Block Diagram for Calculation of System Noise Temperature	122
12.4 General Mode of System Noise Temperature for Cascaded Elements	123

1.0 INTRODUCTION AND SUMMARY

This report documents the analyses and investigations of the Texas Instruments (TI) Digital Multiplex Receiver conducted by Axiomatix. Axiomatix has analyzed this receiver since it is a potential candidate receiver for the Shuttle GPS navigation system. Furthermore, this TI receiver utilizes a unique design approach which has not heretofore been seen or reviewed by NASA or Axiomatix. The TI receiver architecture is summarized in Section 2. The salient performance factors of the receiver are summarized below.

In this report, we primarily analyze multiplex code-tracking performance and multiplex carrier-tracking performance as well as multiplex code acquisition performance. In Section 3, we analyze the carrier loop time-sharing loss and show that the loop threshold increases by $-10 \log(d_F)$, where d_F is the duty factor due to time-sharing among multiple satellites. However, the receiver also multiplexes between L_1 and L_2 frequencies so that there is also some time-sharing loss due to L_1/L_2 sharing. In Section 4, we show that the TI implementation avoids most of this loss and that the actual loss due to L_1/L_2 sharing is between 0.4 and 1.0 dB. In Section 5, we explain how this TI tracking discriminator functions for L_1 and L_2 code tracking. The time-sharing loss due to code tracking-loop multiplexing among satellites is shown in Section 6 to be $L = 10 \log(d_F)$, where d_F is the on-time duty factor of the code loop.

In Section 7, we discuss acquisition strategies for single- and dual-RF channel receivers as well as dedicated-versus-multiplexing receiver channels. We show that, for a single receiver, dedicated pseudochannel or multiplex channels acquire four times slower than a continuous receiver, and dividing the uncertainty among the channels results in acquisition times that are five times longer. Finally, in Section 8, we calculate some actual C/A code acquisition times for a Shuttle scenario and find that a four-channel receiver can acquire with a probability of 0.999 in approximately 60 seconds.

Section 9 discusses the unique frequency plan and processing gain preservation scheme used in the TI receiver. In Section 10, we look at the error response of a third-order carrier loop to a step in jerk. This result is used in deriving receiver threshold for the purposes of calculating a GPS/Shuttle link budget. This link budget is presented in Section 11, along with documentation of the update on TACAN interference analyses.

2.0 OVERVIEW OF TEXAS INSTRUMENTS' MULTIPLEX RECEIVER

The TI multiplex receiver utilizes several innovations in GPS receiver architecture. The major innovation is the multiplex feature whereby one physical RF channel can simultaneously track multiple satellites on both L_1 and L_2 frequencies. This is done by sampling each satellite signal at essentially the Nyquist rate.

An indication of the Nyquist sampling process timing used in the TI multiplex receiver is given in Figure 2.1. This compares multiplex receiver timing with sequential receiver timing. As an aid in gaining perspective, the timing for a typical multiple-channel receiver is shown in Figure 2.2.

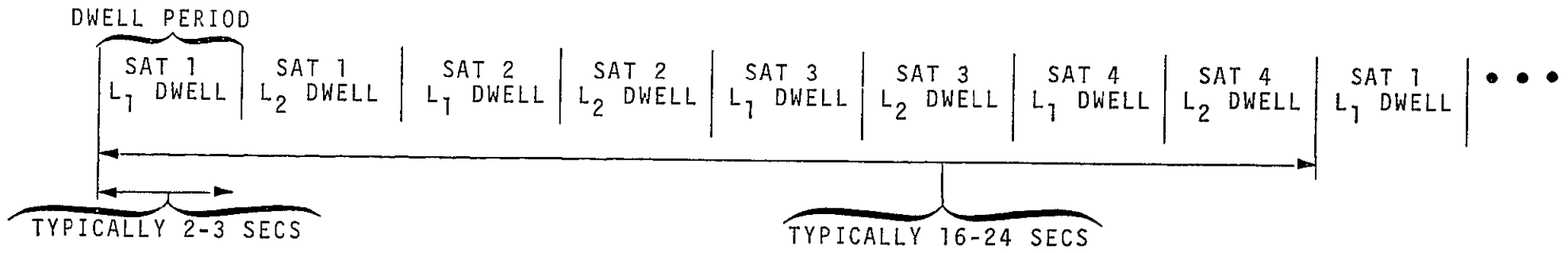
A top-level functional block diagram of the receiver is shown in Figure 2.3. A large portion of the receiver is implemented in software, as indicated by the baseband processor box. The interfaces between the hardware and software functions are indicated in Figure 2.4. It is this software implementation of receiver functions that, for the most part, allows a significant reduction in hardware while enabling multiple satellites to be tracked.

Another important innovation utilized in the TI receiver is the sum and difference tracking loops.

A functional block diagram of the basic TI multiplex carrier loop is shown in Figure 2.5. This diagram highlights the L_1/L_2 time-sharing process through which the usual 3-dB loss is partially avoided. The basic approach is to simultaneously track the sum of the L_1 and L_2 carrier phase errors, ϕ_Σ , and the difference between the L_1 and L_2 carrier phase errors, ϕ_Δ . The loop estimate of the L_1 and L_2 carrier phase errors then proceeds from the simple calculation:

$$\begin{aligned} \phi_\Sigma &= \phi_{L_1} + \phi_{L_2} & \frac{\phi_\Sigma + \phi_\Delta}{2} &= \phi_{L_1} \\ \phi_\Delta &= \phi_{L_1} - \phi_{L_2} & \frac{\phi_\Sigma - \phi_\Delta}{2} &= \phi_{L_2} \end{aligned}$$

SEQUENTIAL RECEIVER TIMING



MULTIPLEX RECEIVER TIMING

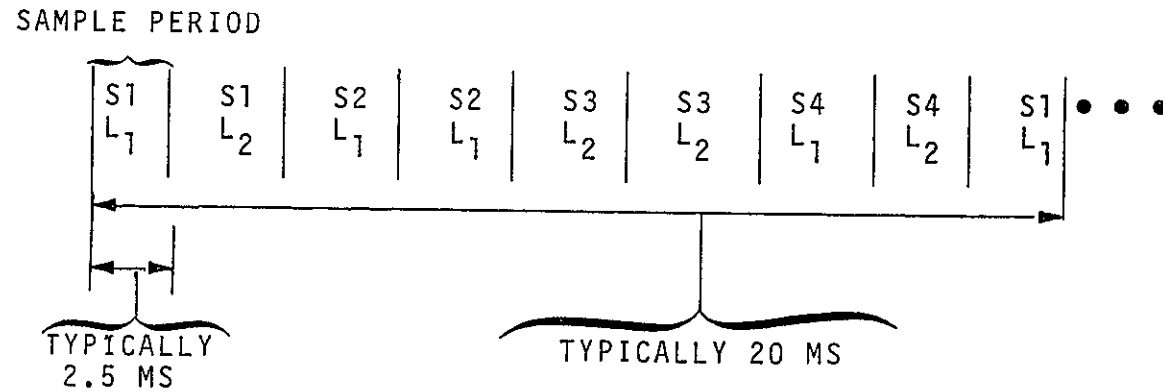
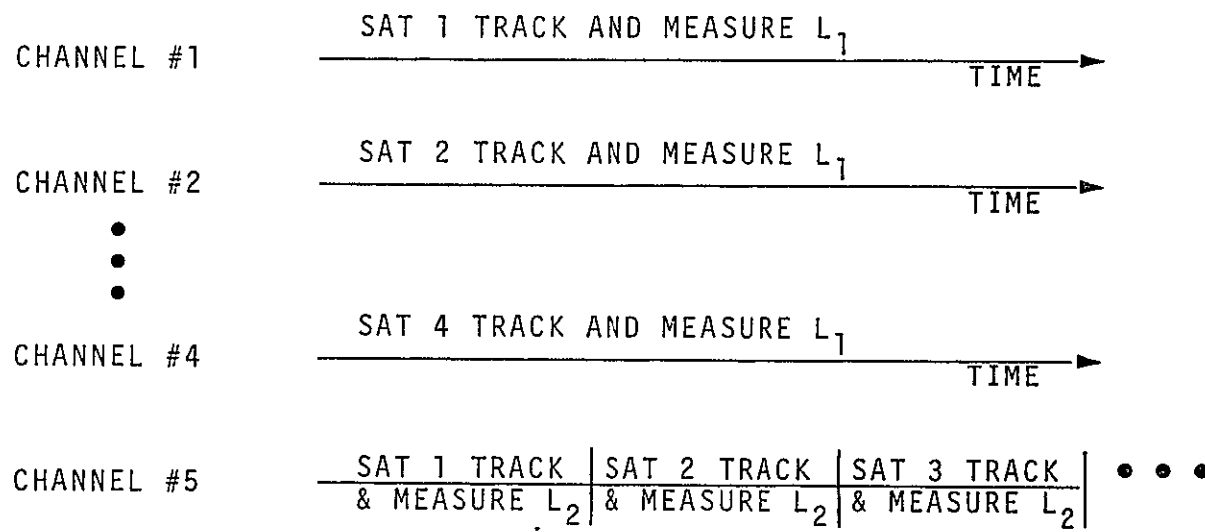


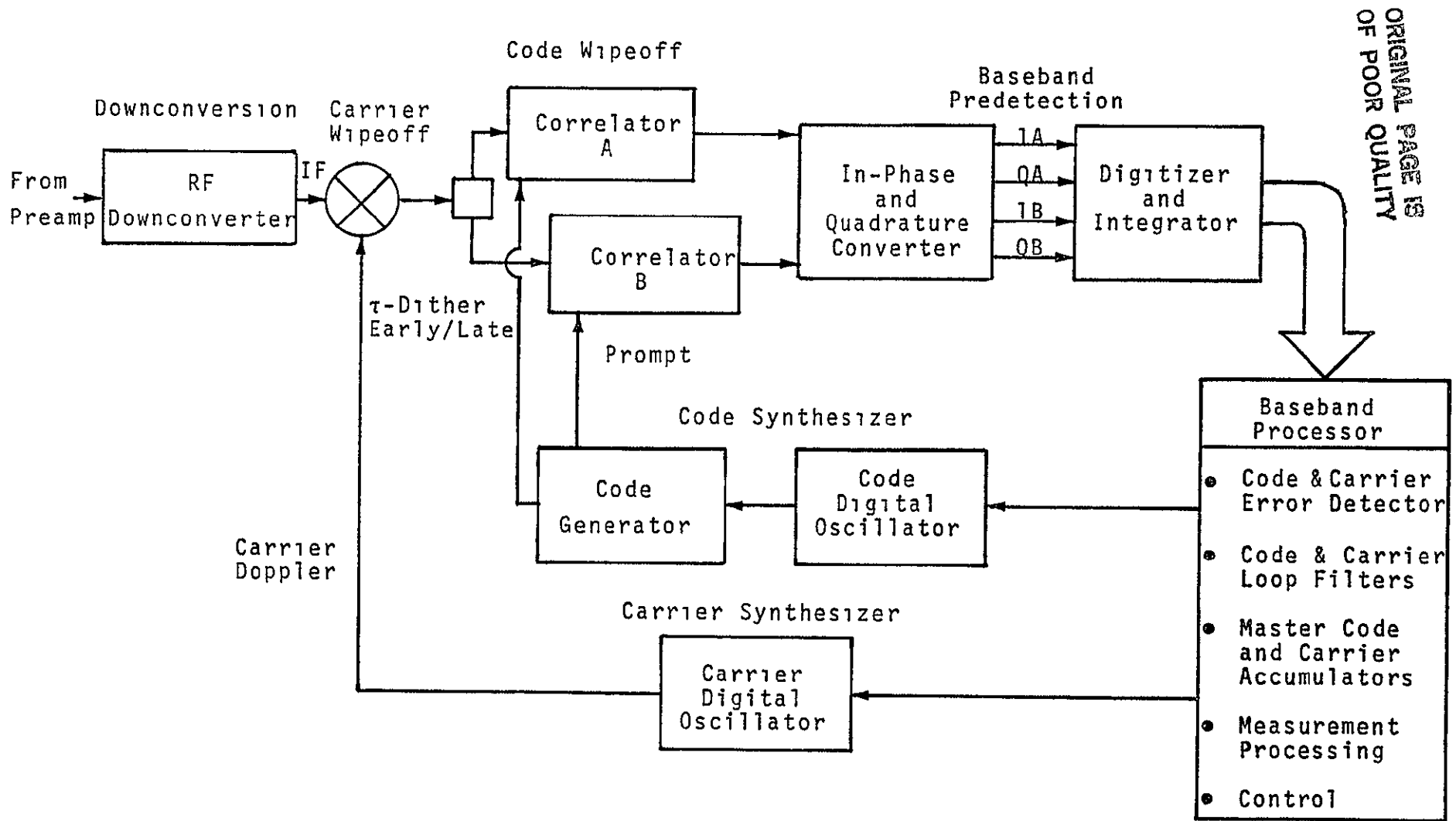
Figure 2.1. Comparison of Sequential and Multiplex Receiver Timing

ORIGINAL PAGE IS
OF POOR QUALITY



ORIGINAL PAGE IS
OF POOR QUALITY

Figure 2.2. Multichannel Receiver Timing



ORIGINAL PAGE IS OF POOR QUALITY

Figure 2.3. Multiplex Receiver Functional Block Diagram

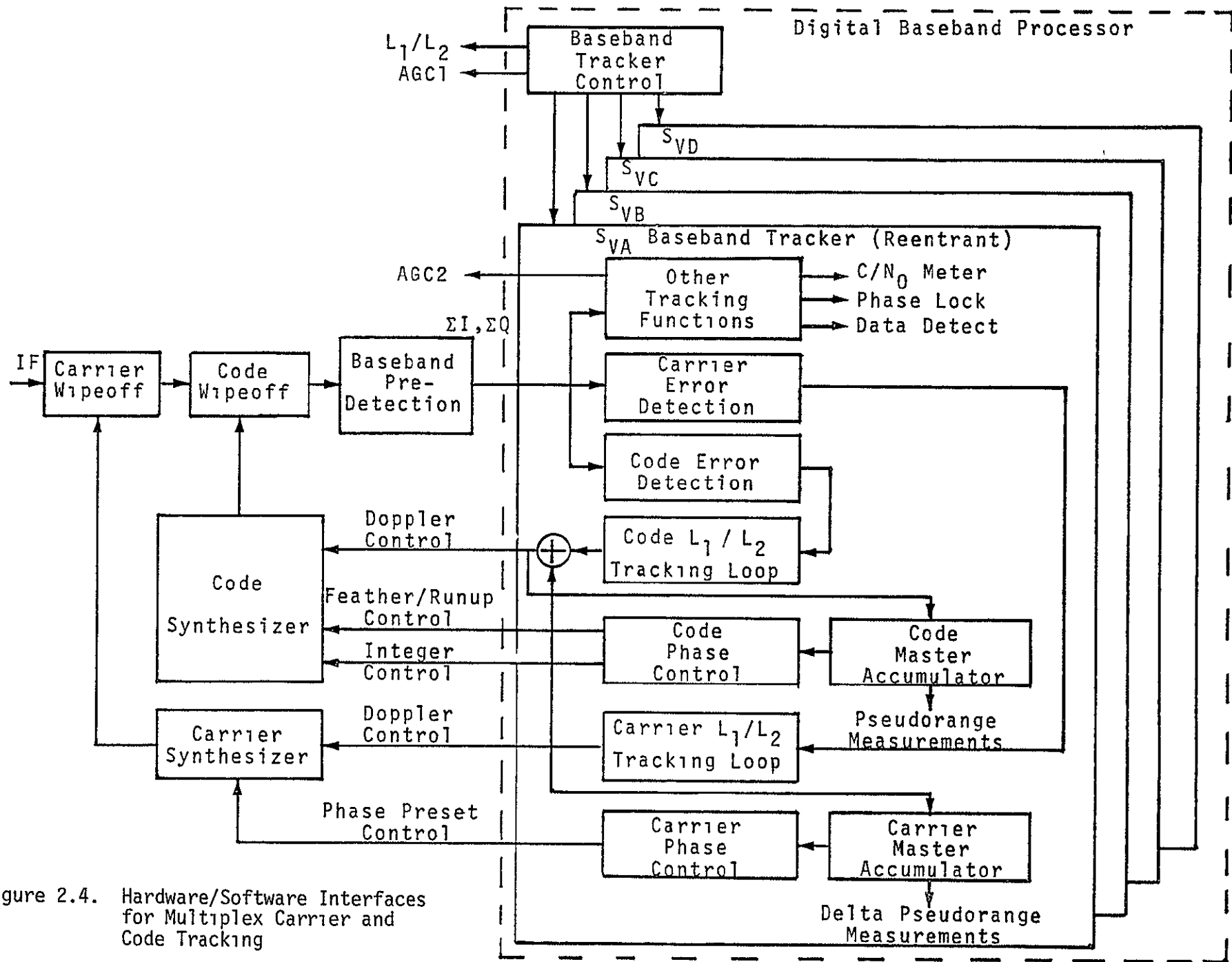


Figure 2.4. Hardware/Software Interfaces for Multiplex Carrier and Code Tracking

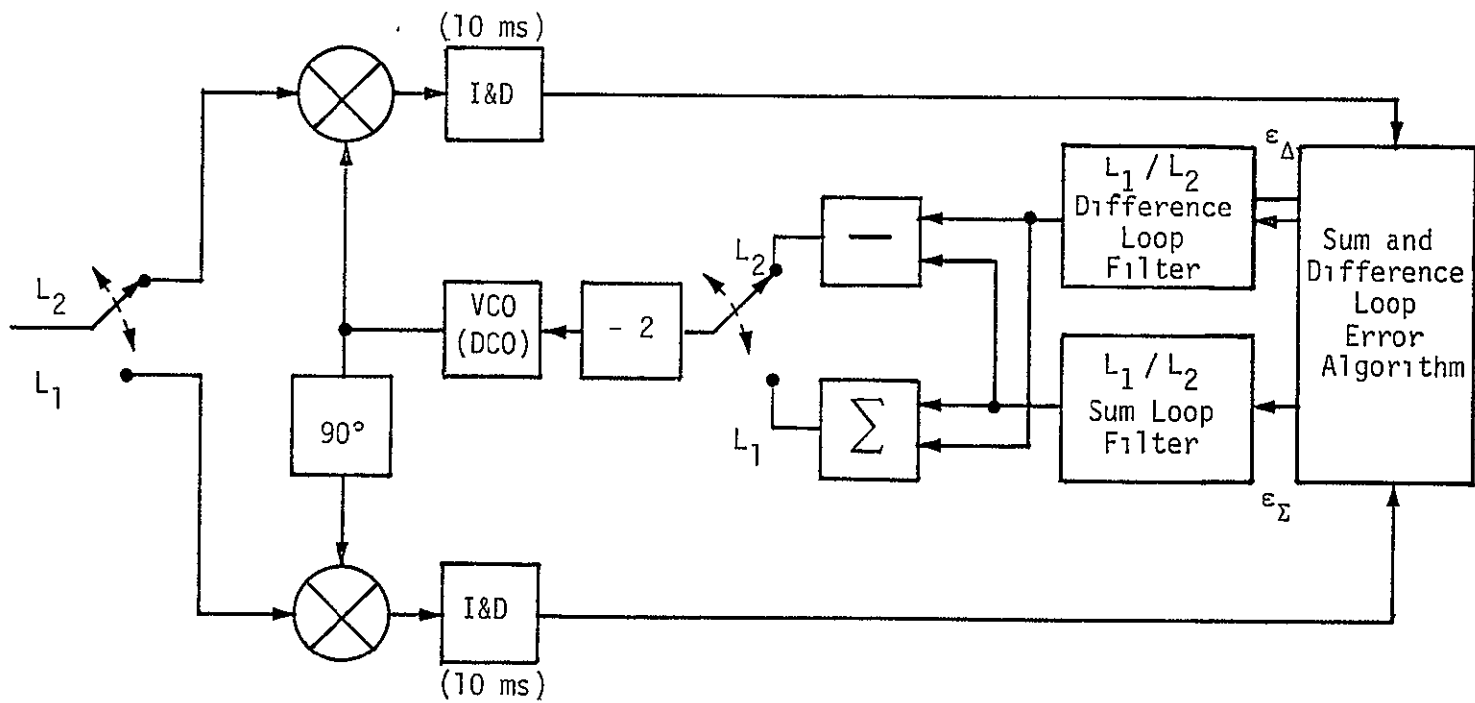


Figure 2.5. Simplified Functional Block Diagram of TI Carrier Loop

ORIGINAL PAGE IS
OF POOR QUALITY

3.0 GPS CARRIER-LOOP TIME-SHARING LOSS

The purpose of this section is to demonstrate that a carrier loop suffers the same multiplexing loss as the code-tracking loop, namely, that the threshold increases by $-10 \log(d_F)$ [dB]. The analysis was carried out for a CW loop, although the result can be generalized to Costas loops as well as quadriphase-tracking loops.

3.1 Analysis

The purpose of this analysis is to establish that ordinary multiplexing of the carrier loop, whether from L_1 or L_2 or from satellite to satellite, yields an increase in required C/N_0 of $-10 \log d_F$, where d_F is the fraction of the time that channel (or satellite) is on. For example, if there are four satellites being tracked and both L_1 and L_2 are used for each satellite, the total loss is then $-10 \log\left(\frac{1}{8}\right) = 9$ dB. This analysis is for ordinary time-sharing and does not include the technique used by TI to reduce the L_1/L_2 time-sharing loss.

3.2 Carrier-Loop Time-Sharing Loss

Consider the phase-locked-loop model in Figure 3.1 and the multiplexing function, $g(t)$, illustrated in Figure 3.2. Model the received signal by

$$y(t) = \sqrt{2P} \sin(\omega_0 t + \theta) + n(t) \quad (1)$$

where ω_0 is the radian carrier frequency, θ is unknown phase and $n(t)$ is white Gaussian noise (WGN).

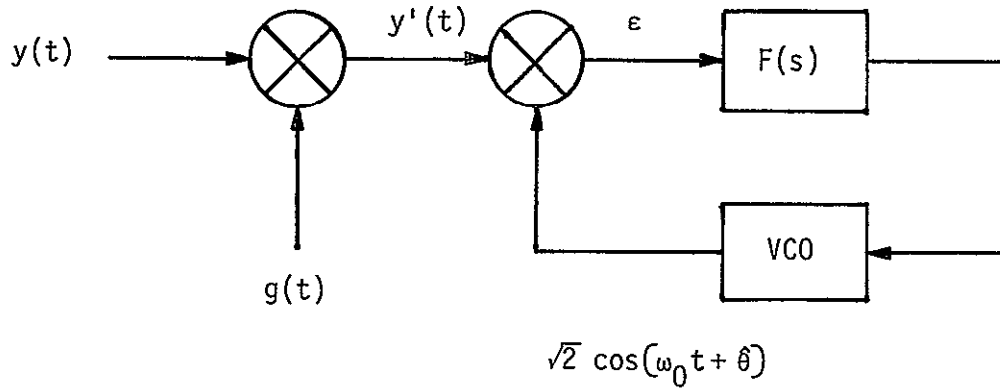


Figure 3.1. Phase-Locked-Loop Model

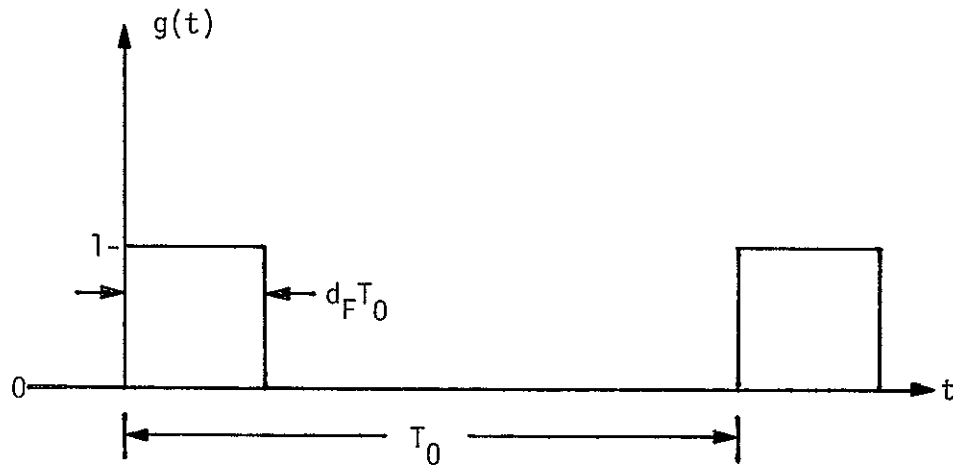


Figure 3 2 Multiplexing Function Where the Value 1 Implies On and 0 Implies Off

After the multiplexing operation, we have

$$y'(t) = \sqrt{2P} g(t) \sin(\omega_0 t + \theta) + g(t)n(t) \quad (2)$$

The error signal, $\epsilon(t)$, is then described by

$$\epsilon(t) = \sqrt{2P} g(t) \sin(\omega_0 t + \hat{\theta}) - \sqrt{2} \cos(\omega_0 t + \hat{\theta}) + g(t) n(t) \cos(\omega_0 t + \hat{\theta}) \quad (3)$$

The noise can be written in terms of its in-phase and quadrature components, as follows:

$$n(t) = \sqrt{2} n_s(t) \sin(\omega_0 t + \theta) + \sqrt{2} n_c(t) \cos(\omega_0 t + \theta) \quad (4)$$

or

$$\epsilon(t) = \sqrt{P} g(t) \sin \phi + g(t) n_c(t) \cos \phi + g(t) n_s(t) \sin \phi \quad (5)$$

It can be shown that, if $\phi(t)$ is very narrowband compared to $n(t)$, (4) has an equivalent noise term described by $g(t)n_c(t)$ which is obvious when $\phi = 0$

Now write $g(t)$ in the Fourier series as

$$g(t) = \frac{C_0}{2} + \sum_{n=1}^{\infty} C_n \cos(n \omega_0 t + \phi_n)$$

where

$$C_n = 2A_{AVG} \left| \frac{\sin(n\pi d_F)}{n\pi d_F} \right| \quad \left(\omega_0 = \frac{2\pi}{T_0} \right) \quad (6)$$

and

$$A_{AVG} = d_F \quad (7)$$

Using (6) and (7) in the first term of (5) produces

$$\epsilon(t) = \sqrt{P} d_F \sin \phi + \sqrt{P} \sin \phi \sum_{n=1}^{\infty} 2d_F \left| \frac{\sin n\pi d_F}{n\pi d_F} \right| \cos(n\omega_0 t + \phi_n) + g(t)n(t)$$

Since $n_c(t)$ and $n(t)$ have the spectral density over the region of interest, we drop the subscript c on $n_c(t)$. Considered as a Heaviside operator, the loop produces the output

$$F(s)\epsilon(t) = F(s) \left\{ \sqrt{P} d_F \sin \phi + g(t)n(t) \right\} + \text{filtered multiplexing harmonics} \quad (8)$$

It follows that the output phase estimate is given by

$$\hat{\theta} = \frac{KF(s)}{s} \left\{ \sqrt{P} d_F \phi + g(t)n(t) \right\} \quad (9)$$

Linearizing the loop equation (9) using $\phi = \theta - \hat{\theta}$ produces

$$\theta - \phi \cong \frac{KF(s)}{s} \left\{ \sqrt{P} d_F \phi + g(t)n(t) \right\} \quad (10)$$

Rearranging, we have

$$\phi + \frac{\sqrt{P} d_F KF(s)}{s} \phi = - \frac{KF(s)}{s} g(t)n(t) \quad (11)$$

Solving for ϕ , we have

$$\phi = H(s) \frac{g(t)n(t)}{\sqrt{P} d_F} \quad (12)$$

where

$$H(s) = \frac{\sqrt{P} d_F \frac{KF(s)}{s}}{1 + \frac{\sqrt{P} d_F KF(s)}{s}} \quad (13)$$

The linearized phase error variance is then given by

$$\sigma_{\phi}^2 = \frac{\mathcal{S}_{gn}(0) 2B_L}{P d_F^2} \quad (14)$$

where $\mathcal{S}_{gn}(0)$ is the spectral density of $g(t)n(t)$ assuming stationarity. The autocorrelation function of $g(t)$ using time averaging produces

$$R_g(\tau) = d_F \bigwedge_{d_F}(\tau) * \sum_{n=-\infty}^{\infty} \delta(\tau + nT_0) \quad (15)$$

where * denotes convolution. Hence, the spectral density of $g(t)n(t)$ at $f=0$ is given by

$$\mathcal{S}_{gn}(0) = \int_{-\infty}^{\infty} \mathcal{S}_g(f) \mathcal{S}_n(f) df \quad (16)$$

The spectral density of $g(t)$ is given by

$$\mathcal{S}_g(f) = \mathcal{F} \left\{ d_F \bigwedge_{d_F}(\tau) * \sum_{n=-\infty}^{\infty} \delta(\tau + nT_0) \right\} \quad (17)$$

$$= \mathcal{F} \sum_{n=-\infty}^{\infty} \delta(\tau + nT_0) \mathcal{F} \left(d_F \bigwedge_{d_F}(\tau) \right) \quad (18)$$

$$= \frac{1}{T_0} \sum_{n=-\infty}^{\infty} \delta(f - n/T_0) d_F(d_F T_0) \left(\frac{\sin(\pi d_F T_0 f)}{\pi d_F T_0 f} \right)^2 \quad (19)$$

or

$$\mathcal{S}_g(f) = d_F^2 \sum_{n=-\infty}^{\infty} \left(\frac{\sin(\pi d_F T_0 f)}{\pi d_F f T_0} \right)^2 \delta(f - n/T_0) df \quad (20)$$

where $\bigwedge_{d_F}(\tau)$ is the autocorrelation function of one $g(t)$ pulse, as shown in Figure 3.3. Therefore, the spectral density at $f=0$ is given by

$$\mathcal{S}_{gn}(0) = d_F^2 \int_{-\infty}^{\infty} \frac{N_0}{2} \sum_{n=-\infty}^{\infty} \left(\frac{\sin(\pi d_F T_0 f)}{\pi d_F f T_0} \right)^2 \delta(f - n/T_0) df \quad (21)$$

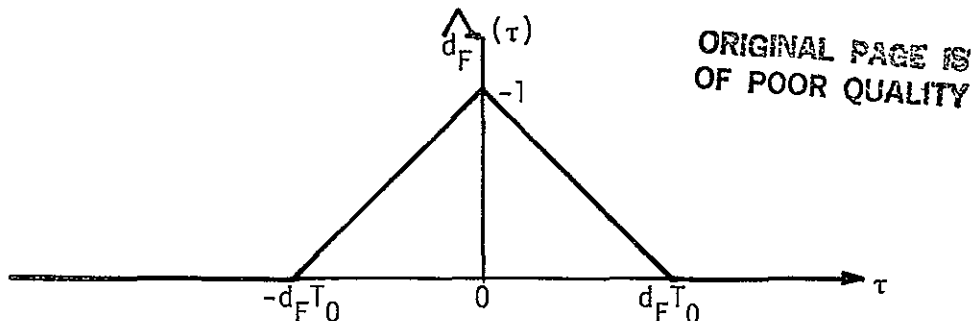


Figure 3.3. Autocorrelation of $g(t)$ for $|\tau| \leq d_F T_0$

or

$$\mathcal{S}_{gn}(0) = \frac{N_0}{2} d_F^2 \sum_{n=-\infty}^{\infty} \left(\frac{\sin(\pi d_F n)}{\pi d_F n} \right)^2 \quad (22)$$

From [1], we have

$$\sum_{n=-\infty}^{\infty} \frac{\sin^2(n \pi d_F)}{(n \pi d_F)^2} = \frac{1}{d_F} \quad (23)$$

It follows that

$$\mathcal{S}_{gn}(0) = \frac{N_0}{2} d_F \quad (24)$$

Therefore, from (14) and (24), we have that the linearized phase error variance is given by

$$\sigma_\phi^2 = \frac{N_0 B_L}{d_F^2} \quad (25)$$

where we have assumed that the non-DC line components of $\mathcal{S}_{gn}(f)$ are negligible on their effect on the loop, i.e., $B_L T_0 \ll 1$, where B_L is the one-sided loop bandwidth

We see that the final result, (25), indicates that the "effective" signal loss is d_F , or $-10 \log d_F$ in decibels. Therefore, if the loop is time-shared 50% of the time, the carrier threshold is 3 dB higher, etc.

4.0 PERFORMANCE OF THE TEXAS INSTRUMENTS' CARRIER-LOOP SCHEME FOR AVOIDING THE L_1/L_2 TIME-SHARING LOSSES

This section analyzes the Texas Instruments' (TI) GPS advanced digital receiver carrier-tracking performance. In particular, the processing of the sum and difference channels are analyzed when they are corrupted in white Gaussian noise. In addition to thermal noise, delay effects due to the 50-Hz digital-processing rate and the integrate-and-dump filters are considered.

4.1 Executive Summary

This section presents an investigation of several aspects of the operation and performance of the TI receiver multiplex carrier-tracking system. Multiplex carrier-tracking allows one physical RF channel to perform the functions of four satellite-tracking channels plus L_1 and L_2 tracking for ionospheric correction. This sharing is, for the most part, realizable due to software implementation of much of the carrier-tracking loop, thus resulting in considerable hardware savings relative to a parallel channel receiver. The price of this hardware savings is a loss of available signal-to-noise ratio (SNR) when multiplexing among satellites. This loss has been documented by Axiomatix [2]. The SNR loss which might be incurred due to L_1/L_2 sharing has been minimized by the TI design. This report describes how this is accomplished and what the actual loss is. In addition, the response to dynamics and limitations to loop bandwidth for the TI design are covered in this report.

A functional block diagram of the basic TI multiplex carrier loop is shown in Figure 4.1. This diagram highlights the L_1/L_2 time-sharing process through which the usual 3-dB loss is partially avoided. The basic approach is to simultaneously track the sum of the L_1 and L_2 carrier phase errors, ϕ_Σ , and the difference between the L_1 and L_2 carrier phase errors, ϕ_Δ . The loop estimate of the L_1 and L_2 carrier phase errors then proceeds from the simple calculation:

$$\begin{aligned} \phi_\Sigma &= \phi_{L_1} + \phi_{L_2} & \frac{\phi_\Sigma + \phi_\Delta}{2} &= \phi_{L_1} \\ \phi_\Delta &= \phi_{L_1} - \phi_{L_2} & \frac{\phi_\Sigma - \phi_\Delta}{2} &= \phi_{L_2} \end{aligned}$$

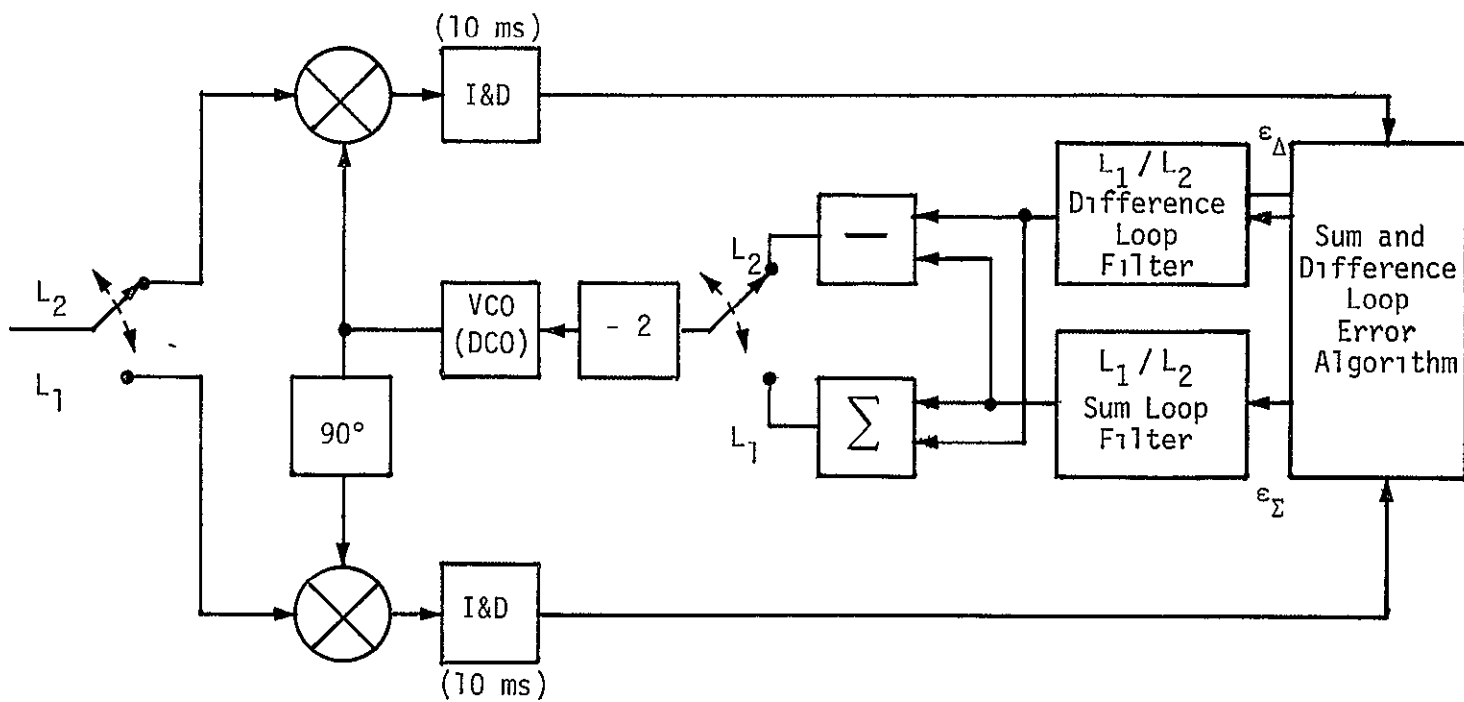


Figure 4.1. Simplified Functional Block Diagram of TI Carrier Loop

ORIGINAL PAGE IS
OF POOR QUALITY

In the analysis which follows, we show that the tracking error variance for channel L_1 (or L_2) for the multiplexed loop is given by

$$\sigma_{\phi_2}^2 = \sigma_{\phi_1}^2 = \frac{N_0 B_{L\Sigma}}{P} + \left(\frac{3 N_0}{4 P} + \frac{N_0^2}{2P^2 T} \right) \left(1 + \frac{2}{6 + \frac{4N_0}{PT}} \right) B_{L\Delta}$$

where T is the GPS 20-ms bit duration. The variance for a nontime-shared loop is simply $N_0 B_{L\Sigma}/P$ and the degradation for the multiplexed loop relative to the nontime-shared loop is shown plotted in Figure 4.2 as a function of the SNR PT/N_0 . As can be seen from Figure 4.2, the ratio of difference to sum loop bandwidths is a factor in the degradation. It can be seen that, to minimize the L_1/L_2 time-sharing degradation, a $B_{L\Sigma}/B_{L\Delta} \geq 10$ should be used.

Two properties of the L_1/L_2 multiplexed loop which affect the ability of the loop to track vehicular dynamics are examined in the report. The first property, discussed in section 4.4, illustrates how the effective closed-loop response of the L_1/L_2 multiplex loop is roughly equivalent to a loop with the average of the sum and difference loop filters. The second property, discussed in section 4.5, is the effect of the delay in the loop on the loop stability and bandwidth. Our simplified model and analysis indicates that the loop bandwidth for a second loop must be less than 3.3 Hz to keep the noise jitter from increasing no more than 20%. Furthermore, at $B_{L0} = 13.3$ Hz, the loop becomes unstable. Thus, in order to track certain vehicular dynamics, it may be necessary to utilize a higher order tracking loop having a narrower bandwidth. We have not yet analyzed the performance of such a loop.

ORIGINAL PAGE IS
OF POOR QUALITY

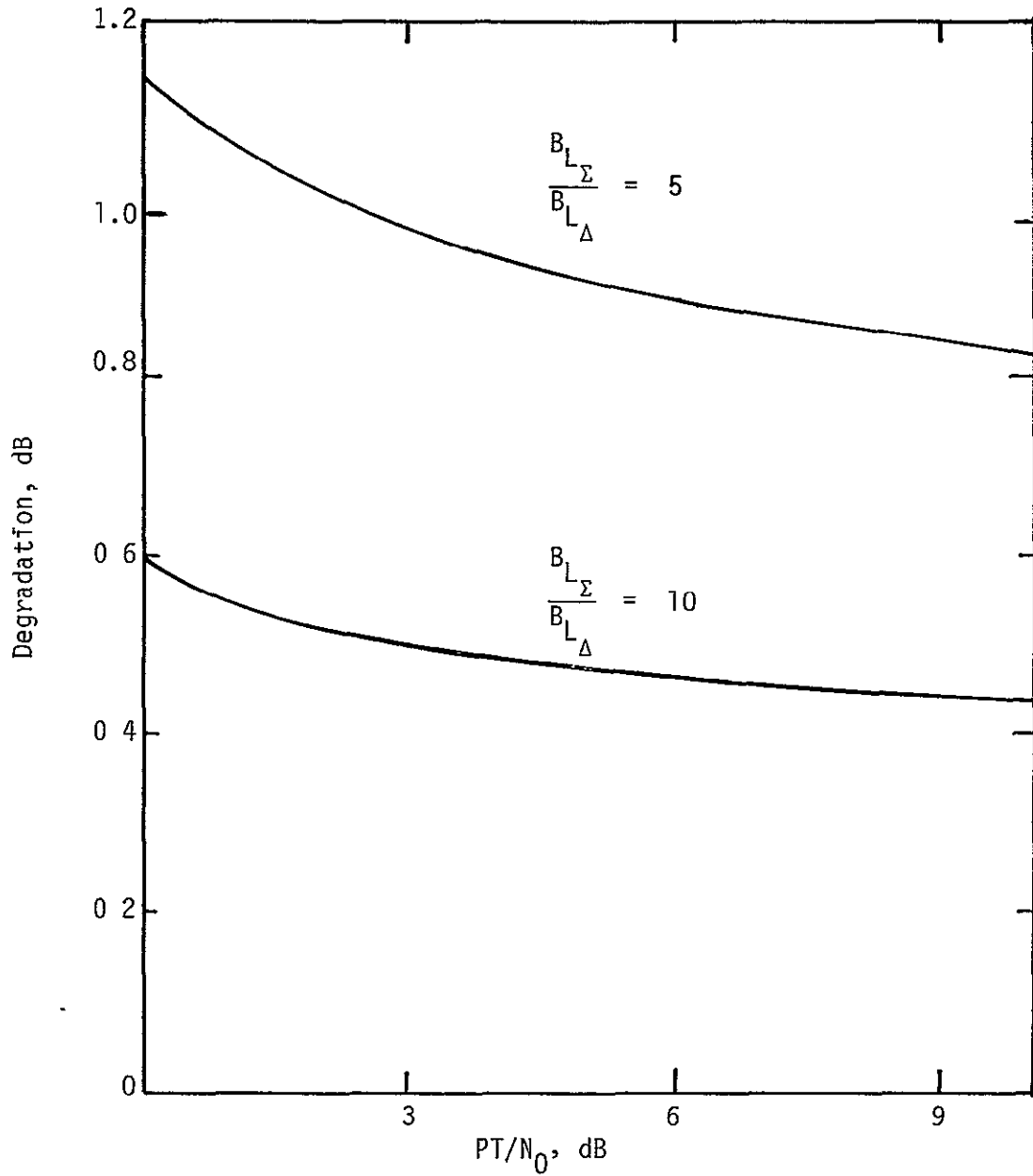


Figure 4 2. L_1/L_2 Time/Multiplex Carrier-Loop Performance Degradation as a function of SNR

4.2 L_1/L_2 Carrier-Loop System

The main purpose of this report is to present the interesting carrier-loop scheme used in the Texas Instruments (TI) GPS receiver [3-6] to avoid the L_1/L_2 carrier-loop time-sharing losses (periodically switching between L_1 and L_2).

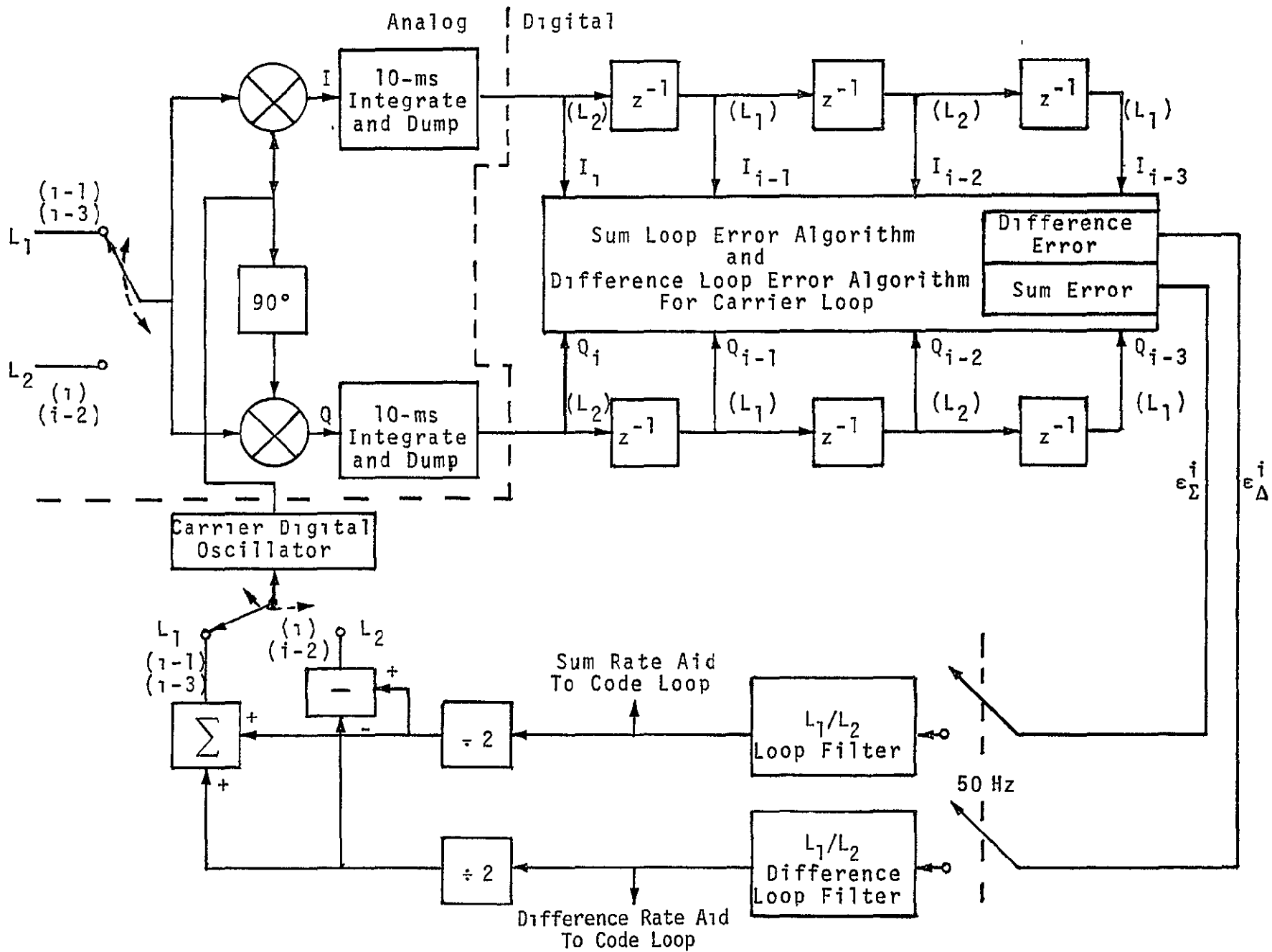
We will discuss the carrier-loop operations first, then the tracking-loop performance. Figure 4.3 illustrates the TI carrier-loop system based on a TI viewgraph presentation in which the L_1 and L_2 frequencies are time shared. The system of Figure 4.3 is configured for one satellite operation; however, the TI receiver can operate simultaneously on four or more satellites. Two carrier frequencies are used L_1 : 1575.42 MHz and L_2 : 1227.6 MHz. Both L_1 and L_2 are quadrature signals, with the in-phase signal being modulated with both data and the P code. The Q phase signal is modulated with both the C/A code and data; further, the in-phase signal is 3 dB higher in average power. The dashed line separates the digital portion from the analog portion.

The loop distinguishes between L_1 and L_2 operations by frequency discrimination, whereas the clear code and P code are separated by the two distinct PN-type codes used on the I and Q phases at the same frequency.

Consider Figure 4.3, which is configured for one satellite operation. Since the data is 50 bps, the bit duration is 20 ms. However, since L_1 and L_2 have to be time shared, only 10 ms are integrated at one time. Both I and Q integrations are performed, digitized, and shifted down a delay circuit one tap every 10 ms.

Figure 4.4 illustrates how L_1 and L_2 are time shared as well as how two error control functions, ϵ_{Σ}^1 and ϵ_{Δ}^1 , are obtained and delivered to the loop filter at a 50-Hz rate. Hence, we see that the first half of the data bit time is devoted to L_1 and the second half to L_2 . It is also clear at this point that the data suffers a 3-dB time-sharing loss.

There are two loop filters used in the L_1/L_2 carrier-loop control. The first is designed to process the sum of the L_1 and L_2 phase errors. In the second loop filter, the difference between the L_1 and L_2 phase errors is processed. The motivation for doing this is that the difference loop filter can be made much narrower than the sum, so that the total noise "seen" by the L_1/L_2 loop is reduced to almost one-half.



ORIGINAL PAGE IS
OF POOR QUALITY

Figure 4.3. Carrier-Loop L_1/L_2 Time-Sharing System for Tracking One Satellite Channel [4,5]

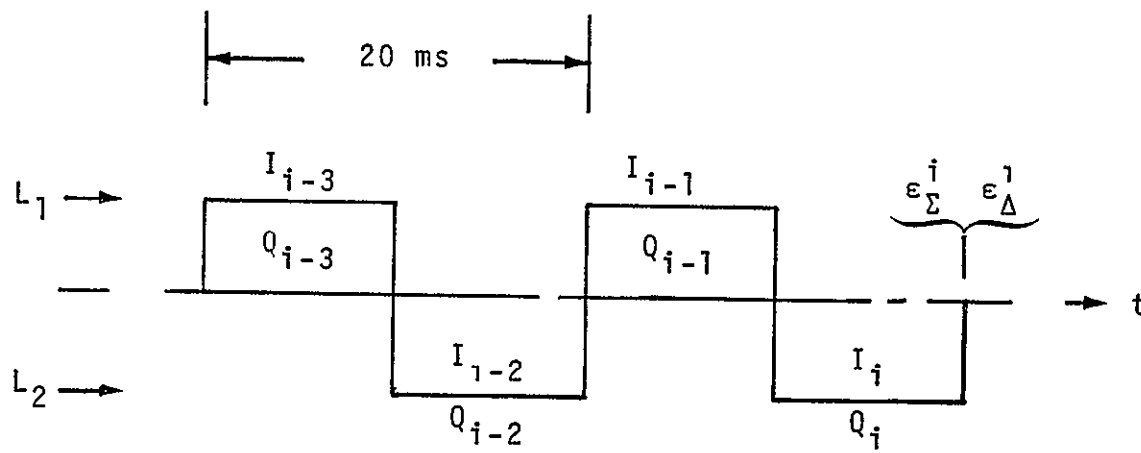


Figure 4 4. L₁/L₂ Time-Sharing Function

ORIGINAL PAGE IS
OF POOR QUALITY

It should be realized that, since the loops are implemented in software, two loop filters do not imply a hardware penalty.

After filtering, the outputs are summed and differenced to yield signals proportional to the L_1 and L_2 carrier phase errors. These error signals are multiplexed into the local carrier digital oscillator, the output of which is an analog signal.

4.3 Analysis of the L₁/L₂ Carrier System

Figure 4.5 illustrates the model used for analysis. It differs from Figure 4.3 by virtue of the fact that some scale factors have been added as well as two sample-and-hold (S&H) circuits. This model allows us to analyze an analog loop rather than a digital loop; however, the performance results will be the same if the sampling is fast enough. One factor which is not included in the following analysis is the delay in the loop. Notice that the delay at the error control ($\epsilon_{\Sigma}^1, \epsilon_{\Delta}^1$) output runs from 0 to 40 ms, with an average of about 20 ms. With a loop bandwidth of around typically 25 Hz, this could be a problem. This effect will be discussed later in more detail. The loop input signal is given by

$$y(t) = \sqrt{2P} d(t) \sin(\omega_0 t + \theta_0) + \sqrt{2} N_c(t) \cos(\omega_0 t + \theta_0) + \sqrt{2} N_s(t) \sin(\omega_0 t + \theta_0) \quad (26)$$

where

- P = P code signal power
- $d(t)$ = NRZ baseband data signal at 50 bps
- ω_0 = carrier radian frequency
- θ_0 = received carrier phase
- $N_s(t)$ = in-phase baseband bandlimited white Gaussian noise process
- $N_c(t)$ = quadrature baseband bandlimited white Gaussian noise process

After beating with the reference carrier signals, assuming the loop is tracking, yields

$$\sqrt{2} \sin(\omega_0 t + \hat{\theta}) y(t) = y_I(t) = \sqrt{P} d(t) \cos\phi + N_c(t) \sin\phi + N_s \cos\phi \quad (27)$$

$$\sqrt{2} \cos(\omega_0 t + \hat{\theta}) y(t) = y_Q(t) = \sqrt{P} d(t) \sin\phi + N_c(t) \cos\phi + N_s \sin\phi \quad (28)$$

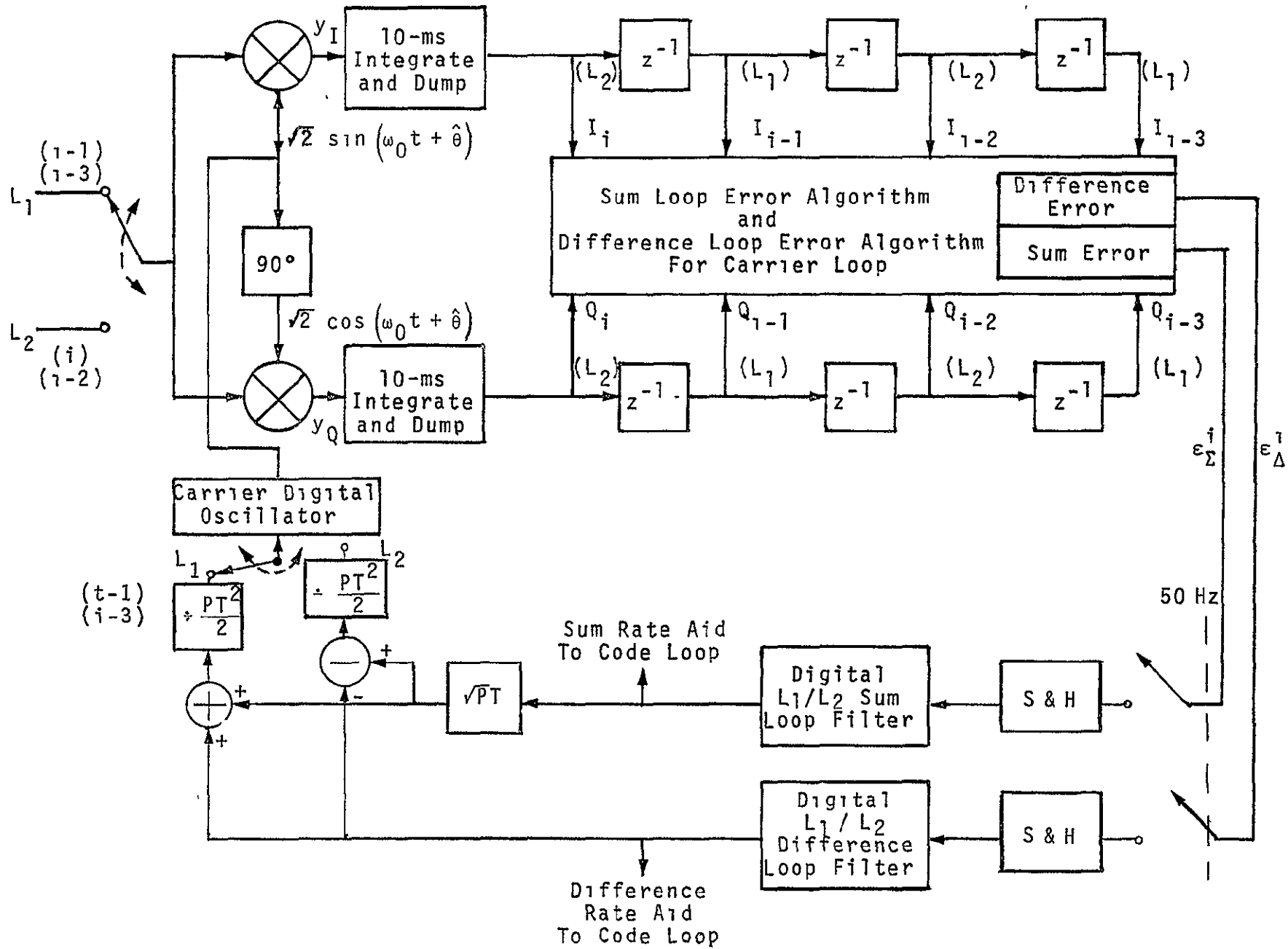


Figure 4.5. Carrier Loop L_1/L_2 Time-Sharing Model Configured for One Satellite Tracking

**ORIGINAL PAGE IS
OF POOR QUALITY**

When $\phi(t)$ is a constant, the two noise terms of (27) can be shown to be independent of the two noise terms of (28). Alternatively, we assume high SNR so that $\phi \approx 0$, which allows us to approximate (27) and (28) by

$$y_I(t) = \sqrt{P} d(t) \cos\phi + N_I(t) \quad (29)$$

$$y_Q(t) = \sqrt{P} d(t) \sin\phi + N_Q(t) \quad (30)$$

with $N_I(t) = N_s(t)$ and $N_Q(t) = N_c(t)$. The error control signals used by TI in the receiver are given by

$$\epsilon_{\Delta}^1 = (Q_{1-1} I_1 - Q_1 I_{1-1}) + (Q_{i-1} I_{1-2} - Q_{1-2} I_{1-1}) S \quad (31)$$

where

$$S = \text{SGN} \left[(Q_{i-3} + Q_{1-2})(Q_{1-1} + Q_1) + (I_{1-3} + I_{1-2})(I_{i-1} + I_1) \right] \\ \epsilon_{\Sigma}^1 = (Q_1 + Q_{1-1}) \text{SGN} (I_1 + I_{1-1}) \quad (32)$$

We recognize ϵ_{Σ}^1 as the usual hard-decision Costas loop error signal; however, ϵ_{Δ}^1 is quite involved. The signals Q_k and I_k are the 10-ms integrations of the Q and I signals, respectively. For convenience in notation, we will label N_Q^{1-k} and N_I^{1-k} by N_I^{-k} and N_Q^{-k} , respectively. Also, we will denote the data bit associated with samples I_1, I_{1-1}, Q_1 or Q_{1-1} as d^0 and that associated with samples $I_{1-2}, I_{1-3}, Q_{1-2}$ and Q_{1-3} as d^{-1} .

First consider ϵ_{Σ}^1 ; from (32), we have

$$\epsilon_{\Sigma}^1 = (Q_1 + Q_{1-1}) \text{SGN} [I_1 + I_{1-1}] \quad (33)$$

$$\epsilon_{\Sigma}^1 = \left(\sqrt{P} \frac{T}{2} d^0(t) \sin \phi_2 + N_Q^0 + \sqrt{P} \frac{T}{2} d^{-1} \sin \phi_1 + N_Q^{-1} \right) \\ \times \text{SGN} \left[\left(\sqrt{P} \frac{T}{2} d^0 \cos \phi_2 + N_I^0 + \sqrt{P} \frac{T}{2} d^{-1} \cos \phi_1 + N_I^{-1} \right) \right] \quad (34)$$

where it has been assumed that $\phi(t)$ is constant over $2T = 40$ ms and T is the bit duration of 20 ms. For small phase errors, we have

$$\epsilon_{\Sigma}^i = \left(\sqrt{P} \frac{T}{2} d^0 \phi_2 + N_Q + \sqrt{P} \frac{T}{2} d^0 \phi_1 + N_Q^{-1} \right) \times \text{SGN} \left[\left(\sqrt{P} \frac{T}{2} d^0 + N_I^0 + \sqrt{P} \frac{T}{2} d^0 + N_I^{-1} \right) \right] \quad (35)$$

or

$$\epsilon_{\Sigma}^i \approx \left(\sqrt{P} \frac{T}{2} \phi_2 + N_Q^0 d^0 + \sqrt{P} \frac{T}{2} \phi_1 + N_Q^{-1} d^0 \right) \times \text{SGN} \left[2 \sqrt{P} \frac{T}{2} + N_I^0 + N_I^{-1} \right] \quad (36)$$

Now, assuming that the noise is small so that $\text{SGN}(\cdot) \approx 1$, we have

$$\epsilon_{\Sigma}^1 = \frac{\sqrt{PT}}{2} \left(\phi_1 + \phi_2 + \frac{N_Q^0}{\sqrt{P} \frac{T}{2}} + \frac{N_Q^{-1}}{\sqrt{P} \frac{T}{2}} \right) \quad (37)$$

where $\bar{N}_Q^0 = d^0 N_Q^0$, $\bar{N}_Q^{-1} = d^0 N_Q^{-1}$, $\bar{N}_I^0 = d^0 N_I^0$ and $\bar{N}_I^{-1} = d^0 N_I^{-1}$. Now look at ϵ_{Δ}^1 :

$$\begin{aligned} \epsilon_{\Delta}^1 &= (Q_{1-1} I_1 - Q_1 I_{1-1}) + (Q_{1-1} I_{1-2} - Q_{1-2} I_{1-1}) \\ &\times \text{SGN} \left[(Q_{1-3} + Q_{1-2})(Q_{1-1} + Q_1) + (I_{1-3} + I_{1-2})(I_{1-1} + I_1) \right] \quad (38) \end{aligned}$$

In terms of the integrals of (29) and (30), we obtain

$$\begin{aligned} \epsilon_{\Delta}^1 &= \left[\left(\sqrt{P} \frac{T}{2} d^0 \sin \phi_1 + N_Q^{-1} \right) \left(\sqrt{P} \frac{T}{2} d^0 \cos \phi_2 + N_Q^0 \right) - \left(\sqrt{P} \frac{T}{2} d^0 \sin \phi_2 + N_Q^0 \right) \left(\sqrt{P} \frac{T}{2} d^0 \cos \phi_1 + N_I^{-1} \right) \right] \\ &+ \left(\sqrt{P} \frac{T}{2} d^0 \sin \phi_1 + N_Q^{-1} \right) \left(\sqrt{P} \frac{T}{2} d^{-1} \cos \phi_2 + N_I^{-2} \right) - \left(\sqrt{P} \frac{T}{2} d^{-1} \sin \phi_2 + N_Q^{-2} \right) \left(\sqrt{P} \frac{T}{2} d^0 \cos \phi_1 + N_I^{-1} \right) \\ &\times \text{SGN} \left[\left(\sqrt{P} \frac{T}{2} d^{-1} \sin \phi_1 + N_Q^{-3} + \sqrt{P} \frac{T}{2} d^{-1} \sin \phi_2 + N_Q^{-2} \right) \left(\sqrt{P} \frac{T}{2} d^0 \sin \phi_1 + N_Q^{-1} + \sqrt{P} \frac{T}{2} d^0 \sin \phi_2 + N_Q^0 \right) \right. \\ &\left. + \left(\sqrt{P} \frac{T}{2} d^{-1} \cos \phi_1 + N_I^{-3} + \sqrt{P} \frac{T}{2} d^{-1} \cos \phi_2 + N_I^{-2} \right) \left(\sqrt{P} \frac{T}{2} d^0 \cos \phi_1 + N_I^{-1} + \sqrt{P} \frac{T}{2} d^0 \cos \phi_2 + N_I^0 \right) \right] \quad (39) \end{aligned}$$

For small ϕ_1 and ϕ_2 , we have

$$\begin{aligned} \epsilon_{\Delta}^1 \approx & \frac{PT^2}{4} \left[\left(\sin \phi_1 + \frac{\bar{N}_I^{-1}}{\sqrt{P} \frac{T}{2}} \right) \left(\cos \phi_2 + \frac{\bar{N}_Q^{-1}}{\sqrt{P} \frac{T}{2}} \right) - \left(\sin \phi_2 + \frac{\bar{N}_Q^0}{\sqrt{P} \frac{T}{2}} \right) \left(\cos \phi_1 + \frac{\bar{N}_I^{-1}}{\sqrt{P} \frac{T}{2}} \right) \right] \\ & + \frac{PT^2}{4} \left[\left(\sin \phi_1 + \frac{\bar{N}_Q^{-1}}{\sqrt{P} \frac{T}{2}} \right) \left(\cos \phi_2 + \frac{\bar{N}_I^{-2}}{\sqrt{P} \frac{T}{2}} \right) - \left(\sin \phi_2 + \frac{\bar{N}_Q^{-2}}{\sqrt{P} \frac{T}{2}} \right) \left(\cos \phi_1 + \frac{\bar{N}_I^{-1}}{\sqrt{P} \frac{T}{2}} \right) \right] \\ & \times \text{SGN} \left[\left(\frac{\bar{N}_Q^{-3}}{\sqrt{P} \frac{T}{2}} + \frac{\bar{N}_Q^{-2}}{\sqrt{P} \frac{T}{2}} \right) \left(\frac{\bar{N}_Q^{-3}}{\sqrt{P} \frac{T}{2}} + \frac{\bar{N}_Q^{-2}}{\sqrt{P} \frac{T}{2}} \right) + \left(2 + \frac{\bar{N}_I^{-3}}{\sqrt{P} \frac{T}{2}} + \frac{\bar{N}_I^{-2}}{\sqrt{P} \frac{T}{2}} \right) \left(2 + \frac{\bar{N}_I^{-1}}{\sqrt{P} \frac{T}{2}} + \frac{\bar{N}_I^0}{\sqrt{P} \frac{T}{2}} \right) \right] \end{aligned} \quad (40)$$

where we have used

$$\begin{aligned} \bar{N}_Q^{-2} &= d^{-1} N_Q^{-2} ; \quad \bar{N}_I^{-2} = d^{-1} N_I^{-2} \\ \bar{N}_Q^{-3} &= d^{-1} N_Q^{-3} ; \quad \bar{N}_I^{-3} = d^{-1} N_I^{-3} \end{aligned} \quad (41)$$

Again assuming that the noise is small so that $\text{SGN}(\cdot) = 1$, we have

$$\frac{\epsilon_{\Delta}^1}{\frac{PT^2}{4}} \approx \left[2 \sin(\phi_1 - \phi_2) + \frac{4\bar{N}_Q^{-1} (\bar{N}_I^0 + \bar{N}_I^{-2})}{PT^2} + 4 \frac{\bar{N}_Q^{-1}}{\sqrt{PT}} - \frac{4\bar{N}_I^{-1}}{PT^2} (\bar{N}_Q^0 + \bar{N}_Q^{-2}) - 2 \frac{(\bar{N}_Q^0 + \bar{N}_Q^{-2})}{\sqrt{PT}} \right] \quad (42)$$

To summarize, we have

$$\epsilon_{\Delta}^1 = \frac{\sqrt{PT}}{2} \left(\phi_1 + \phi_2 + \frac{2\bar{N}_Q^0}{\sqrt{PT}} + \frac{2\bar{N}_I^{-1}}{\sqrt{PT}} \right) \quad (43)$$

$$\epsilon_{\Delta}^1 = \left(\frac{PT^2}{2} \right) \left[(\phi_1 - \phi_2) + \frac{2\bar{N}_Q^2 (\bar{N}_I^0 + \bar{N}_I^{-2})}{PT^2} + 2 \frac{\bar{N}_Q^{-1}}{\sqrt{PT}} - \frac{2\bar{N}_I^{-1} (\bar{N}_Q^0 + \bar{N}_Q^{-2})}{PT^2} - \frac{(\bar{N}_Q^0 + \bar{N}_Q^{-2})}{\sqrt{PT}} \right] \quad (44)$$

Hence, we see that the scale factors are not equal. So we multiply ϵ_{Σ}^1 by \sqrt{PT} and obtain

$$\sqrt{PT} \epsilon_{\Sigma}^1 = \frac{PT^2}{2} \left(\phi_1 + \phi_2 + \frac{2\bar{N}_Q^0}{\sqrt{PT}} + \frac{2\bar{N}_I^{-1}}{\sqrt{PT}} \right) \quad (45)$$

$$\epsilon_{\Delta}^1 = \frac{PT^2}{2} (\phi_1 - \phi_2) + \frac{2\bar{N}_Q^{-1} (\bar{N}_I^0 + \bar{N}_I^{-2})}{PT^2} + 2 \frac{\bar{N}_Q^{-1}}{\sqrt{PT}} - \frac{2\bar{N}_I^{-1} (\bar{N}_Q^0 + \bar{N}_Q^{-2})}{PT^2} - \frac{(\bar{N}_Q^0 + \bar{N}_Q^{-2})}{\sqrt{PT}} \quad (46)$$

After the loop filters, we have

$$K_{\Sigma} \sqrt{PT} F_{\Sigma}(s) \epsilon_{\Sigma}^1 = K_{\Sigma} F_{\Sigma}(s) \left[\phi_1 + \phi_2 + \frac{2\bar{N}_Q^0}{\sqrt{PT}} + \frac{2\bar{N}_I^{-1}}{\sqrt{PT}} \right] \quad (47)$$

$$K_{\Delta} F_{\Delta}(s) \epsilon_{\Delta}^1 = K_{\Delta} F_{\Delta}(s) \left[\phi_1 - \phi_2 + \frac{2\bar{N}_Q^{-1} (\bar{N}_I^0 + \bar{N}_I^{-2})}{PT^2} + 2 \frac{\bar{N}_Q^{-1}}{\sqrt{PT}} - \frac{2\bar{N}_I^{-1} (\bar{N}_Q^0 + \bar{N}_Q^{-2})}{PT^2} - \frac{(\bar{N}_Q^0 + \bar{N}_Q^{-2})}{\sqrt{PT}} \right] \quad (48)$$

where K_{Σ} and K_{Δ} are the total loop gains including the term PT^2 . Summing (47) and (48) produces the error signal for L_1 :

$$Y_{\phi_1} = K_{\Delta} F_{\Delta}(s) \epsilon_{\Delta}^1 + K_{\Sigma} F_{\Sigma}(s) \epsilon_{\Sigma}^1$$

or

$$\begin{aligned} Y_{\phi_1} = & \frac{1}{2} K_{\Sigma} F_{\Sigma}(s) \phi_1 + K_{\Sigma} F_{\Sigma}(s) \phi_2 + \frac{2K_{\Sigma} F_{\Sigma}(s) N_Q^0}{\sqrt{PT}} + \frac{2K_{\Sigma} F_{\Sigma}(s) N_Q^{-1}}{\sqrt{PT}} \\ & K_{\Delta} F_{\Delta}(s) \phi_1 - K_{\Delta} F_{\Delta}(s) \phi_2 + \frac{2K_{\Delta} F_{\Delta}(s) N_Q^{-1} (N_I^0 + \bar{N}_I^{-2})}{PT^2} + \frac{2K_{\Delta} F_{\Delta}(s) N_Q^{-1}}{\sqrt{PT}} \\ & - \frac{2K_{\Delta} F_{\Delta}(s) N_I^{-1} (N_Q^0 + N_Q^{-2})}{PT^2} - \frac{K_{\Delta} F_{\Delta}(s) (N_Q^0 + N_Q^{-2})}{\sqrt{PT}} \end{aligned} \quad (49)$$

where we have left off the overbar on the noise terms for convenience.

Now assume that $K_{\Sigma} F_{\Sigma}(s) \phi_2 = K_{\Delta} F_{\Delta}(s) \phi_2$ at dc and frequencies which are small compared to the loop bandwidth. We then have

$$\begin{aligned} Y_{\phi_1} \approx & \left[\frac{K_{\Sigma} F_{\Sigma}(s) + K_{\Delta} F_{\Delta}(s)}{2} \right] \phi_1 + \frac{K_{\Sigma} F_{\Sigma}(s) N_Q^0}{\sqrt{PT}} + \frac{K_{\Sigma} F_{\Sigma}(s) N_Q^{-1}}{\sqrt{PT}} + \frac{K_{\Delta} F_{\Delta}(s) N_Q^{-1} (N_I^0 + N_I^{-2})}{PT^2} \\ & + \frac{K_{\Delta} F_{\Delta}(s) N_2}{\sqrt{PT}} - \frac{K_{\Delta} F_{\Delta}(s) N_I^{-1} (N_Q^0 + N_Q^{-2})}{PT^2} - \frac{K_{\Delta} F_{\Delta}(s) (N_Q^0 + N_Q^{-2})}{2\sqrt{PT}} \end{aligned} \quad (50)$$

It is to be noted that $F_{\Delta}^{\Sigma}(s)$ and $F_{\Sigma}(s)$ do not have to be of the same order, only the low-frequency values must be equal. Now the L_1 carrier phase estimate is given by

$$\hat{\theta}_1 = \frac{1}{s} \left(K_{\Sigma} F_{\Sigma}(s) N_1 + K_{\Delta} F_{\Delta}(s) N_2 + \frac{K_{\Delta} F_{\Delta}(s) + K_{\Sigma} F_{\Sigma}(s)}{2} \phi_1(t) \right) \quad (51)$$

and the phase error is given by $\phi_1 = \theta_1 - \hat{\theta}_1$ so that

$$\theta - \phi - \frac{1}{s} \frac{K_{\Delta} F_{\Delta}(s) + K_{\Sigma} F_{\Sigma}(s)}{2} \phi = \frac{1}{s} \left[K_{\Sigma} F_{\Sigma}(s) N_1 + K_{\Delta} F_{\Delta}(s) N_2 \right] \quad (52)$$

Hence, after rearranging, we have

$$\phi_1 = \frac{-\frac{1}{s} \left[K_{\Sigma} F_{\Sigma}(s) N_1 + K_{\Delta} F_{\Delta}(s) N_2 \right]}{1 + \frac{1}{s} \left[\frac{K_{\Delta} F_{\Delta}(s) + K_{\Sigma} F_{\Sigma}(s)}{2} \right]} \quad (53)$$

which is the phase error of the L_1 carrier. The two noise terms, $N_1(t)$ and $N_2(t)$ are the first two noise terms and the last four noise terms, respectively, as indicated in (50).

Now we shall compute the phase error variance of the L_1 carrier from the linearized phase error ϕ_1 given by (53). Let

$$H'(s) = \frac{\frac{1}{s} K_{\Sigma} F_{\Sigma}(s)}{1 + \frac{1}{s} \left[\frac{K_{\Delta} F_{\Delta}(s) + K_{\Sigma} F_{\Sigma}(s)}{2} \right]} \quad (54)$$

$$H''(s) = \frac{\frac{1}{s} K_{\Delta} F_{\Delta}(s)}{1 + \frac{1}{s} \left[\frac{K_{\Delta} F_{\Delta}(s) + K_{\Sigma} F_{\Sigma}(s)}{2} \right]} \quad (55)$$

Then we can write (53) as

$$\phi_1(t) = -H'(s)N_1(t) - H''(s)N_2(t) \quad (56)$$

The autocorrelation function of $\phi(t)$ is given by

$$R_{\phi_1}(\tau) = \overline{(H'^*(s)N_1(t) + H''^*(s)N_2(t))(H'(s)N_1(t+\tau) + H''(s)N_2(t+\tau))} \quad (57)$$

After evaluating, we have

$$\begin{aligned} R_{\phi_1}(\tau) = & |H'(s)|^2 R_{N_1}(\tau) + \overline{H''^*(s)H'(s)N_2(t)N_1(t+\tau)} \\ & + \overline{H''(s)H'^*(s)N_1(t)N_2(t+\tau)} + |H''(s)|^2 R_{N_2}(\tau) \end{aligned} \quad (58)$$

Integrating on τ yields the spectral density of ϕ_1 so that[†]

$$\begin{aligned} \mathcal{S}_{\phi_1} = & |H'(s)|^2 \mathcal{S}_{N_1}(f) + H''^*(s)H'(s) \mathcal{S}_{N_2N_1}(f) \\ & + H''(s)H'^*(s) \mathcal{S}_{N_1N_2}(f) + |H''(s)|^2 \mathcal{S}_{N_2}(f) \end{aligned} \quad (59)$$

Using the fact that the noise terms are flat near $f=0$ yields

$$\begin{aligned} \sigma_{\phi_1}^2 = & \int_{-\infty}^{\infty} \mathcal{S}_{\phi_1}(f)df = \mathcal{S}_{N_1}(0) \int_{-\infty}^{\infty} |H'(2\pi f)|^2 df + \mathcal{S}_{N_1N_2}(0) \int_{-\infty}^{\infty} H''^*(2\pi f)H'(2\pi f)df \\ & + \mathcal{S}_{N_1N_2}(0) \int_{-\infty}^{\infty} H''(2\pi f)H'^*(2\pi f)df + \mathcal{S}_{N_2}(0) \int_{-\infty}^{\infty} |H''(2\pi f)|^2 df \end{aligned} \quad (60)$$

[†] Where we define $\mathcal{S}\{N_2(t)N_1(t+\tau)\} = \mathcal{S}_{N_2N_1}(f)$ and $\mathcal{S}\{N_1(t)N_2(t+\tau)\} = \mathcal{S}_{N_1N_2}(f)$

This is the basic equation relating the linearized phase error variance of L_1 to the loop parameters in the case where high loop SNR is assumed. We will now evaluate this expression first in terms of arbitrary loop filters and later using second-order loop filters.

First consider the first term of (60). Let

$$\begin{aligned} 2B_{L_\Sigma} &= \int_{-\infty}^{\infty} |H'(2\pi f)|^2 df \\ 2B_{L_\Delta} &= \int_{-\infty}^{\infty} |H''(2\pi f)|^2 df \end{aligned} \quad (61)$$

then

$$\sigma_\phi^2 = \sigma_{T_1}^2 + \sigma_{T_2}^2 + \sigma_{T_3}^2 + \sigma_{T_4}^2 \quad (62)$$

where T_1 is the 1th term of equation (60). We now consider the value of $\mathcal{S}_{N_1}(\sigma)$ in order to evaluate T_1 .

$$N_1(t) = \frac{N_Q^0}{\sqrt{PT}} + \frac{N_Q^{-1}}{\sqrt{PT}} \quad , \quad 0 \leq t \leq 20 \text{ ms} \quad (63)$$

which are piecewise constant functions changing every 200 ms. To obtain the spectral density of $N_1(t)$ at $t=0$, we first obtain the autocorrelation function which is defined by†

$$R_{N_1}(\tau) = \frac{1}{T} \int_{-T/2}^{T/2} E \left[N_1(t) N_1(t+\tau) \right] dt \quad (64)$$

† We take both the time and ensemble average so that the spectral density exists.

Now let us define $N_1(t)$ for all t to be

$$N_1(t) = \sum_{n=-\infty}^{\infty} N_1(n) p(t - nT) \quad (65)$$

where $p(t)$ is a pulse function equal to one when $-T/2 \leq t < T/2$ and is zero otherwise. Using (65) in (64) produces

$$R_{N_1}(\tau) = \frac{1}{T} \int_{-T/2}^{T/2} E \left[\sum_{n=-\infty}^{\infty} N_1(n) p(t - nT) \sum_{m=-\infty}^{\infty} N_1(m) p(t - mT + \tau) \right] dt \quad (66)$$

At $t=0$, we obtain

$$R_{N_1}(0) = \sigma_1^2 = E \left[N_1^2(0) \right] \quad (67)$$

Now at $t=T$, we have

$$R_{N_1}(T) = \frac{1}{T} \int_{-T/2}^{T/2} E \left[N_1(0) N_1(1) \right] dt = \sigma_1^2 \rho_{0,1} \quad (68)$$

at $t = -T$, we have

$$R_{N_1}(-T) = \frac{1}{T} \int_{-T/2}^{T/2} E \left[N_1(0) N_1(-1) \right] dt = \sigma_1^2 \rho_{0,-1}$$

Since the statistics are stationary at the sample points, we have $\rho_{0,-1} = \rho_{0,1} = \rho = 0$ from (63) and (65). To evaluate (67), we have

$$\sigma_1^2 = E \left[N_1^2(0) \right] = E \left[\left(\frac{N_Q^0}{\sqrt{PT}} + \frac{N_Q^{-1}}{\sqrt{PT}} \right)^2 \right] \quad (70)$$

or

$$\sigma_1^2 = \frac{N_0}{2PT} \quad (71)$$

since N_Q^0 and N_Q^{-1} are statistically independent of each other and since each term has variance $N_Q/4PT$. Now a random amplitude sequence such as $N_1(n)$ that is statistically independent from sample to sample spaced T seconds apart has a two-sided density at the origin given by

$$\mathcal{S}_{N_1}(0) = \int_{-T}^T R_{N_1}(\tau) d\tau \quad (72)$$

Clearly, $R_{N_1}(\tau)$ is linear between $\tau = 0$ and $\tau = \pm T$. Hence,

$$\mathcal{S}_{N_1}(0) = \sigma_1^2 T \quad (73)$$

since $R_{N_1}(0) = \sigma_1^2$. It follows from (60), (61), (71) and (73) that

$$\sigma_1^2 = \frac{N_Q B_{L\Sigma}}{P} \quad (74)$$

Now we consider the fourth term of (62). We consider evaluating $\mathcal{S}_{N_2}(0)$ in order to evaluate T_4 . We have from (50) that

$$N_2(t) = \frac{N_Q^{-1} (N_I^0 + N_I^{-2})}{PT^2} + \frac{N_Q^{-1}}{\sqrt{PT}} - \frac{N_I^{-1} (N_Q^0 + N_Q^{-2})}{PT^2} - \frac{N_Q^0 + N_Q^{-2}}{2\sqrt{PT}} \quad (75)$$

First we compute the variance which we denote by σ_2^2 . Since each term is statistically independent of each other and has zero mean, we have that

$$\begin{aligned} \text{Var}(N_2) = & \frac{E\left\{\left(N_Q^{-1}\right)^2 \left[\left(N_I^0\right)^2 + \left(N_I^{-2}\right)^2\right]\right\}}{P^2 T^4} + \frac{E\left\{\left(N_Q^{-1}\right)^2\right\}}{PT^2} \\ & + \frac{E\left\{\left(N_I^{-1}\right)^2 \left[\left(N_Q^0\right)^2 + \left(N_Q^{-2}\right)^2\right]\right\}}{P^2 T^4} + \frac{E\left\{\left(N_Q^0\right)^2 + \left(N_Q^{-2}\right)^2\right\}}{4PT^2} \end{aligned} \quad (76)$$

Since each term in the above products are statistically independent, we have

$$\text{Var}(N_2) = \frac{N_0^2}{4P^2T^2} + \frac{3}{8} \frac{N_0}{PT} = \sigma_{N_2}^2 \quad (77)$$

where we have used the fact that

$$E[(N_Q)^2] = E[(N_I)^2] = \frac{N_0}{4} T \quad (78)$$

for any of the I or Q noise terms. In general, to compute the spectral density of a correlated sequence, one must determine the Fourier transform of the autocorrelation function so that

$$S_{N_2}(0) = \int_{-\infty}^{\infty} R_{N_2}(\tau) d\tau \quad (79)$$

We must now determine $R_{N_2}(\tau)$ in order to evaluate (79) for the spectral density. Now consider evaluating

$$R_{N_2}(\tau) = E[N_2(t) N_2(t+\tau)] \quad (80)$$

we have

$$E[N_2(t) N_2(t+\tau)] = E \left\{ \left(\frac{N_Q^{-1}(N_I^0 + N_I^{-2})}{PT^2} + \frac{N^{-1}}{\sqrt{PT}} - \frac{N_I^{-1}(N_Q^0 + N_Q^{-2})}{PT^2} - \frac{N_Q^0 + N_Q^{-2}}{2\sqrt{PT}} \right) \right. \\ \left. \left(\frac{N_Q^{-3}(N_I^{-2} + N_I^{-4})}{PT^2} + \frac{N_Q^{-3}}{\sqrt{PT}} - \frac{N_I^{-3}(N_Q^{-2} + N_Q^{-4})}{PT^2} - \frac{N_Q^{-2} + N_Q^{-4}}{2\sqrt{PT}} \right) \right\} \quad (81)$$

Evaluating, we obtain

$$E[N_2(t) N_2(t+T)] = \frac{E(N_0^{-2})^2}{4PT^2} = \frac{N_0}{16PT} \quad (82)$$

By definition, this is equal to

$$R_{N_2}(T) = \sigma_{N_2}^2 \rho = \frac{N_0}{16PT} \quad (83)$$

Using (83) with (82) yields

$$\rho = \frac{1}{6 + 4 \frac{N_0}{PT}} \quad (84)$$

It follows that the autocorrelation function is as shown in Figure 4.6. Therefore, the spectral density from (79) is given by

$$S_{N_2}(0) = 2 \sigma_{N_2}^2 \int_0^T \left[1 - (1-\rho) \frac{\tau}{T} \right] d\tau + 2 \sigma_{N_2}^2 \int_T^{2T} \left[2\rho - \rho \frac{\tau}{T} \right] d\tau \quad (85)$$

Evaluating (85) yields

$$N_2(0) = T \sigma_{N_2}^2 (1 + 2\rho) \quad (86)$$

Hence from (62), (77), (84) and (86), we obtain

$$\sigma_{T_2}^2 = \left(\frac{3}{4} \frac{N_0}{P} + \frac{N_0^2}{2P^2T} \right) \left(1 + \frac{2}{6 + 4 \frac{N_0}{PT}} \right) B_{L\Delta} \quad (87)$$

ORIGINAL PAGE IS
OF POOR QUALITY

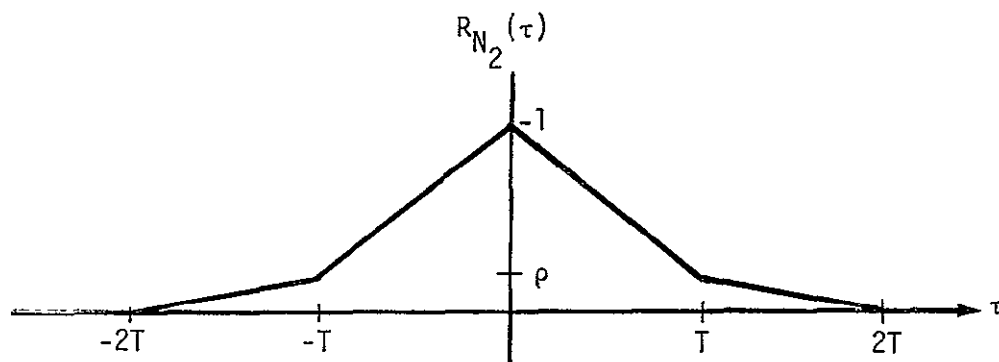


Figure 4.6. Autocorrelation Function for $N_2(t)$

Now consider the second term of equation (60). Hence, we need to evaluate

$$R_{N_2 N_1}(\tau) = E \left[N_2(t) N_1(t-\tau) \right] \quad (88)$$

First consider the case when $\tau=0$, then

$$\begin{aligned} R_{N_2 N_1}(0) &= \frac{1}{T} \int_{-T/2}^{T/2} E \left[N_2(t) N_1(t) \right] dt \\ &= E \left[\left(\frac{N_Q^{-1} (N_I^0 + N_I^{-2})}{PT^2} + \frac{N_Q^{-1}}{\sqrt{PT}} - \frac{N_I^{-1} (N_Q^0 + N_Q^{-2})}{PT^2} - \frac{(N_Q^0 + N_Q^{-2})}{2\sqrt{PT}} \right) \right. \\ &\quad \left. \times \left(\frac{N_Q^0}{\sqrt{PT}} + \frac{N_Q^{-1}}{\sqrt{PT}} \right) \right] \end{aligned} \quad (90)$$

After evaluating, we obtain

$$R_{N_2 N_1}(0) = \frac{-E \left\{ (N_Q^0)^2 \right\}}{2 PT^2} + \frac{E \left\{ (N_Q^{-1})^2 \right\}}{PT^2} \quad (91)$$

or

$$R_{N_2 N_1}(0) = \frac{N_0}{8PT} \quad (92)$$

Now consider $R_{N_2 N_1}(-T)$. We have

$$\begin{aligned} R_{N_2 N_1}(-T) &= E \left[\left(\frac{N_Q^{-1} (N_I^0 + N_I^{-2})}{PT^2} + \frac{N_Q^{-1}}{\sqrt{PT}} - \frac{N_I^{-1} (N_Q^0 + N_Q^{-2})}{PT^2} - \frac{N_Q^0 + N_Q^{-2}}{2\sqrt{PT}} \right) \right. \\ &\quad \left. \times \left(\frac{N_Q^{-2}}{\sqrt{PT}} + \frac{N_Q^{-3}}{\sqrt{PT}} \right) \right] \end{aligned} \quad (93)$$

After evaluating, we obtain

$$R_{N_2 N_1}(-T) = \frac{E\left\{\left(N_Q^{-2}\right)^2\right\}}{2PT^2} = -\frac{N_Q}{8PT} \quad (94)$$

Now we evaluate $R_{N_2 N_1}(T)$. We have

$$\begin{aligned} R_{N_2 N_1}(T) &= E\left\{N_2(t) N_1(t-T)\right\} \\ &= E\left\{N_2(t+T) N_1(t)\right\} \\ &= E\left\{\left(\frac{N_Q^{-3}\left(N_I^{-3} + N_I^{-4}\right)}{PT^2} + \frac{N_Q^{-3}}{\sqrt{PT}} - \frac{N_I^{-3}\left(N_Q^{-2} + N_Q^{-4}\right)}{PT^2} - \frac{\left(N_Q^{-2} + N_Q^{-4}\right)}{2\sqrt{PT}}\right)\right. \\ &\quad \left.\times\left(\frac{N_Q^0}{\sqrt{PT}} + \frac{N_Q^{-1}}{\sqrt{PT}}\right)\right\} \quad (95) \end{aligned}$$

so that

$$R_{N_2 N_1}(T) = 0 \quad (96)$$

Summarizing, we see that

$$R_{N_1 N_2}(\tau) = \begin{cases} 0 & \tau = T \\ \frac{N_Q}{8PT} & \tau = 0 \\ -\frac{N_Q}{8PT} & \tau = -T \end{cases} \quad (97)$$

Therefore, we deduce that the cross-correlation function is as shown in Figure 4.7 since $R_{N_1 N_2}(\pm 2T) = 0$. Clearly, the spectral density is zero at $f = 0$ since

$$\int_{-2T}^{2T} R_{N_1 N_2}(\tau) d\tau = 0 \quad (98)$$

It is also evident from (59) that

$$R_{N_1 N_2}(\tau) = R_{N_2 N_1}(-\tau) \quad (99)$$

and therefore

$$\int_{-2T}^{2T} R_{N_2 N_1}(\tau) d\tau = 0 \quad (100)$$

We conclude from (60), (74), (87), (98) and (100) that we have

$$\sigma_{\phi_1}^2 = \frac{N_0 B_{L_\Sigma}}{P} + \left(\frac{3}{4} \frac{N_0}{P} + \frac{N_0^2}{2P^2 T} \right) \left(1 + \frac{2}{6 + \frac{4N_0}{PT}} \right) B_{L_\Delta} \quad (101)$$

which is our first major result. This is the linearized (first-order) tracking-error variance of channel L_1 . For the cases $B_{L_\Sigma} = 10 B_{L_\Delta}$ and $B_{L_\Sigma} = 5B_{L_\Delta}$, $\sigma_{\phi_1}^2$ is compared with $N_0 B_{L_\Sigma}/P$, which is the ideal nontime-shared tracking-error variance in Table 4.1. Note that an ordinary time-sharing loss would yield 3 dB of degradation [2]. That is, let $PT/N_0 \rightarrow \infty$ and $B_{L_\Delta} = 5B_{L_\Sigma}$, then $\sigma_{\phi_1}^2 = 2 N_0 B_{L_\Sigma}/P$, yielding 3 dB of degradation.

Thus, we see that TI's scheme of differencing and summing the L_1 and L_2 signals yields a substantial recovery of the 3-dB time-sharing loss neglecting other factors such as delay and dynamics. Basically this reduction in L_1/L_2 multiplexing loss can be attributed to the fact that the difference loop filter can be made considerably narrower than the sum loop filter so that the overall noise can be cut roughly in half. It should be pointed out that the degradation in Table 4.1 is relative to the situation in which it is assumed that the same bandwidth loop filter for tracking $\phi_1^{(t)} + \phi_2^{(t)}$ is required for tracking either $\phi_1(t)$ or $\phi_2(t)$.

ORIGINAL PAGE IS
OF POOR QUALITY

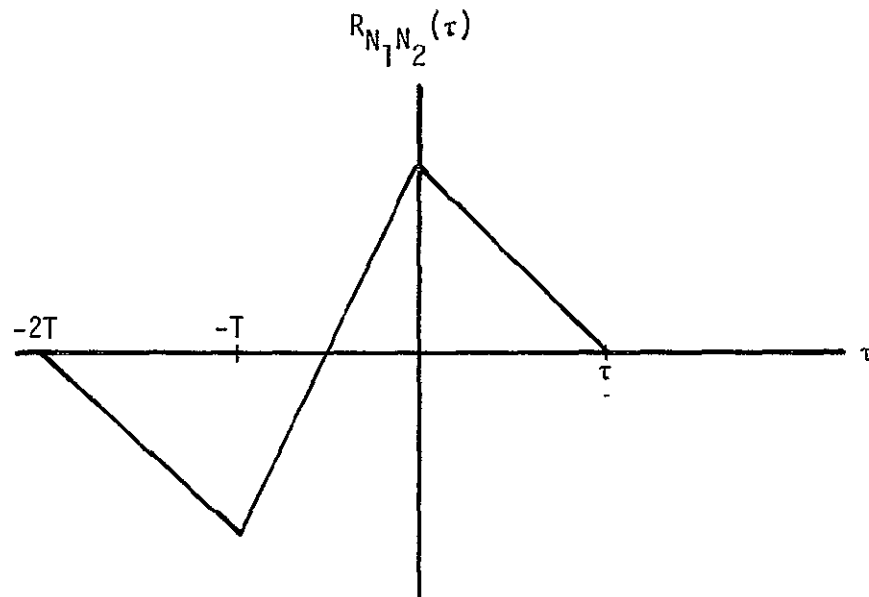


Figure 4.7. Cross-Correlation Function $R_{N_1 N_2}(\tau)$

Table 4.1. Degradation from Ideal Nontime-Shared Loop

$\frac{PT}{N_0}$ (dB)	Degradation $B_{L_\Sigma} = 10 B_{L_\Delta}$	Degradation $B_{L_\Sigma} = 5 B_{L_\Delta}$
-3	0.8	1.46
0	0.6	1.14
3	0.51	0.97
4.9	0.48	0.91
6	0.46	0.88
10	0.43	0.83

In general, this would not be the case; in other words, a larger bandwidth would be needed to track $\phi_1(t) + \phi_2(t)$ than either one individually, which would therefore increase the degradation values in Table 4.1.

Now consider the loss on channel L_2 . From (47) and (48), we have (again neglecting the overbars for convenience)

$$Y_{\phi_2} = K_\Sigma F_\Sigma(s) \epsilon_\Sigma^1 - K_\Delta F_\Delta(s) \epsilon_\Delta^1 \quad (102)$$

or

$$\begin{aligned}
 Y_{\phi_2} = \frac{PT^2}{2} & \left[\cancel{K_\Sigma F_\Sigma(s) \phi_1} + K_\Sigma F_\Sigma(s) \phi_2 + K_\Sigma F_\Sigma(s) \frac{2N_Q^0}{\sqrt{PT}} + K_\Sigma F_\Sigma(s) \frac{2N_Q^{-1}}{\sqrt{PT}} \right. \\
 & - \cancel{K_\Delta F_\Delta(s) \phi_1} + K_\Delta F_\Delta(s) \phi_2 - K_\Delta F_\Delta(s) \frac{2N_Q^{-1}(N_I^0 + N_I^{-2})}{PT^2} \\
 & \left. - K_\Delta F_\Delta(s) \frac{2N_Q^{-1}}{\sqrt{PT}} + K_\Delta F_\Delta(s) \frac{2N_I^{-1}(N_I^0 + N_Q^{-2})}{PT^2} + K_\Delta F_\Delta(s) \frac{(N_Q^0 + N_Q^{-2})}{\sqrt{PT}} \right] \quad (103)
 \end{aligned}$$

Hence, we have

$$\begin{aligned}
 Y_{\phi_2} = PT^2 & \left[\frac{K_{\Sigma F_{\Sigma}}(s) + K_{\Delta F_{\Delta}}(s)}{2} \phi_2 + \overbrace{K_{\Sigma F_{\Sigma}}(s) N_1}^{K_{\Sigma F_{\Sigma}}(s) N_1} \frac{N_Q^0}{\sqrt{PT}} + K_{\Sigma F_{\Sigma}}(s) \frac{N_Q^{-1}}{\sqrt{PT}} \right. \\
 & \left. - \overbrace{K_{\Delta F_{\Delta}}(s) N_2}^{K_{\Delta F_{\Delta}}(s) N_2} \frac{N_Q^{-1} (N_I^0 + N_I^{-2})}{PT^2} - K_{\Delta F_{\Delta}}(s) \frac{N_Q^{-1}}{\sqrt{PT}} \right. \\
 & \left. + K_{\Delta F_{\Delta}}(s) \frac{N_I^{-1} (N_Q^0 + N_Q^{-2})}{PT^2} + K_{\Delta F_{\Delta}}(s) \left(\frac{N_Q^0 + N_Q^{-2}}{2\sqrt{PT}} \right) \right] \quad (104)
 \end{aligned}$$

Now let

$$\hat{\theta}_2 = \frac{1}{s} \frac{Y_{\phi_2}}{PT^2} \quad (105)$$

or

$$\hat{\theta}_2 = \frac{1}{s} \left[\frac{K_{\Sigma F_{\Sigma}}(s) + K_{\Delta F_{\Delta}}(s)}{2} \phi_2 + K_{\Sigma F_{\Sigma}}(s) N_1(t) + K_{\Delta F_{\Delta}}(s) N_2(t) \right] \quad (106)$$

where

$$N_1(t) = \frac{N_Q^0}{\sqrt{PT}} + \frac{N_Q^{-1}}{\sqrt{PT}} \quad (107)$$

and

$$N_2(t) = \frac{-N_Q^{-1} (N_I^0 + N_I^{-2})}{PT^2} - \frac{N_Q^{-1}}{\sqrt{PT}} + \frac{N_I^{-1} (N_Q^0 + N_Q^{-2})}{PT^2} + \frac{N_Q^0 + N_Q^{-2}}{2\sqrt{PT}} \quad (108)$$

By comparing (107) and (108) with (63) and (75), we see that the noise terms are the same, hence, L_2 suffers the same degradation as channel 1. Also, the loop bandwidth tracking is the same as L_2 , i.e., $\sigma_{\phi_1} = \sigma_{\phi_2}$.

ORIGINAL PAGE IS
OF POOR QUALITY

Basically the method discussed here and used by TI is composed of two loop filters, i.e., the sum filter and the difference filter, which may be of different orders but must be equal over the bandwidth of either $\phi_2(t)$ or $\phi_1(t)$. For comparison purposes, we consider two second-order loop filters. Let

$$K_{\Sigma} F_{\Sigma}(s) = 2\zeta_{\Sigma} \omega_{n_{\Sigma}} + \frac{\omega_{n_{\Sigma}}^2}{s} \quad \zeta_{\Sigma} = \zeta \quad (109)$$

and

$$K_{\Delta} F_{\Delta}(s) = \sqrt{2} \omega_{n_{\Delta}} + \frac{\omega_{n_{\Delta}}^2}{s} \quad \zeta_{\Delta} = \frac{1}{\sqrt{2}} \quad (110)$$

From (49), we must have that

$$K_{\Sigma} F_{\Sigma}(s) = K_{\Delta} F_{\Delta}(s) \quad (111)$$

over the bandwidth of $\phi_1(t)$ and $\phi_2(t)$. From (109), (110) and (111), it follows that we must have

$$\omega_{n_{\Sigma}}^2 = \omega_{n_{\Delta}}^2 = \omega_n^2 \quad (112)$$

Since $\sigma_{\phi_1}^2$ and $\sigma_{\phi_2}^2$ depend upon both $B_{L_{\Sigma}}$ and $B_{L_{\Delta}}$ from (101), as defined in (61) and (62), we now desire that $B_{L_{\Sigma}} \gg B_{L_{\Delta}}$. Using (109) and (110) with (112), we write

$$K_{\Sigma} F_{\Sigma}(s) = 2\zeta \omega_n + \frac{\omega_n^2}{s} \quad (113)$$

$$K_{\Delta} F_{\Delta}(s) = \sqrt{2} \omega_n + \frac{\omega_n^2}{s} \quad (114)$$

where we have let $\zeta_{\Sigma} = \zeta$ and $\zeta_{\Delta} = 1/\sqrt{2}$. Using (54) and (55), we have

$$H'(s) = \frac{2\zeta \omega_n s + \omega_n^2}{s^2 + \omega_n^2 + \left(\zeta + \frac{1}{\sqrt{2}}\right) \omega_n s} \quad (115)$$

Evaluating the closed-loop bandwidth, we obtain [see (61)]

$$2B_{L_{\Sigma}} = \frac{\omega_n (1 + 4\zeta^2)}{2\left(\zeta + \frac{1}{\sqrt{2}}\right)} \quad (116)$$

In a similar manner, we have

$$H''(s) = \frac{\sqrt{2} \omega_n s + \omega_n^2}{s^2 + \omega_n^2 + \left(\zeta + \frac{1}{\sqrt{2}}\right) \omega_n s} \quad (117)$$

and

$$2B_{L_{\Delta}} = \frac{3\omega_n}{2\left(\zeta + \frac{1}{\sqrt{2}}\right)} \quad (118)$$

We note that only the numerators differ between $H'(s)$ and $H''(s)$. We may plot the ratio $B_{L_{\Sigma}}$ to $B_{L_{\Delta}}$ to see what value of ζ will yield a ratio of, say, 5 or 10; Table 4.2 does just that. Hence, we see that picking a damping factor of $\zeta = 1.87$ yields $B_{L_{\Sigma}}/B_{L_{\Delta}} = 5.0$ and $\zeta = 2.69$ yields $B_{L_{\Sigma}}/B_{L_{\Delta}} = 10.0$. Thus, any reasonable bandwidth ratio can be handled with reasonable damping factors using second-order loop filters.

4.4 Response to Dynamics

In this section, we consider the response of the L_1 and L_2 loops to dynamics. Letting the noise terms be zero, we have, from (51), that

$$\hat{\theta}_1 = \frac{K_{\Delta} F_{\Delta}(s) + K_{\Sigma} F_{\Sigma}(s)}{2} \left(\frac{1}{s}\right) \phi_1 \quad (119)$$

Since

$$\phi_1 = \theta_1 - \hat{\theta}_1 \quad (120)$$

we have that

$$\hat{\theta}_1 = \frac{\frac{K_{\Delta} F_{\Delta}(s) + K_{\Sigma} F_{\Sigma}(s)}{2s}}{1 + \frac{K_{\Delta} F_{\Delta}(s) + K_{\Sigma} F_{\Sigma}(s)}{2s}} \quad (121)$$

ORIGINAL PAGE IS
OF POOR QUALITY

Table 4.2. Results for $\frac{B_{L\Sigma}}{B_{L\Delta}} = \frac{1 + 4\zeta^2}{3}$

ζ	$\frac{B_{L\Sigma}}{B_{L\Delta}}$
0.1	0.35
0.2	0.39
0.3	0.45
0.4	0.55
0.5	0.67
0.6	0.81
0.7	0.99
0.707	1.0
0.8	1.19
0.9	1.41
1.0	1.67
1.2	2.25
1.4	2.95
1.6	3.75
1.9	4.65
2.0	5.67
2.25	7.00
2.50	8.67
2.75	10.42
3.0	12.33
4.0	21.67
5.0	33.67

and therefore the transfer function (overall) of the L_1 channel is composed of a loop filter which is the average of the sum loop filter and the difference loop filter. From (106), it follows that the transfer function of the L_2 channel is identical to that of the L_1 channel.

Therefore, if the difference loop filter is much narrower than the sum loop filter, the overall L_1 and L_2 closed-loop response would be roughly equivalent to a loop with the average of the sum and difference loop bandwidths. Consequently, the performance in dynamics of this combined loop would not be as good as a loop designed for L_1 or L_2 separately. Of course, this latter loop would pass more noise to the carrier phase estimate.

4.5 Delay Effects on the Carrier Loop

In this section, we wish to determine how delay in the loop affects the tracking performance. For convenience, consider an analog Costas loop which is a simplified model of the TI carrier-tracking loop for L_1 or L_2 illustrated in Figure 4.8.

In order to determine the closed-loop transfer function, the integrator will be modeled as an ideal delay of τ_1 seconds to the signal. Let the received signal be of the form

$$y(t) = \sqrt{2} P d(t) \sin(\omega_0 t + \theta) + \sqrt{2} n_c(t) \cos(\omega_0 t + \theta) + \sqrt{2} n_s(t) \sin(\omega_0 t + \theta) \quad (122)$$

Out of the upper and lower integrators, we have

$$\begin{aligned} I(T) &= \sqrt{P} d(T) \left[e^{-\tau_1 S} \cos \phi \right] - N_c(T) \sin \phi + N_s(T) \cos \phi \\ Q(T) &= \sqrt{P} d(T) \left[e^{-\tau_1 S} \sin \phi \right] + N_c(T) \cos \phi + N_s(T) \sin \phi \end{aligned} \quad (123)$$

where

$$\begin{aligned} N_c(T) &= \int_0^T n_c(t) dt \\ N_s(T) &= \int_0^T n_s(t) dt \end{aligned} \quad (124)$$

ORIGINAL PAGE IS
OF POOR QUALITY

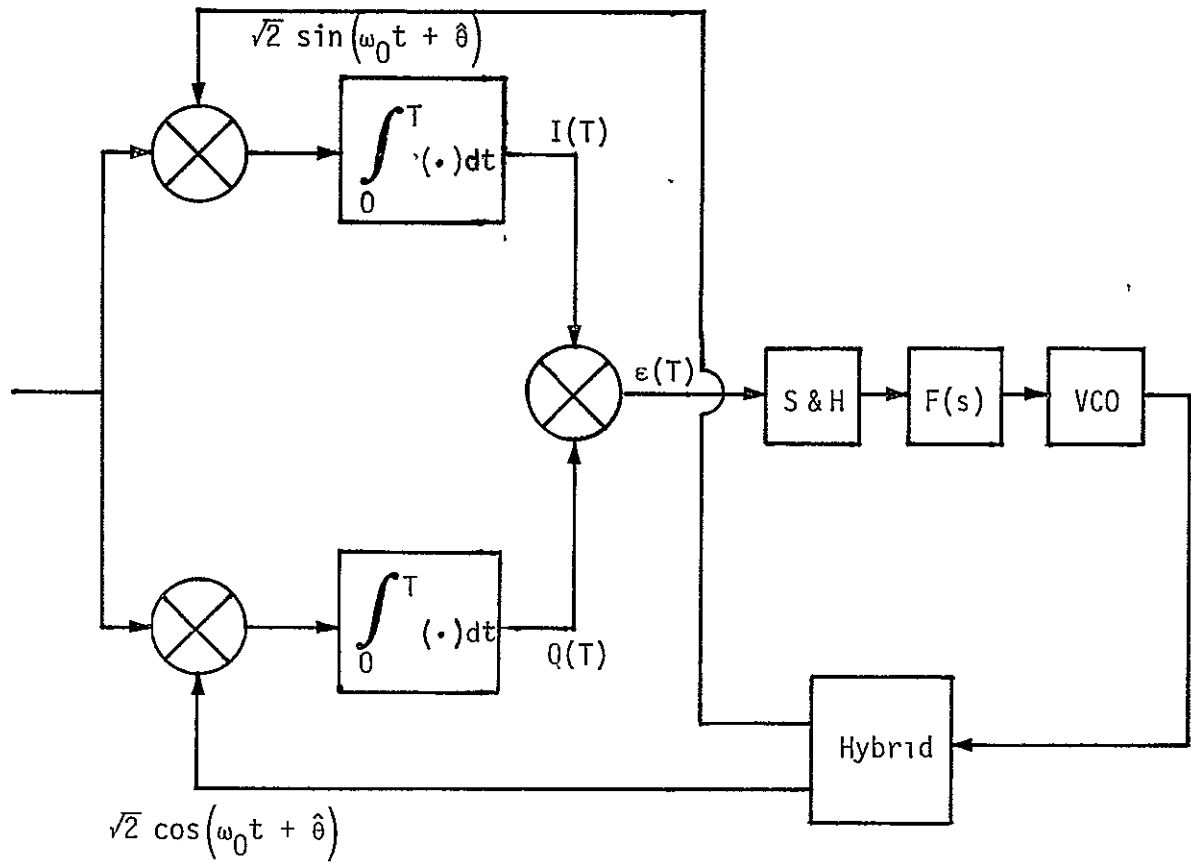


Figure 4 8 Costas Loop Model with I&D Arm Filters

and $d(T)$ denotes the value of the data symbol (± 1) just prior to a transition, i.e., at $t = T^-$. As is common practice, $F(s)g(t)$ denotes the Heaviside operator $F(s)$ operating on the time function $g(t)$. $F(s)$ is also numerically equal to a function of the Laplace variable s . For example, in (123), $F(s) = e^{-\tau_1 s}$ and $g(t) = \cos[\phi(t)]$.

It can be shown that the I and Q noise terms are independent so that, for simplicity, we write

$$\begin{aligned} I(T) &= \sqrt{P} d(T) + N_I(T) \\ Q(T) &= \sqrt{P} d(T) \left[e^{-\tau_1 s} \sin\phi \right] + N_Q(T) \end{aligned} \quad (125)$$

For high SNR

$$\sin\phi \approx \phi$$

and

$$\cos\phi \approx 1 \quad (126)$$

so that the error signal is given by

$$\epsilon(T) = P \left[e^{-\tau_1 s} \phi \right] + \sqrt{P} d(T) \left[e^{-\tau_1 s} \phi \right] N_I(T) + \sqrt{P} d(T) N_Q(T) + N_I(T) N_Q(T) \quad (127)$$

After grouping all the noise terms together and calling them $N(T)$, we have

$$\epsilon(T) = P \left[e^{-\tau_1 s} \phi \right] + N(T) \quad (128)$$

Modeling the sample-and-hold as a τ_2 -second delay yields for the phase estimate

$$\hat{\theta}(t) = \frac{KPF(s)e^{-\tau_1 s} e^{-\tau_2 s} \phi}{s} + \frac{KF(s)e^{-(\tau_1 + \tau_2)s} N(T)}{s} \quad (129)$$

where $F(s)$ is the loop filter transfer function and is assumed to be of the form $\omega_n^2 \left(1 + \frac{2\zeta}{\omega_n} s\right)$, corresponding to a second-order loop. Using the fact that

$$\phi = \theta - \hat{\theta} \quad (130)$$

produces

$$\left\{1 + \frac{KP}{s} F(s) e^{-\tau s}\right\} \phi = \frac{KPF(s) e^{-\tau s} \frac{N(T)}{P}}{s} \quad (131)$$

with $\tau = T_1 + T_2$. Solving for $\phi(t)$ yields

$$\phi(t) = \frac{-KPF(s) e^{\tau s} \frac{N(T)}{s}}{s + KPF(s) e^{-\tau s}} = H(s) \frac{N(T)}{P} \quad (132)$$

The corresponding phase error variance is given by

$$\sigma_\phi^2 = \frac{N_0'}{2} (2B_L) \quad (133)$$

where

$$2B_L = \int_{-\infty}^{\infty} |H(j\omega)|^2 \frac{d\omega}{2\pi} \quad (134)$$

N_0' is the one-sided noise spectral density, and $H(j\omega)$ is $H(s)$, the closed-loop transfer function evaluated at $s = j\omega$. Since the noise term for small ϕ is essentially independent of the delay τ , we consider the closed-loop bandwidth B_L as a function of τ only. Now

$$H(j\omega) = \frac{\left[1 + \frac{2\zeta}{\omega_n} j\omega\right] e^{j\omega\tau}}{\left[-\frac{\omega^2}{\omega_n^2} + 2j\zeta \frac{\omega}{\omega_n} e^{-j\omega\tau} + e^{-j\omega\tau}\right]} \quad (135)$$

where ζ is the loop damping factor and ω_n is the loop natural frequency. Simplifying, we obtain from (135)

$$2B_L = \int_{-\infty}^{\infty} \frac{\left[1 + \frac{4\zeta^2 \omega^2}{\omega_n^2}\right] \frac{d\omega}{2\pi}}{\left[-\left(\frac{\omega}{\omega_n}\right)^2 + 2\zeta \frac{\omega}{\omega_n} \sin \tau\omega + \cos \tau\omega\right]^2 + \left[2\zeta \frac{\omega}{\omega_n} \cos \tau\omega - \sin(\tau\omega)\right]^2} \quad (136)$$

It is convenient to parameterize the expression by the normalized variable $B_{L0}\tau$, where B_{L0} is the value of B_L when $\tau=0$. Figures 4.9 through 4.12 illustrate the ratio of B_L/B_{L0} as a function of $B_{L0}\tau$. Notice that, at a value of $B_{L0}\tau$ near 0.4, the bandwidth becomes unbounded due to internal loop delay.

Now that we have determined the effect of delay on loop performance as far as bandwidth expansion is concerned, we turn to the question of stability. From (132), the open-loop transfer function is given by

$$OL(s) = \frac{KP}{s} F(s) e^{-\tau s} \quad (137)$$

Again using the transfer function

$$F(s) = \omega_n^2 \frac{\left(1 + \frac{2\zeta s}{\omega_n}\right) e^{-\tau s}}{s^2} \quad (138)$$

The point at which the loop becomes unstable occurs when

$$OL(s) = -1 \quad (139)$$

Expressing (137) and (139) in complex form yields

$$\frac{\omega_n^2}{\omega^2} = \sqrt{1 + \frac{4\zeta^2}{\omega_n^2} \omega^2} = 1 \quad (140)$$

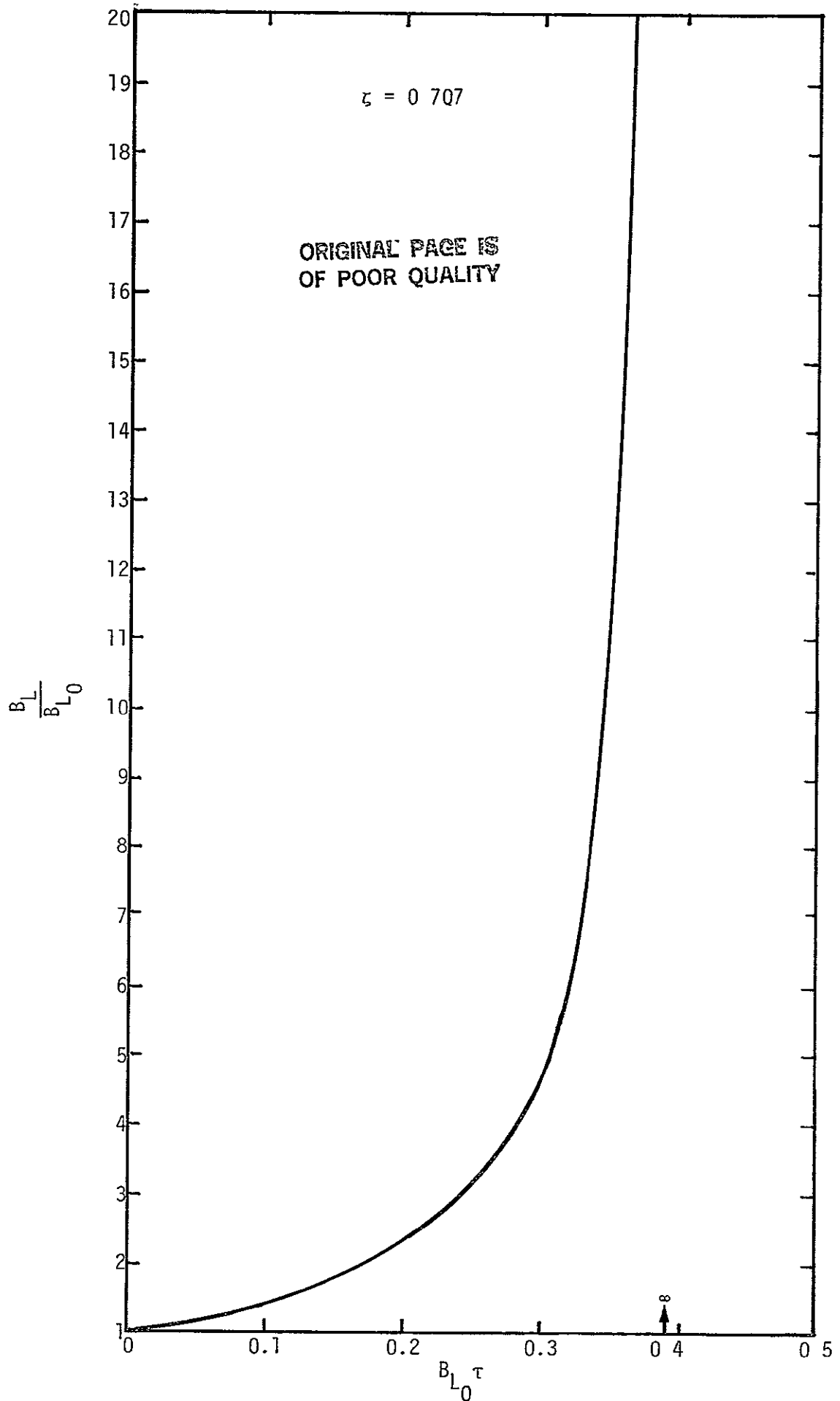


Figure 4.9 Closed-Loop Bandwidth Expansion with Delay

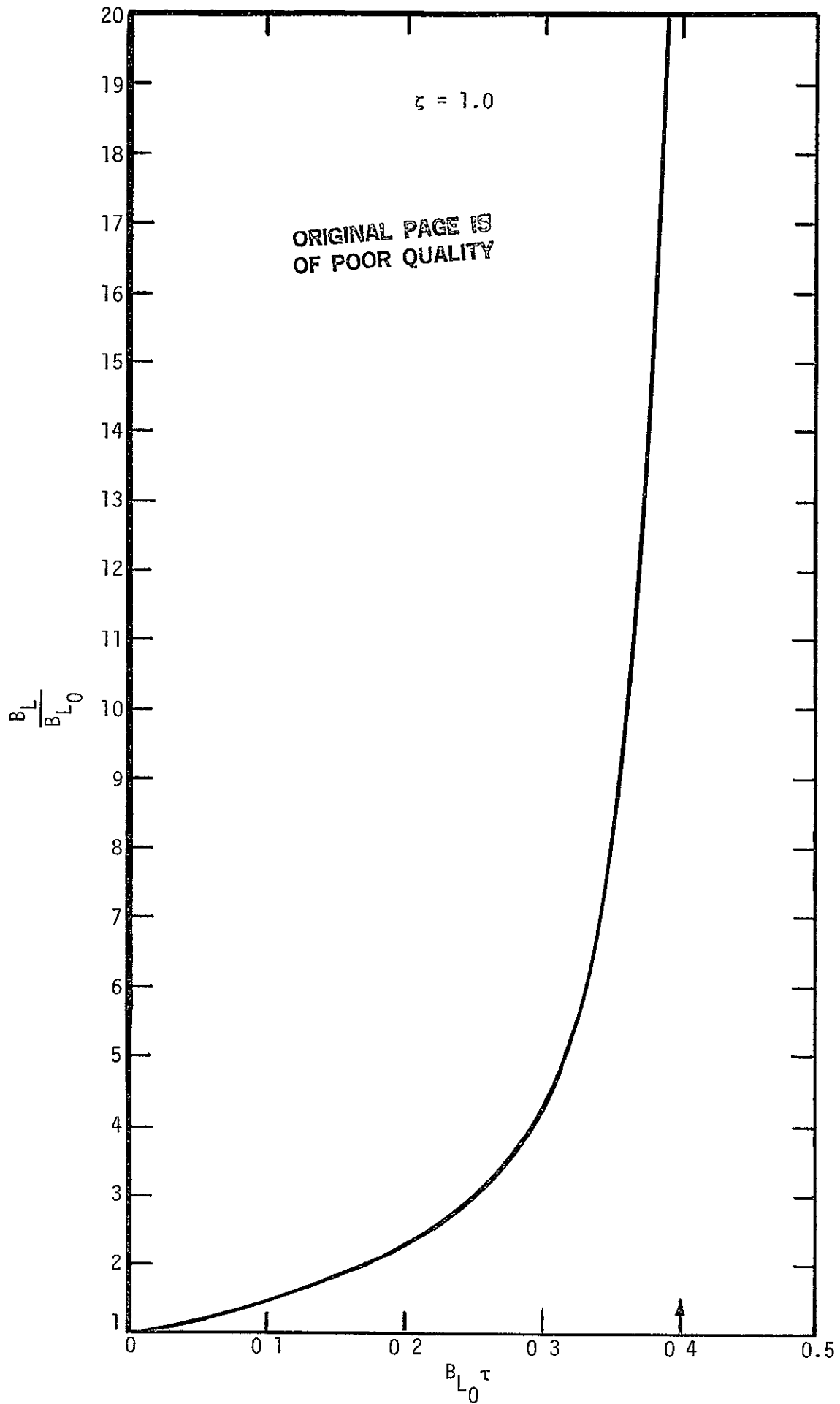


Figure 4.10. Closed-Loop Bandwidth Expansion with Delay

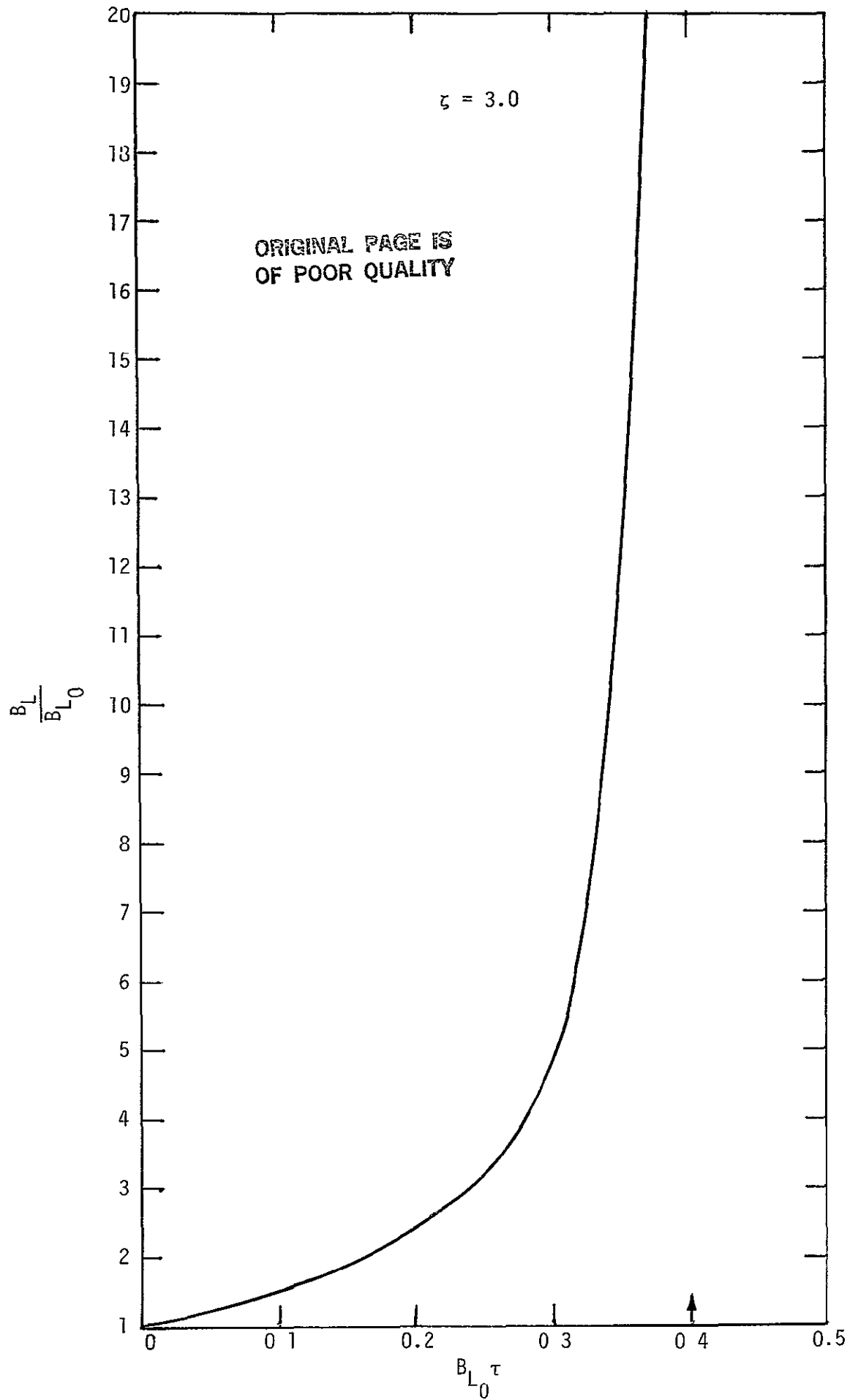


Figure 4.11. Closed-Loop Bandwidth Expansion with Delay

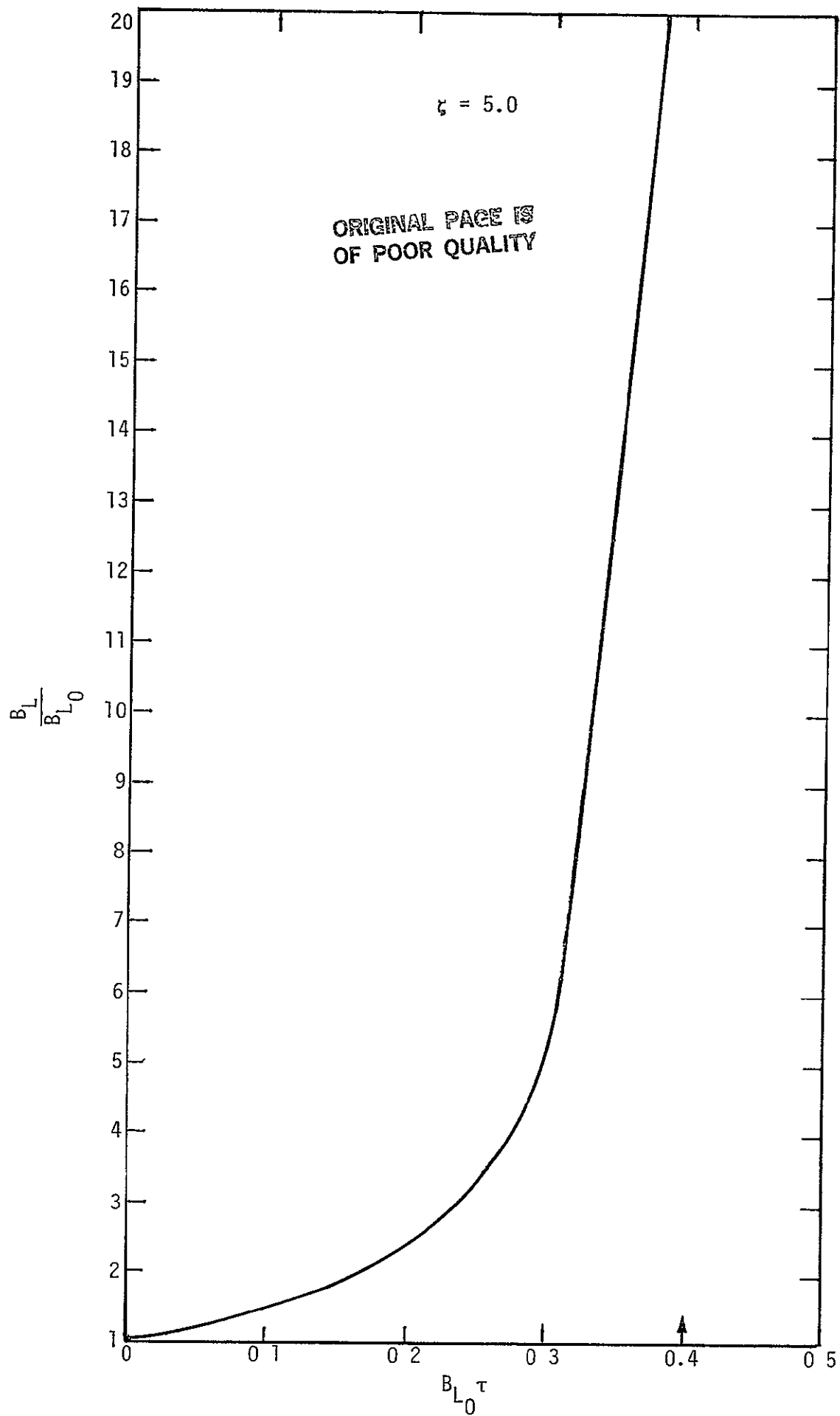


Figure 4 12 Closed-Loop Bandwidth Expansion with Delay

$$\tan^{-1} \left(\frac{2\zeta\omega}{\omega_n} \right) - \tau\omega = 0, 2\pi, 4\pi, \dots \quad (141)$$

To solve (140) and (141), we first square (140) to yield

$$\frac{\omega_n}{\omega^4} \left(1 + \frac{4\zeta^2}{\omega_n^2} \omega^2 \right) = 1 \quad (142)$$

Rearranging (142), we obtain

$$x^2 + 4\zeta^2 x - 1 = 0 \quad (143)$$

where

$$x = \left(\frac{\omega_n}{\omega} \right)^2 \quad (144)$$

The only positive root of (143) is given by

$$\left(\frac{\omega_n}{\omega} \right)^2 = x_1 = 2\zeta^2 + \sqrt{4\zeta^4 + 1} \quad (145)$$

Using the value of $\frac{\omega}{\omega_n}$ given by (145) in (141) yields

$$\tan^{-1} \left[\frac{2\zeta}{-2\zeta^2 + \sqrt{4\zeta^4 + 1}} \right] = \tau\omega_{N0} \left[\frac{1}{\sqrt{-2\zeta^2 + \sqrt{4\zeta^4 + 1}}} \right] \quad (146)$$

from which $\tau\omega_{N0}$ can be obtained for a given value of ζ . For a second-order loop, we have

$$2B_{L0} = \omega_{n0} \left[\zeta + \frac{1}{4\zeta} \right] \quad (147)$$

Therefore,

$$\tau_{B_{L_0}} = \frac{\tan^{-1} \left[\frac{2\zeta}{-2\zeta^2 + \sqrt{4\zeta^4 + 1}} \right]}{2 \sqrt{\frac{1}{-2\zeta^2 + \sqrt{4\zeta^4 + 1}}}} \left[\zeta + \frac{1}{4\zeta} \right] \quad (148)$$

Numerical evaluation yields the results of Table 4.3.

Thus we see that, within the accuracy of the curves (Figures 4.9-4.12), the point at which delay causes loop instability is the same as the point where the loop bandwidth becomes unbounded (Table 4.3).

Now apply these results to our loop of Figure 4.5. The average delay of the loop is

$$\frac{40 \text{ ms}}{2} + \frac{20 \text{ ms}}{2} = 30 \text{ ms} \quad (149)$$

Therefore, the closed-loop bandwidth required to yield a 20% increase in tracking jitter due to delay satisfies the constraint (using Figure 4.9)

$$B_{L_0}(0.03) \leq 0.1 \quad (150)$$

or

$$B_{L_0} \leq 3.3 \text{ Hz} \quad (151)$$

In fact, at $B_{L_0} = 13.3 \text{ Hz}$, the simplified delay model predicts that the loop becomes unstable. We conclude from this approximate analysis that the digital implementation limits the allowable carrier loop bandwidth.

Table 4.3. Normalized τB_{L_0} to Achieve Instability versus Damping Factor

ζ	τB_{L_0}
0.707	0.44
1	0.44
3	0.40
5	0.40
∞	0.39

4.6 Conclusions

The claim by TI that their L_1/L_2 carrier-loop processing scheme does not lose any of the 3-dB time-sharing loss appears to be a little ambitious. Calculations in this report proved that 0.5 dB to 1.0 dB is lost without considering two additional sources of degradation, namely, stability and dynamics. The first is the delay in the loop covered in the last section due to both TI's algorithm and the 50-Hz sampling rate. This delay effect could be anywhere from very critical to negligible, depending upon the time-delay/loop bandwidth product. Another effect is the fact that the loop bandwidth required to track the sum dynamics (L_1 plus L_2) could well be on the order of 1.5 dB wider than that which would be required for tracking L_1 or L_2 alone. The result of the above losses seems to indicate that there is perhaps a 1-dB advantage for their scheme, not 3 dB as claimed. The actual values depend upon the loop bandwidths, dynamics, etc. It should be noted that phase noise was not considered in the analysis, however, it is not anticipated that it should be a special problem.

The basic idea of processing the sum and difference channels appears to be a clever approach. Under certain conditions, it might well be possible to realize 2 dB of the 3-dB time-sharing loss and, as such, is an appreciable advantage

It is also to be pointed out that, when time-sharing L_1/L_2 , a 3-dB loss in data bit error rate performance occurs. Further, when time-sharing more than one satellite, an additional multiplexing loss of $10 \log(N)$ dB occurs, where N is the number of satellite channels.

Finally, it was established that, as far as tracking dynamics is concerned, the closed-loop response of either the L_1 or L_2 channel was determined by a loop filter that is the average of the sum loop filter and the difference loop filter.

In summary, in order to predict a precise L_1/L_2 multiplexing loss, it is necessary to know the exact dynamics of the signals as well as phase noise characteristics.

5.0 TEXAS INSTRUMENTS' GPS TRACKING DISCRIMINATOR
FOR L₁ AND L₂ CODE TRACKING

In this section, the Texas Instruments (TI) GPS code-tracking loop error signal is discussed. The L₁ and L₂ signals are time-shared, as are the early and late code timing. Sum and difference signals are processed separately, then added and subtracted to yield the error control of the L₁ and L₂ signals.

The TI code-tracking loop is capable of simultaneously tracking the L₁ and L₂ signals. This is accomplished by time-sharing between the L₁ and L₂ channels and simultaneously generating early and late code error signals from which the loop error signals are generated.

Figure 5 1, a TI viewgraph used for a briefing [3], shows how the L₁, L₂, early and late signals are processed. The square wave under the "sum loop error algorithm" in the figure indicates that L₁ and L₂ signals are alternately switched in, however, the early (E) and late (L) time-sharing is of the form E, L, L, E, then L, E, E, L, then E, L, L, E, etc.

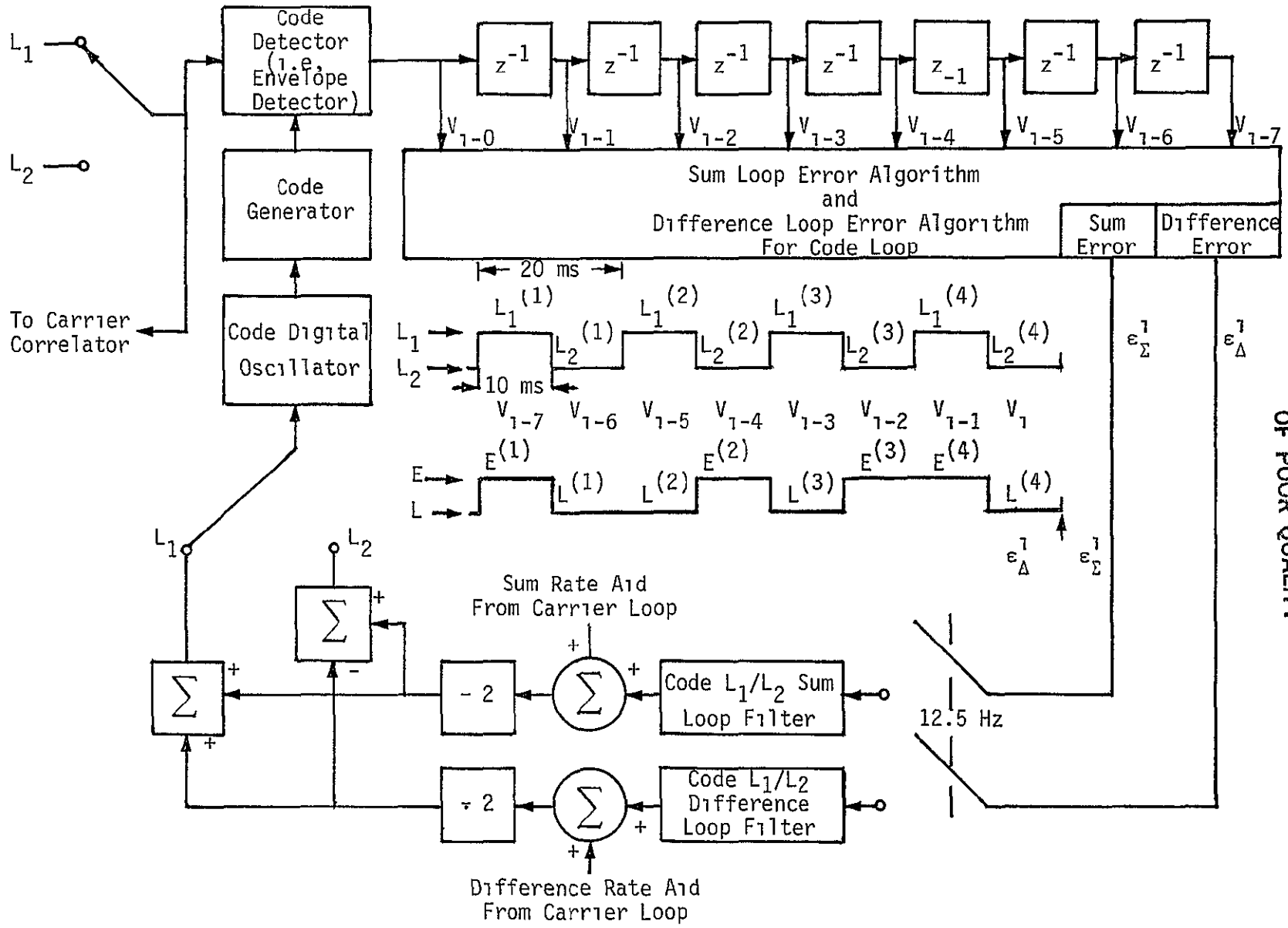
Two signals are processed simultaneously in two distinct loop filters. One is the L₁/L₂ sum signal (ϵ_{Σ}^1) and the other is the L₁/L₂ difference signal (ϵ_{Δ}^1). These two signals are given in (152) and (153).

$$\epsilon_{\Sigma}^1 = \frac{(V_{1-5} + V_{1-3}) - (V_{1-7} + V_{1-1})}{(V_{1-5} + V_{1-3}) + (V_{1-7} + V_{1-1})} + \frac{(V_{1-6} + V_1) - (V_{1-4} + V_{1-2})}{(V_{1-6} + V_1) + (V_{1-4} + V_{1-2})} \quad (152)$$

$$\epsilon_{\Delta}^1 = \frac{(V_{1-5} + V_{1-3}) - (V_{1-7} + V_{1-1})}{(V_{1-5} + V_{1-3}) + (V_{1-7} + V_{1-1})} + \frac{(V_{1-6} + V_1) - (V_{1-4} + V_{1-2})}{(V_{1-6} + V_1) + (V_{1-4} + V_{1-2})} \quad (153)$$

with the V_{1-j} (j=0, ..,7) being successive samples of signal-plus-noise.

If we related (152) and (153) in terms of the L₁ and L₂ channels and the early and late channels, we would have



ORIGINAL PAGE IS
OF POOR QUALITY

Figure 5.1. Code Sum and Difference Tracking Loops

$$\begin{aligned} \epsilon_{\Sigma}^1 &= \frac{(L_1^{(2)}L^{(2)} + L_1^{(3)}L^{(3)}) - (L_1^{(1)}E^{(1)} + L_1^{(4)}E^{(4)})}{(L_1^{(2)}L^{(2)} + L_1^{(3)}L^{(3)}) + (L_1^{(1)}E^{(1)} + L_1^{(4)}E^{(4)})} \\ &+ \frac{(L_2^{(1)}L^{(1)} + L_2^{(4)}L^{(4)}) - (L_2^{(2)}E^{(2)} + L_2^{(3)}E^{(3)})}{(L_2^{(1)}L^{(1)} + L_2^{(4)}L^{(4)}) + (L_2^{(2)}E^{(2)} + L_2^{(3)}E^{(3)})} \end{aligned} \quad (154)$$

$$\begin{aligned} \epsilon_{\Delta}^1 &= \frac{(L_1^{(2)}L^{(2)} + L_1^{(3)}L^{(3)}) - (L_1^{(1)}E^{(1)} + L_1^{(4)}E^{(4)})}{(L_1^{(2)}L^{(2)} + L_1^{(3)}L^{(3)}) + (L_1^{(1)}E^{(1)} + L_1^{(4)}E^{(4)})} \\ &- \frac{(L_2^{(1)}L^{(1)} + L_2^{(4)}L^{(4)}) - (L_2^{(2)}E^{(2)} + L_2^{(3)}E^{(3)})}{(L_2^{(1)}L^{(1)} + L_2^{(4)}L^{(4)}) + (L_2^{(2)}E^{(2)} + L_2^{(3)}E^{(3)})} \end{aligned} \quad (155)$$

In the above equations, the superscript denotes the time sequence of the early and late or L_1 and L_2 samples, as shown in Figure 5.1. Now notice that the outputs denoted by L_1 and L_2 in Figure 5.1 are given by

$$L_2: \quad \epsilon_{\Sigma}^1 - \epsilon_{\Delta}^1 = -2 \frac{(L_2^{(1)}L^{(1)} + L_2^{(4)}L^{(4)}) - (L_2^{(2)}E^{(2)} + L_2^{(3)}E^{(3)})}{(L_2^{(1)}L^{(1)} + L_2^{(4)}L^{(4)}) + (L_2^{(2)}E^{(2)} + L_2^{(3)}E^{(3)})} \quad (156)$$

$$L_1: \quad \epsilon_{\Sigma}^1 + \epsilon_{\Delta}^1 = 2 \frac{(L_1^{(2)}L^{(2)} + L_1^{(3)}L^{(3)}) - (L_1^{(1)}E^{(1)} + L_1^{(4)}E^{(4)})}{(L_1^{(2)}L^{(2)} + L_1^{(3)}L^{(3)}) + (L_1^{(1)}E^{(1)} + L_1^{(4)}E^{(4)})} \quad (157)$$

Notice that (156) contains L_2 samples only and (157) contains L_1 samples only so that the two error signals are separated. Further, the numerator of each expression contains a late detected signal minus and early detected signal, which is the normal code-tracking loop error signal. However, this error in both the L_1 and L_2 tracking cases is normalized by the sum of the late and early terms. This normalization would tend to act as an AGC to keep the loop bandwidth relatively constant.

It is to be noted, however, that in [7], J. D. Holmes and S. R. Buddles of TI describe the same algorithm for code tracking but indicate that the denominator is filtered in a one-pole recursive lowpass

filter. It is the author's feeling that substantial filtering of the denominator of (156) and (157) would be desirable since, in effect, the denominator term tends to keep signal gain nearly constant if it is heavily filtered.

6.0 GPS TIME-SHARING CODE-TRACKING PERFORMANCE LOSSES

It is shown in this section that the effect of time-sharing, for an analog code-tracking loop under the assumption that the loop bandwidth is much less than the time-sharing rate which in turn is much less than the data rate, is to suffer a loss of the form

$$L = 10 \log (d_F)$$

where d_F is the on-time duty factor of the code loop. For example, when the loop is on one-quarter of the time, the loss is 6 dB. This result also holds for other loops, such as carrier loops.

6.1 Analysis

The point of this analysis of a time-shared or time-gated code-tracking loop is to theoretically ascertain the time-sharing loss in a code-tracking loop. For example, in a TI GPS system implementation, four satellites are typically time-shared and, hence, one expects some losses. The purpose of this memo is to determine the amount of the losses and under what conditions they occur. The method of analysis used here differs from that of Spilker [8] in that his analysis was open-loop and our analysis is closed loop

It is assumed that the received, time-gated, signal is in synchronization with the receiver time gating and that the switch rate, $1/T_0$, is much greater than the one-sided loop noise bandwidth, B_L . The gating function is shown in Figure 6.1. The gating pulse is on for $d_F T_0$ seconds,

ORIGINAL PAGE IS
OF POOR QUALITY

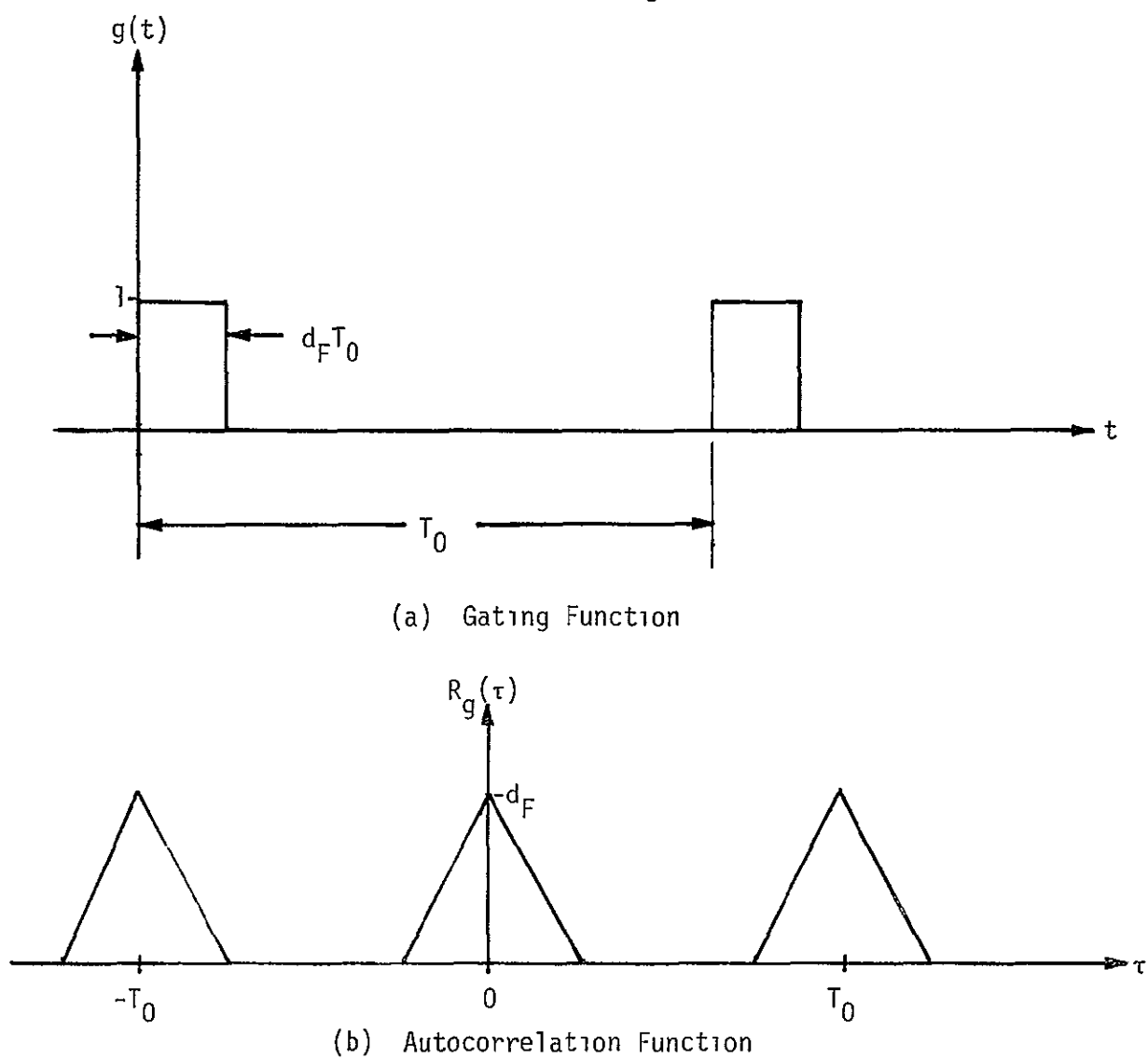


Figure 6.1. Gating Function and its Autocorrelation Function

d_F is the duty factor and is off for the remaining $(1-d_F)T_0$ seconds, with T_0 the period of one cycle of the gating function. The gated received signal is modeled by

$$y(t) = \sqrt{2P} d(t) PN(t-T) g(t) \cos(\omega_0 t + \theta) + g(t)n(t) \quad (158)$$

with P the received signal power, $d(t)$ the received baseband data sequence, $PN(t)$ the pseudonoise spreading code, $g(t)$ the gating function, and $n(t)$ white Gaussian noise

In Figure 6.2, the time-gated code-tracking loop model is illustrated. We now briefly indicate the calculations necessary to determine the variance of the timing error.

The two correlator outputs are given by

$$\begin{aligned} \tilde{e}_L &= \sqrt{2P} L(s) \left\{ d(t)g(t)R_{PN} (T - \hat{T} - T_c/2) \cos(\omega_0 t + \theta) \right\} + n_L g(t) \\ \tilde{e}_E &= \sqrt{2P} L(s) \left\{ d(t)g(t)R_{PN} (T - \hat{T} - T_c/2) \cos(\omega_0 t + \theta) \right\} + n_E g(t) \end{aligned} \quad (159)$$

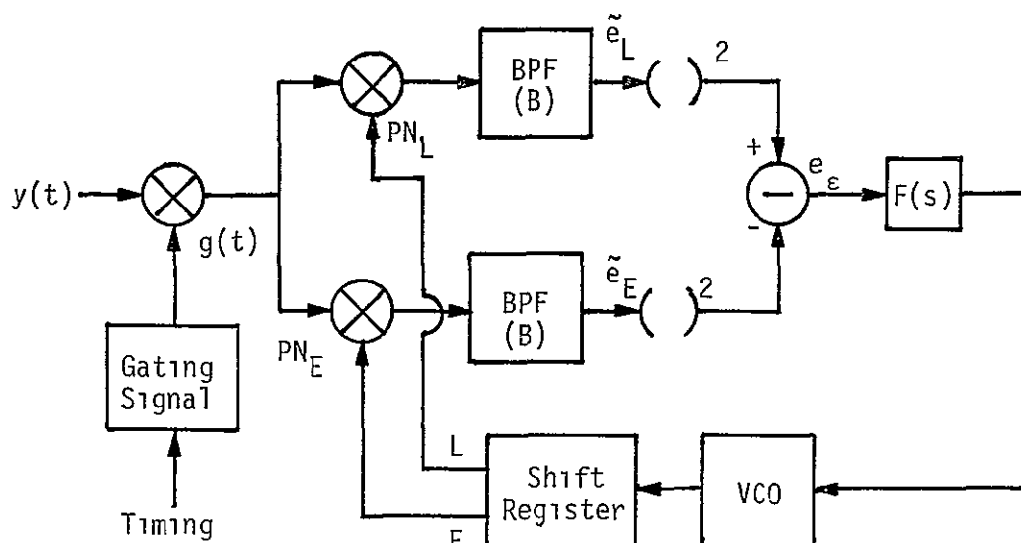
where $L(s)$ is the Heaviside operator representing the bandpass filters. The two noise terms are given by

$$\begin{aligned} n_L(t) &= L(s) \left\{ n(t) PN(t - \hat{T} - T_c/2) \right\} \\ n_E(t) &= L(s) \left\{ n(t) PN(t - \hat{T} + T_c/2) \right\} \end{aligned} \quad (160)$$

After squaring and forming the difference, we obtain

$$\begin{aligned} e_\epsilon &= P L'(s) \left\{ d(t)^2 g(t) \right\} \left[R_{PN}^2 (T - \hat{T} - T_c/2) - R_{PN}^2 (T - \hat{T} + T_c/2) \right] + 2\sqrt{2P} L(s) \\ &\quad \times \left\{ \tilde{d}(t)g(t)\cos(\omega_0 t + \theta) \right\} \left[n_L(t)g(t)R_{PN}(T - \hat{T} - T_c/2) - n_E(t)g(t)R_{PN}(T - \hat{T} + T_c/2) \right] \\ &\quad + n_L(t)^2 g(t) - n_E(t)^2 g(t) \end{aligned} \quad (161)$$

ORIGINAL PAGE IS
OF POOR QUALITY



$$PN_E = PN(t - \hat{T} + T_c/2)$$

$$PN_L = PN(t - \hat{T} - T_c/2)$$

Figure 6 2. Time-Gated Code-Tracking Loop with Arm Filters Having Bandwidth B [Hz]

where $L'(s)$ is the baseband equivalent Heaviside operator of the bandpass filter operator $L(s)$ and $\tilde{d}(t)$ is the baseband equivalent filtered data sequence. Neglecting harmonics outside the loop bandwidth B_L allows us to write

$$e_\epsilon \cong \frac{2P\epsilon}{T_c} \alpha d_F + n_1(t) + n_2(t) \quad (162)$$

where

$$n_1(t) = 2\sqrt{P} \tilde{d}(t)g(t) \left\{ n_{L_c}(t)R_{PN}(T - T - T_c/2) - n_{E_c}(t)R_{PN}(T - T + T_c/2) \right\} \quad (163)$$

$$n_2(t) = n_L^2(t) g(t) - n_E^2(t) g(t) \quad (164)$$

$$\alpha = \int_{-\infty}^{\infty} |L'(f)|^2 \mathcal{P}_d(f) df \quad (165)$$

and it has been assumed that the data symbol rate $1/T_d$ is much larger than the gating rate $1/T_0$.

The noise processes $n_{L_c}(t)$ and $n_{E_c}(t)$ are defined by

$$n_L(t) = \sqrt{2} n_{L_c}(t) \cos(\omega_0 t + \theta) + \sqrt{2} n_{L_s}(t) \sin(\omega_0 t + \theta) \quad (166a)$$

$$n_E(t) = \sqrt{2} n_{E_c}(t) \cos(\omega_0 t + \theta) + \sqrt{2} n_{E_s}(t) \sin(\omega_0 t + \theta) \quad (166b)$$

where $n_L(t)$ and $n_E(t)$ are defined by (160) and can be shown [9] to be essentially independent. Further, $n_{L_c}(t)$, $n_{L_s}(t)$, $n_{E_c}(t)$ and $n_{E_s}(t)$ are all essentially statistically independent Gaussian random processes having the two-sided spectral density $N_0/2$.

With the assumption that the gating process is independent of the noise processes, we find that $R_{n_1}(\tau)$ is given by

$$R_{n_1}(\tau) = 2P R_d^*(\tau) R_{n_{L_c}}(\tau) R_g(\tau) \quad (167)$$

In order to compute $\mathcal{P}_{n_1}(0)$, it is necessary to determine the autocorrelation function of $g(t)$.

The autocorrelation function $R_g(t)$ of $g(t)$ is shown in Figure 6.1. Therefore, defining

$$\begin{aligned} \Delta_{d_F}(\tau) &= \left[1 - \frac{|\tau|}{d_F T_0} \right], \quad |\tau| \leq d_F T_0 \\ &= 0 \quad , \text{ elsewhere} \end{aligned} \quad (168)$$

we have

$$R_g(\tau) = d_F \Delta_{d_F}(\tau) * \sum_{n=-\infty}^{\infty} \delta(\tau + nT_0) \quad (169)$$

where "*" denotes convolution and $\delta(t)$ is the Dirac delta function. Consequently,

$$\mathcal{S}n_1(0) = 2P \int_{-\infty}^{\infty} R_d(\tau) R_{n_{LC}}(\tau) \left\{ d_F \left[\Delta_{d_F}(\tau) \right] * \sum_{n=-\infty}^{\infty} \delta(\tau + nT_0) \right\} d\tau \quad (170)$$

or since

$$\mathcal{S}\{f_1(\tau) * f_2(\tau)\} = F_1(f)F_2(f) \quad (171)$$

we have

$$\mathcal{S}n_1(0) = 2P \int_{-\infty}^{\infty} \int_{-\infty}^{\infty} \mathcal{S}n_{LC}(f') \mathcal{S}_d(f-f') df' \left[d_F^2 T_0 \text{sinc}^2(\pi f d_F T_0) \right] \frac{1}{T_0} \sum_{n=-\infty}^{\infty} \delta\left(f + \frac{n}{T_0}\right) df \quad (172)$$

Evaluating

$$\mathcal{S}n_1(0) = 2 d_F^2 P \int_{-\infty}^{\infty} \sum_{n=-\infty}^{\infty} \mathcal{S}n_{LC}(f') \mathcal{S}_d\left(\frac{n}{T_0} - f'\right) \text{sinc}^2(\pi n d_F) df' \quad (173)$$

By our assumption that the symbol rate was much larger than the gating rate, we obtain

$$S_{n_1}(0) = N_0 d_F^2 P \int_{-\infty}^{\infty} |L'(f)|^4 S_d(f) \left\{ \sum_{n=-\infty}^{\infty} \text{sinc}^2(\pi n d_F) \right\} df \quad (174)$$

Consider the summation

$$S = \sum_{n=-\infty}^{\infty} \frac{\sin^2(n \pi d_F)}{(n \pi d_F)^2} = \frac{1}{\pi^2 d_F^2} \sum_{n=-\infty}^{\infty} \frac{\sin^2(n \theta)}{n^2} \quad (175)$$

Now let $\theta = \pi d_F$ so that we have

$$S = \frac{1}{\pi^2 d_F^2} \left[\pi^2 d_F^2 + 2 \sum_{n=1}^{\infty} \frac{\sin^2 n \theta}{n^2} \right] \quad (176)$$

From Jolly [10], number 520, we have

$$\sum_{n=1}^{\infty} \frac{\sin^2 n \theta}{n^2} = \frac{1}{2} \theta (\pi - \theta) \quad , \quad 0 \leq \theta \leq \pi \quad (177)$$

So that finally, we have simply

$$S = \frac{1}{d_F} \quad (178)$$

Therefore,

$$S_{n_1}(0) = d_F P N_0 \alpha' \quad (179)$$

ORIGINAL PAGE IS
OF POOR QUALITY

where

$$\alpha' = \int_{-\infty}^{\infty} |L'(f)|^4 \mathcal{S}_d(f) df \quad (180)$$

Now we consider the noise-times-noise term. From (164), we have

$$R_{n_2}(\tau) = E \left\{ \left(n_L^2(t) - n_E^2(t) \right) g(t) \left(n_L^2(t+\tau) - n_E^2(t+\tau) \right) g(t+\tau) \right\} \quad (181)$$

where $E(\cdot)$ denotes both the ensemble average and the time average since $g(t)$ is not a random function. From (181), we obtain

$$R_{n_2}(\tau) = R_g(\tau) \left[R_{n_L^2}(\tau) - 2 \overline{n_E^2} \overline{n_L^2} + R_{n_E^2}(\tau) \right] \quad (182)$$

where the overbar denotes the ensemble average. Now it is true that, when $n_E(t)$ and $n_L(t)$ are modeled as independent Gaussian random processes,

$$R_{n_L^2}(\tau) = \overline{n_L^2} \overline{n_L^2} + 2 R_{n_L}^2(\tau) = R_{n_E^2}(\tau) \quad (183)$$

Hence, using (183) in (182) yields

$$R_{n_2}(\tau) = 4R_g(\tau) R_{n_L}^2(\tau) \quad (184)$$

or rearranging yields

$$R_{n_2}(\tau) = N_0^2 \left(\int_{-\infty}^{\infty} |L(f)|^2 e^{-12\pi f\tau} df \right)^2 R_g(\tau) \quad (185)$$

Therefore, using dummy variables, we write

$$S_{n_2}(0) = N_0^2 \int_{-\infty}^{\infty} \int_{-\infty}^{\infty} \int_{-\infty}^{\infty} |L(f'')|^2 |L(f')|^2 e^{-i2\pi f' \tau} e^{i2\pi f'' \tau} R_g(\tau) d\tau df' df'' \quad (186)$$

Continuing, using (169) and the fact that

$$\int_{-\infty}^{\infty} f_1(t) f_2(t) dt = \int_{-\infty}^{\infty} F_1(f) F_2^*(f) df$$

we achieve

$$S_{n_2}(0) = N_0^2 d_F^2 \int_{-\infty}^{\infty} \int_{-\infty}^{\infty} |L(f'')|^2 |L(f')|^2 \int_{-\infty}^{\infty} e^{i(f'' - f' + f)\tau} d\tau \left\{ \text{sinc}^2(\pi f d_F T_0) \right. \\ \left. \times \sum_{n=-\infty}^{\infty} \delta\left(f + \frac{n}{T_0}\right) df df' df'' \right. \quad (187)$$

Finally,

$$S_{n_2}(0) = N_0^2 d_F^2 \sum_{n=-\infty}^{\infty} \int_{-\infty}^{\infty} |L(f')|^2 \left| L\left(f' + \frac{n}{T_0}\right) \right|^2 \text{sinc}^2(\pi n d_F) df' \quad (188)$$

Assuming that the time gating is slow compared to the data rate yields

$$S_{n_2}(0) \approx N_0^2 d_F^2 \sum_{n=-\infty}^{\infty} \text{sinc}^2(\pi n d_F) \int_{-\infty}^{\infty} |L(f)|^4 df \quad (189)$$

From (178), we have

$$S_{n_2}(0) = d_F N_0^2 (2B') \quad (190)$$

with

$$2B' = \int_{-\infty}^{\infty} |L(f)|^4 df \quad (191)$$

Now from (162) and Figure 6.2, we have that the code timing estimate is \hat{T} where

$$\hat{T} = \frac{K_{VCO}}{s} F(s) \left\{ \frac{2\alpha d_F P}{T_C} \epsilon + n_1(t) + n_2(t) \right\} \quad (192)$$

where s is the Heaviside operator variable, $F(s)$ is the loop filter expressed in the variable s , K_{VCO} is the VCO gain constant, and ϵ is the timing error given by

$$\epsilon = T - \hat{T} \quad (193)$$

with T the input timing variation and \hat{T} the code loop estimate of the same. Rearranging (192) with the aid of (193) yields the linearized stochastic differential equation

$$\epsilon = -H(s) \left\{ \frac{n_1(t)}{A} + \frac{n_2(t)}{A} \right\} \quad (194)$$

where

$$H(s) = \frac{\frac{AK_V F(s)}{s}}{1 + \frac{AK_V F(s)}{s}} \quad (195)$$

is the closed-loop response of the code-tracking loop and A is the equivalent gain given by

$$A = \frac{2\alpha d_F P}{T_C} \quad (196)$$

Hence, the variance of the timing error is given by

$$\sigma_{\epsilon}^2 = \int_{-\infty}^{\infty} |H(f)|^2 \frac{\mathcal{S}_{n_1+n_2}(f)}{A^2} df \approx \frac{\mathcal{S}_{n_1+n_2}(0)}{A^2} (2B_L) \quad (197)$$

where the two-sided loop noise bandwidth is given by

$$2B_L = \int_{-\infty}^{\infty} |H(f)|^2 df \quad (198)$$

The spectral density of $n_1(t)$ and $n_2(t)$, $\mathcal{S}_{n_1+n_2}(f)$, is given by the sum of (179) and (180) to yield, from (197), the result

$$\sigma_{\epsilon}^2 = \frac{\{d_F N_0^2 (2B') + d_F N_0 P \alpha'\} 2B_L}{\left(\frac{2\alpha P d_F}{T_C}\right)^2}, \text{ seconds}^2 \quad (199)$$

Simplifying and using the result that $B' \approx B$ for multipole bandpass filters lead us to the result for the linearized and normalized timing error variance

$$\left(\frac{\sigma_{\epsilon}}{T_C}\right)^2 = \frac{N_0 B_L}{2\alpha(d_F P)} \left[\frac{\alpha'}{\alpha} + \frac{2N_0 B}{\alpha(d_F P)} \right], \text{ (fractions of a cycle)}^2 \quad (200)$$

We see from our main result (200) that, using the linearized model under the assumption that $B_L \ll 1/T_0 \ll 1/T_d$, the tracking performance of the time-shared code loop is identical to the full-time code-tracking loop of the same type [9], except that the power is reduced by the factor d_F ! We conclude that the effective loss is therefore

$$L = 10 \log d_F, \text{ dB} \quad (201)$$

6.2 Conclusions

This result should hold for all types of loops, including carrier loops. In [11, Figure 9], it is seen that going from one space vehicle to two space vehicles time-shared causes a carrier increase in threshold of 3 dB and going to four space vehicles causes a total increase in threshold of 6 dB. These results agree directly with (201).

7.0 COMPARISON OF SINGLE/DUAL RECEIVER SCHEMES TO ACHIEVE FAST PN CODE ACQUISITION TIMES

7.1 Summary

A simplified model of a PN code search process has been used to compare two competing satellite acquisition strategies for both single- and dual-channel receivers.

Based on a simplified acquisition model, we conclude that the single-GPS receiver with dedicated pseudochannels (one for each satellite) provides a faster acquisition time than the strategy which uses all the pseudochannels for satellite 1; then, after its acquisition, the remaining three channels are used for satellite 2, etc. This latter strategy has been referred to as the divide-down strategy. However, for the dual-GPS receiver set, the divide-down strategy is more efficient than the dedicated pseudochannel approach.

7.2 Preliminary Discussion

The purpose of this analysis is to determine the optimum allocation of the four pseudochannel receivers for both single- and dual-receiver GPS sets. Each receiver, whether single or dual, is assumed to have four pseudochannels per receiver.

In order to simplify the details of the analysis, certain simplifying assumptions were made. First, it was assumed that the true timing position was distributed uniformly over the uncertainty region. Second, that the probability of detection is unity rather than, say, 0.9; and, finally, that the probability of false alarm was zero instead of some small value.

First we will consider the single-channel receiver for two competitive algorithms to achieve four satellite acquisitions.

7.3 Single-Receiver Acquisition

We consider a time-shared single-channel receiver which, by virtue of its multiplexing capability, can provide four time-shared channels which we will call pseudochannels. We will consider two competitive schemes for this single-channel receiver.

7.3.1 Four-Dedicated-Pseudochannel Approach--Single Receiver

In this approach, time slot 1 is dedicated to satellite 1, time slot 2 is dedicated to satellite 2, etc., up to satellite 4, as shown in Figure 7.1.

First the receiver local PN code is set to the earliest minimum time delay timing point of the code uncertainty of satellite 1 and the search proceeds for τ_D seconds. For simplicity in our analysis, we assume that one code position is searched in this multiplexing time period although a number of code chips could be searched. Next, the local code generator is jam set to the earliest timing point of the code uncertainty of satellite 2 and the search on satellite 2 proceeds for τ_D seconds (one code position or one-half chip). This process continues until satellite 4 is search for one code position. The receiver then sets the local coder to the first satellite, code-phase retarded one-half chip from the first chip search on satellite 1. After τ_D seconds, the coder is jam set to the second cell position of satellite 2, etc., until one satellite is finally acquired (true synchronization is found). To make matters concrete, assume that the third satellite was acquired first. Then the multiplexing process continues with the dwell time on satellite 3 being used for tracking and the remaining multiplexing slots being used for acquisition of satellites, 1, 2 and 4. The resulting multiplexing scheme for a particular sequence of satellite acquisitions is shown in Figure 7.2; the crosshatch lines denote tracking, with acquisition denoted by the lack of crosshatch lines.

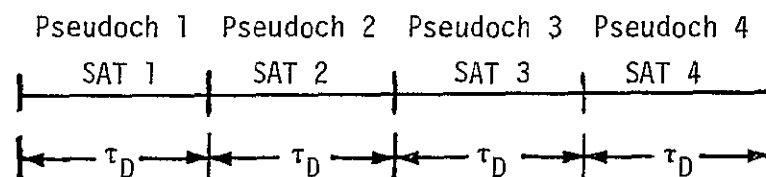


Figure 7.1. Satellite Multiplexing Pattern for a Single Receiver with Four Dedicated Channels

According to Figure 7.2, satellite 3 was acquired first, satellite 1 second, satellite 4 third, and satellite 2 last. After all the satellites are acquired, acquisition is completed. Note that, after each acquisition, the satellite goes into tracking.

In order to determine the mean acquisition time of this dedicated four pseudochannel approach, we must model the distribution function of the time it takes to achieve acquisition for any of the four pseudochannels. Denote the distribution function of the time it takes to acquire one satellite by $F(t)$ where

$$F(t) = P(T \leq t) \quad (202)$$

that is, the probability that the acquisition time is less than or equal to t seconds. Since acquisition doesn't occur until the last satellite has been acquired, we desire the distribution of the last satellite acquisition. This is an order statistic, and the distribution of the last satellite acquisition time is given by [12]

$$F_4(t) = [F(t)]^4 \quad (203)$$

In order to obtain the mean acquisition time of the last satellite acquisition, we must specify the distribution function $F(t)$. Since we have made the simplifying assumptions that $P_d = 1$ and $P_{FA} = 0$, we know that acquisition will occur with probability one after the uncertainty range is completely searched. The acquisition probability density function is therefore as shown in Figure 7.3, along with the continuous approximation

The actual probability density function is discrete in nature, with the probability density function being represented by N delta functions. It is convenient to approximate this density function by a continuous uniform density, as shown in Figure 7.3b. We shall use this approximation to evaluate the mean acquisition time. Since the pseudochannels are searched sequentially, the mean acquisition time is given by

$$\bar{T} = 4 \int_0^{N\tau_D} t p^{(4)}(t) dt \quad (204)$$

ORIGINAL PAGE IS
OF POOR QUALITY

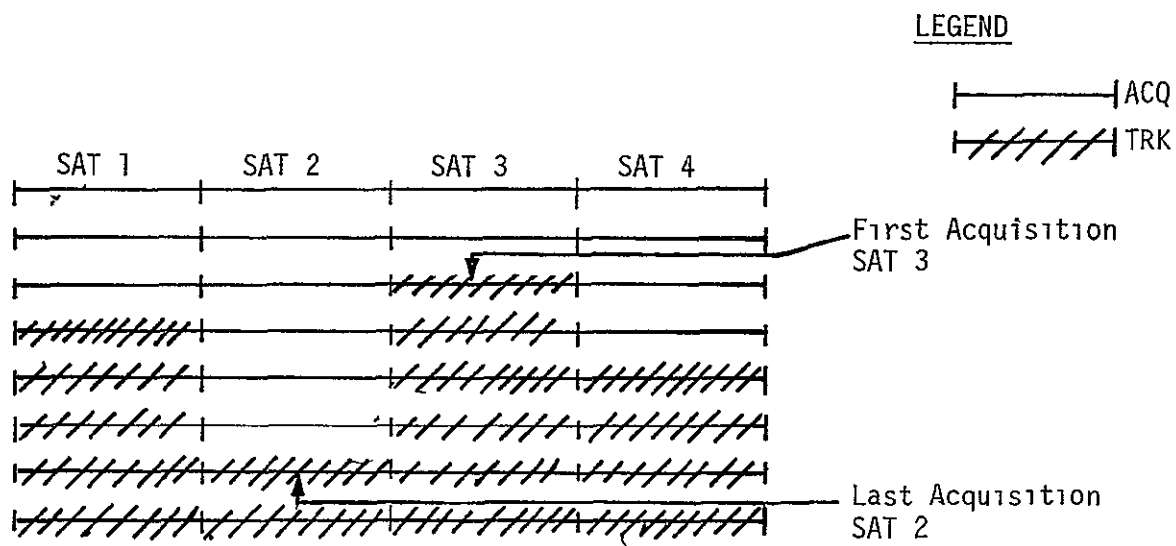
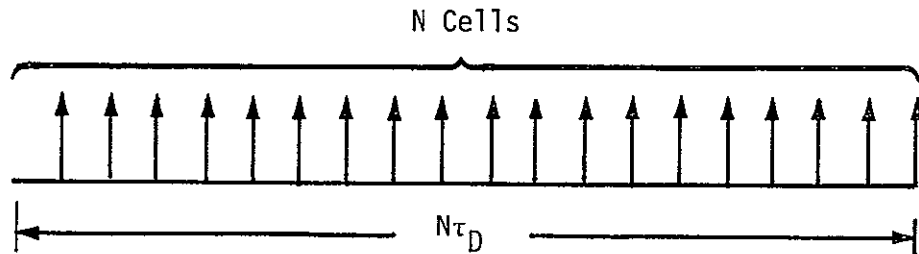
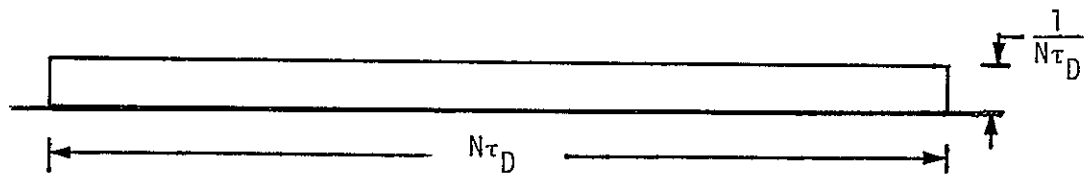


Figure 7 2 One Possible Satellite Acquisition Sequence
for the Dedicated Pseudochannel Approach

ORIGINAL PAGE IS
OF POOR QUALITY



(a) Actual Model of Acquisition Time Probability Density



(b) Approximate Model of Acquisition Time Probability Density

Figure 7.3 Models of the Acquisition Time Probability Density Function

where the 4 comes from the fact that the channels are multiplexed sequentially in time, not in parallel. Using (203) in (204) produces

$$\bar{T} = 4 \int_0^{N\tau_D} t \left\{ 4 [F(t)]^3 p(t) \right\} dt \quad (205)$$

with $F(t)$ defined in (202) and $p(t)$ defined by

$$p(t) = \frac{dF(t)}{dt} \quad (206)$$

Clearly, from Figure 7.3b, the distribution function is given by

$$F(t) = \begin{cases} \frac{t}{N\tau_D} & 0 \leq t \leq N\tau_D \\ 1 & t \geq N\tau_D \\ 0 & 0 \leq t \end{cases} \quad (207)$$

Since $p(t)$ is specified by

$$p(t) = \frac{1}{N\tau_D} \quad 0 \leq t \leq N\tau_D \quad (208)$$

we obtain

$$\bar{T} = 16 \int_0^{N\tau_D} \frac{t^4}{(N\tau_D)^4} dt \quad (209)$$

or evaluating*

$$\bar{T} = 3.2 N\tau_D \quad (210)$$

*Quantization effects in the search of Figure 7.2 have been neglected in this mean acquisition time calculation. In reality, (210) is a slight upper bound but, for large N , it is essentially exact.

Now we can determine the mean acquisition time of the divide-down strategy and compare it to the dedicated pseudochannel approach which we will consider next.

7.3.2 Divide-Down Strategy for Four Satellites--Single Receiver

This strategy allocates all four pseudochannels to the first satellite and, after acquisition, allocates the one pseudochannel that has acquired satellite 1 to tracking and the remaining three pseudochannels to acquisition of satellite 2. This process continues until all four satellites are acquired. Figure 7.4 illustrates the sequence of satellite acquisitions and trackings.

First the satellite 1 uncertainty is divided up into four equal amounts and all four pseudochannels start search in a time-multiplexed manner, as can be seen in Figure 7.4. Notice that, after three channels have been acquired, only one-fourth of the channel is dedicated to acquisition whereas, for the first satellite, all of the channel (four fourths) is dedicated to channel acquisition.

We can now determine the mean time to acquisition. For satellite 1, the uncertainty for each pseudochannel is $N_{\tau_D}/4$ chips. Since the true acquisition position must be in one of the four pseudochannels, the mean time to acquire for satellite 1 is given by

$$\bar{T}_1 = \frac{1}{2} \left(\frac{N_{\tau_D}}{4} \right) (4) \quad (211)$$

where $N_{\tau_D}/4$ is the uncertainty time required to search one-fourth the code uncertainty and the 1/2 comes from the mean-to-total uncertainty ratio. The last factor of four comes from the fact that the four channels are searched serially rather than in parallel. The mean acquisition time for the second satellite is given by

$$\bar{T}_2 = \frac{1}{2} \left(\frac{N_{\tau_D}}{3} \right) 4 = \frac{2}{3} N_{\tau_D} \quad (212)$$

Continuing, we have for the third satellite,

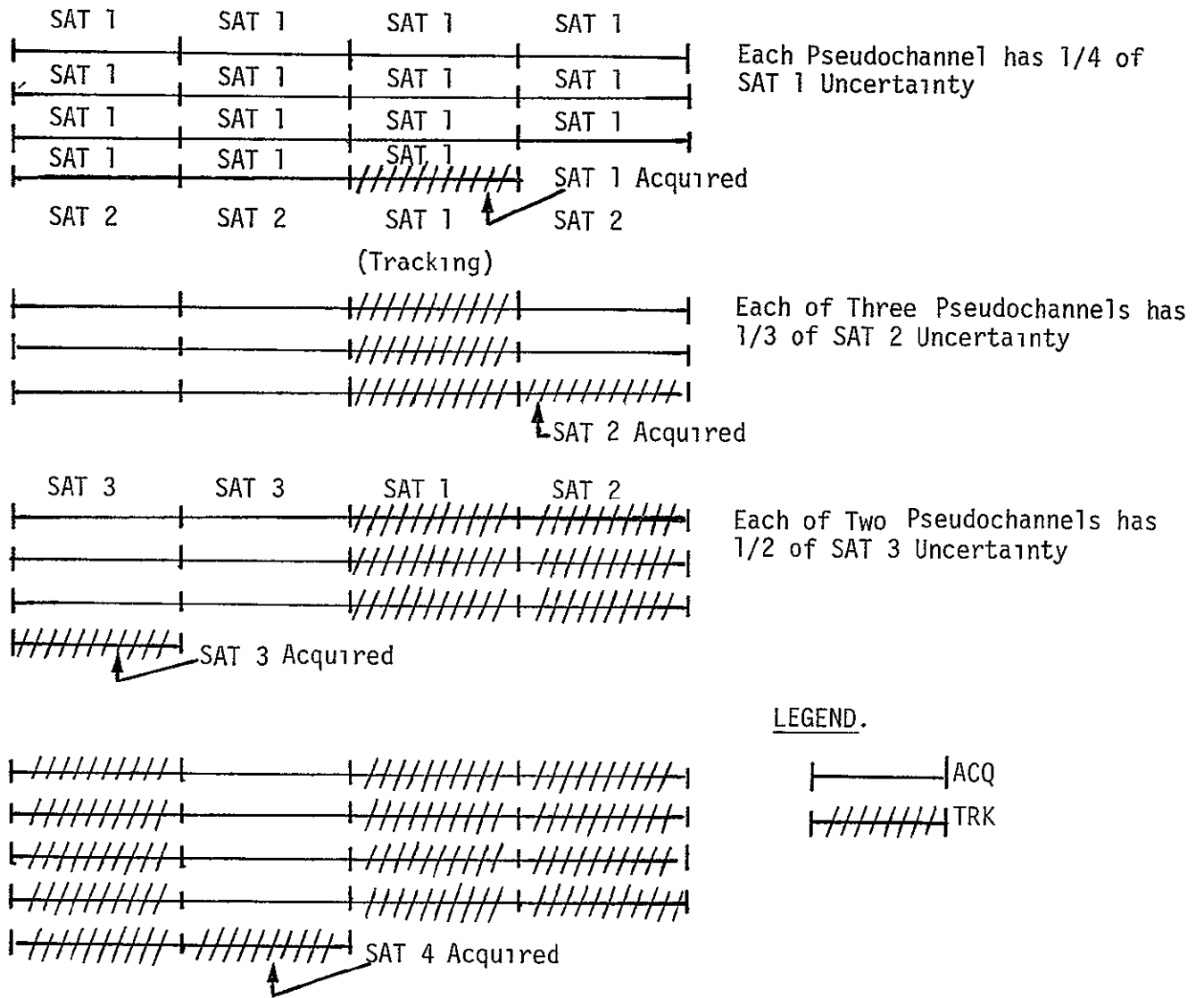


Figure 7 4. One Possible Satellite Acquisition Sequence for the Divide-Down Strategy

$$\bar{T}_3 = \frac{1}{2} \left(\frac{N\tau_D}{2} \right) 4 = N\tau_D \quad (213)$$

Finally, the mean time to acquire the last satellite is given by

$$\bar{T}_4 = \frac{1}{2} (N\tau_D)(4) = 2N\tau_D \quad (214)$$

Summing (211) through (214) produces

$$\bar{T} = 4.17 N\tau_D \quad (215)$$

In comparing (210) and (215), we see that, for the single-channel receiver the dedicated-pseudochannel approach is faster in the sense of mean acquisition time.

7.4 Dual-Receiver Acquisition

In this section, we consider the same two approaches with a dual-channel receiver. By a dual-channel receiver, we mean that two independent receivers are available for independent code acquisition and tracking, and independent carrier-loop acquisition and tracking, etc. We first consider dedicated channels.

7.4.1 Eight-Dedicated-Pseudochannel Approach--Dual Receiver

In this approach, the eight available pseudochannels are dedicated to four satellites, with the result that each pseudochannel has an uncertainty range of $N\tau_D/2$ seconds. Figure 7.5 illustrates the eight-pseudochannel allocation. In this scheme, each satellite uncertainty is broken into one-half ($N\tau_D/2$ seconds) and there is no reallocation of receiver capability after any satellite acquisition.

A typical acquisition (and tracking) scenario is illustrated in Figure 7.6. In this example, satellite 3 is acquired first, satellite 4 is acquired, then satellite 1, and finally, satellite 2.

ORIGINAL PAGE IS
OF POOR QUALITY

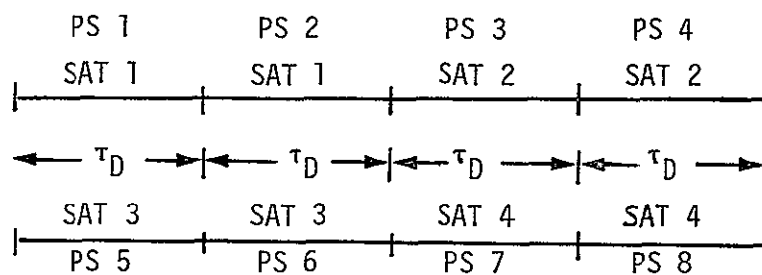


Figure 7.5 Satellite Multiplexing Pattern for a Dual-Receiver with Eight Dedicated Channels

ORIGINAL PAGE IS
OF POOR QUALITY

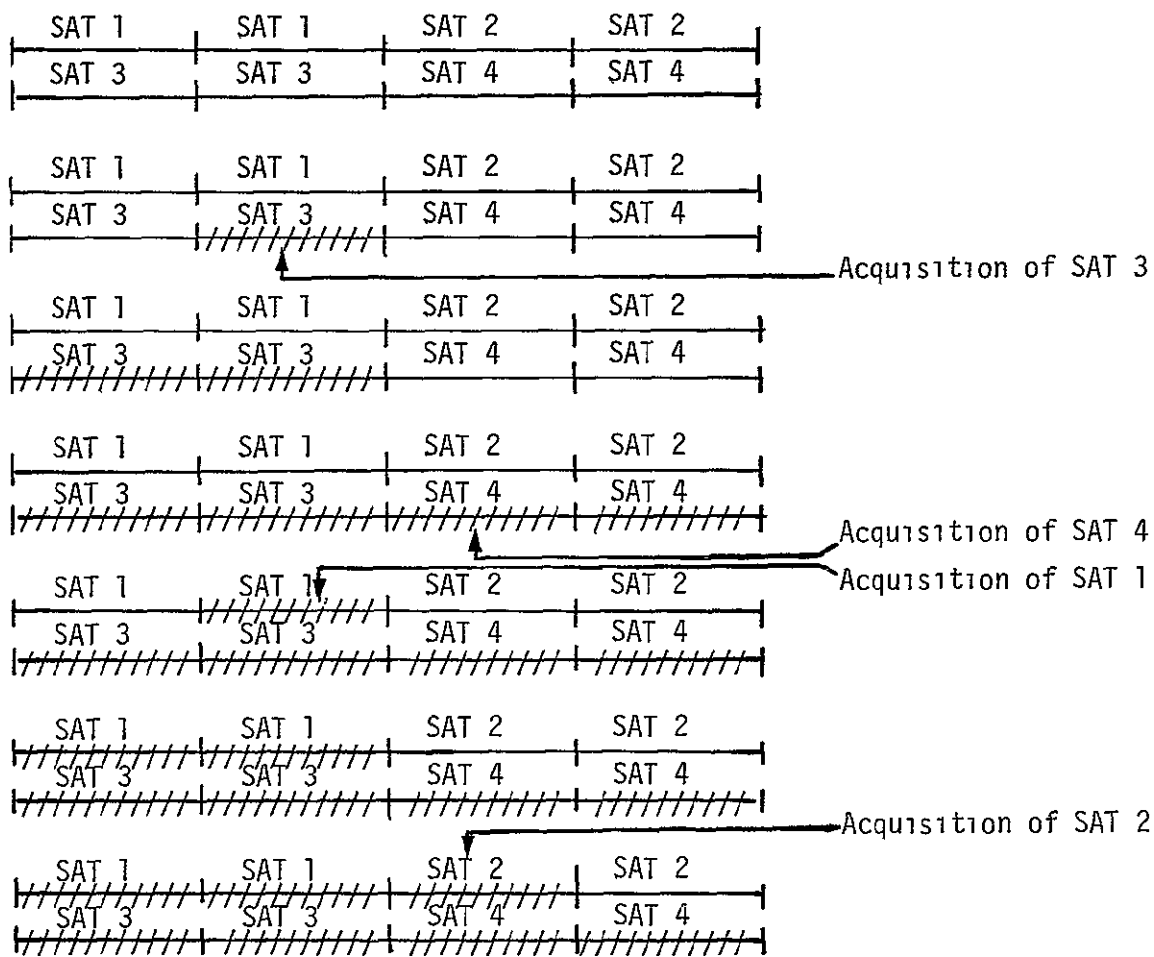


Figure 7 6 Typical Acquisition Scenario for the Dedicated-Pseudochannel Case

We now compute the mean time to acquire for the dedicated-channel, two-receiver approach. Again we denote by $F(t)$ the probability of acquisition on or before t seconds. Again the distribution function of the last satellite acquisition (ordered distribution) is given by

$$F_4(t) = [F(t)]^4 \quad (216)$$

The mean acquisition time is given by

$$\bar{T} = 4 \int_0^{N\tau_D} \frac{t}{2} \left\{ 4 [F(t)]^3 p(t) \right\} dt \quad (217)$$

where $p(t)$ is the probability density function of the unordered acquisition time. The distribution for the (unordered) acquisition time is given by

$$F(t) = \left[\frac{2t}{N\tau_D} \right] \quad (218)$$

Hence,

$$\bar{T} = 16 \int_0^{N\tau_D} \frac{t}{2} \left(\frac{2t}{N\tau_D} \right)^3 \left(\frac{2}{N\tau_D} \right) dt \quad (219)$$

Evaluating (219) yields

$$\bar{T} = 1.6N\tau_D \quad (220)$$

By comparing with the single-receiver acquisition time (210), we see that this dual-receiver approach halves the acquisition time, as one would expect.

7.4.2 Divide-Down Strategy for Four Satellites with Two Receivers

In this scheme, all eight pseudochannels are utilized to acquire satellite 1. After its acquisition, one pseudochannel is allocated to satellite 1 for tracking and the remaining seven pseudochannels are allocated to satellite 2 for acquisition. After satellite 2 is acquired, it is tracked, and all six pseudochannels are utilized for satellite 3. After satellite 3 is acquired, all five pseudochannels are utilized to acquire satellite 4.

Initially, the search time required to cover the uncertainty is $N\tau_D/8$ for each pseudochannel since there are eight pseudochannels available. Therefore, the mean acquisition time for satellite 1 is given by

$$\bar{T}_1 = \frac{1}{2} \left(\frac{N\tau_D}{8} \right) 4 = \frac{1}{4} N\tau_D \text{ seconds} \quad (221)$$

The second satellite has seven pseudochannels available so that the mean acquisition time for satellite 2 is given by

$$\bar{T}_2 = \frac{1}{2} \left(\frac{N\tau_D}{7} \right) 4 = \frac{2}{7} N\tau_D \quad (222)$$

In the same manner, the remaining satellites, 3 and 4, have mean acquisition times given by

$$\bar{T}_3 = \frac{1}{2} \left(\frac{N\tau_D}{6} \right) 4 = \frac{1}{3} N\tau_D \quad (223)$$

and

$$\bar{T}_4 = \frac{1}{2} \left(\frac{N\tau_D}{5} \right) 4 = \frac{2}{5} N\tau_D \quad (224)$$

Summing (221) through (224) yields

$$\bar{T} = 1.27 N\tau_D \text{ seconds} \quad (225)$$

Comparing (225) to (215) points out that doubling the number of receivers more than halves the mean acquisition time for the divide-down acquisition strategy.

By comparing (225) with (220), we see that the dual-receiver with divide strategy is faster than the dedicated pseudochannel approach with two receivers. However, for single-receiver systems, we found that the dedicated-pseudochannel approach was superior.

7.5 Single-Receiver Acquisition--Refined Model

We now consider a refinement on the model in which $P_d < 1$ but $P_{FA} = 0$. In order to make the calculations tractable, we compute the median acquisition time which is the time it takes for the acquisition probability to accrue to 0.5.

7.5.1 Four-Dedicated-Pseudochannel Approach

First we consider the distribution function of acquisition time. Figure 7.7 illustrates the distribution function without multiplexing. Let us designate the median acquisition time by $T_{0.5}$. Then if $T_{0.5} \leq N\tau_D$, we have

$$0.5 = \int_0^{T_{0.5}} F_4(t) dt = \int_0^{T_{0.5}} 4 [F(t)]^3 p(t) dt \quad (226)$$

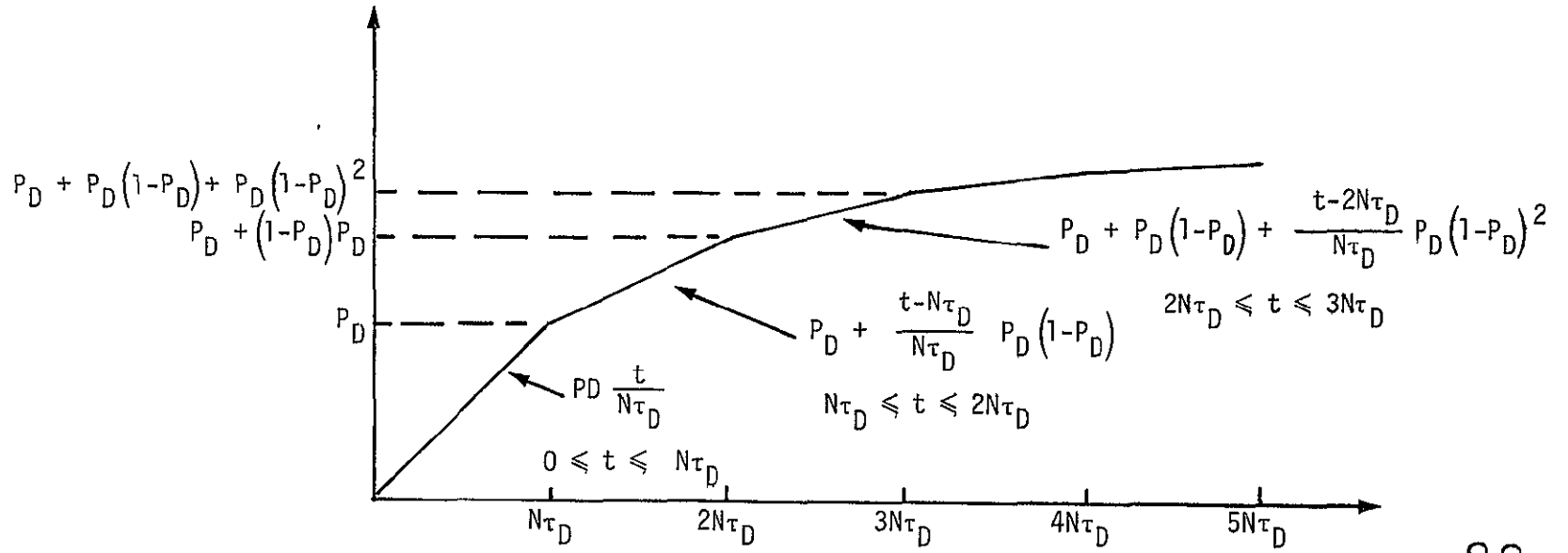
neglecting multiplexing When $T_{0.5} \leq N\tau_D$, we have from Figure 7.7 that

$$F(t) = P_D \left(\frac{t}{N\tau_D} \right) \quad (227)$$

From (226), we have

$$0.5 = 4 P_D^4 \left(\frac{1}{N\tau_D} \right)^4 \int_0^{T_{0.5}} t^3 dt \quad (228)$$

Acquisition Probability, $F(t)$



ORIGINAL PAGE IS
OF POOR QUALITY

Figure 7 7. Distribution Function of Acquisition Time When $P_D < 1$

Solving (228) yields

$$0.5 = \frac{P_D^4}{(N\tau_D)^4} (T_{0.5})^4 \quad (229)$$

or

$$T_{0.5} = \frac{0.841 N\tau_D}{P_D} \quad (230)$$

neglecting time-sharing.

Now to include the four-pseudochannel time-sharing effect, the result of (230) must be multiplied by four so that we have

$$T_{0.5} = \frac{3.36 N\tau_D}{P_D}, \quad P_D \geq 0.841 \quad (231)$$

To obtain solutions for smaller values of P_D , a quartic equation must be solved but will not be pursued here since, normally, $P_D \geq 0.841$. By comparing (231) with $P_D = 1$ and (210), we see that the mean and the median are almost equal.

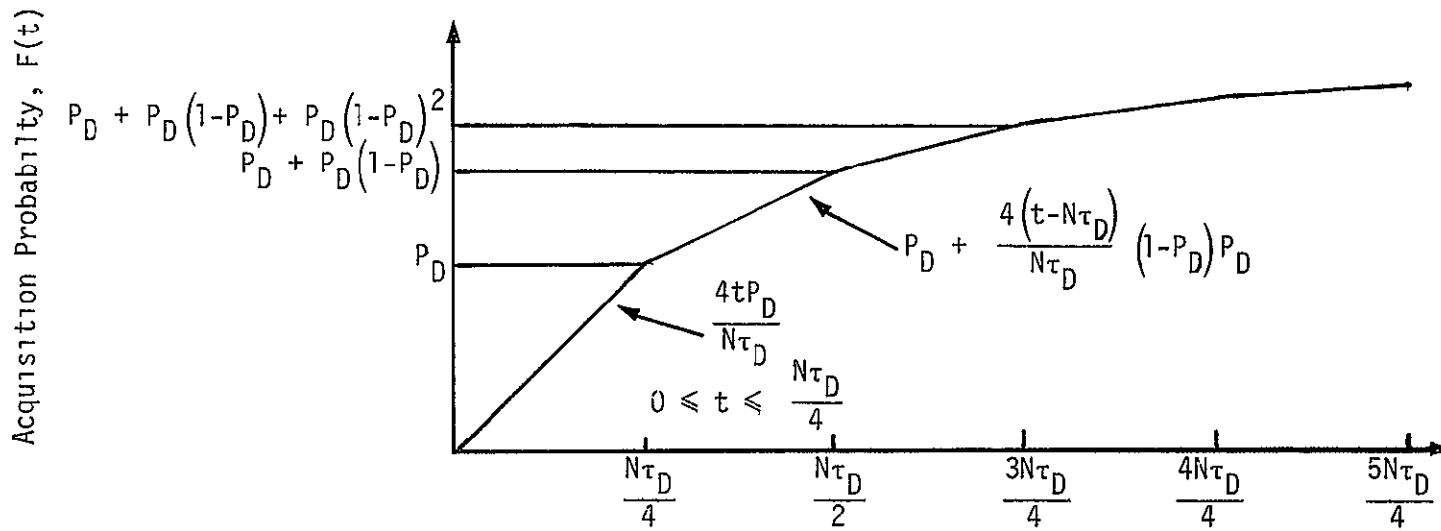
Now we consider the divide-down strategy to compare it with the dedicated-pseudochannel approach.

7.5.2 Divide-Down Strategy for One Receiver

In this scheme, as has already been discussed, the four pseudochannels are dedicated to satellite 1. When $P_D < 1$, the distribution function is as shown in Figure 7.8. We consider the case $0.841 \leq P_D \leq 1$.

For the first satellite, we have that the median acquisition time satisfies, without accounting for the time spent on the other three channels, the equation

$$0.5 = \frac{(4)_1 T_{0.5} P_D}{N\tau_D} \quad 0.841 \leq P_D \leq 1 \quad (232)$$



ORIGINAL PAGE IS
OF POOR QUALITY

Figure 7.8. Distribution Function of Acquisition Time for the Case When $P_D < 1$ and the Uncertainty per Pseudochannel is $N\tau_D/4$

or

$$1T_{0.5} = \frac{N\tau_D}{8P_D} \quad 0.841 \leq P_D \leq 1 \quad (233)$$

Accounting for all four channels yields

$$1T_{0.5} = \frac{N\tau_D}{2P_D} \quad 0.841 \leq P_D \leq 1 \quad (234)$$

For the second satellite, the uncertainty search time per pseudochannel is $N\tau_D/3$ so that

$$2T_{0.5} = \frac{2}{P_D} \left(\frac{N\tau_D}{3} \right) \quad (235)$$

Further, for the third satellite, the uncertainty search time is $N\tau_D/2$ so that

$$3T_{0.5} = \frac{2}{P_D} \left(\frac{N\tau_D}{2} \right) \quad (236)$$

Finally, for the last satellite, we have

$$4T_{0.5} = \frac{2}{P_D} (N\tau_D) \quad (237)$$

Summing (234) through (237) yields

$$T_{0.5} = 4.17 \frac{N\tau_D}{P_D} \quad P_D \geq 0.841 \quad (238)$$

Comparing (238) to (231) again substantiates the results of the mean acquisition time for a single-channel receiver. That is, the dedicated-pseudochannel approach is faster than the divide-down scheme with the refined acquisition parameter model.

7.6 Conclusions

Based on a simplified acquisition model, we conclude that, for the single GPS receiver, dedicated pseudochannels, one for each satellite, provide a faster acquisition time than the strategy that uses all the pseudochannels for satellite "1" then, after its acquisition, the remaining three channels are used for satellite 2, etc. This latter strategy has been referred to as the divide-down strategy.

However, for the dual-receiver set, the divide-down strategy is more efficient than the dedicated-pseudochannel approach. The relative mean acquisition times are summarized below, with the continuous receiver used as a reference point.

Table 7.1. Single-Receiver Relative Acquisition Time Comparison

Receiver Type	Relative Mean Acquisition Time
Continuous Receiver	100%
Dedicated Pseudochannels	400%
Uncertainty-Dividing Strategy	521%

Table 7.2. Dual-Receiver Relative Acquisition Time Comparison

Receiver Type	Relative Mean Acquisition Time
Continuous Receiver	100%
Dedicated Pseudochannels	400%
Uncertainty-Dividing Strategy	318%

Note that the values of Table 7.2 should be one-half those indicated if they are compared to the continuous receiver of Table 7.1.

8.0 PRELIMINARY C/A CODE ACQUISITION TIME ESTIMATES

8.1 Summary

This section describes the results of our estimates of the C/A code acquisition time and associated probabilities for acquiring with single-channel receivers, dual-channel receivers and four-channel receivers utilizing sequential detection. The basic assumptions used in the calculation include the following: (1) the full C/A code uncertainty of 1023 chips must be searched (in one-half-chip elements), (2) code doppler is negligible and, (3) residual carrier doppler corresponding to 60 m/s is ± 315 Hz. The results are summarized below in Table 8.1. Due to limited simulation data, complete optimizations over all types of systems were not tried.

Table 8.1. Summary of Acquisition Times and Probabilities for a Two-Doppler 1023-Chip Search

Receiver Type	Acquisition Time (seconds)	Probability of Acquisition
Single-Channel	68.8	0.686
	137.6	0.968
Dual-Channel	34.4	0.686
	51.6	0.815
	68.8	0.986
Four-Channel	17.2	0.686
	34.4	0.986
	51.6	0.997
	68.8	0.9997

8.2 Analysis

The purpose of this section is to determine the C/A code acquisition time by utilizing sequential detection. Sequential detection is an optimal method of sequentially acquiring code synchronization. A typical analog implementation of a PN code sequential detector is shown in Figure 8.1. In Figure 8.2, a particular sample function of noise only and signal-plus-noise are shown. Typically, the noise-only case is rejected considerably prior to the truncation time T_{TR} . The average rejection or dismissal time \bar{T}_D is an important parameter in determining the acquisition time. Given that the signal is present, the probability that the signal-plus-noise is above the value of zero at the truncation time is called the probability of detection and is denoted by P_D . If noise only remains above the value of zero for T_{TR} seconds, then a false alarm has occurred and the false-alarm probability is denoted by P_{FA} .

Holmes [13,14] has shown that the mean sweep time for a fixed-dwell-time system with a false-alarm penalty of $K\tau$ seconds is given by

$$T_{SW} = q\tau \left[1 + KP_{FA} \right] \quad (239)$$

where

q = number of cells to be searched, usually $q = 2N$

τ = single-dwell dismissal time

P_{FA} = false-alarm probability

K = false-alarm penalty in units of τ .

Now let us consider how the acquisition probability improves as additional sweeps through the code uncertainty are made. Clearly, after one sweep, the probability of acquisition equals the probability of detection, i.e.,

$$P_{ACQ}^{(1)} = P_D \quad (240)$$

After n complete sweeps, the probability of acquisition is one minus the probability of no acquisition, or

$$P_{ACQ}^{(n)} = 1 - (1 - P_D)^n \quad (241)$$

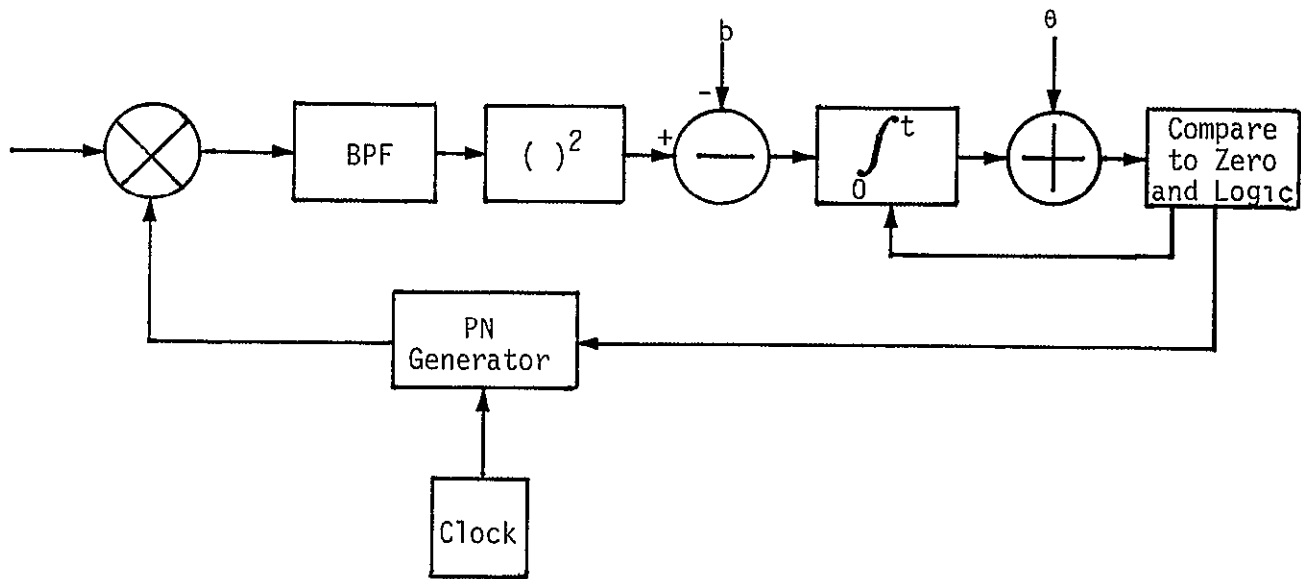


Figure 8.1. PN Code Sequential Detector

ORIGINAL PAGE IS
OF POOR QUALITY

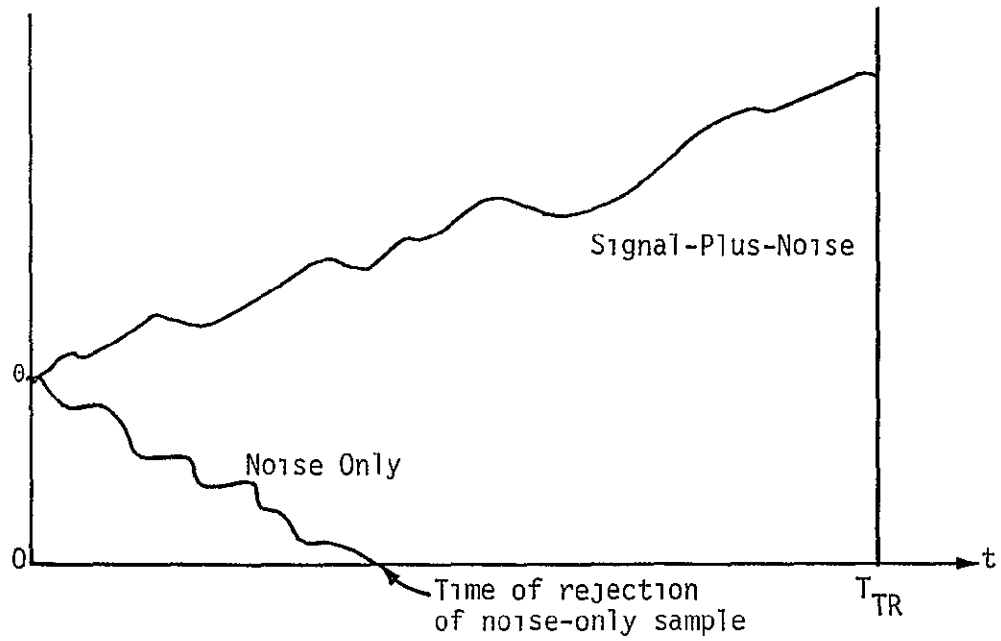


Figure 8.2. Noise-Only and Signal-Plus-Noise Realization

ORIGINAL PAGE IS
OF POOR QUALITY

Now (239) also applies (approximately) to sequential detection schemes if τ now represents the mean dismissal time $\bar{\tau}$. Therefore, after n sweeps, the associated acquisition time (of n sweeps) is (approximately)

$$T_{ACQ}^{(n)} = n q \bar{\tau} [1 + K P_{FA}] \quad (242)$$

and

$$K = \frac{T_{TR} + T_V}{\bar{\tau}} \quad (243)$$

where the associated probability of acquisition at time $T_{ACQ}^{(n)}$ is given by

$$P_{ACQ}^{(n)} = 1 - (1 - P_D)^n \quad (244)$$

In (243), T_{TR} is the truncation time and T_V is the verification time needed to verify a false alarm.

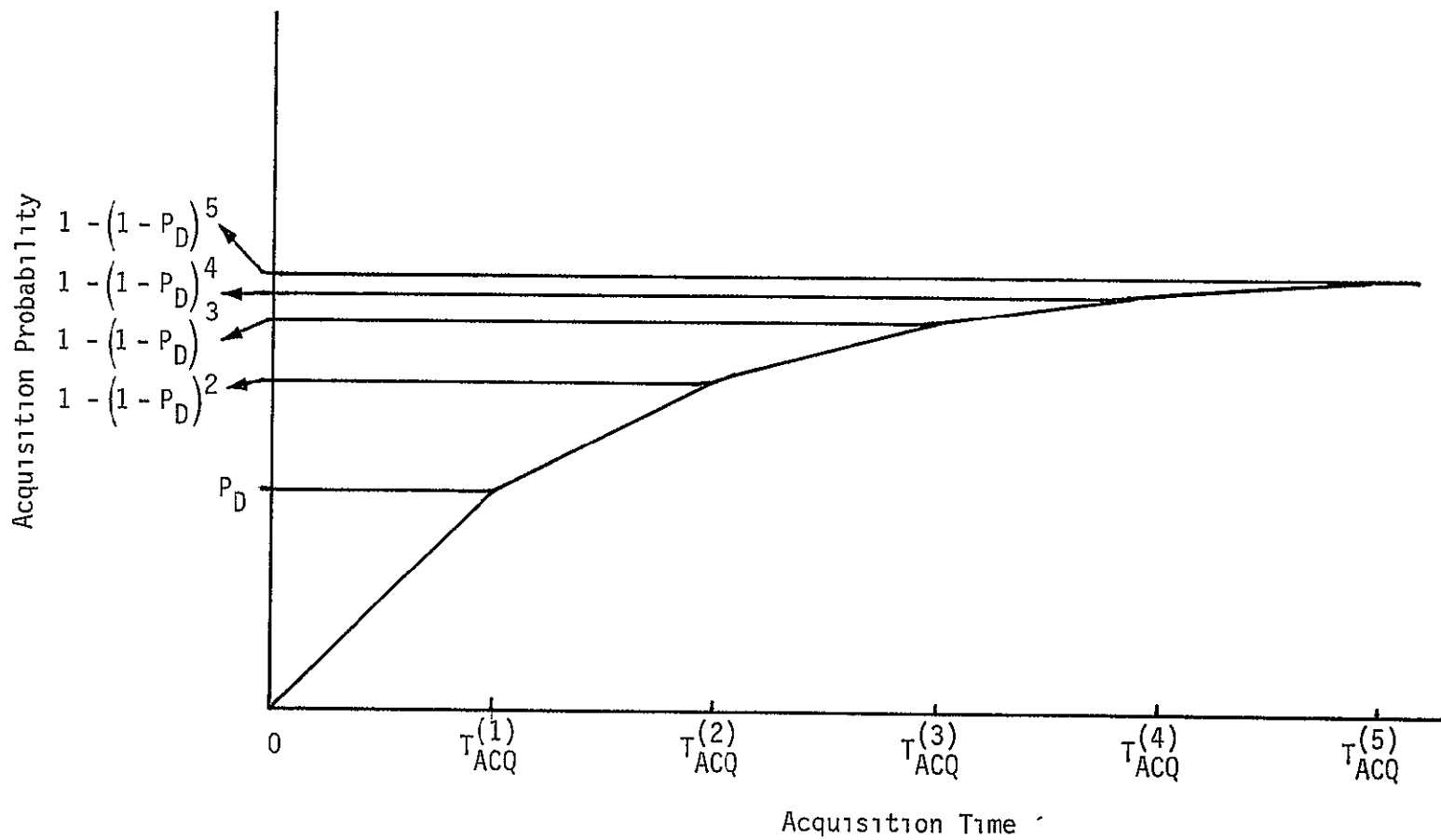
A plot of $P_{ACQ}^{(n)}$ is illustrated in Figure 8.3. As an example, if $P_D = 0.91$, $P_{ACQ}^{(n)}$ is given in Table 8.2.

Table 8.2. Acquisition Probability versus Number of Sweeps

n	$P_{ACQ}^{(n)}$
1	0.91
2	0.992
3	0.9993
4	0.99993
5	0.999994

Now consider the associated parameters of the system. With aiding, the system must tolerate ± 60 m/s velocity uncertainty, which corresponds to a carrier uncertainty of

$$\Delta f = \pm \frac{60}{3 \times 10^8} (1.575 \times 10^9) = \pm 315 \text{ Hz} \quad (245)$$



ORIGINAL PAGE IS
OF POOR QUALITY

Figure 8 3. Acquisition Probability versus Acquisition Time Indexed by the Number of Complete Sweeps of the Code Uncertainty

With a bandpass filter bandwidth of about 400 Hz, two doppler bins are needed to cover the doppler uncertainty of 630 Hz and provide overlap of the uncertainty region. Figure 8.4 illustrates the doppler uncertainty and the corresponding doppler bins.

From a sequential detection simulation [15], the following parameters were determined for $C/N_0 = 34$ dB-Hz (after losses):

$$\begin{aligned} P_{FA} &= 0.001 & \bar{\tau} &= 3.18 \text{ ms} \\ P_D &= 0.91 & T_{TR} &= 25 \text{ ms} \end{aligned} \quad (246)$$

Using a noise bandwidth of 400 Hz along with a C/N_0 of 34 dB-Hz yields a predetection SNR of 8 dB. From (242) - (244) and (246), we have

$$T_{SW}^{(1)} = 2 \times 1023 \left[1 + \frac{1+0.025}{0.00318} (0.001) \right] 0.00318 \text{ sec} \quad (247)$$

or

$$T_{SW}^{(1)} = 8.6 \text{ seconds} \quad (248)$$

for one bin search of the full C/N code uncertainty of 1023 chips*. When both doppler bins are swept, the probability of acquisition is still 0.91 in 17.2 seconds.

Consider a single-channel receiver. Because of time-sharing among four satellites, the acquisition time is 4×17.2 seconds, or 68.8 seconds. However, the probability of acquisition is the fourth power of 0.91, or 0.686. Consider the case where two sweeps rather than one were used to increase the detection probability to 0.992 (from Table 8.2). Then the acquisition time doubles to 137.6 seconds and the probability of detection is $(0.992)^4 = 0.968$.

Now consider the use of a dual-channel receiver. Again, for a single sweep over both doppler bins, the probability is 0.91 in 17.2 seconds for one satellite. Due to time-sharing two channels, the acquisition time becomes 34.4 seconds with a probability of $(0.91)^4 = 0.686$. With two sweeps per doppler bin, the acquisition time is 68.8 seconds with a

* Note that this is about 80% of the time estimated in [16].

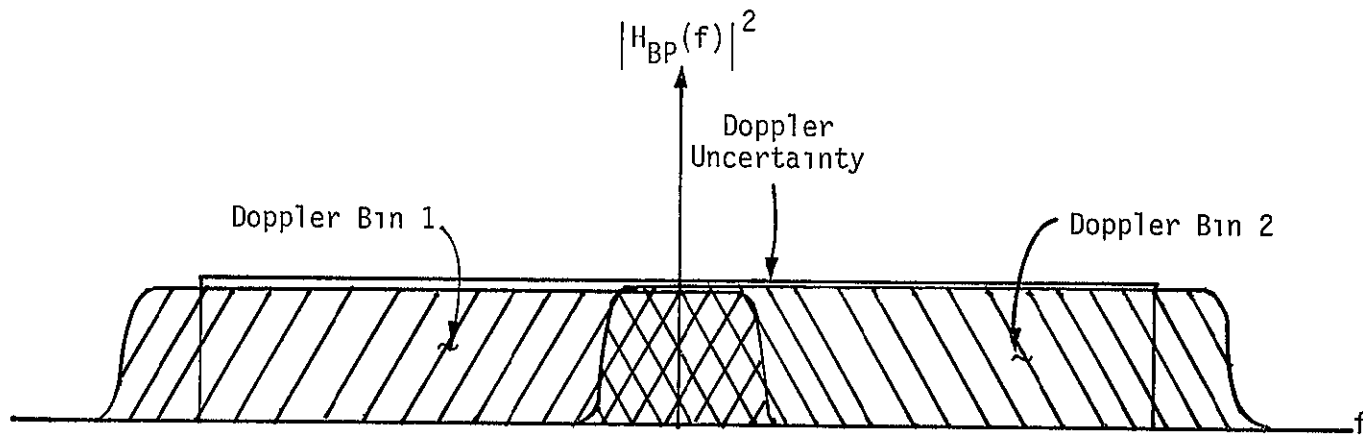


Figure 8.4 Doppler Uncertainty and the Associated Doppler Bins

ORIGINAL PAGE IS
OF POOR QUALITY

corresponding acquisition probability of $(0.992)^4 = 0.968$. If, however, two sweeps are used on the first two satellites and one sweep is used on the third and fourth satellite acquisitions, then the time to acquire is just the average of 34.4 and 68.8 seconds, or 51.6 seconds with a probability of $(0.992)^2(0.91)^2 = 0.815$.

As a final case, we consider a four-channel receiver used for acquisition. We have that, for a single sweep of each doppler, the acquisition time is 17.2 seconds for an acquisition probability of 0.686. Using two sweeps per doppler bin yields an acquisition time of 34.4 seconds with a detection probability of 0.968. If three sweeps are made per doppler cell, the time to acquire is then 51.6 seconds with a probability of acquisition of $(0.9993)^4 = 0.997$. Furthermore, if four sweeps per doppler bin are made, then the acquisition time is 68.8 seconds with a corresponding probability of acquisition of $(0.99993)^4 = 0.9997$. The results obtained above are summarized in Table 8.1.

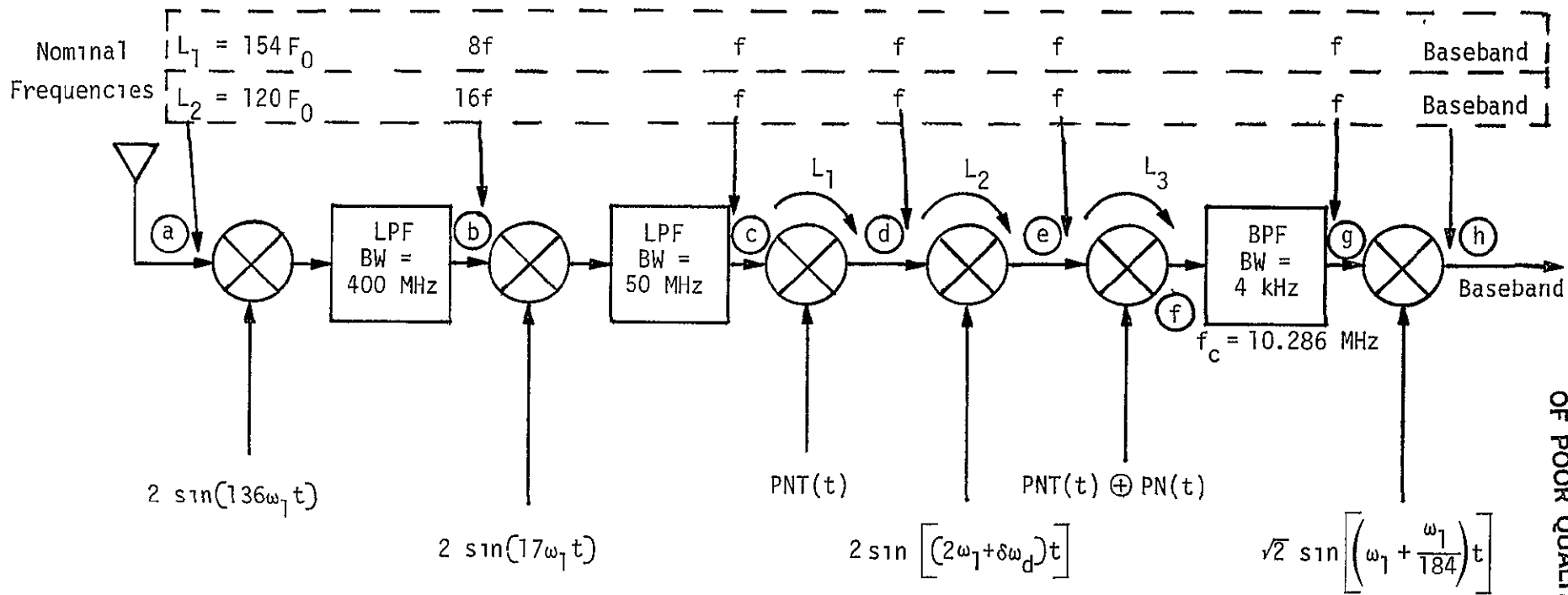
8.3 Conclusions

Based on a full 1023-chip C/A code search and a doppler uncertainty of ± 315 Hz, the dual-channel receiver using sequential detection would take about 69 seconds for an acquisition probability of 0.99 and about 55 seconds for an acquisition probability of 0.9.

9.0 PRESERVATION OF THE PROCESSING GAIN FOR THE TI GPS RECEIVER
L₁/L₂ AND DISCUSSION OF THE RECEIVER FREQUENCY PLAN

9.1 Summary

The Texas Instruments (TI) GPS receiver frequency plan is analyzed along with their method of ensuring that the processing gain is obtained. Based on the analysis contained in this section, it is concluded that the full processing gain of both the C/A and P codes is achieved by utilizing the TI T code with mixers providing at least 35 dB isolation. The details are omitted from this copy of the annual report because they contain TI proprietary information that could possibly compromise the TI competitive position on GPS receiver procurements.



NOTES f is nominally F_0
 f_c is the center frequency of the BPF

Figure 9.1. Equivalent Frequency Plan Model for the TI GPS Receiver

ORIGINAL PAGE IS OF POOR QUALITY

where P is the desired signal power, $d(t)$ the 50-bps modulation, $PN(t)$ the P code, P_I the interference power, and $154\omega_0$ and ω_I are the respective angular frequencies. In fact, L_1 is nominally 1.575 GHz. It is to be noted that the L_1 signal is centered at $154F_0$ nominally and the L_2 signal is centered at $120F_0$ nominally, where $\omega_0/2\pi = F_0 = 10.23$ MHz. At the first mixer, the desired P -code signal is spread so that its leakage is not important. Also, the local oscillator (LO) frequency of $136F_1$ will leak across the first mixer; however, the lowpass filter following the mixer prevents it from having a nonnegligible level out of the filter.

Hence, at point (b) of Figure 9.1, the signals of interest are

$$x_b(t) = \sqrt{2P} PN(t) d(t) \cos(18\omega_0 - 136\Delta\omega)t + \sqrt{2P_I} \cos[(\omega_I - 136\omega_1)t] \quad (252)$$

At the second mixer, there are no important leakage terms so that, at point (c) of Figure 9.1, we have

$$x_c(t) = -\sqrt{2P} PN(t) d(t) \sin(\omega_0 - 153\Delta\omega)t - \sqrt{2P_I} \sin[(\omega_I - 153\omega_1)t] \quad (253)$$

At the third mixer, the T code is modulated onto (253); also, the first significant leakage term arises. This leakage term is the heterodyned-down interference CW signal which appears at the output of the third mixer attenuated by $10 \log L_1$ dB, where L_1 is the absolute CW leakage of the third mixer. Consequently, the signal at point (d) of Figure 9.1 is given by

$$x_d(t) = -\sqrt{2P} PN(t) d(t) PNT(t) \cos[(\omega_0 - 153\Delta\omega)t] - \sqrt{2P_I} PNT(t) \cos[(\omega_I - 153\omega_1)t] \\ - \sqrt{2P_I L_1} \sin[(\omega_I - 153\omega_1)t] \quad (254)$$

At the fourth mixer, both doppler and L_1/L_2 frequency compensation are employed such that, when heterodyned by $F_1 + F_1/184$, the carrier is beat down to zero. The correction term is denoted by δf_d . Therefore, at point (e) of Figure 9.1, the signal is expressed by

$$\begin{aligned}
 x_e(t) = & -\sqrt{2P} PN(t) PNT(t) d(t) \sin\left[(\omega_0 + 155\Delta\omega + \delta\omega_d)t\right] \\
 & -\sqrt{2P_I} PNT(t) \sin\left[(155\omega_1 - \omega_I + \delta\omega_d)t\right] \\
 & -\sqrt{2P_I L_1 L_2} \sin\left[(\omega_I - 153\omega_1)t\right] \\
 & -\sqrt{2P_I L_1} \cos\left[(155\omega_1 - \omega_I)t + \delta\omega_d t\right] \quad (255)
 \end{aligned}$$

where the third term is due to leakage of the fourth mixer and the fourth term is a heterodyned version of the leakage term from the third mixer.

The fifth mixer multiplies the input signal by $PNT(t) \oplus PN(t)$ and is then followed by a bandpass filter centered at 10.286 MHz with a bandwidth of 4 kHz. Into this filter, we have, at point (f) of Figure 9.1,

$$\begin{aligned}
 x_f(t) = & -\sqrt{2P} d(t) \sin\left[(\omega_0 + 155\Delta\omega + \delta\omega_d)t\right] - \sqrt{2P_I} PN(t) \sin\left[(155\omega_1 - \omega_I + \delta\omega_d)t\right] \\
 & -\sqrt{2P_I L_1 L_2} PN(t) PNT(t) \sin\left[(\omega_I - 153\omega_1)t\right] \\
 & -\sqrt{2P_I L_1} PN(t) PNT(t) \cos\left[(155\omega_1 - \omega_I + \delta\omega_d)t\right] \\
 & -\sqrt{2P_I L_1 L_2 L_3} \sin\left[(\omega_I - 153\omega_1)t\right] - \sqrt{2P_I L_1 L_3} \cos\left[(155\omega_1 - \omega_I + \delta\omega_d)t\right] \quad (256)
 \end{aligned}$$

Now only those signals at $10.286 \text{ MHz} \pm 2 \text{ kHz}$ will be passed through the BPF following the fifth mixer. The first signal of (256) has a center frequency* of

$$\frac{\omega_0 + 155\Delta\omega + \delta\omega_d}{2\pi} = 10\,286 \text{ MHz} \quad (257)$$

The next nonspread term, the fifth one, has a frequency given by

$$\frac{\omega_I - 153\omega_1}{2\pi} = 10\,1688 \text{ MHz} \quad (258)$$

* Note that $\frac{\delta\omega_d}{2\pi} = 6000 \text{ Hz}$ in the L_1 mode.

when $\omega_I/2\pi$ is essentially F_0 . This term, attenuated by three mixer isolation values, would be at least 90 dB, as well as being heavily filtered by the 4-kHz bandwidth filter since it is 117.2 kHz away from the center frequency. Now, since the third and fourth terms are on the order of 30 dB and 60 dB down from the second term, we have that the important terms are

$$x_g(t) = -\sqrt{2P} d(t) \sin \left[(\omega_0 + 155\Delta\omega + \delta\omega_d)t \right] - \sqrt{2P_I} \tilde{P}N(t) \sin \left[(155\omega_1 - \omega_I + \delta\omega_d)t \right] \\ - \sqrt{2P_I L_1 L_3} \cos \left[(155\omega_1 - \omega_I + \delta\omega_d)t \right] \quad (259)$$

where $\tilde{P}N(t)$ denotes a 4-kHz bandwidth bandpass-filtered version of $PN(t)$.

After heterodyning at the sixth mixer, we obtain

$$x_h(t) = -\sqrt{P} d(t) \cos \left[\left(154\Delta\omega + \delta\omega_d - \frac{\omega_1}{184} \right) t \right] - \sqrt{P_I} \tilde{P}N(t) \cos \left[\left(154\omega_1 - \omega_I + \delta\omega_d - \frac{\omega_1}{184} \right) t \right] \\ + \sqrt{P_I L_1 L_3} \sin \left[\left(154\omega_1 - \omega_I + \delta\omega_d - \frac{\omega_1}{184} \right) t \right] \quad (260)$$

Now, since the carrier loop (which is not shown in Figure 9.1), when operating properly, causes the argument of the first term to be zero, the first term becomes a baseband data term. Unless the interferer is coherent with the signal (which is highly unlikely), the second and third terms could be centered at a few tens to hundreds of hertz. Greater offsets would not be of much importance since the second term is spread over a 10-MHz bandwidth. In either case, the third signal of (260) is not a problem due to the TI design. To clarify this statement, note that, even if the interferer frequency is near the desired signal center frequency ($154 F_0$), it is attenuated by the product $\sqrt{L_1 L_3}$, which would provide about 60-70 dB reduction in its effect. Consequently, as long as the processing gain is an order of magnitude less than the CW isolation, the processing gain will be preserved. Since the processing gain is about 53 dB in this case, it is clear that reasonable mixers (at least 30-dB isolation) will allow realization of the full processing gain. Again the above is true as long as the TI T code is utilized in the design.

9.3 Processing Gain

Now consider the processing gain. We define the processing gain to be the reduction in power in the data (noise) bandwidth after carrier demodulation with a spread spectrum system compared to a system without spreading. Figure 9.2 illustrates the signal, coherent interference and carrier demodulation model.

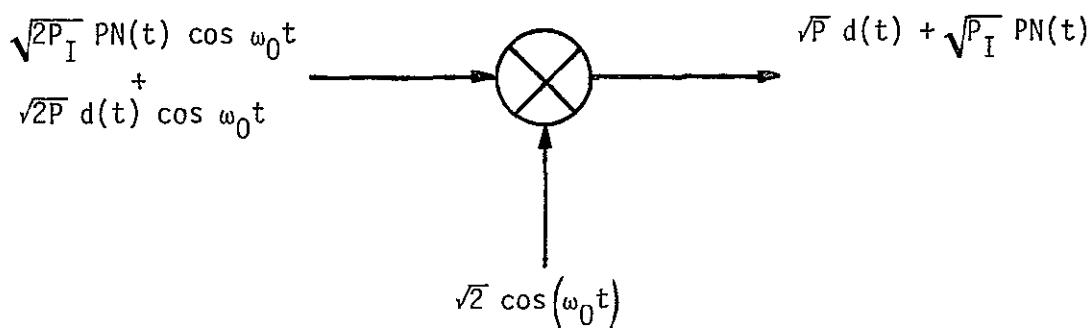


Figure 9.2. Interference Model and Signals

The P code is denoted by PN(t) and the data by d(t).

Since the GPS P code is very long, about 2.354×10^{14} chips, the periodic line structure is separated by approximately

$$\Delta f = 4.36 \times 10^{-8} \text{ Hz} \quad (261)$$

so that the P code, modeled as a maximum length code, has a spectral density* near $f=0$ of

$$S_I(0) = P_I T_C, \quad \forall f \quad (262)$$

where P_I is the tone interference power and T_C is the chip duration. Since the two-sided noise bandwidth of a matched filter $\left(\frac{1}{T} \int_0^T () dt\right)$ to an NRZ waveform is $1/T$, where T is the data bit duration, we have that the power out of the matched filter is

* We assume a continuous spectral density.

$$P_0 = P_I T_c / T = P_I \frac{R_B}{R_C} \quad (263)$$

where R_B is the data rate and R_C is the chip (P-code) rate. From Figure 9.1, see that, if the interference was not spread, its demodulated power out of the matched filter would be P_I . We therefore conclude that the reduction in interference power is $R_B/R_C = PG$ (processing gain) which, for GPS, is

$$PG = \frac{R_C}{R_B} = 53.1 \text{ dB} \quad (264)$$

Therefore, if mixers L_1 and L_3 each offer about 35-dB isolation, then the processing gain would be reduced negligibly to 53.1 dB so that the processing gain is preserved.

However, if the T code was not used, the isolation of the interfering carrier would then be equal to only L_3 or about 35 dB. In this case, the processing gain would be only about 35 dB, which means that about 18 dB would be lost due to poor design.

9.4 L_2 Frequency Plan

We again use Figure 9.1 to consider the L_2 frequency plan. At point (a), the received signal-plus-tone jammer is of the form

$$x_a(t) = \sqrt{2P} PN(t) d(t) \sin(120\omega_0 t) + \sqrt{2P_I} \sin(\omega_I t) \quad (265)$$

where $120 F_0$ (L_2 frequency) is nominally 1.2276 GHz. At point (b) after the lowpass filter, we have

$$x_b(t) = \sqrt{2P} PN(t) d(t) \cos \left[(16\omega_0 + 136\Delta\omega)t \right] + \sqrt{2P_I} \cos \left[(-\omega_I + 136\omega_1)t \right] \quad (266)$$

Again the leakage term is removed by the 50-MHz filter since it is centered at about $16 \times 10^{23} \times 10^6$ MHz. Therefore, at point (c), we have the resulting signal

$$x_c(t) = \sqrt{2P} PN(t) d(t) \sin\left[(\omega_0 - 119\Delta\omega)t\right] + \sqrt{2P_I} \sin\left[(\omega_I - 119\omega_0 - 119\Delta\omega)t\right] \quad (267)$$

Now at the third mixer, the T code is modulated onto the signals and a leakage term that is not filtered out also occurs. Hence, at point (d), we have

$$x_d(t) = \sqrt{2P} PN(t) PNT(t) d(t) \cos\left[(\omega_0 - 119\Delta\omega)t\right] + \sqrt{2P_I} PNT(t) \cos\left[(\omega_I - 119\omega_0 - 119\Delta\omega)t\right] + \sqrt{2P_I L_1} \sin\left[(\omega_I - 119\omega_0 - 119\Delta\omega)t\right] \quad (268)$$

At the fourth mixer, both doppler and L_1/L_2 frequency compensation are employed such that, when heterodyned by $F_1 + F_1/184$, the carrier is beat down to zero. Again the correction term is denoted by δf_d . Hence, at point (e), the signal can be modeled as

$$x_e(t) = \sqrt{2P} PN(t) PNT(t) d(t) \sin\left[(\omega_0 + \delta\omega_d + 121\Delta\omega)t\right] + \sqrt{2P_I} PNT(t) \sin\left[(121\omega_0 - \omega_I + 12\Delta\omega + \delta\omega_d)t\right] + \sqrt{2P_I L_1} \cos\left[(121\omega_0 - \omega_I + 12\Delta\omega + \delta\omega_d)t\right] + \sqrt{2P_I L_1 L_2} \sin\left[(\omega_I - 119\omega_0 - 119\Delta\omega)t\right] \quad (269)$$

The third term is due to leakage at the third mixer, whereas the fourth term is due to leakage at the fourth mixer

The fifth mixer functions to multiply the input signals by the product of the T and PN codes. At point (f) at the input to the 4-kHz bandwidth filter, we have

$$\begin{aligned}
 x_f(t) = & \sqrt{2P} d(t) \sin \left[(\omega_0 + \delta\omega_d + 121\Delta\omega)t \right] \\
 & + \sqrt{2P_I} PN(t) \sin \left[(121\omega_0 - \omega_I + 121\Delta\omega + \delta\omega_d)t \right] \\
 & + \sqrt{2P_I L_1} PNT(t) PN(t) \cos \left[(121\omega_0 - \omega_I + 121\Delta\omega + \delta\omega_d)t \right] \\
 & + \sqrt{2P_I L_1 L_2} PNT(t) PN(t) \sin \left[(\omega_I - 119\omega_0 - 119\Delta\omega)t \right] \\
 & + \sqrt{2P_I L_1 L_3} \cos \left[(121\omega_0 - \omega_I + 121\Delta\omega + \delta\omega_d)t \right] \\
 & + \sqrt{2P_I L_1 L_2 L_3} \sin \left[(\omega_I - 119\omega_0 - 119\Delta\omega)t \right] \quad (270)
 \end{aligned}$$

Again the fifth and sixth terms are due to mixer leakage. Only those signals of $x_f(t)$ which are passed through the 4-kHz bandwidth bandpass filter are of concern. The correction in L_2 is +7600 Hz, which is contained in $\delta\omega_d/2\pi$ (which includes the doppler component).

Hence, the first term of (270) is centered in the bandpass filter. The second term is spread and, hence, will pass a portion of its signal into the filter. The third and fourth terms are also spread but are at least on the order of 30 dB down from the second term which is also spread. Both the fifth and sixth terms are leakage terms of the interferer; however, the fifth term is at least 30 dB (minimum value of L_2) weaker. Therefore, the essential terms at point (g) are

$$\begin{aligned}
 x_g(t) = & \sqrt{2P} d(t) \sin \left[(\omega_0 + 120\Delta\omega + \delta\omega_d)t \right] \\
 & + \sqrt{2P_I} \tilde{PN}(t) \sin \left[(121\omega_0 - \omega_I + 121\Delta\omega + \delta\omega_d)t \right] \\
 & + \sqrt{2P_I L_1 L_3} \cos \left[(121\omega_0 - \omega_I + 121\Delta\omega + \delta\omega_d)t \right] \quad (271)
 \end{aligned}$$

where $\tilde{PN}(t)$ is the filtered version of $PN(t)$. After heterodyning at the sixth mixer, we obtain

ORIGINAL PAGE IS
OF POOR QUALITY

$$\begin{aligned}
 x_h(t) = & \sqrt{2P} \tilde{d}(t) \cos \left[\left(120\Delta\omega - \frac{\omega_1}{184} + \delta\omega_d \right) t \right] \\
 & + \sqrt{2P_I} \tilde{P}\tilde{N}(t) \cos \left[\left(120\omega_1 - \omega_I + \delta\omega_d - \frac{\omega_1}{184} \right) t \right] \\
 & + \sqrt{P_I L_1 L_3} \sin \left[\left(120\omega_0 - \omega_I + 120\Delta\omega + \delta\omega_d - \frac{1}{184} \right) t \right] \quad (272)
 \end{aligned}$$

Again we see that the leakage term is reduced by two mixer isolation values and, hence, does not significantly degrade the processing gain. If the T code was not used, then in effect $L_1 \rightarrow 1$, and we would have just one mixer's worth of isolation which could be in the 30-35 dB range and, as such, would not be sufficient.

9.5 Conclusions

The TI frequency plan for both L_1 and L_2 frequencies is well thought out and, by use of their T code with good mixers, the processing gain is preserved for both the C/A and P codes

10.0 RESPONSE OF THIRD-ORDER PLL TO STEP IN JERK

This section documents the derivation of the expression for the error response of a third-order phase-lock-loop with a step in jerk input. The error response of the perfect third-order loop is given by

$$\frac{\theta_e(S)}{\theta_1(S)} = \frac{S^3}{S^3 + 2\omega_n S^2 + 2\omega_n S + \omega_n^3} \quad (273)$$

where the loop noise bandwidth is given by $B_L = \omega_n/1.2$. The loop input phase angle for a step in jerk is given by

$$\theta_1(S) = \left(\frac{\theta}{S}\right) \frac{1}{S^3} = \frac{J2\pi f}{C} \frac{1}{S^4} \quad (274)$$

so that the time response is given by

$$\theta_e(t) = \frac{J2\pi f}{C} \mathcal{L}^{-1} \left\{ \frac{1}{S} \frac{1}{S^3 + 2\omega_n S^2 + 2\omega_n S + \omega_n^3} \right\} \quad (275)$$

The Laplace transform pair [17].

$$F(S) = \frac{1}{(S-a)(S-b)(S-c)} \cdot f(t) = Ae^{at} + Be^{bt} + Ce^{ct}$$

where

$$A = \frac{1}{(a-b)(a-c)}, \quad B = \frac{1}{(b-a)(b-c)}, \quad C = \frac{1}{(c-a)(c-b)}$$

is used after factoring the denominator and treating the $1/S$ by integrating the $f(t)$. Thus,

$$\begin{aligned}
 \theta_e(t) &= \frac{J2\pi f}{C} \int_0^t \mathcal{L}^{-1} \left\{ \frac{1}{\left((s + \omega_n) \left(s + \frac{\omega_n}{2} (1 - j\sqrt{3}) \right) \left(s + \frac{\omega_n}{2} (1 + j\sqrt{3}) \right) \right)} \right\} dt \\
 &= \frac{J2\pi f}{C} \int_0^t \frac{1}{\omega_n} \left[e^{-\omega_n t} + e^{-\omega_n t/2} \left\{ \frac{1}{\sqrt{3}} \sin \sqrt{3} \frac{\omega_n t}{2} - \cos \sqrt{3} \frac{\omega_n t}{2} \right\} \right] dt \\
 &= \frac{J2\pi f}{C} \frac{1}{\omega_n} \left[1 - e^{-\omega_n t} - \frac{2\sqrt{3}}{3} e^{-\omega_n t/2} \sin \sqrt{2} \frac{\omega_n t}{2} \right] \quad (276)
 \end{aligned}$$

A normalized plot of (276) is given in Figure 10.1.

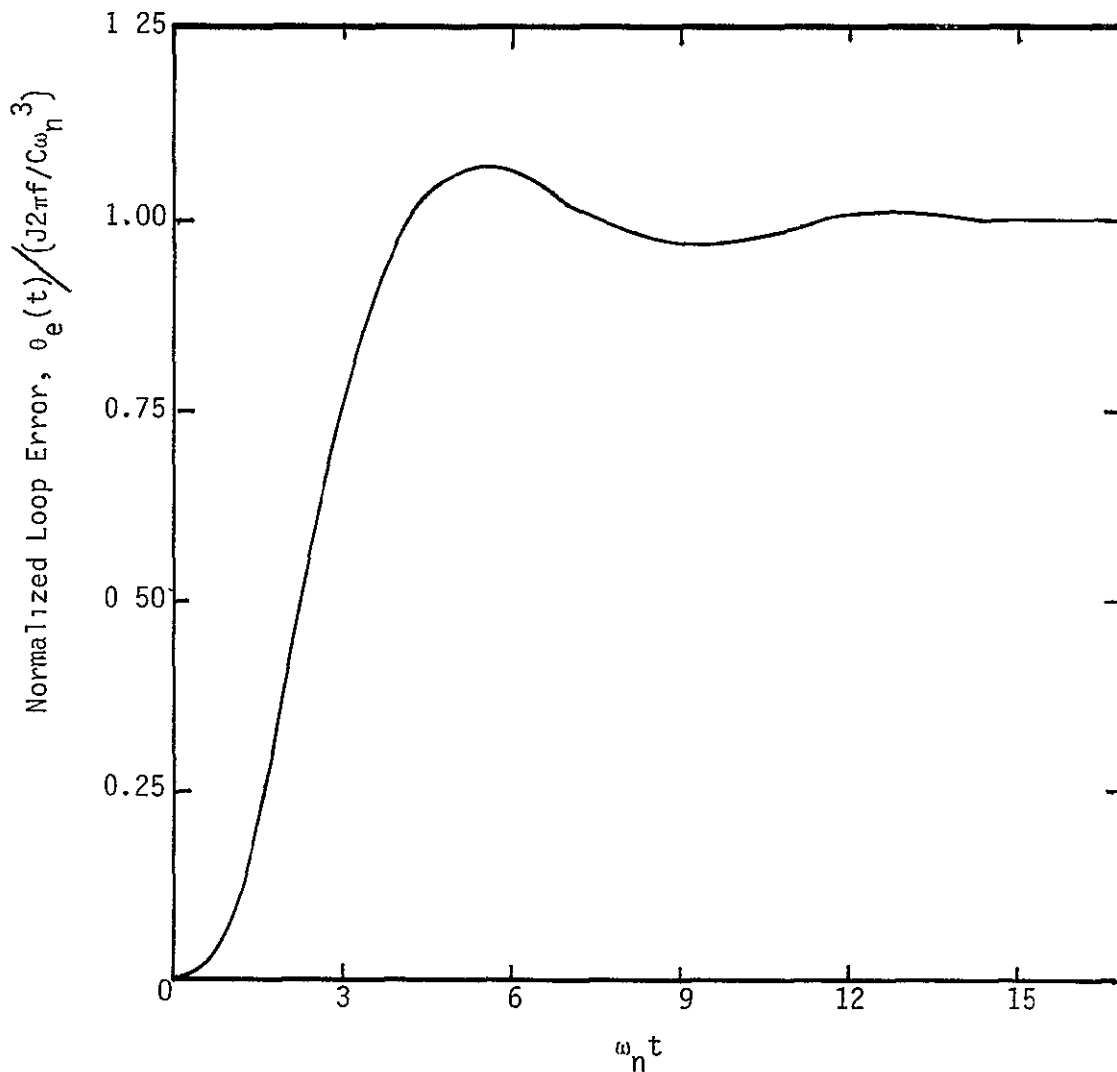


Figure 10.1. Plot of Normalized Loop-Tracking Error for Third-Order Phase-Lock-Loop with Jerk Step Input

11.0 SHUTTLE GPS RECEIVER MINIMUM REQUIRED SNR

This section documents the minimum required C/N_0 derivation for a Shuttle GPS receiver. The minimum C/N_0 is utilized in the following section to calculate the GPS/Shuttle link budget.

The minimum C/N_0 is based on obtaining an acceptable probability of the Costas loop not losing lock during the Shuttle mission. The probability of not losing lock is given by

$$P = e^{-t/\bar{T}}$$

where \bar{T} is the mean time to loop slip and t is the observation or mission duration over which we require the probability P . We have previously shown that the mean time to Costas loop slipping is given by [18]

$$\bar{T} = \frac{\pi}{4B_L} \exp \left[\frac{\pi}{4B_L} \left(\frac{L}{N_0} \right)^2 \left(B + 2 \frac{C}{N_0} \right)^{-1} (1 + \sin 2\phi) \right] \quad (277)$$

where B_L is the loop one-sided noise bandwidth, B is the arm filter bandwidth ≈ 40 kHz, and ϕ is the phase error or offset due to dynamics. The phase error ϕ is dependent on the type of dynamics, i.e., acceleration, jerk, etc., and the order of the loop, i.e., second order, third order, etc. However, we know that, for constant acceleration, the phase error ϕ for a third-order loop is zero. Furthermore, for changing acceleration, or jerk, we have derived the phase error ϕ in Section 10.

Thus, all that remains to be described in order to calculate P is the dynamics profile. The Rockwell GPS/Shuttle specification requires dynamics consisting of 0.02 seconds of jerk equal to 150 m/s^3 , five seconds of jerk equal to 25 m/s^3 , and 900 seconds of acceleration at 40 m/s^2 . If we assume that, for purposes of calculating loss-of-lock probabilities, these three dynamic events are arranged in a contiguous fashion, then the total probability of not losing lock is given by

$$P_T = P_1 P_2 P_s = e^{-t_1/\bar{T}_1} e^{-t_2/\bar{T}_2} e^{-t_3/\bar{T}_3} = e^{-(t_1/\bar{T}_1 + t_2/\bar{T}_2 + t_3/\bar{T}_3)} \quad (278)$$

where

$$\begin{aligned} t_1 &= 0.02 \text{ s} & , & & J_1 &= 150 \text{ m/s}^3 \\ t_2 &= 5 \text{ s} & , & & J_2 &= 25 \text{ m/s}^3 \\ t_3 &= 900 \text{ s} & , & & J &= 0 . \end{aligned}$$

The \bar{T} 's are given by

$$\bar{T}_1 = \frac{\pi}{4B_L} \exp \left[\frac{\pi}{4B_L} \left(\frac{C}{N_0} \right)^2 \left(B + 2 \frac{C}{N_0} \right)^{-1} (1 + \text{SNR} \ 2\phi_1) \right] \quad (279)$$

and

$$\phi_1 = \frac{J_i 2\pi f}{C} \frac{1}{\omega_n^3} \left[1 - e^{-\omega_n t_i} - \frac{2\sqrt{3}}{3} e^{-\omega_n t_i/2} \sin \sqrt{2} \frac{\omega_n t_i}{2} \right] \quad (280)$$

for $i=1,2$ and $\phi_i = 0$ for $i=3$. It should be noted that, for the 900-second period, $\phi = 0$ because we have postulated a third-order loop. The total probability of not losing lock P_T is shown plotted in Figure 11.1 as a function of B_L , with C/N_0 a parameter. It can be seen that a C/N_0 of 27.5 dB-Hz is necessary to achieve a P_T of 0.99 and the optimum bandwidth is $B_L = 13.5$ Hz. If we relax the 900-second interval to 300 seconds, we see that the probability of not losing lock improves slightly. However, since several approximations have been made in deriving (277), it is better to remain on the conservative side. Furthermore, since parts of (277) were originally derived for a first-order loop, it is appropriate to add an additional 1 dB to the result yielded by (278), (279) and (280). This 1 dB is already incorporated into Figure 11.1. Thus, we shall consider the minimum required C/N_0 to be 27.5 dB-Hz plus a 2-dB implementation loss, or 29.5 dB-Hz.

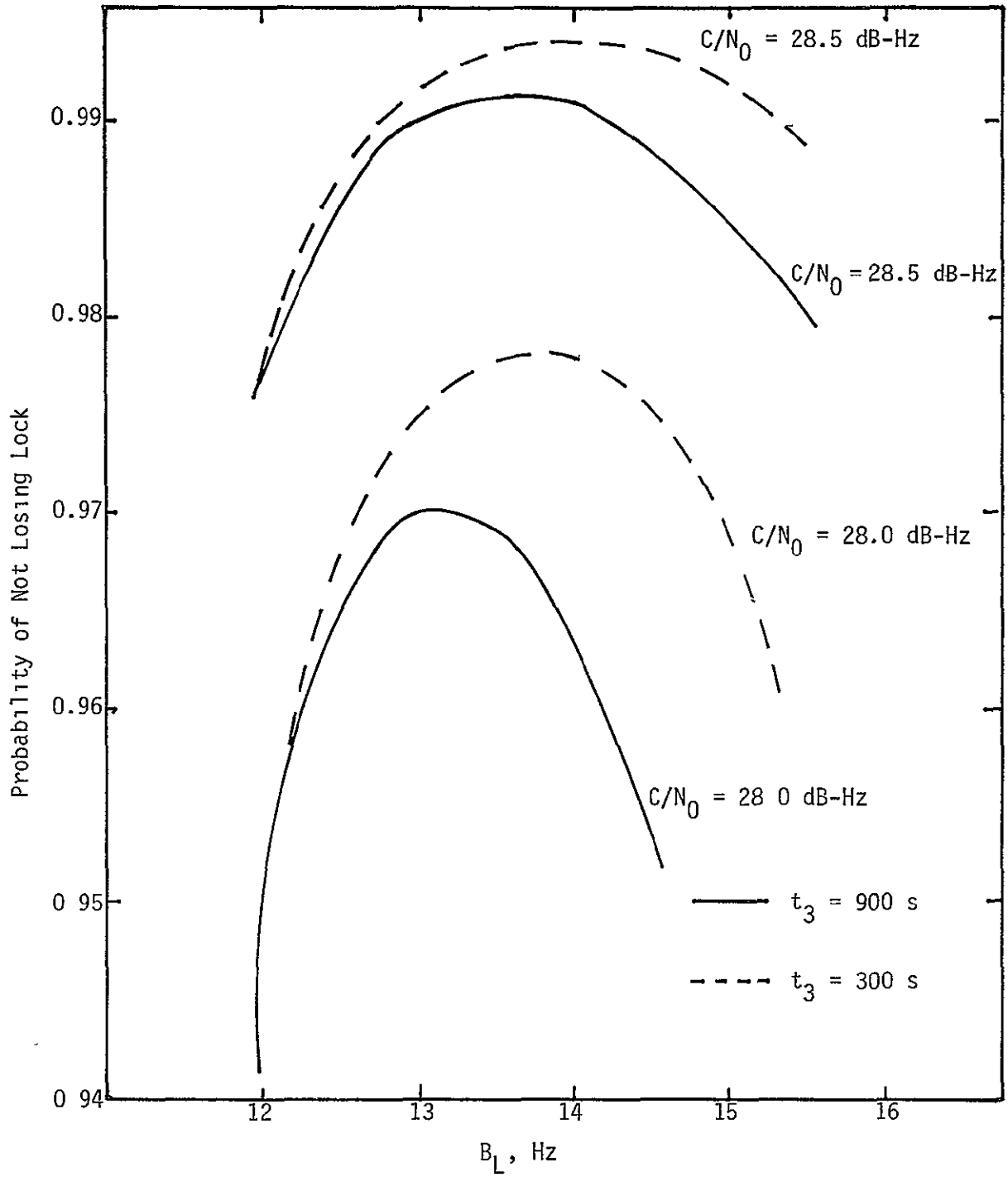


Figure 11.1. Probability of Not Losing Lock

12.0 SHUTTLE/GPS LINK BUDGET

This section presents an update on the Shuttle/GPS link budget. The link chosen is the on-orbit (200 nmi) L_1 link using the Orbiter upper GPS antenna. The budget for both a continuous-channel receiver and a four-satellite multiplex receiver is given in Table 12.1. The link margin for the continuous receiver is shown to be 4.2 dB, while the multiplex receiver has a margin of -1.8 dB. An explanation of each of the entries in the budget follows.

12.1 GPS/Shuttle Link Budgets

12.1.1 Satellite EIRP

These values are for the edge-of-earth coverage, as specified in GPS Space Segment Specification No. CID-SV-101. The actual performance of the two on-orbit spacecraft has been reported to be better than the specification values.

12.1.2 Space Loss

The two space loss numbers of -184.6 and -182.4 dB for L_1 and L_2 , respectively, are based on the orbital geometry shown in Figure 12.1. From this figure, the line of sight (LOS) is given by

$$R = 26,650 \cos \left[\sin^{-1} \frac{6698}{26,650} \right] = 25,795 \text{ km}$$

The space loss is given by

$$\begin{aligned} L &= 92.45 + 20 \log f \text{ (GHz)} + \log R \text{ (km)} \\ &= 92.45 + 40 \log 1.575 + 20 \log 25,795 \\ &= 184.6 \text{ dB} . \end{aligned}$$

* Information source: RI Memo #1024-20, Glen Yates, May 8, 1981.

Table 12.1. Shuttle/GPS Link Budget Update

	Continuous Tracking		Multiplex Tracking
Satellite EIRP		Spec CID-SV-101	23.8 dBW
Space Loss	-184.6 dB	Path tangent to orbit	-184.6 dB
Pointing Loss	-0.4 dB	See text	-0.4 dB
Polarization Loss	0.1 dB	See text	0.1 dB
Atmospheric Loss	0		0
Shuttle Antenna Gain	-4.0 dB		4.0 dB
Received Power	-165.3 dBW		-165.3 dB
System Noise Temperature	28.6 dBW	See text	28.6 dBK
Boltzmann's Constant	-228.6 dB-W/K/Hz		-228.6 dB-W/K/Hz
Noise Spectral Density	-200.1 dB-W/Hz		-200.0 dB-W/Hz
C/N ₀	34.7 dB-Hz		34.7 dB-Hz
Time-Sharing Loss	0		-6.0 dB
Effective C/N ₀	34.7 dB-Hz		28.7 dB-Hz
Required C/N ₀ (Theoretical)	28.5 dB-Hz	See Section 11	28.5 dB-Hz
Implementation Loss	2.0 dB		2.0 dB
Required C/N ₀	30.5 dB		30.5 dB
Link Margin*	4.2 dB		

* Assumes no loop-tracking aiding

ORIGINAL PAGE IS
OF POOR QUALITY

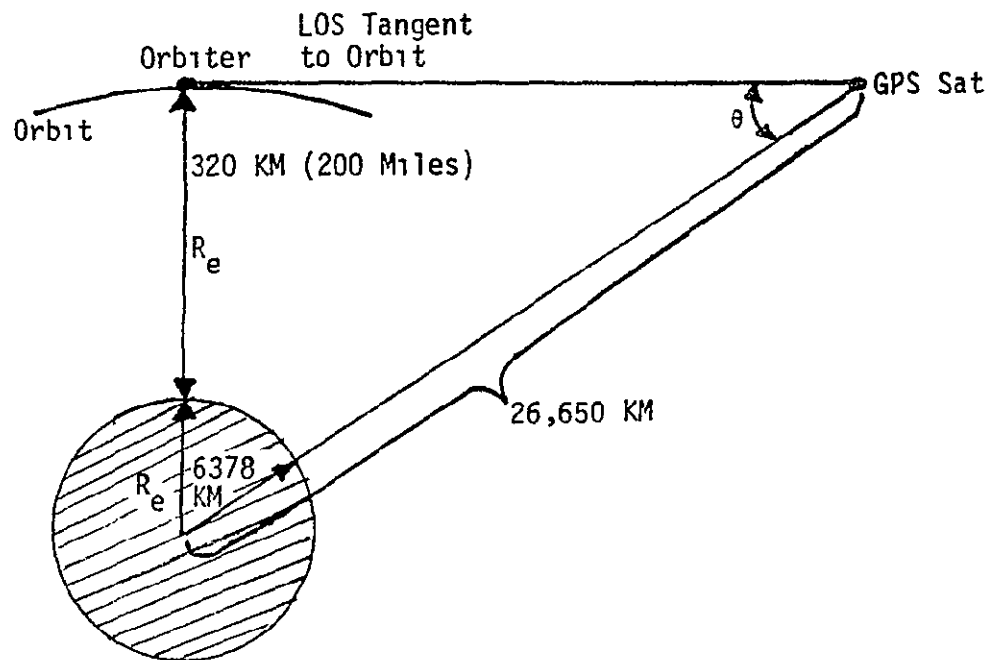


Figure 12.1. Geometry for Shuttle/GPS Link Space-Loss Calculation

This geometry, called LOS tangent-to-orbit, is considered a nominal baseline case. Some links, such as the overhead viewing links, will have less space loss and other links, such as those where the Orbiter may be in higher orbits and viewing tangent to the earth (or the earth's atmosphere), will have greater loss.

12.1.3 Pointing Loss

The pointing loss value of -0.4 dB occurs because the GPS satellite antenna coverage is designed to provide maximum radiated power at the edge of the earth. Since the Orbiter is some 200 miles above the edge of the earth, there is a reduction in EIRP. The GPS satellite antenna pattern for FSV #1 has a gain slope of approximately 0.5 dB/°. From Figure 12.2, the angle seen by the GPS satellite antenna is 0.72° for the 200-mile Shuttle orbit. Thus, the EIRP loss is equal to 0.5 dB x 0.72° ≈ 0.4 dB.

12.1.4 Polarization Loss

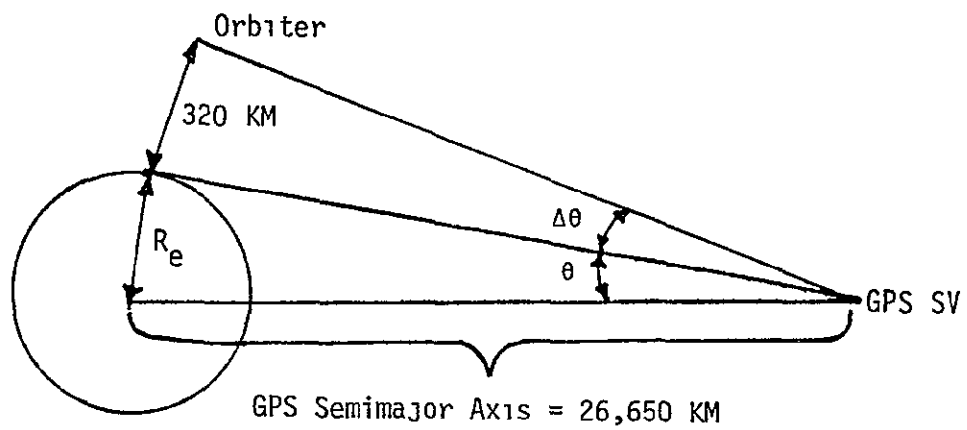
The polarization loss occurs because the GPS antenna and Orbiter GPS antenna are not perfectly circular polarized. The GPS satellite antenna is specified to have an axial ratio no greater than 0.8 [19]. The GPS satellite axial ratio is specified at a maximum of 0.7 dB at edge-of-earth coverage, or 14.3°. At the Shuttle-look angle of 15° (see Figure 12.2), the axial ratio is not expected to change much. The actual maximum polarization loss will be the polarization loss difference between the GPS antenna against the JSC test horn and between the GPS antenna against the GPS satellite*. Thus,

$$L_p = 10 \log \frac{(R_{GPS \text{ SAT}} + R_{GPS \text{ ANT}})^2}{(1 + R_{GPS \text{ SAT}}^2)(1 + R_{GPS \text{ ANT}}^2)} - 10 \log \frac{(R_{TEST \text{ HORN}} + R_{GPS \text{ ANT}})^2}{(1 + R_{TEST \text{ HORN}}^2)(1 + R_{GPS \text{ ANT}}^2)}$$

where $R_{GPS \text{ SAT}} = 0.7 \text{ dB}$, $R_{GPS \text{ ANT}} = 12 \text{ dB}$ and $R_{TEST \text{ HORN}} = 0.5 \text{ dB}$. The $R_{GPS \text{ ANT}} = 12 \text{ dB}$ is based on extrapolation of the test data at $\theta = 60^\circ$, $R = 11.5 \text{ dB}$ [20]. From this calculation, the polarization loss is found to be 0.06 dB and, because of the extrapolation uncertainty of $R_{GPS \text{ ANT}}$, we use $L_p = 0.1 \text{ dB}$.

*This formulation was suggested by J. Porter of JSC.

ORIGINAL PAGE IS
OF POOR QUALITY



$$\Delta\theta = \tan^{-1} \left[\frac{320 \tan \theta}{R_e} \right]$$

$$\theta = \sin^{-1} \left[R_e / 26,650 \right]$$

$$\Delta\theta \approx 0.72^\circ$$

Figure 12.2. Derivation of Off-Axis Pointing Error for Orbiter in 200-Mile Orbit

12.1.5 Antenna Gain

The 4-dB gain is with respect to perfect RHCP and has been chosen by Rockwell to give the desired angular coverage. It is based on prototype antenna measurements. It should be noted that a decrease in overall actual antenna gain can translate into a decrease in antenna coverage volume, rather than a decrease in link margin.

12.1.6 Circuit Loss

The circuit losses used for the link budget calculations have been provided by RI and are given in Table 12.2. Two types of losses are given: the loss from the antenna to the preamplifier and that from the preamplifier to the receiver. The latter loss includes a 6-dB power-splitting loss for adding a third-string receiver. Although the baseline link design is a two-string system, it is cost effective to install and connect the necessary power splitters for a three-string system.

Table 12.2. RF Circuit Loss*

Antenna Circuit	Antenna Circuit (L ₁) (dB)	PA/RPA Circuit (L ₂) (dB)
Upper Antenna	1.84	14.0

12.1.7 System Noise Temperature

The SNR required for all GPS receiver processing functions is proportional to C/kT_e (C/N_0), where C is the available signal power, k is Boltzmann's constant, and T_e is the effective noise temperature. Since the Shuttle GPS receiving system is comprised of a cascade of elements, it is necessary to derive the effective noise temperature T_e for the desired point for the definition of C/kT_e .

The Shuttle GPS system is modeled in the block diagram shown in Figure 12.3. As will be shown, it is inconsequential as to which point is picked as a reference point for definition of C/N_0 since the ratio is constant, i.e., independent of the point in the circuit. A generalized model of a cascaded system is used to illustrate this point. This model is shown in Figure 12.4. The effective noise temperature at the input to the cascade, T_e , is given by

$$T_e = T_1 + \frac{T_2}{G_1} + \frac{T_3}{G_1 G_2} + \frac{T_4}{G_2 G_2 G_3} + \dots$$

* Information source: RI Memo #1024-20, Glen Yates, May 8, 1981.

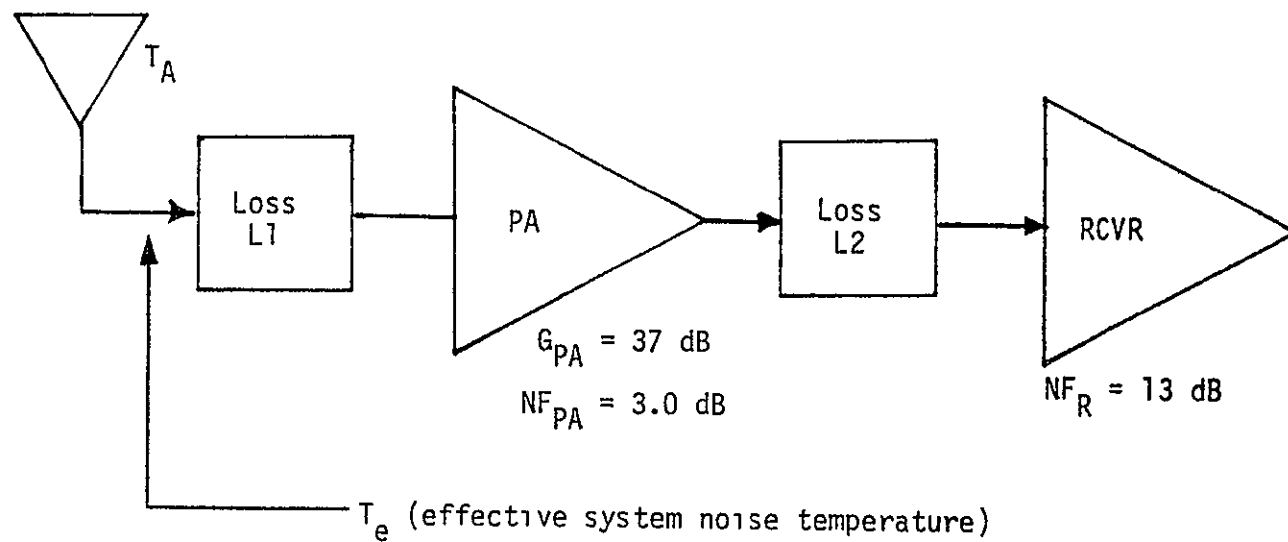
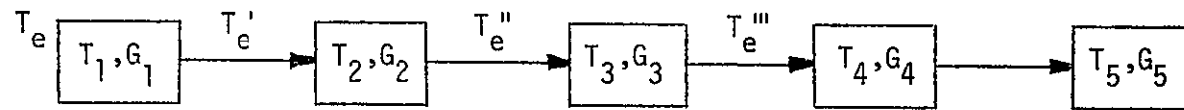


Figure 12.3. System Block Diagram for Calculation of System Noise Temperature



$$T_{A,1} \quad (L_1 - 1)T_0, \frac{1}{L_1} \quad (NF_{PA} - 1)T_0, G_{PA} \quad (L_2 - 1)T_0, \frac{1}{L_2} \quad NF_{RPA}$$

$$T_e = T_1 + \frac{T_2}{G_1} + \frac{T_3}{G_1 G_2} + \frac{T_4}{G_1 G_2 G_3} + \dots$$

$$T_{e'} = T_1 G_1 + T_2 + \frac{T_3}{G_2} + \frac{T_4}{G_2 G_3} + \dots$$

Figure 12.4. General Mode of System Noise Temperature for Cascaded Elements

and the input signal power is C . Now, to find the system effective noise temperature at point (2), T_e' , we note that noise at (2) from the input to the first box will have been increased by the gain of this box, G_1 . Thus,

$$T_e' = G_1 T_e = T_1 G_1 + T_w + \frac{T_3}{G_2} + \frac{T_4}{G_2 G_3} + \dots$$

Similarly, the signal power at (2) is increased by G_1 so that $C' = G_1 C$ and the SNR is given by

$$\frac{C'}{KT_e'} = \frac{G_1 D}{KG_1 T_3} = \frac{C}{KT_e}$$

which, of course, is the same as the SNR at the input to the cascade. The same reasoning can be applied to show that the SNR at (3) is also the same by multiplying both signal and noise at (2) by gain G_3 . The noise temperature at (3) is given by

$$T_e'' = T_1 G_1 G_2 + T_2 G_2 + T_3 + \frac{T_4}{G_3} + \dots$$

The generalized model of Figure 12.4 is now applied to the Shuttle GPS system. Box 1 is taken as the antenna with temperature T_A , box 2 is the loss between the antenna and preamp, L_1 , box 3 is the preamp, box 4 is the loss between the preamp and the receiver, L_2 , and box 5 is the receiver. The equivalent noise temperature of an active element of noise figure NF and gain G is given by $T = (NF - 1)T_0$, where T_0 is the reference temperature (290°K). The noise temperature of a passive element of loss L and gain $G = 1/L$ is given by $T = (L - 1)T_0$. Thus, the equivalent noise temperature of the GPS system at the antenna terminal (T_e') is given by

$$T = T_A + (L_1 - 1)T_0 + \frac{(NF_{PA} - 1)T_0}{\frac{1}{L_1}} + \frac{L_2 - 1}{\frac{1}{L_1} G_{PA}} T_0 + \frac{(NF_{RPA} - 1)T_0}{\frac{1}{L_1} \frac{1}{L_2} G_{PA}}$$

The system noise temperature and the signal power in the link budgets which follow are referenced to the GPS antenna terminals. Therefore, the system signal power-to-noise density ratio is written as

$$\frac{C}{N_0} = \frac{C}{kT_0 \left[\frac{T_A}{T_0} + (L_1 - 1) + L_1(NF_{PA} - 1) + L_1 \frac{L_1 - 1}{G_{PA}} + \frac{L_1 L_2 (NF_{RPA} - 1)}{G_{PA}} \right]}$$

The system equivalent noise temperatures for the GPS system have been calculated for the antenna and loss combination using the parameters $NF_{PA} = 3.0$ dB, $G_{PA} = 40$ dB, $NF_{RPA} = 24$ dB, and $L_1, L_2 =$ values given in Table 12.1. The equivalent noise temperature for the upper antenna, with an antenna temperature of 125°K , is found to be 722.4°K , or 28.6 dB- $^\circ\text{K}$. The required C/N_0 is derived in Section 11, and is 28.5 dB-Hz. The implementation loss is 2 dB, and is documented in [19].

REFERENCES

1. J. K. Holmes, "GPS Time-Sharing Code-Tracking Performance Losses," Axiomatix Technical Memorandum No. M8103-2, March 9, 1981.
2. J. K. Holmes, "GPS Carrier-Loop Time-Sharing Loss," Axiomatix Technical Memorandum No. M8106-2, June 11, 1981.
3. Texas Instruments Viewgraph Presentation of Receiver for the Early GPS Receiver, dated January 18, 1980.
4. Texas Instruments Presentation for the New GPS Receiver, undated (early 1981).
5. P. Ward, "An Advanced NAVSTAR GPS Multiplex Receiver," IEEE 1980 Position Location and Navigation Symposium, December 9, 1980.
6. P. Ward of TI, private communications.
7. J. K. Holmes and S. R. Buddle, "GPS Receiver Simulation and Software Verification," 1980 International Telemetry Conference, San Diego, California, page 497.
8. J. J. Spilker, Jr., Digital Communications by Satellite, Prentice-Hall, Englewood Cliffs, New Jersey, 1977.
9. J. K. Holmes, Coherent Communication with Applications to Pseudo-Noise Spread Spectrum Synchronization, to be published by Wiley Interscience, 1981.
10. L. B. W. Jolly, Summation of Series, Second Revised Dover Edition, New York, 1961.
11. P. Ward, "An Advanced NAVSTAR GPS Multiplex Receiver," 1980 PLANS (Position Location and Navigation Symposium) Conference, Atlantic City, New Jersey, December 9, 1980, pp. 51-58.
12. R. V. Hogg and A. T. Craig, Introduction to Mathematical Statistics, Chapter 6, MacMillan Co., New York.
13. J. K. Holmes and C. C. Chen, "Acquisition Time Performance of PN Spread-Spectrum Systems," IEEE Trans on Comm., Vol. COM-25, No. 8, August 1977.
14. J. K. Holmes, "Mean Time to Sweep the S-Band Shuttle PN Code Once with Data Off," Axiomatix Report No. R8010-4, October 6, 1980.
15. P. Nilsen, "Shuttle Global-Positioning System (GPS) System Design Study," Axiomatix Final Report No. R7901-4, January 20, 1979.

16. P. Nilsen and J. K. Holmes, Axiomatix Presentation entitled "A Review of Axiomatix's GPS Receiver Evaluation Activity," dated August 11, 1981.
17. G. A. Korn, Mathematical Handbook for Scientists and Engineers, McGraw-Hill, page 909.
18. P. Nilsen, "An Investigation of the Shuttle GPS Receiver Threshold Performance," Axiomatix Report No. R8004-1, April 15, 1980.
19. "Air Force Prime-Item Development Specification for the Space Vehicle of the Space Vehicle System Segment of the NAVSTAR Global Positioning System, Phase I."
20. "Shuttle Orbiter Hemi/GPS and Payload Orbiter Data," Job Order No. 13-339 NASA No. EE3-81-14112, August 1981.

APPENDIX A

REVIEW OF TACAN/GPS INTERFERENCE

APPENDIX A
REVIEW OF TACAN/GPS INTERFERENCE

1.0 INTRODUCTION AND SUMMARY

This appendix provides an updated assessment of the interference effects from the Orbiter TACAN transmitter to the Orbiter GPS navigation system. Previous memoranda on this subject reported that the TACAN interference was not a serious problem if the GPS preamplifier did not saturate [1]. Here we extend those analyses to the case of a saturating GPS preamplifier. The conclusion reached is that the TACAN interference is not a problem, even with a saturating preamplifier; however, recommendations for rather benign filter characteristics to be included in the preamplifier specification are made, along with several other preamplifier parameter specification recommendations.

2.0 ANALYSIS

The block diagram of the system analyzed is given in Figure A.1. We begin by considering the TACAN signal. A good model for the TACAN pulse train is a raised cosine pulse train. Figure A.2 shows the similarity between the actual TACAN pulse and the raised cosine pulse. The raised cosine pulse train (baseband) can thus be expanded in a Fourier series and written as

$$P(t) = \sum_{n=-\infty}^{n=+\infty} D_n \exp(j n \pi \frac{t}{T}) \quad (1)$$

where

$$D_n = \frac{1}{2} A \frac{t_0}{T} \frac{\sin\left(n \pi \frac{t_0}{T}\right)}{\left(n \pi \frac{t_0}{T}\right) \left[1 - \left(\frac{nt_0}{T}\right)^2\right]} \exp(j\phi_n) \quad (2)$$

with

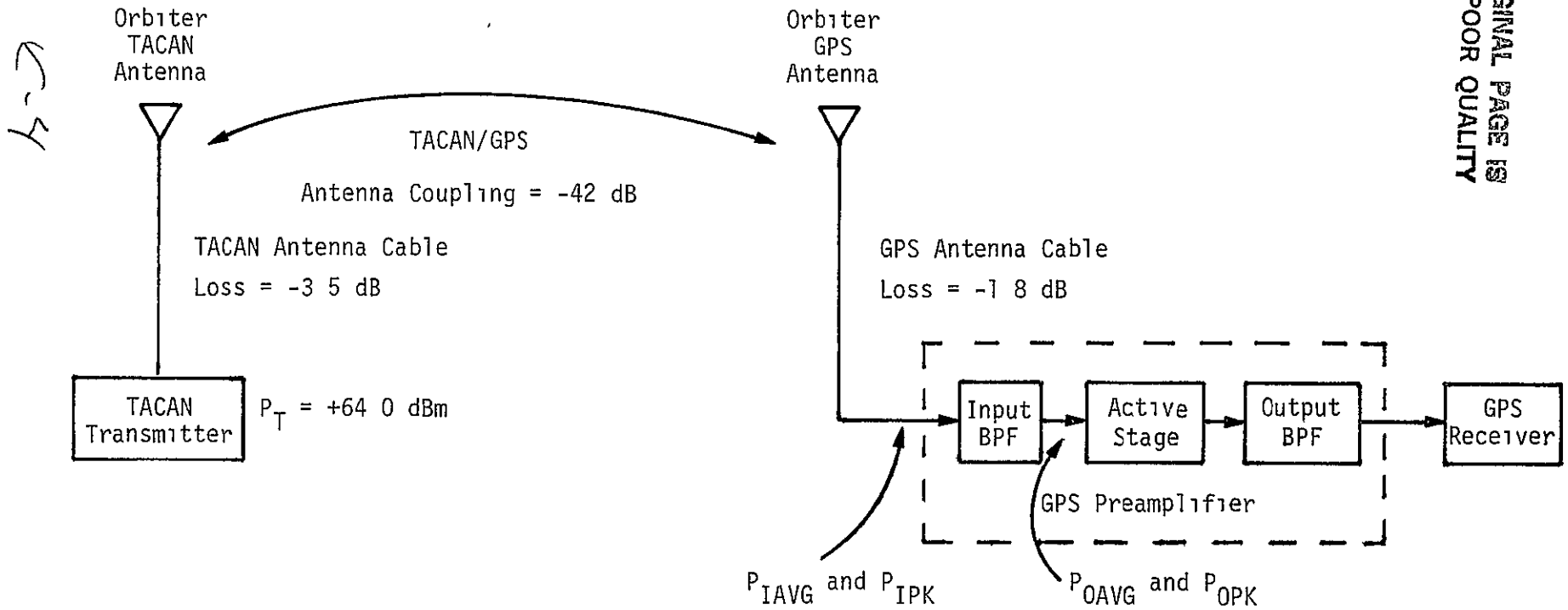
$$t_0 = 2.5 \times 10^{-6} \text{ seconds (from Figure 2),}$$

$$T = 1/150, \text{ 150 pulses per second is the TACAN rep rate,}$$

$$A = \text{peak voltage level corresponding to +64.0 dBm pulse power,}$$

and

$$\phi_n = \text{phase of the Fourier component.}$$



ORIGINAL PAGE IS OF POOR QUALITY

Figure A 1. Block Diagram of System Analyses

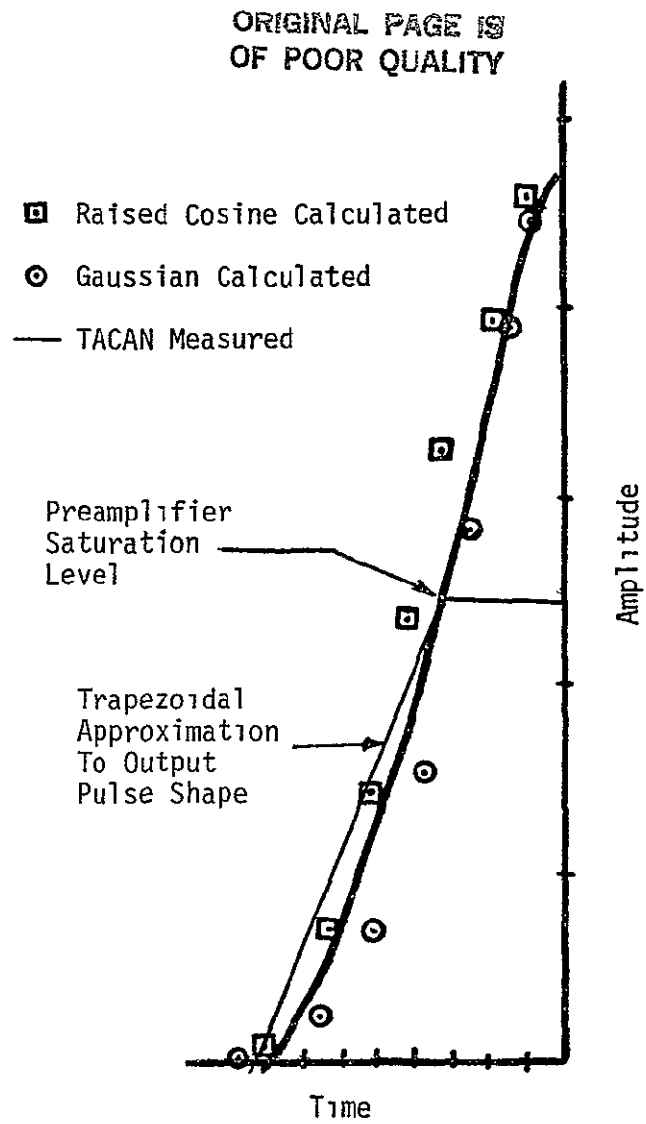


Figure A.2. Measured TACAN Pulse Shape Compared with Calculated Pulse Shapes

The RF expansion is given by

$$V(t) = P(t) \left[\sqrt{2} \cos \omega_0 t \right] = \sqrt{2} \cos \omega_0 t \sum_{-\infty}^{\infty} D_n \exp \left[j n \pi \frac{t}{T} \right] \quad (3)$$

where D_n is recognized as the value of the spectral lines of the TACAN pulse train.

The signal $V(t)$ is filtered by the preamplifier input bandpass filter $H_f(j\omega)$. In order to numerically evaluate the effect of this filter, the filter characteristic shown in Figure A.3 was used. This filter is the manpack preamplifier (Magnavox) filter and is also the same filter used in the GPSPAC preamplifier.

The average input power to the preamplifier filter is given by

$$P_{IAVG} = \frac{1}{T} \int_0^T |V(t)|^2 dt = \sum_{-\infty}^{\infty} |D_n|^2 \quad (4)$$

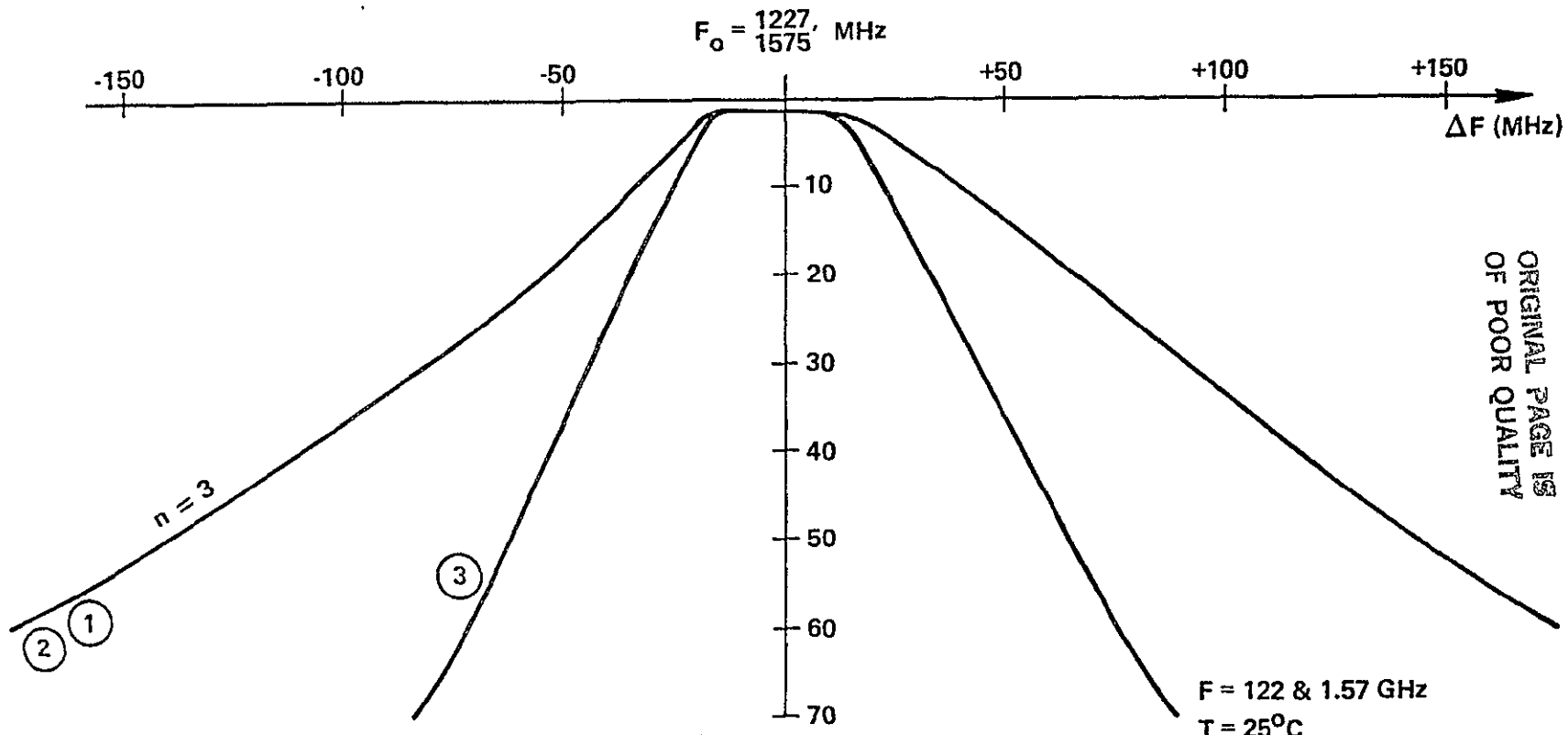
and the average filter output power is given by

$$P_{OAVG} = \sum_{-\infty}^{\infty} |D_n|^2 \left| H \left[\left(f - \left(f_1 + n \pi \frac{t}{T} \right) \right) \right] \right|^2 \quad (5)$$

where f_1 is the TACAN center frequency (1150 MHz). Evaluation of (5) was performed on a computer, where the summation was done over an equivalent bandwidth of approximately 120 MHz. Interestingly, it was found that the output power calculated from (5) was within 0.1 dB of the power calculated by weighting the average input power with the filter gain at the TACAN center frequency, i.e.,

$$P_{OAVG} \cong P_{IAVG} |H(f = 1150 \text{ MHz})|^2 = P_{IAVG}(\text{dB}) - 24 \text{ dB} \quad (6)$$

The average input power for the raised cosine pulse train is related to the peak input power by



	<u>n</u>	<u>BW₃</u>	<u>BW₅₀</u>	<u>I_L</u>	<u>BW₇₀</u>
IN (1)	3	35	260	0.75	
OUT (2)	3	35	260	1.4	
IN & OUT (3)	3+3	33	150	—	200

ORIGINAL PAGE IS
OF POOR QUALITY

Figure A.3. Pre-amplifier Bandpass Filter Characteristics

$$P_{AVG} = \frac{3}{8} P_{PK} \frac{t_0}{T} \quad (7)$$

The average and peak powers at the filter output, or active stage input, are thus calculated to be

$$P_{OAVG} = -45.8 \text{ dBm} \quad \text{and} \quad P_{OPK} = -7.3 \text{ dBm} \quad (8)$$

where the basic calculation is shown in Table A.1 below.

Table A.1. Calculation of Power Input to Preamplicifier Active State

TACAN Transmitter Peak Power	+64.0 dBm	(Rockwell)
TACAN Cable Loss	- 3.5 dB	(Rockwell)
Antenna Isolation	-42.0 dB	(JSC)
GPS Cable Loss	- 1.8 dB	(Rockwell)
Preamplicifier Input Filter Loss	-24.0 dB	(Magnavox)
Preamplicifier Peak Power Input To Active Stage	-7.3 dBm	
$\frac{3}{8} \frac{t_0}{T}$	-38.5 dB	
Preamplicifier Average Power Input to Active Stage	-45.8 dBm	

It is obvious that, on an average-power basis, the TACAN signal presents no danger of damage to the preamplicifier. Furthermore, on a peak-power basis, provided that the preamplicifier has a damage threshold no lower than +13 dBm, there is no danger of damage to the preamplicifier (20 dB margin).

In order to determine the effect of the TACAN signal on the GPS receiver following the preamplicifier, it is first necessary to consider if the preamplicifier is saturated by the TACAN pulses. We will consider the preamplicifier saturation point to be the 1 dB gain compression point +3 dB.

In a previous report, we saw that a typical 1 dB gain compression point is approximately -15 dBm so that the saturation point is approximately -12 dBm. Thus, the -7.3 dBm peak power at the input to the preamplifier active stage will cause some clipping, as shown in Figure A.3. A reasonable way to model the clipped raised cosine pulse is as a trapezoidal pulse, as shown in Figure A.4. This is a conservative model for the interference analysis. The value of the Fourier coefficient that determines the TACAN power in the spectral lines is given by

$$D_n = A \left(\frac{t_0+t_1}{T} \right) \frac{\sin\left(\pi n \frac{t_1}{T}\right) \sin\left(\pi n \frac{t_0+t_1}{T}\right)}{\left(\pi n \frac{t_1}{T}\right) \pi n \left(\frac{t_0+t_1}{T}\right)} \quad (9)$$

If we allow $\sin^2(\) = 1/2$ as a worst case, we find that

$$|D_n| = \frac{A^2}{(\pi n)^4 \left(\frac{t_1}{T}\right)^2} \quad (10)$$

so that the power falls off as the inverse of the frequency to the fourth power as compared to the inverse of the frequency to the sixth power for the raised cosine pulse train. As a worst-case assumption, we have that the peak power in the trapezoidal pulse is the raised cosine pulse (-7.3 dBm). Thus, the power in the spectral line centered at 1227 MHz ($n = 77 \times 10^6 / 150$) is found to be approximately -187 dBm. This is an insignificant amount of power compared to the GPS signal of at least -140 dBm. Furthermore, the power density of the TACAN lines in the receiver bandwidth is approximately

$$N_{\text{OBW}} = -187 - 10 \log 150 = -209 \text{ dBm-Hz} \quad (11)$$

where the 150-Hz line spacing arises from the 150 pulse-per-second repeat rate. This power density is significantly lower than the thermal noise power density. Thus, even though the preamplifier clips the raised cosine TACAN pulse, the spectral components that fall within the GPS receiver

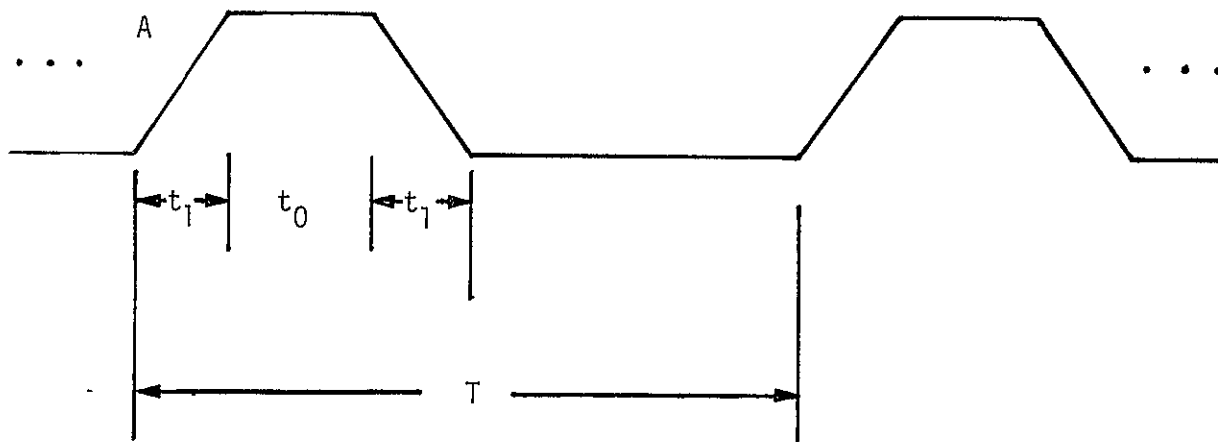


Figure A.4. Trapezoidal Wave Approximation to Saturated Preamplifier TACAN Pulse Output

ORIGINAL PAGE IS
OF POOR QUALITY

bandwidth centered at 1227 MHz do not affect the receiver performance. This holds true for either the P or C/A code. It should be noted that, because of the doublet nature of the TACAN pulse train, the actual average power will be 3 dB greater than calculated herein. However, the 3-dB difference does not affect the conclusions whatsoever.

3.0 SUMMARY OF TECHNICAL MEETING WITH ROCKWELL INTERNATIONAL (RI) ON TACAN/GPS INTERFERENCE

A meeting was held on May 11, 1981 with P. Nilsen, E. Rosen, M. Reuterma, G. Yates, K. Barry and F. Hybart to discuss Axiomatix's recommendations on this problem. The following is a summary of the meeting.

Axiomatix presented a review of its latest analysis of the TACAN/GPS interference* as well as a summary of my recommendations for the preamp specification. The most important of these are as follows:

(1) Based on the 42-dB of measured antenna isolation, nothing needs to be done to the GPS system design as far as high-power limiters or blanking provisions are concerned.

(2) The preamp specification should include, as a minimum, a three-pole filter both preceding and following the active stage (filter specification as per Section 2.0, Appendix A).

Rockwell was in agreement with these recommendations except that they objected to the 0.75-dB insertion loss of the three-pole filter. Upon further discussion, it was stated that the most current RI GPS/Shuttle circuit margin calculations do not include insertion loss for this filter. The additional 0.75-dB loss would result in a less-than-satisfactory calculated margin (according to RI). The RI margin was stated to be based on a preamplifier noise figure of 1.8 dB and 40 dB of preamplifier gain. Rockwell has calculated the overall system noise temperature to be 155°K, or an equivalent overall system noise figure of 1.86 dB. The Axiomatix position on this noise figure, as stated at the meeting, is that these numbers are not realistic program numbers, but represent performance which might be attainable from a high-risk development program.

*"TACAN/GPS Interference Analysis for GPS-Saturated Preamplifier," P. Nilsen, Axiomatix Report No. R8103-1, March 31, 1981.

Further discussion resulted in the following Axiomatix recommendations:

(1) Axiomatix will reevaluate the C/N_0 requirements for Shuttle GPS.

(2) Axiomatix will review/recalculate the link circuit margins for Shuttle GPS.

(3) Axiomatix will talk to NASA about getting a standard link (i.e., space loss) for GPS/Shuttle circuit margin calculations. This was done once by Axiomatix approximately four years ago, but it's time to review it and get concurrence among NASA, RI and Axiomatix.

Axiomatix commented on the RI preamp specification and stated that the filter characteristics should be specified to at least meet our recommendations and that the preamp filter should be broken down into input and output characteristics, not just a composite characteristic. Furthermore, Axiomatix recommended including detailed information on the TACAN EMI characteristics, e.g., peak power at the preamp input terminal, pulse shape, and PRF. The peak power included in the specification should include a 4-dB margin.

At the conclusion of the meeting, Axiomatix made the final recommendation that all elements of Rockwell's circuit margin calculation be kept in a controlled document. Although we're not sure what the official vehicle is for this, we feel it is necessary so that any future changes in cable losses, antenna gains, etc., can be adequately and timely reflected in everyone's understanding of the link margins.

4.0 RECOMMENDATIONS

As a result of the TACAN/GPS interference analysis, Axiomatix recommends that the Shuttle GPS preamplifier specification include the following provisions:

(1) Maximum-allowable input power for no damage--the preamplifier shall tolerate, with no damage, input power levels up to and including +15 dBm (in center of passbands).

(2) A 1-dB gain compression point (referenced to the preamplifier) \geq -15 dBm.

(3) Preamplifier filter characteristics:

(a) Input filter

Center frequency = 1227 MHz and 1575 MHz

Minimum of three poles

3-dB bandwidth = 35 MHz

50-dB bandwidth = 260 MHz

Insertion loss \leq 0.75 dB

Rolloff \geq 18 dB/octave

(b) Output filter

Same as input filter except that insertion loss can be relaxed to 1.50 dB.

Axiomatix further recommends that no provision for pulse blanking or high-power limiting be added to the preamplifier.

Reference

1. "Shuttle Global Positioning System (GPS) System Design Study," Axiomatix Final Report on Contract NAS 9-15387C No. R7901-4, January 20, 1979.

APPENDIX B

REVIEW OF GPS PHASE IIB PROGRAM TESTING

APPENDIX B

REVIEW OF GPS PHASE IIB PROGRAM TESTING

1.0 INTRODUCTION AND SUMMARY

On May 29, 1981, Bruce Jamison, the Magnavox Phase IIB GPS Program Manager, briefed Axiomatix on the Phase IIB testing approach. This appendix summarizes that briefing. The purpose of the briefing was to develop parallels for Shuttle/GPS testing.

The major testing phases are depicted in the flowchart shown in Figure B.1. Testing begins with the "In-Plant Performance Tests" (IPPT's). The IPPT's consist of software as well as hardware tests and are designed to confirm the design and evaluate the performance and functional operation of the user equipment with simulated signals, host-vehicle interfaces and controls that, to the greatest extent practicable, emulate the operating conditions of the intended host vehicle. These tests include software Preliminary Qualification Test (PQT) as well as hardware qualification and acceptance testing. Essential to the tests is the Peculiar Support Equipment (PSE) whose block diagram is shown in Figure B.2. This PSE is an "all out", no-holds-barred, system simulator. It includes simulation of user vehicle motion, satellite motion, antenna shadowing, antenna and ionospheric effects, the usual waveform generation for up to eight satellites and other functions shown in Figure B.2.

Following the in-plant testing, the Development Test and Evaluation (DT&E) and the System Integration Laboratories (SIL) testing commences. In actuality, the SIL testing commences before completion of in-plant testing, with testing performed on engineering model hardware and interim software. The SIL testing is performed for each platform and utilizes a simulator of the platform interface which is provided by the platform contractor or system integration contractor. This test could be a multiple-phase test, starting with I/O verification using interim software and, perhaps, using breadboard or engineering model hardware. The final phase SIL test must be performed with the final software.

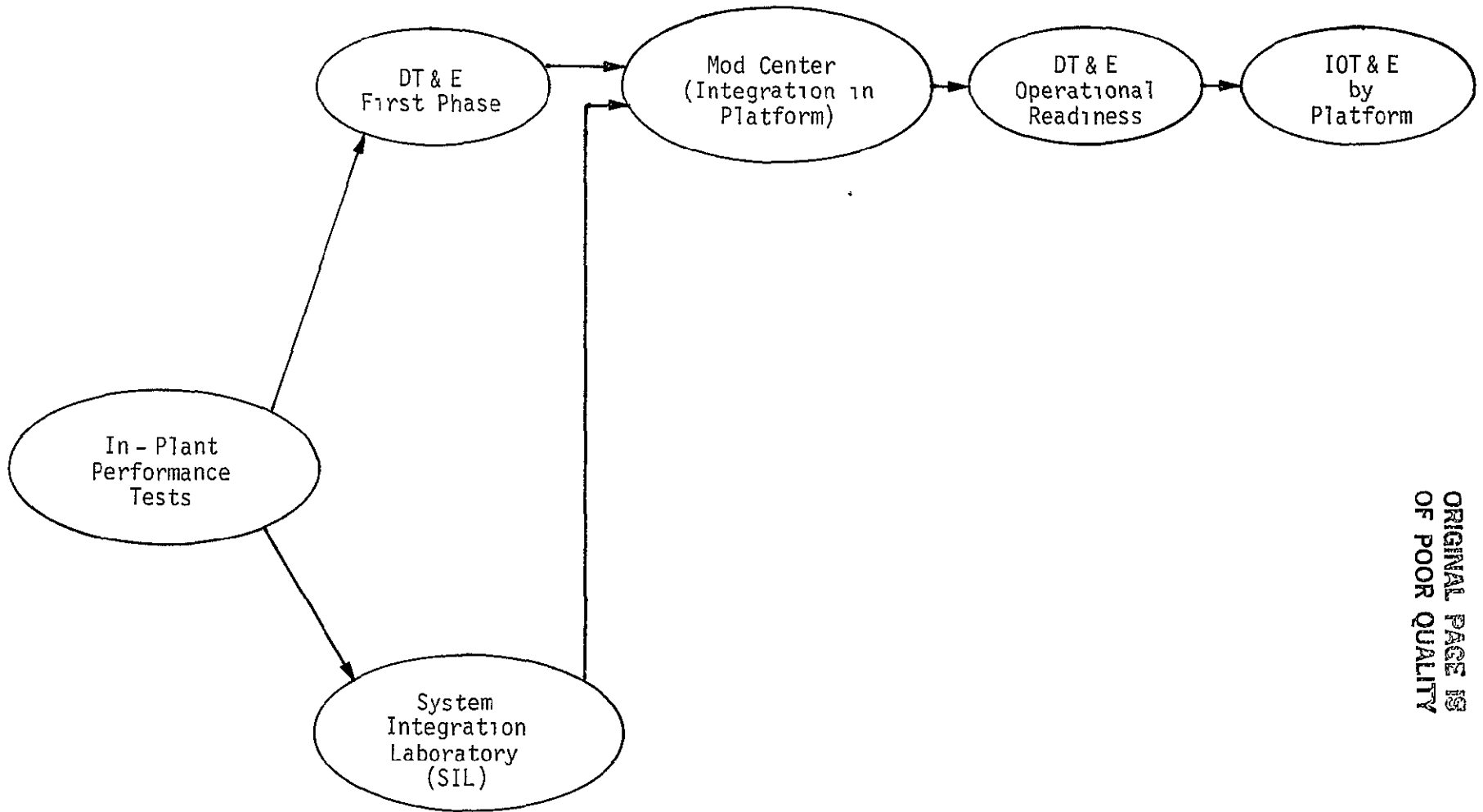
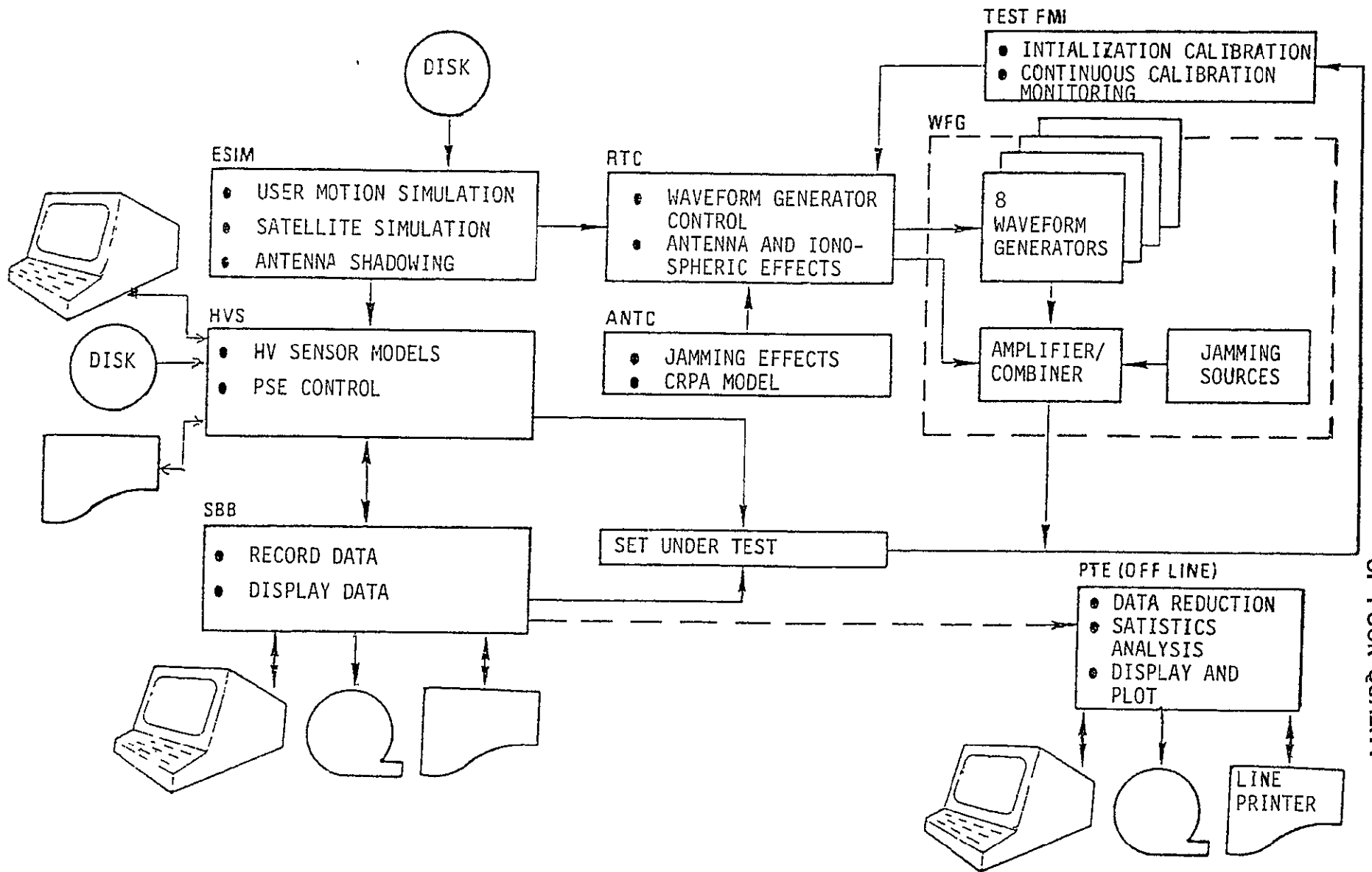


Figure B.1 Flowchart for Major Test Phase for GPS Phase IIB

ORIGINAL PAGE IS
OF POOR QUALITY



ORIGINAL PAGE IS
OF POOR QUALITY

Figure B.2. Full PSE Configuration

The SIL test is supported by a subset of the PSE, referred to as a "test pack." The test pack may have only one or two waveform generators and only limited signal dynamics capability. This is because the main intent of SIL is to verify operation of the user equipment with the host vehicle interfaces, with the emphasis on interface and software compatibility. The host vehicle interface may be actual hardware or hardware simulators.

The DT&E (first phase) consists of flying the user equipment (in the case of airborne users) in test bed aircraft, such as a C130. The testing done in these fully instrumented platforms is primarily intended to verify receiver performance and, to this end, the testing will be done over the Yuma inverted range. The interface with the test aircraft is minimal. Test results are closely compared with the simulation tests run in the in-plant phase. Any anomalies can cause additional in-plant simulations as well as further DT&E tests. This phase of the testing is controlled by the contractor.

Following this phase of DT&E, the user equipment is sent to the "Mod Center", where it is integrated into the host vehicle. Additional testing is done at the Mod Center with support from the test pack (scaled-down PSE). After this, each vehicle and its equipment enters the operational readiness phase of DT&E. It is my understanding that this may not be a flight test, but consists of the full system checkout on board the vehicle, perhaps parked on the flight line. This test concludes with the formal software qualification test (FQT).

Finally, the vehicle and its equipment enters the Initial Operational Test and Evaluation (IOT&E) phase. This consists of the vehicles utilizing the equipment for operational missions.

At this point, it is appropriate to discuss the parallels between the Phase IIB testing discussed above and the traditional Shuttle avionics testing. The in-plant testing corresponds to the normal in-plant qualification and acceptance testing, with the exception of the software. The SIL testing is a close analogy to a combined SAIL and ESTL test. There is no clear-cut analogy with the first phase of DT&E. The exception may be a GPS experiment flown aboard the Shuttle wherein the NAV data from the GPS is merely recorded for post-flight analysis and comparison.

with laboratory simulation data. The Mod Center corresponds to the equipment installation at KSC (or Palmdale, if schedule permits). DT&E operational readiness corresponds to KSC operational readiness testing. Of course, IOT&E corresponds to Shuttle flights with GPS on board as an operational NAV system.

Perhaps the two most significant comparisons between Phase IIB and Shuttle GPS testing are as follows: First, the in-plant performance tests are designed to high-fidelity exercise the receiver processor RF and NAV performance to specifications and mission profiles to the greatest extent possible. Second, the SIL tests are designed to fully wring out the interfaces with the host vehicle and, as such, are very similar in concept and function to a combined SAIL/ESTL test or a SAIL test with good RF stimulation. An example cited by Jamison was the SSN submarine host vehicle. In this case, the SIL tests are totally complete and exhaustive before the equipment "ever sets foot aboard the sub."

Magnavox diagrams and charts showing the PSE test configurations for supporting test requirements are included with this memorandum.



TESTS TO BE SUPPORTED BY PSE

- DESIGN VERIFICATION
- ACCEPTANCE TESTING
- HARDWARE QUALIFICATION
- COMPUTER PROGRAM QUALIFICATION
- INTERFACE COMPATIBILITY
- INSTRUMENTATION READINESS
- DT&E HOST VEHICLE
- FIELD DT&E
- PSE READINESS
- MOD CENTER TESTS
- DT&E OPERATIONAL READINESS
- ARMY DEVELOPMENT TESTS
- IOT&E TESTS
- MAINTAINABILITY
- RELIABILITY GROWTH
- COMBINED ENVIRONMENTAL RELIABILITY TESTS (CERT)



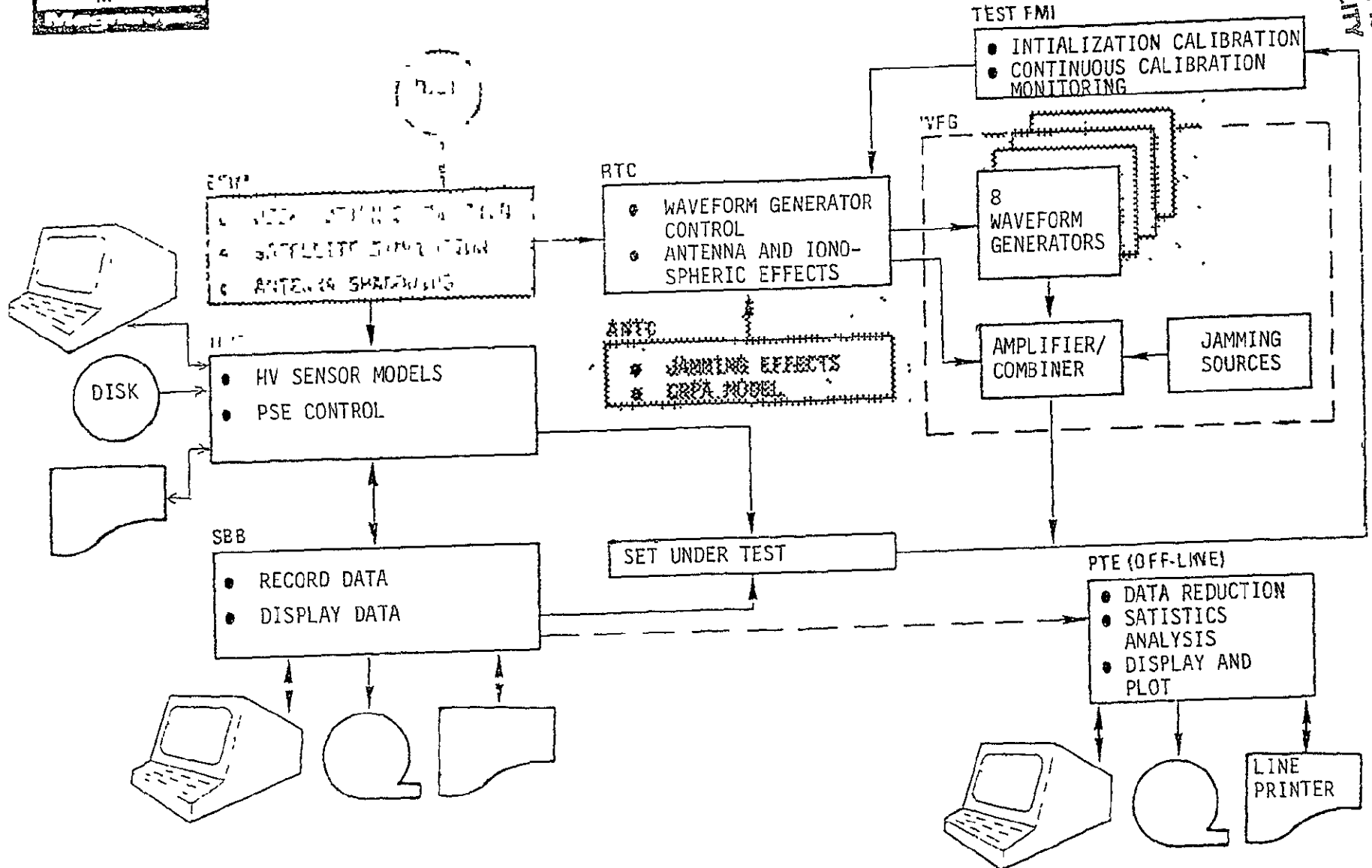
PSE TEST CONFIGURATIONS TO SUPPORT TEST REQUIREMENTS

TEST EQUIPMENT		RECEIVER TEST	NAVIGATION SOFTWARE TEST	FULL n CHANNEL PSE	FIELD TEST* CONFIGURATION	QUAL TEST* CONFIGURATION	PGSE	MOBILE* UNIT	CERT* CONFIGURATION	DT&E INSTRUMENT	IOT&E INSTRUMENTATION	POST TEST EVALUATOR
SPECIFICATION REFERENCE	TEST NAME											
4 1	DESIGN VERIFICATION	X	X	X								X
4 2 1	ACCEPTANCE TESTING			X		X						
4 2 2	QUALIFICATION TEST			X		X						
	HARDWARE	X	X	X								
	SOFTWARE L0/L1	X	X	X								
	SOFTWARE L2			X								X
	FORMAL S/W QUAL			X								
4 2 3	INTERFACE COMPATIBILITY											
4 3	DT&E											
	TEST INST READINESS			X	X					X		
	DT&E HOST VEHICLE COMPATIBILITY				X					X		
	FIELD DT&E				X					X		
	PSE READINESS						X					
4 4	MOD CENTER TESTS							X			X	X
	IOT&E HOST VEH MODS						X				X	X
	INSTALLATION CHECK						X	X			X	X
	EMC						X	X			X	X
4 5	IOT&E FIELD TESTS							X			X	X
	DT&E OP READINESS							X			X	X
	ARMY DEV TESTS (DTII)						X	X			X	X
	IOT&E						X	X			X	X
4 6	MAINTAINABILITY						X					
	CERT					X	X		X			
	RELIABILITY											

*TEST PECULIAR CONFIGURATIONS OF THE STANDARDIZED TEST PACK

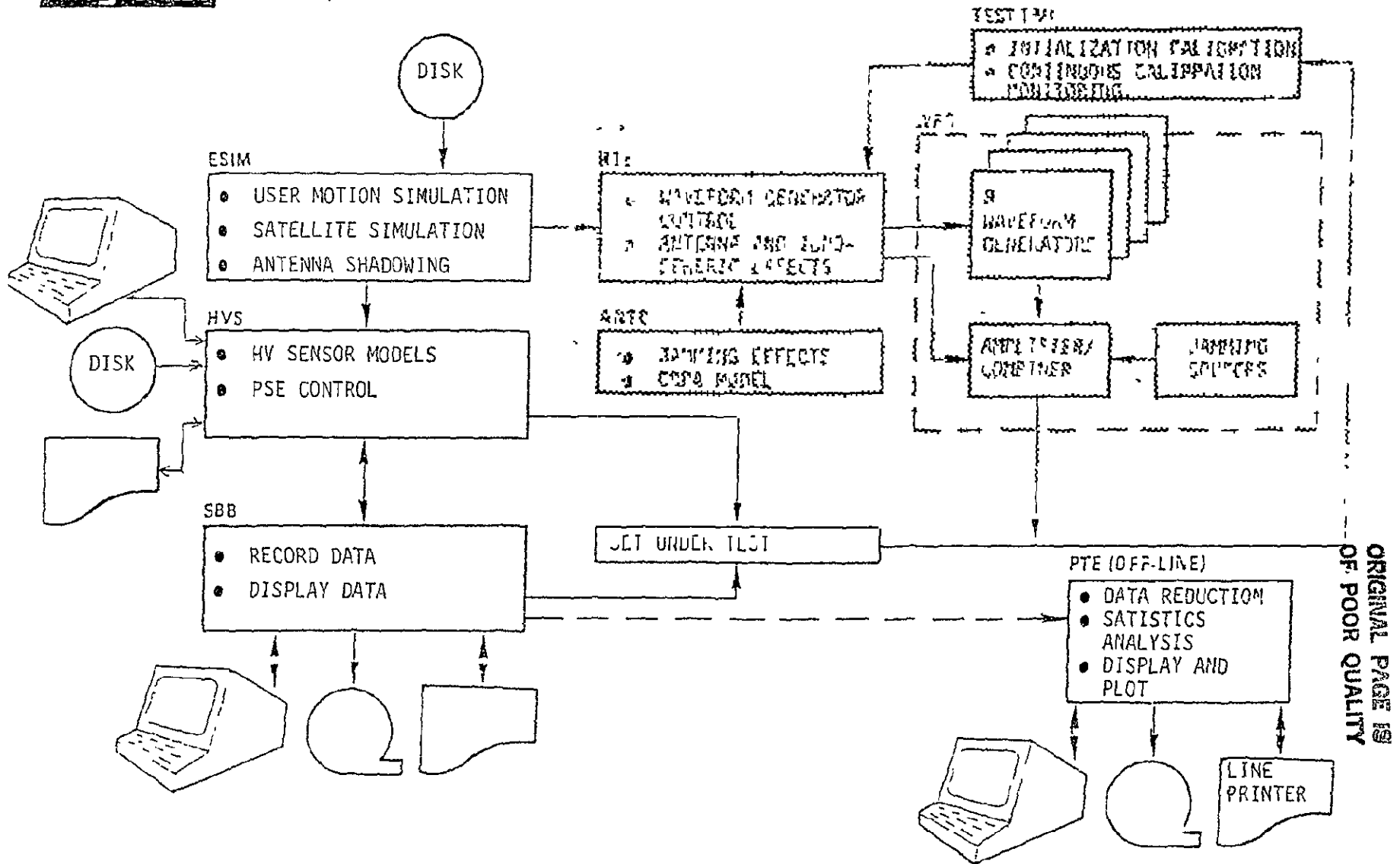


RECEIVER TEST CONFIGURATION

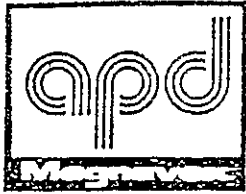




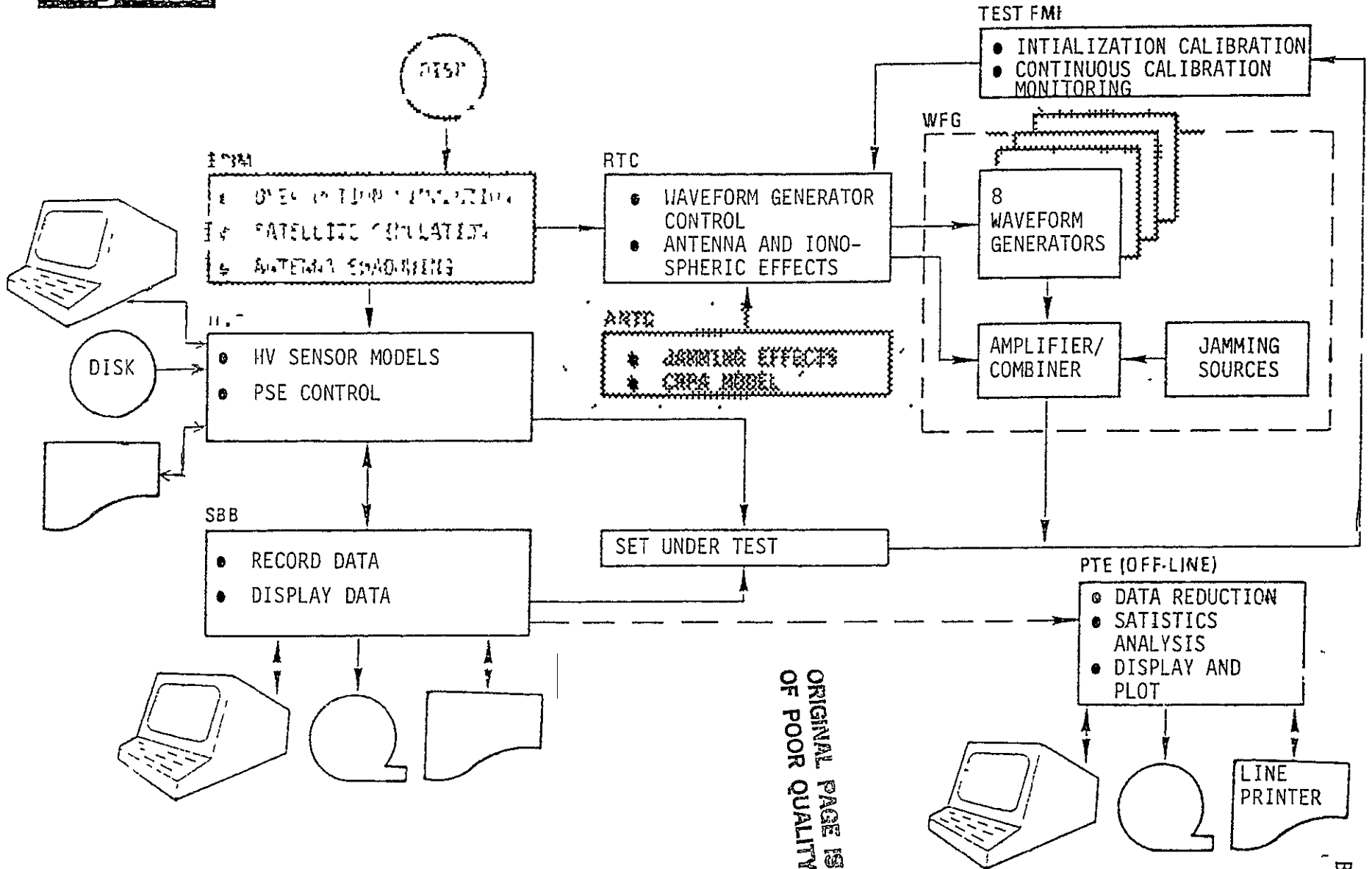
NAVIGATION S/W TEST CONFIGURATION



ORIGINAL PAGE IS
OF POOR QUALITY



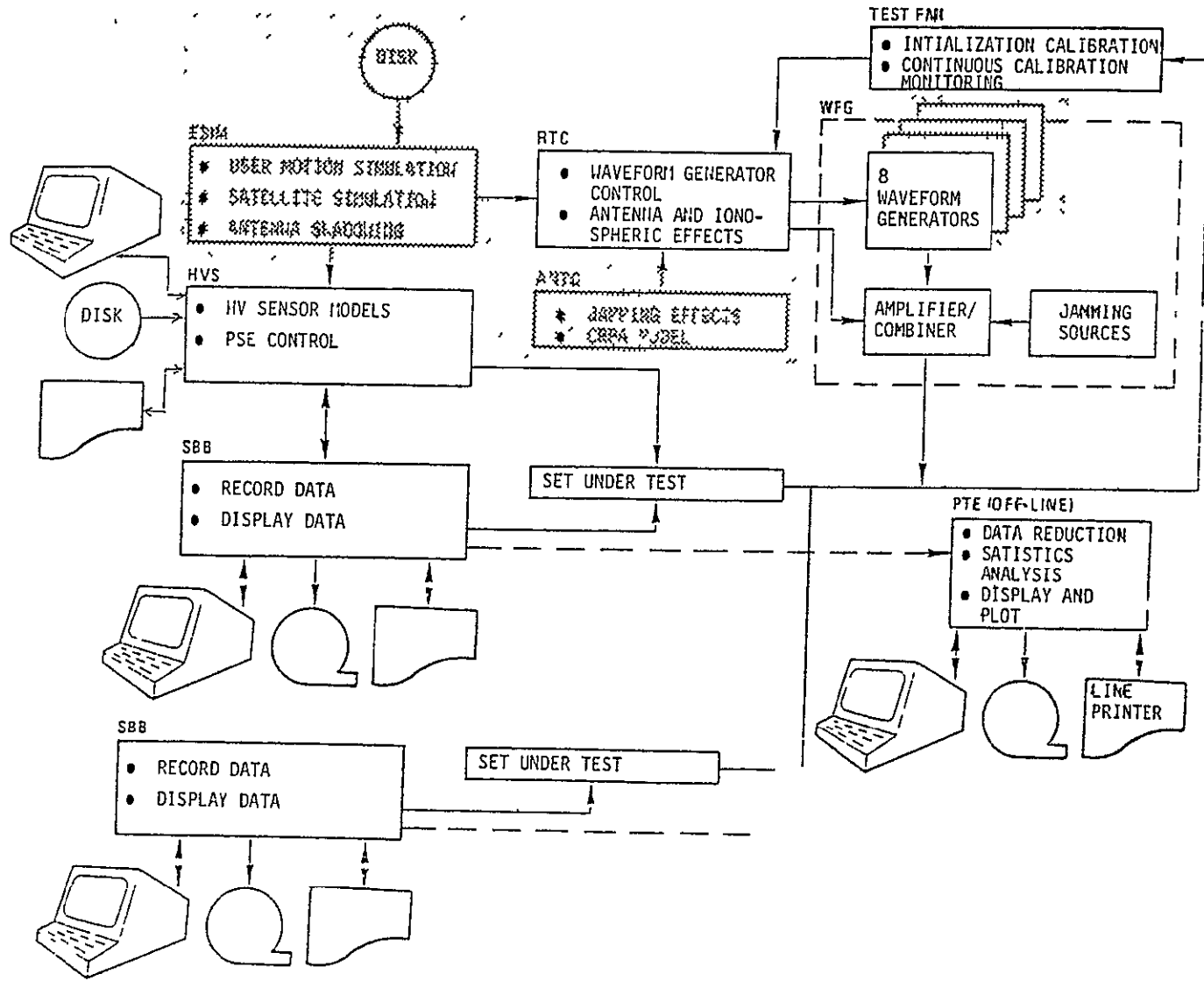
QUALIFICATION TEST PACK



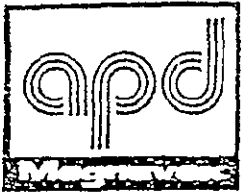
ORIGINAL PAGE IS OF POOR QUALITY



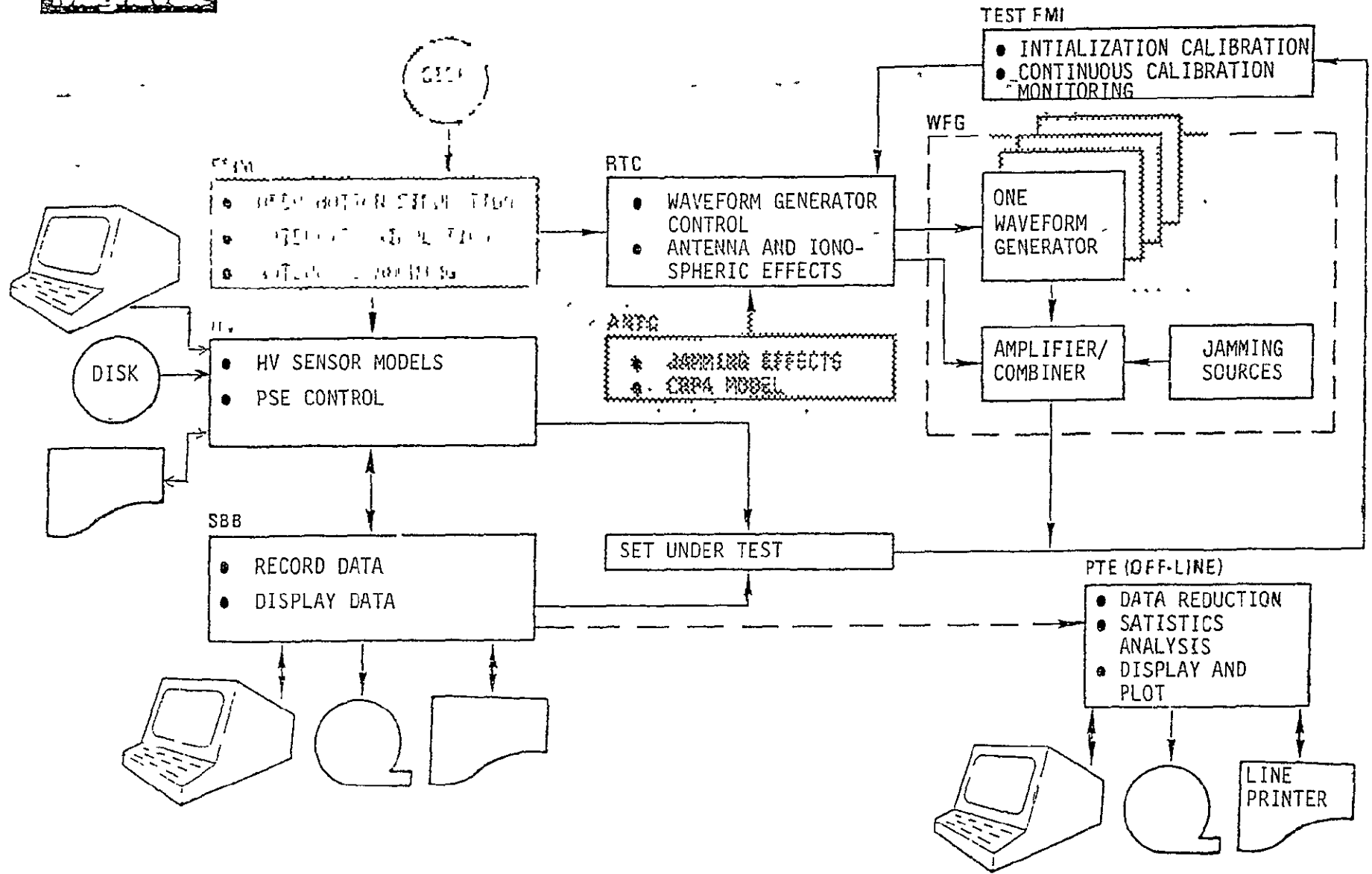
CERT TEST CONFIGURATION



ORIGINAL PAGE IS
OF POOR QUALITY



MOBILE UNIT TEST PACK



ORIGINAL PAGE IS
OF POOR QUALITY



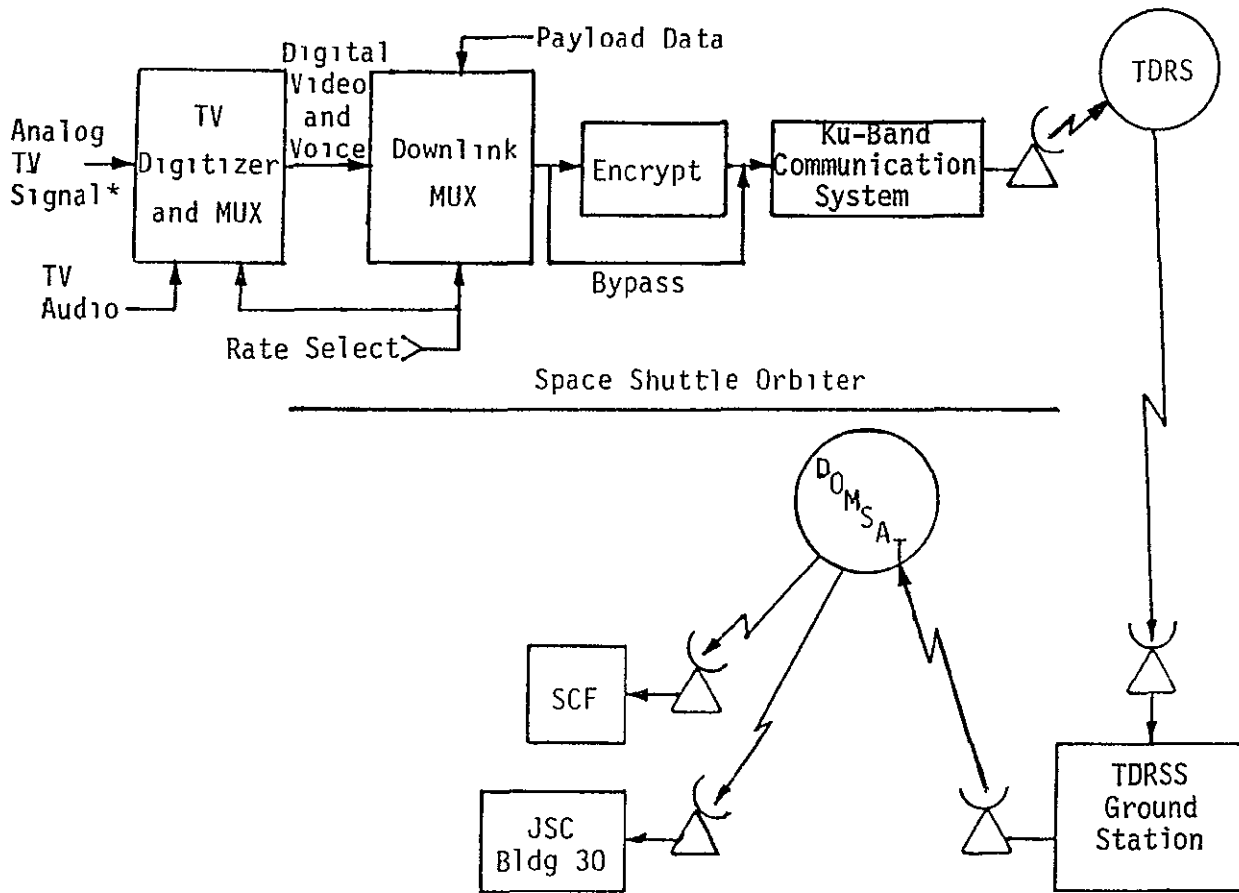
THROUGHPUT AND MEMORY ESTIMATES (8-CHANNEL CONFIGURATION)

	<u>THROUGHPUT</u>	<u>MEMORY (BYTES)</u>
ESIM	64%	112K
RTC	54%	70K
ANTC	57%	102K
HVS	60%	80K
SBB	57%	61K
FMIU9	TBD	TBD

13.0 TELEVISION DIGITIZER DEVELOPMENT

The objective of the development program reported herein was to demonstrate, via a working breadboard, the feasibility of digitizing an NTSC-format color-TV signal for run-length (R/L) encoding. The ultimate use of such a TV digitizer would be for Space Shuttle downlink transmissions via the Ku-band wideband link. The specific technique implemented by AXIOMATIX uses tri-state delta modulation (TSDM), which is more adaptable to R/L encoding than conventional bistate delta modulation. This technique is also applicable to digitizing a black-and-white (B/W) TV signal for field-sequential color transmissions.

ORIGINAL PAGE IS
OF POOR QUALITY



* Black and white, field-sequential color or NTSC format color

Figure 13.1. Digital TV and Multiplex System Architecture: General Requirements

13.1 Background

The existing Space Shuttle onboard equipment provides for transmission of TV signals via an S-band (2250-MHz) FM downlink. This downlink, however, is available only when the Shuttle is within line of sight of a ground station. Furthermore, due to the severe constraints on the effective radiated power, the bandwidth of this link is limited, thus precluding the use of any "privacy" feature for the downlink TV signal.

The anticipated requirements for Shuttle Orbiter Ku-band downlink communication include the transmission of a digital video signal which, in addition to accommodating B/W TV pictures, must also be able to relay to the ground the color-TV information encoded in either field-sequential or NTSC-color formats. Furthermore, at the expense of additional onboard hardware and increased bandwidth due to the digitization process, the picture-privacy feature can be provided for the downlink. Thus, an objective for future Space Shuttle TV equipment is the development of a digitization technique which is not only compatible with data rates in the range of 20-30 Mbps, but also provides for good quality pictures.

Figure 13.1 shows the overall space and ground functional configuration that could be used to accommodate Shuttle digital TV with scrambling for privacy to be transmitted to the U.S. Air Force Satellite-Control Facility (SCF) and to NASA Johnson Space Center (JSC). As shown there, the Ku-band communication system [4] onboard the Shuttle Orbiter utilizes a high-gain steerable-dish antenna to communicate with NASA's Tracking and Data-Relay Satellite System (TDRSS) to provide a TV transmission capability simultaneous with two other communication channels. Alternately, 50 Mbps of payload digital data can be provided simultaneously with the other two communication channels. Initially, the TV modulation technique will be analog FM, similar to S-band, with no privacy capability. A potential requirement for privacy, however, can be provided by digital techniques. Scrambled digital TV, if implemented at moderately low data rates, can also provide the possibility of simultaneous transmission of payload digital data as long as the total data rate (TV plus payload data) is within the 50-Mbps Ku-band system capability.

13.2 Principles of Delta Modulation

13.2.1 Conventional Bistate Delta Modulation

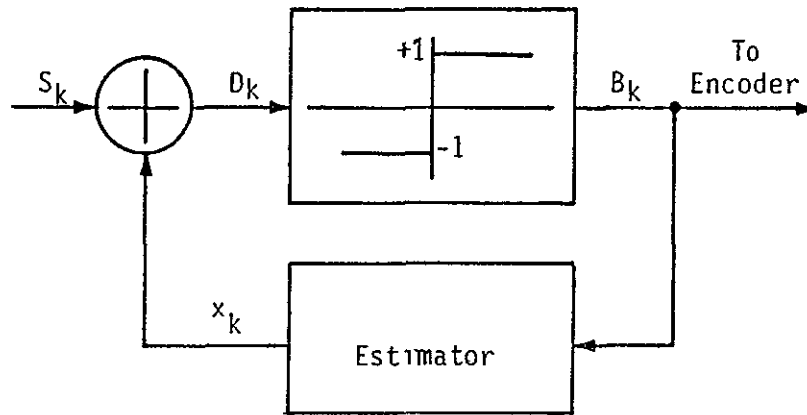
The commonly used delta-modulation encoder produces a sequential output that indicates whether the final output voltage should increase or decrease. It acts like a DPCM system with only one bit per sample; hence, it is referred to as a "bistate" encoder. Acceptable performance with this encoding scheme is realized by an increased sampling rate as compared to a PCM coding scheme. Because the bistate delta modulator requires relatively low data rates compared to PCM, considerable effort has been spent trying to perfect a delta modulation system [5,6].

The goal of every design approach is to trade off fidelity of reproduction versus the allowable data-transmission rate and the amount of hardware used. The best solution also depends on the qualities of the signal being sampled. Video information tends to be a series of amplitude steps from one luminance level to another. These level steps are connected by voltage changes with large dV/dt values. When handling a video signal, a delta modulator must handle very sharp rise and fall time signals, then settle rapidly to a new luminance value, with no overshoot, ringing or other added noise. The relative delay for different frequency components in the picture is also important.

Figure 13.2 is a block diagram of a bistate delta modulator, which illustrates its operation. D_k is the difference between the input signal S_k and the output of the estimator X_k . This difference signal is passed through a hard limiter whose output is a bit B_k that causes the estimator to change its output. This bit is the signal transmitted over a communication link to the receiver. The receiver consists of only the estimator portion of the transmitter block diagram. The sampling rate of the delta modulator determines the amount of delay inherent in the digitizing process. The faster the sampling rate, the smaller the inherent delay.

The hard limiter depicted in Figure 13.2 guarantees that the estimator will increase or decrease its output every time the sample clock cycles. This characteristic of indicating only changes results in the inherent "granularity" in the reproduction of a constant-luminance signal since the modulation scheme must always output a sample corresponding to an increase or decrease in voltage. The reconstructed signal will average to the correct level by varying up or down around the desired output level. Any attempt to smooth the delta demodulation output will slow the response to step changes and, therefore, reduce picture "sharpness."

Conversely, if the bistate delta-modulation scheme is designed to provide good rise and fall times, the amplitude of the level jitter around the desired output will increase and more granularity will appear. Furthermore, the amount of overshoot and ringing after an abrupt edge will, in general, increase as the delta-modulator system is designed to reduce slew time. Various attempts to alleviate these conflicting requirements and reduce the overshoot and ringing have been proposed [7,8].



where.

S_k = Signal to be transmitted (sampled and digital)

X_k = Estimate of signal to be transmitted

D_k = Quantized Difference ($D_k = S_k - X_k$)

B_k = Activity vector (signal rising or falling)

Figure 13.2. Conventional (Bistate) Delta Modulator Functional Block Diagram

13.2.2 Tri-State Delta Modulation

The tri-state delta modulator (TSDM) [9,10] has characteristics that make it especially suitable for encoding video information. By indicating the "no-change condition" with a special code, the TSDM breaks the connection between rise-time performance and steady-state level jitter inherent in a bistate delta modulator.

In comparison with the bistate delta modulator, the TSDM approach shown in Figure 13.3 quantizes D_k into three values instead of two. The third value indicates that D_k is between $-\epsilon_v$ and $+\epsilon_v$. This condition causes the output of the estimator to remain at its previous value. Just as in the case of bistate delta modulation, the receiver consists of the estimator only. This third state eliminates the granularity inherent in bistate delta modulation; it permits the TSDM to be optimized for transient performance without considering granularity problems. With the exception of the third state, the TSDM operation is identical to the bistate delta modulator shown in Figure 13.2.

As indicated in Figure 13.3, the TSDM state is determined by comparing the estimate X_k with the input signal S_k to produce a voltage difference signal D_k . This voltage D_k is tested for sign and magnitude to produce B_k . The rule is

$$B_k = \begin{cases} \text{Sgn } [D_k], & \text{whenever } |D_k| > \epsilon_v \\ 0, & \text{whenever } |D_k| \leq \epsilon_v \end{cases}$$

Since $D_k = S_k - X_k$, a positive value for D_k signifies that X_k must be made more positive to match S_k ; therefore, $B_k = +1$ must cause X_k to become more positive. The equation used to calculate X_{k+1} from X_k is simply

$$X_{k+1} = X_k + B_k |\Delta_{k+1}|$$

where B_k may be +1, 0 or -1 and $|\Delta_{k+1}|$ is given by

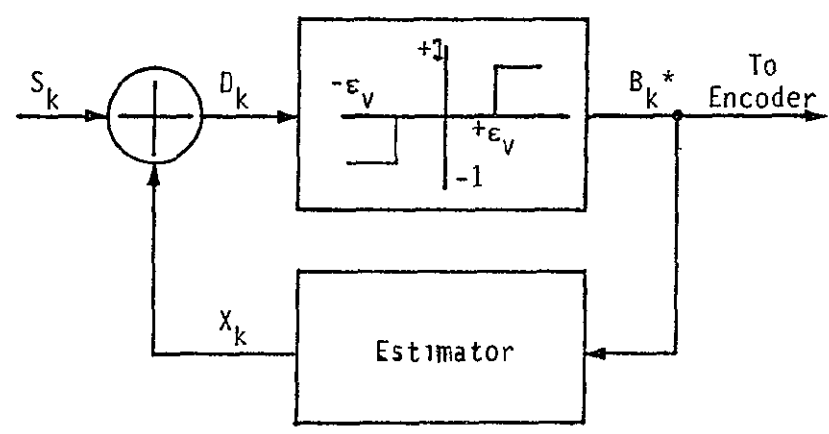


Figure 13.3. Tri-State Delta Modulator (TSDM) Functional Block Diagram

*With TSDM, the B_k vector can also represent a "signal-steady" condition.

$$|\Delta_{k+1}| = \begin{cases} 1.5 \Delta_k & \text{if } B_k = B_{k-1} \neq 0 \text{ and } |\Delta_k| > 2\Delta_0 \\ 3\Delta_0 & \text{if } B_k = B_{k-1} \neq 0 \text{ and } |\Delta_k| \leq 2\Delta_0 \\ 0.5 \Delta_k & \text{if } B_k \neq B_{k-1}, B_k \neq 0, B_{k-1} \neq 0 \\ 0 & \text{if } B_k = 0 \\ 3\Delta_0 & \text{if } B_{k-1} = 0, B_k \neq 0 \end{cases}$$

When $|D_k| \leq \epsilon_v$, the feedback signal X_k is close enough in value to the input signal S_k so that the system should maintain its state. It does this by making $X_{k+1} = X_k$ and setting $\Delta_{k+1} = 0$ whenever $B_k = 0$. That process is unique to tri-state delta modulation.

The adaptive characteristic of the system is realized by the $|\Delta_{k+1}| = 1.5 \Delta_k$ term. When B_k has the same sign m times in sequence, the value of Δ_k is multiplied by $(1.5)^{m-1}$ so that the slope of the feedback signal increases without limit until $X_k \geq S_k$. Once that happens, the B_k vector changes sign and the values of $|\Delta_{k+1}| = 0.5 \Delta_k$ reduce the slope as the X_k signal changes direction. This provides for the eventual settling of X_k to a value near S_k by reducing the value of Δ_k by a factor of two every time X_k crosses S_k . If S_k remains constant long enough, X_k will eventually settle to within $\pm \epsilon_v$ of it, if ϵ_v is at least as large as one-half the resolution of the DAC that produces X_k . Once this happens, B_k will be equal to zero and the systems will stay at rest until S_k changes again.

When B_k changes from $B_{k-1} = 0$ to either $B_k = +1$ or $B_k = -1$, the system must inject a starting value for $|\Delta_{k+1}|$ since $|\Delta_k|$ was 0. That is handled by the $2\Delta_0$ term which is simply a constant value selected to provide a large enough initial slope to the S_k feedback signal when it must adjust to a step input in S_k so that the slew time is minimized.

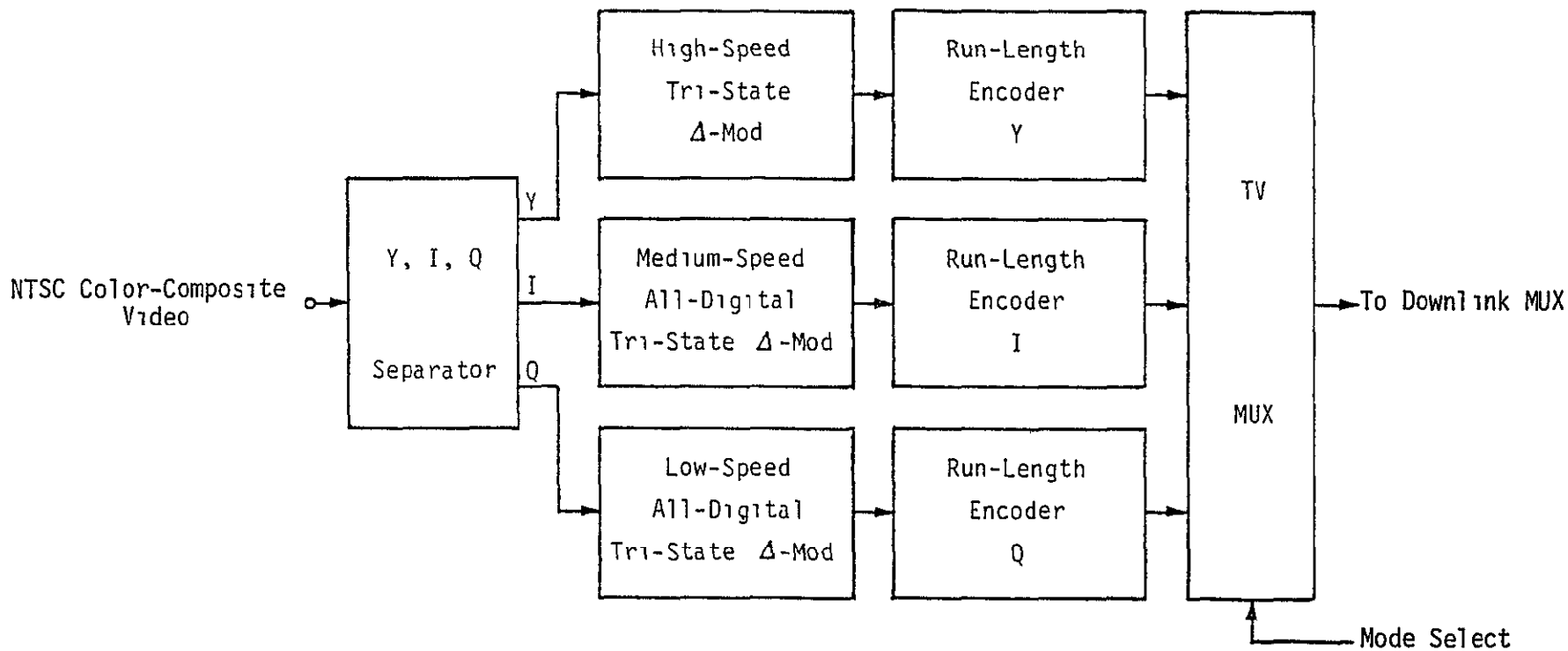
The initial value of $2\Delta_0$ must be injected whenever $\Delta_k = 0$ and $B_k \neq 0$. Two terms are required for this injection because the values of B_k, B_{k-1} , etc. are the only data available to the estimator. A sufficient condition for $\Delta_k = 0$ is that $B_{k-1} = 0$. Therefore, whenever $B_{k-1} = 0$ and $B_k \neq 0$, the system must inject $2\Delta_0$ for Δ_k . However, it is possible for Δ_k to work its way down to zero without ever having $B_k = 0$. This requires S_k to change value at just the right time during the process of X_k settling toward the input voltage. This eventuality is handled by the term for $|\Delta_{k+1}|$ which injects $3\Delta_0$ whenever $B_k = B_{k-1} \neq 0$ and $|\Delta_k| < 2\Delta_0$.

13.2.3 Application of TSDM to NTSC Color TV

The previous discussion considered TSDM as a technique for digitizing a single video signal that is presumed to be the NTSC luminance component used for black-and-white TV transmission. Because field-sequential color transmission utilizes a sequence of such components, as provided at the output of a rotating color-wheel filter, the approach described is applicable without modification for systems such as those in use today by the Space Shuttle. For standard NTSC color-TV transmission, however, the TSDM technique is applied to each of the three color components, Y, I and Q, where Y is the luminance component and I and Q are the chrominance components.

Figure 13.4 shows the method of handling those components, each potentially with its own R/L encoder. For maximum data compression, each component should have its own R/L encoder before multiplexing. Otherwise, since the color and luminance components do not correlate well, there is little data-rate reduction for the chrominance components when multiplexed with the luminance information.

Relative time delays are quite important in this scheme and differential delays have to be added to the I and, especially, the Y channel in order to compensate for the long delay inherent in the channel due to its narrow bandwidth. This narrow bandwidth implies a low sampling frequency which produces more delay in the digitizing process.



Component	Maximum Bandwidth (MHz)	Maximum* Bit Rate (Mbps)
Y	4.2	15 - 20
I	1.5	4 - 8
Q	0.5	1 - 2
		Total ≈ 20 - 30

*After coding.

ORIGINAL PAGE IS OF POOR QUALITY

Figure 13.4. NTSC Color-TV Component Digitization

13.3 Breadboard System Description

13.3.1 Overall Test Setup

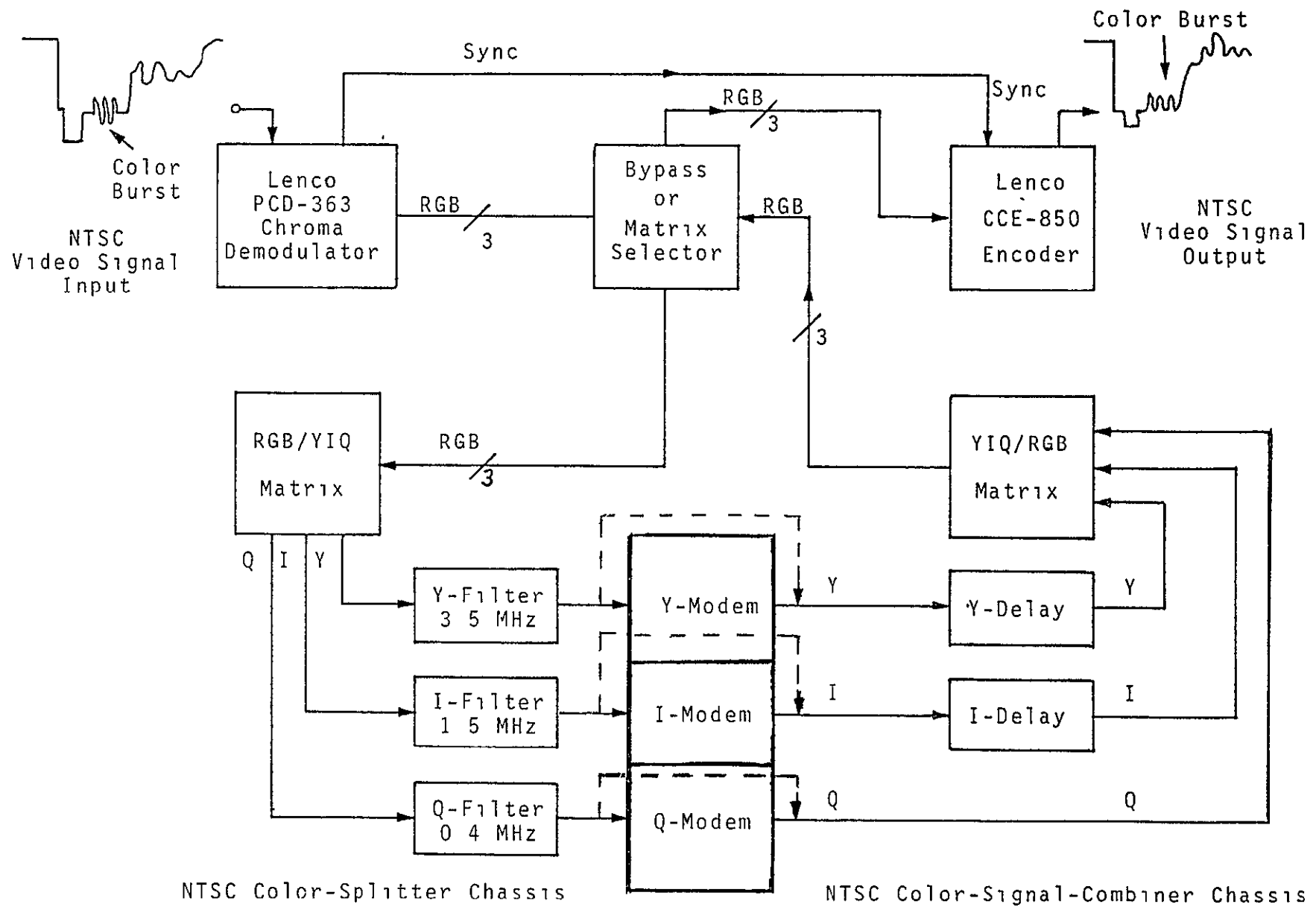
Figure 13.5 shows the block diagram of a digital TV test setup based on tri-state delta modulation (TSDM). This is the test setup used by Axiomatix to evaluate the TSDM technique.

As shown in this block diagram, the NTSC video signal is applied to the Lenco Model PCD-363 chroma demodulator. This demodulator extracts the RGB components of the video signal. These three components can then be routed to either the Lenco Model CCD-850 encoder or to the RGB/YIQ matrix. When they are routed to the encoder, the digital system is bypassed and the decoder/encoder equipment can be checked out and adjusted back to back.

When the RGB signals are routed to the RGB/YIQ matrix, they enter the Axiomatix-built breadboard equipment. As shown in Figure 13.5, the Y, I and Q signals can be applied to either their respective digital modems or directly to the YIQ/RGB matrix. In the latter case, the digital equipment is bypassed and the decoder-RGB/YIQ-YIQ/RGB-encoder analog signal chain can be tested and properly adjusted for color balance.

With the digital modems in the chain, the TSDM operation is implemented and the Y, I and Q components are processed by their respective modulators and demodulators (modems). It must be noted that there are delay lines in the Y and I channels prior to the YIQ/RGB matrix. The purpose of these delay lines is to compensate for analog-delay time differentials introduced by the I and Q lowpass filters that are located at the output of the RGB/YIQ matrix. Figure 13.6 depicts the nominal delays of the compensating delay lines.

It is important to note that all three modems (Y, I and Q) can also be operated in the bistate mode. This feature is incorporated in the breadboard so as to compare the relative picture quality of the bistate and TSDM-encoded video.



ORIGINAL PAGE IS
OF POOR QUALITY

Figure 13.5. Digital-TV TSDM Test-Setup Block Diagram

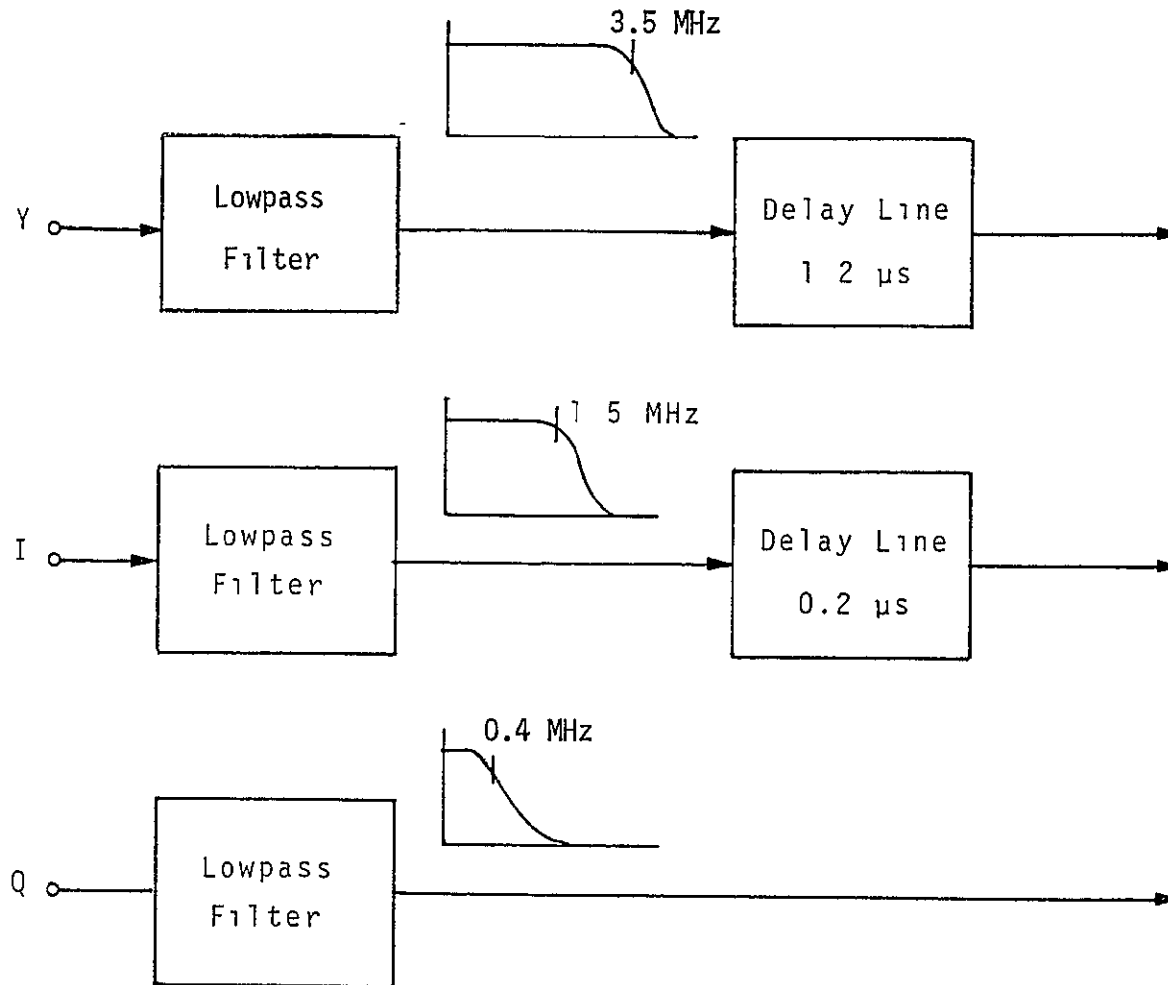


Figure 13.6. Analog Signal Lowpass Filters and Compensating-Delay Lines

ORIGINAL PAGE IS
OF POOR QUALITY



13.3.2 Transmitter Functional Block Diagram Description

The transmitter functional block diagram in Figure 13.7 depicts the important signal interfaces between the various blocks.

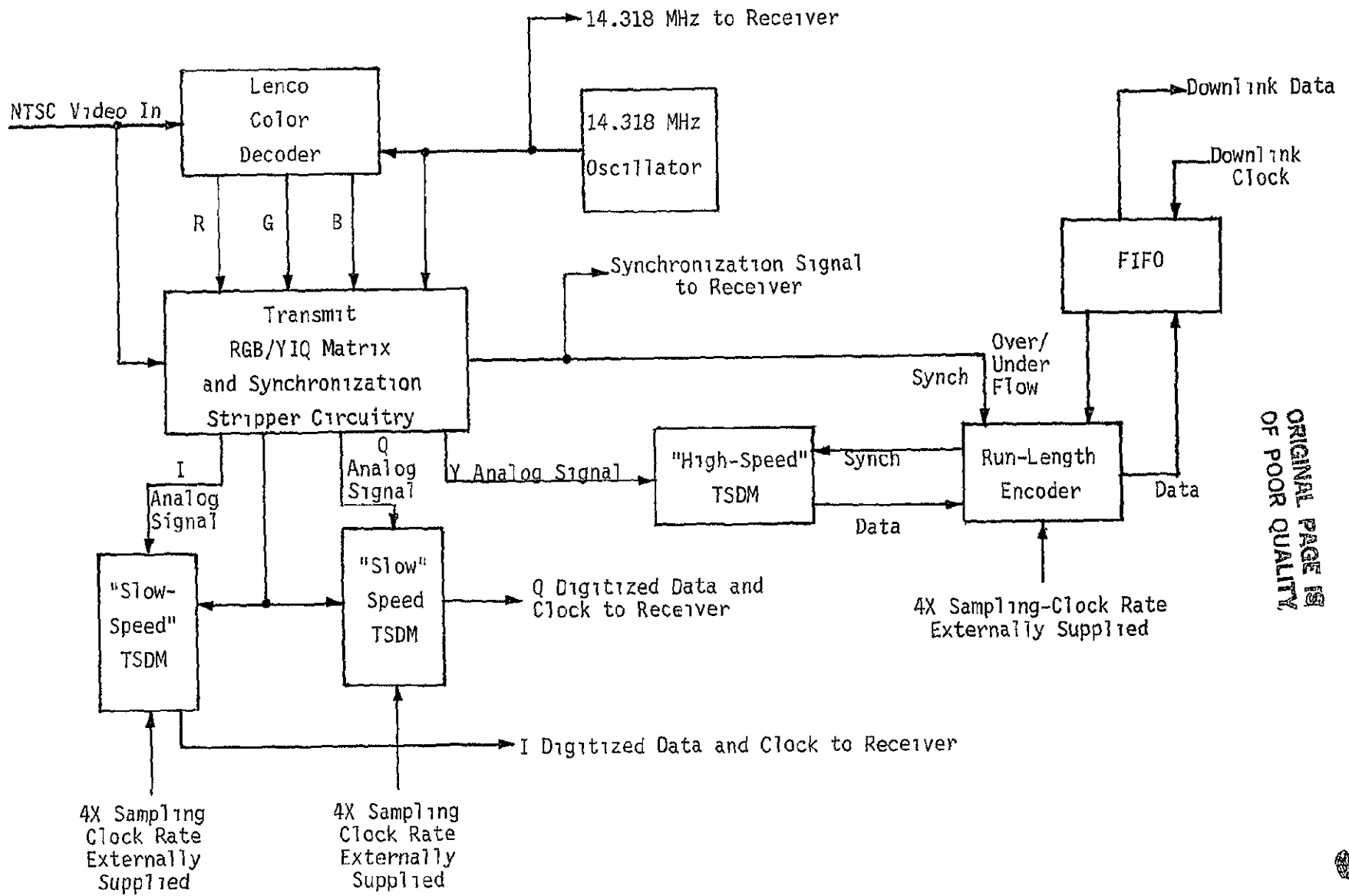
Starting with the video input, the Lenco color decoder block produces red, green and blue drive signals by demodulating the color information in the NTSC signal. The synchronization-stripper circuitry in the block below the Lenco recovers horizontal and vertical synchronization signals. These signals are used to reset the Tx and Rx delta modulators in addition to their normal synchronization function. This process guarantees that any errors in the channel will not propagate longer than one horizontal sweep.

The transmit RGB/YIQ matrix block converts the wide-bandwidth R, G and B signals into narrow-bandwidth I and Q signals and a wide-bandwidth Y signal. The synchronization-stripper circuitry counts down from four times the color-subcarrier frequency to the horizontal and vertical repetition rates. This countdown chain is phased to the video input, then produces solid, jitter-free, horizontal and vertical synchronization signals.

The narrow-bandwidth I and Q analog signals drive two "slow-speed" transmitters which digitize them. The synchronization signals reset the transmitters after every horizontal-line interval.

The high-speed TSDM block digitizes the Y-channel signal and supplies that signal to the R/L encoder at the sampling rate. The R/L encoder block generates the downlink data at a rate that depends on the actual samples. However, encoding efficiency is picture dependent and, hence, variable.

In order to maintain a constant-downlink data rate with a variable-encoded data rate being generated in the R/L encoder, a buffer memory is used to provide variable-length storage. This memory, titled FIFO in the diagram, prevents loss of data by providing this buffer function and feeding back potential overflow or underflow signals to the R/L encoder. Potential underflow is guarded against by outputting dummy data from the R/L encoder. This data is ignored by the receiver. Potential overflow is handled by halving the sample rate and going to the bistate mode with only one bit per sample.



ORIGINAL PAGE IS
OF POOR QUALITY

Figure 13.7. Transmitter Functional Block Diagram

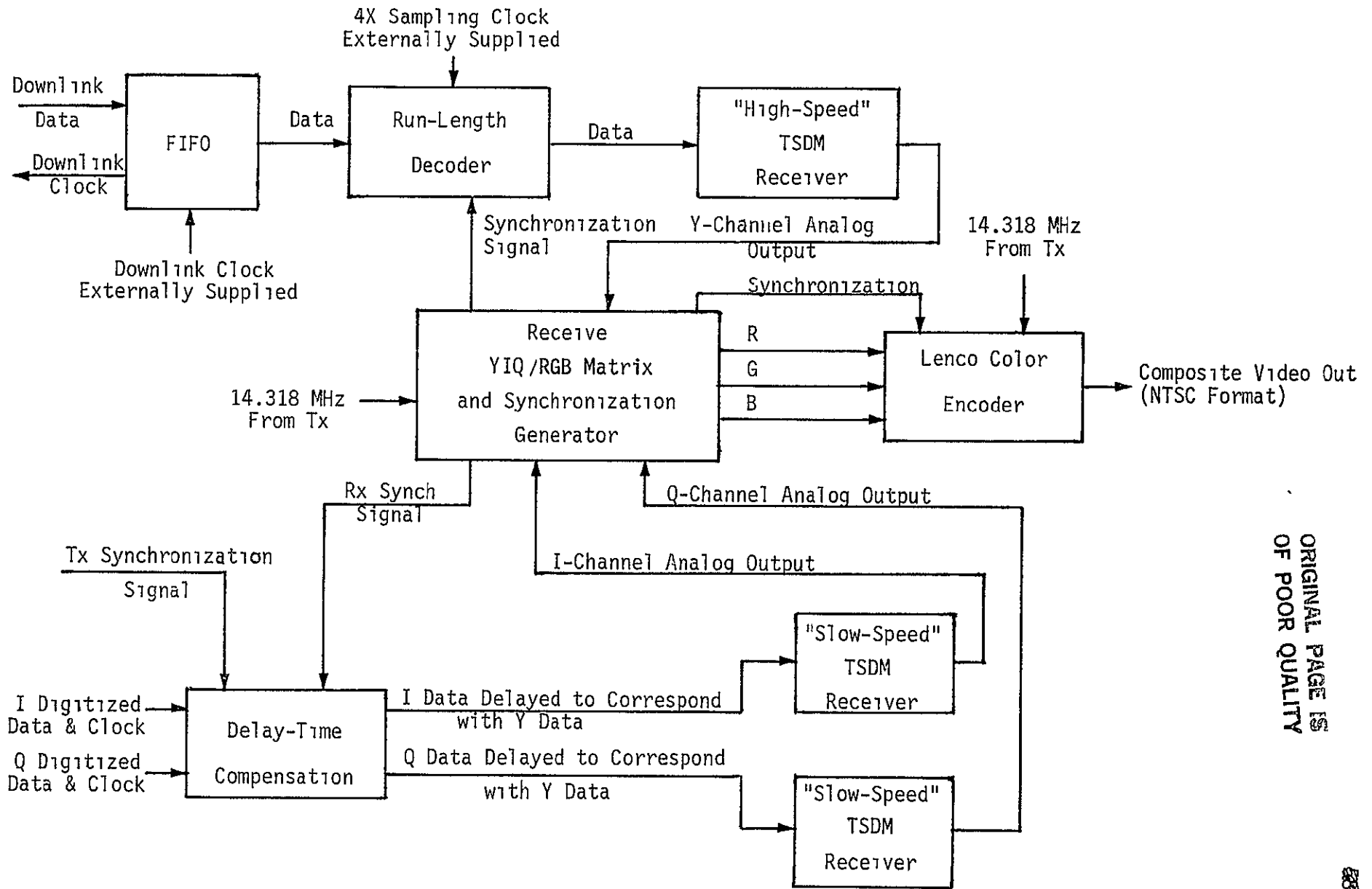
13.3.3 Receiver Functional Block Diagram Discussion

Figure 13.8 shows a functional block diagram of the delta-modulation receiver section of the breadboard. The digitized data streams from the transmitter enter two types of memory, depending on their characteristics. The Y-channel data encoded in the high-speed transmitter comes over a simulated downlink channel and is stored in a variable-length memory called an FIFO. This memory is necessary because the R/L decoder must be able to input data at a variable rate in order to supply samples to the high-speed TSDM receiver at a fixed data rate. The fixed data rate of the simulated downlink cannot supply the R/L decoder with the variable rate that it requires.

The I and Q channel digital data is stored in two variable-length digital-delay lines in the delay-time compensation block. These delay lines provide a delay for I and Q which correspond to the delay in the Y-channel produced by the transmit and receive signals and setting the length of I and Q channel delays to correspond.

The R/L decoder block undoes the encoding process and provides sampled data and a clock to the high-speed receiver that produces an analog output. Since the I and Q channel data were not R/L encoded, it is merely supplied directly to two slow-speed receivers to be converted back to analog signals. Since the I and Q data have been delayed to match the Y data, the received signal is employed to reset all three receivers. This resetting process is necessary to eliminate possible offsets between Tx and Rx delta modulators due to bit errors in the simulated downlink.

Once the three analog signals have been reconstituted, the receive YIQ/RGB matrix circuitry is used to convert back to the R, G and B signals that are necessary to drive the Lenco color-encoder block. Thus, the receiver unit ultimately outputs the NTSC-format video signal.



ORIGINAL PAGE IS
OF POOR QUALITY

Figure 13-8. Receiver Functional Block Diagram

13.3.4 TSDM Digitizer/Reconstructor Implementation

Figure 13.9 is a block diagram of the Y-channel tri-state video digitizer with the receiver input and output indicated by dotted lines. Because the receiver is only a portion of the transmitter, it will not be discussed separately. As shown in this diagram, the analog video signal S_k is compared with the reconstructed analog estimate of the previous sample X_k . The analog difference D_k is applied to the A/D converter. The hysteresis bias, or "dead zone," $\pm\epsilon_V$, is also applied to the analog bias input of the A/D converter. The analog error is then sampled by the A/D unit and transformed into B_k values according to the previously described algorithm. Each B_k value which is a two-bit number is then applied to the B_k storage register. At the same time, the previous value of B_k is clocked into the B_{k-1} storage register. Once B_k and B_{k-1} are clocked into their respective storage registers, the logic-and decision unit (LDU) initiates its analysis of the condition of these vectors.

The hardware block diagram of Figure 13.9 implements the required tri-state algorithm. To provide the fastest sampling rate possible, the various alternative computations are performed in parallel and the appropriate result is selected by a 4-to-1 MUX. There are two 4-to-1 multiplexers: one for the next value of x and one for the next value of Δx . The decision as to which input to select is made by the output of the A/D converter B_k and by the comparator that operates on both $2\Delta_0$ and the output of the Δx register. The implementation shown in Figure 13.9 provides the maximum amount of time for the DAC, analog subtractor and three-state A/D converter to settle by performing all possible calculations while they are settling, then selecting the actual output needed. The x register input, for example, may be any one of the following numbers: x , $x + 3\Delta_0$, $x - 3\Delta_0$, $x + 1.5 \Delta x$, $x - 1.5 \Delta x$, $x + 0.5 \Delta x$, and $x - 0.5 \Delta x$. Of these seven possible values, three may be eliminated by using the previous value of B_k , i.e., B_{k-1} . That is the reason why the decoding logic driven by the B_{k-1} register in turn drives the x register adder/subtractor units comprised of ALU's A, B and C. However, at any particular sample time, only one of these ALU's has the correct value of the next X_k .

As shown in Figure 13.9, there are three output line groups emerging from the LDU. One of these output line groups (a dual line) controls the two 4-to-1 multiplexers. The second single line controls the 2-to-1 multiplexer. Finally, a six-wire output line group (comprised of three dual lines) controls the three ALU's. Depending on the present vector B_k and the preceding vector

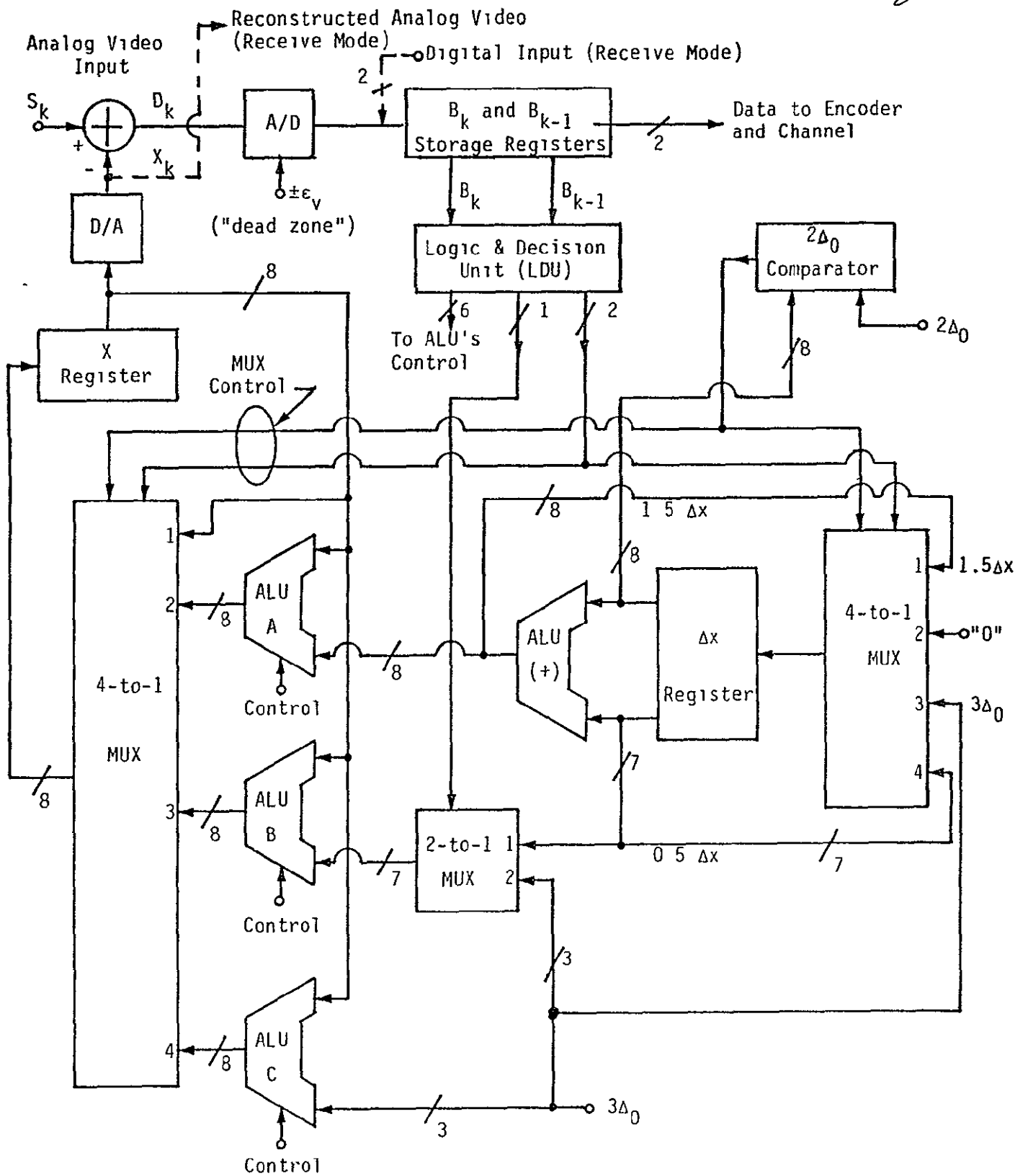
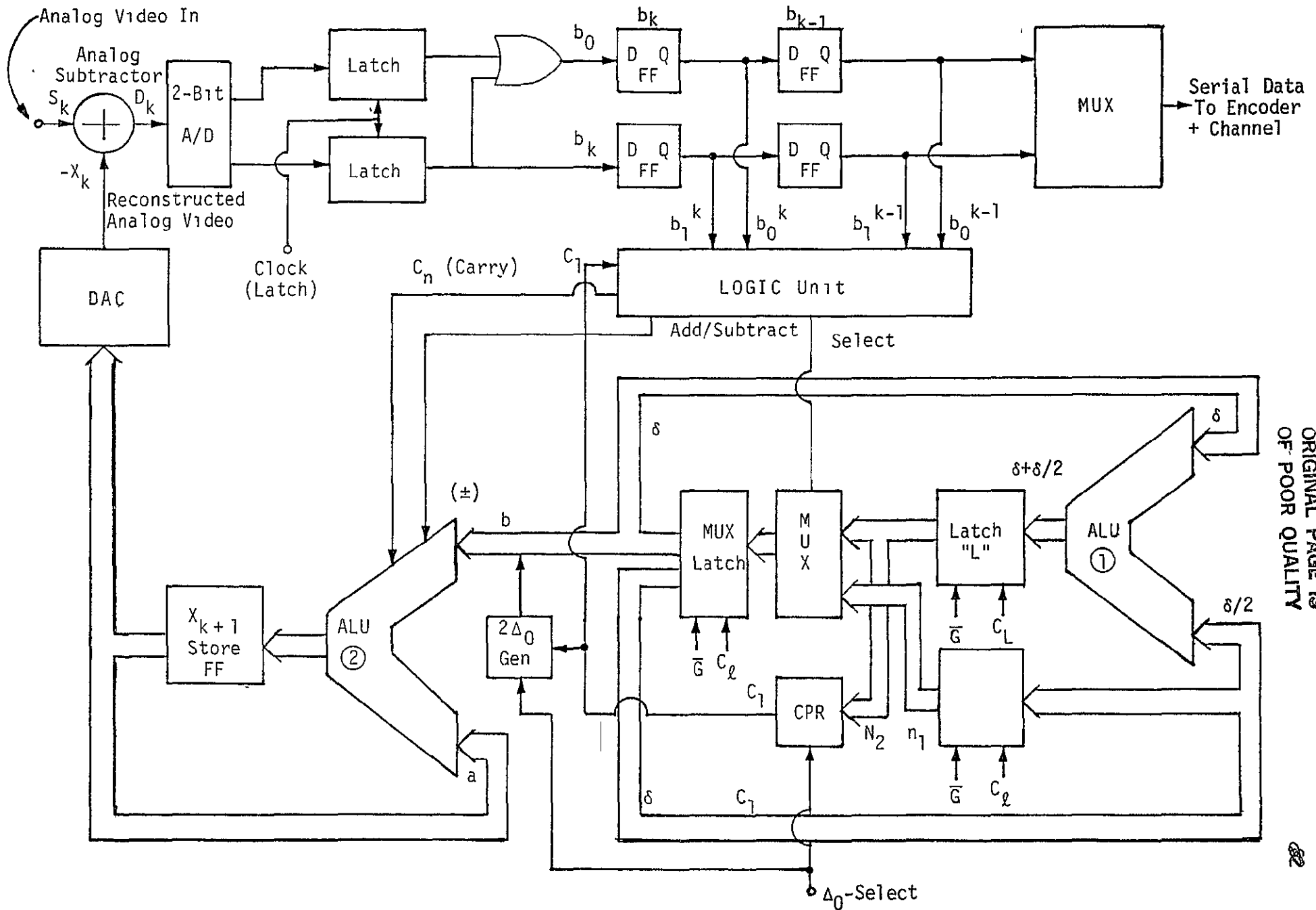


Figure 13.9. High-Speed, Tri-State, Video Digitizer (and Reconstructor) Block Diagram

B_{k-1} , the LDU sends the appropriate commands to the 4-to-1 multiplexers. It also sends the appropriate add/subtract commands to the x-register ALU's A, B and C. The ALU at the output of the Δx register, however, is always in the "add" mode. In this ALU, the value of Δx is added to a "right-shifted" value of itself (i.e., $0.5 \Delta x$), thus providing the next value of $1.5 \Delta x$. To ensure that the Δ -modulator does not "hang up" within a dead zone, the output of the Δx register is always compared with the $2\Delta_0$ value. If the value of the Δx register is less than $2\Delta_0$, the comparator controls the 4-to-1 multiplexers to select $3\Delta_0$ as the next increment. The value of $3\Delta_0$ is also selected when the LDU indicates that a transition from a no-change state (i.e., constant intensity) to a change state, i.e., an increase or decrease in intensity, has occurred on the latest sample.

For the receive mode, the logic implementation is the same as that shown in Figure 13.9, but without the analog subtractor or A/D converter. As indicated by dotted lines, the received data stream is applied directly to the B_k and B_{k-1} storage registers and the reconstructed analog video is taken from the output of the D/A converter.

The TSDM digitizer/reconstructor implementation for the I and Q channels is illustrated in Figure 3.10. This implementation is a simplified version of the Y-channel digitizer/reconstructor.



ORIGINAL PAGE IS
OF POOR QUALITY

Figure 13.10. Slow-Speed TSDM Digitizer/Reconstructor (I and Q Channels)

13.3.5 Run-Length Encoder Implementation

The run-length (R/L) encoder used in the transmitter side of the link is shown in the block diagram of Figure 13.11. The high-speed encoding circuitry accepts the B_k values at the sample clock rate and outputs a sequence from that sample, as shown in Table 13.1; the sample clock rate is fixed. Since the encoding process produces a variable number of bits out, depending on the sample inputs, the data-output rate of the encoder varies. Sixteen (16) bits of the encoder output are grouped together and transferred in parallel to the FIFO block. This parallel transfer reduces the data-transfer rate to one acceptable to the rotating buffer.

The rotating buffer provides the necessary elastic storage between the varying input-data rate and the fixed-output rate. Under normal circumstances, the output of the FIFO is clocked by the transmission-channel clock which is supplied to the TSDM from an external source. If the picture being transmitted happens to encode very efficiently so that insufficient data is entering the FIFO to replace the data being clocked out, the R/L encoder circuitry is apprised of this by the "potential-underflow" line shown in Figure 13.11. When a potential underflow problem exists, the R/L encoder circuitry waits until a new horizontal-synchronization pulse occurs. At this time, the R/L encoder generates a codeword indicating the end of valid data. When the synchronization pulse is complete, the R/L encoder transmits another codeword, which signifies the start of valid data. Inbetween these two times, the R/L encoder may generate fill bits of all zeros to maintain the FIFO buffer in its proper state of fill. Handling of those pictures which encode very efficiently is thus relatively simple. The rotating buffer has another output that indicates potential overflow. This output feeds back to the encoding circuitry, which changes its operating mode when the possibility of overflow occurs.

The basic reason for potential overflow is the type of picture being encoded. The picture with large areas of constant-brightness encode very efficiently (see Table 13.1) and the buffer does not have an overflow problem. Pictures having a great deal of detail with very few constant-brightness areas do not encode very efficiently. Since the tri-state delta modulator has three, instead of two, states for every sample, it inherently generates more data bits for a given number of samples than a bistate delta modulator. However, the general tendency for bistate delta modulation to produce granularity is less objectionable in those pictures with a large amount of detail. Therefore, the

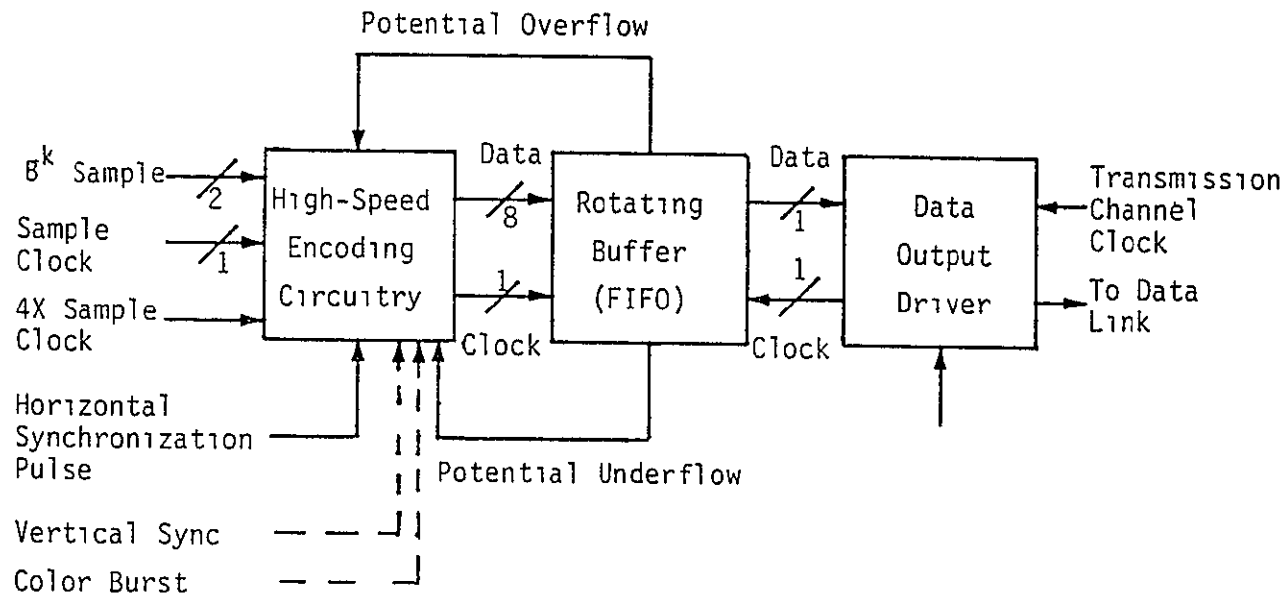


Figure 13.11. Run-Length Encoder (Transmitter Side)

ORIGINAL PAGE IS
OF POOR QUALITY

Table 13.1. Encoding Table

B _k Vector	Transmitted Sequence
+1	10
-1	11
0	01110
Two 0's in a row	01101
Three 0's in a row	01100
Four 0's in a row	01011
Five 0's in a row	01010
Six 0's in a row	01001
Seven 0's in a row	01000
Eight 0's in a row	00

R/L encoder circuitry can change its mode of operation when the buffer is in danger of overflowing. The encoder then sends a special sequence for its horizontal synchronization word that indicates the change of mode, and the encoder switches to bistate delta modulation. This removes the encoding table and merely sends a normal bistate-delta-modulation stream over the data link until the potential for buffer overflow has been eliminated.

13.3.6 Implementation of the Run-Length Decoder

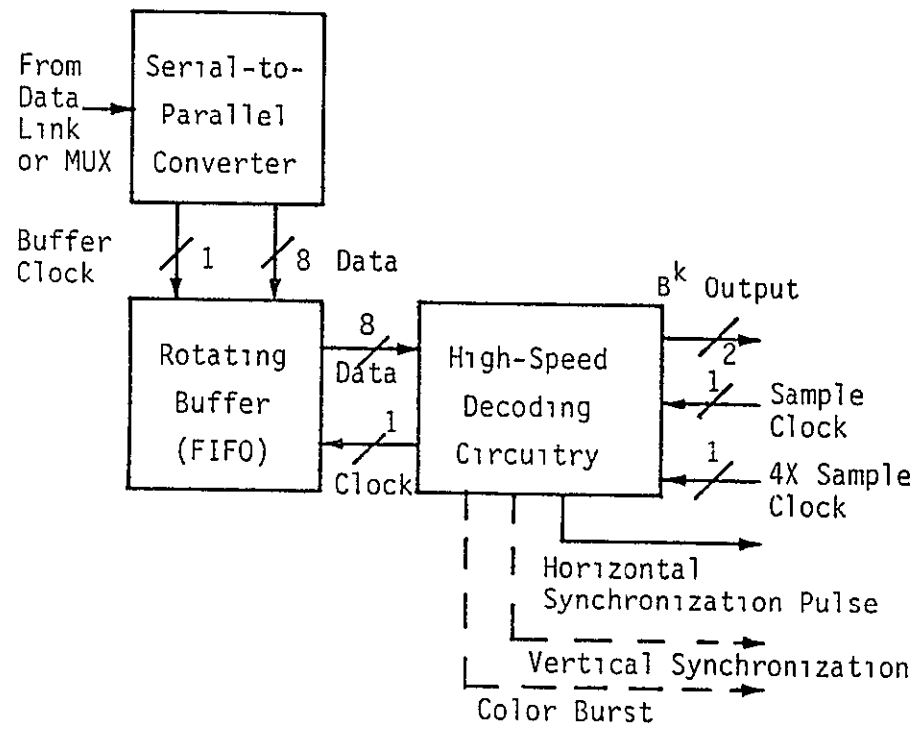
Figure 13.12 is a block diagram of the receiver R/L decoder. It is essentially the encoder turned around. The FIFO provides data to the decoding circuitry upon demand so that the output of the decoder can be a constant sample rate despite the variable-length decoding process. The elastic storage in the receiver rotating buffer forms the other half of the elastic storage in the transmitter. The total information stored in the two memories should vary, roughly together, depending on how the picture data is modified by the encoding algorithm. The sample rate into the encoder is constant, as is the output at the decoding end of the link. The link between the encoder and decoder also has a fixed rate which is somewhat less than the sample rate. The actual link data rate and the type of picture being scanned determine how often the system degrades to bistate delta modulation.

13.4 Summary and Conclusions

The main advantages of TSDM are summarized as follows:

(1) It permits R/L encoding techniques to reduce the required channel data rate. Depending on the particular picture being scanned, the TSDM scheme with three states per sample and R/L encoding requires less channel data rate than bistate delta modulation. While this statement does not apply to all possible pictures, R/L encoding of the TSDM output can consistently reduce the required data rate well below one bit per sample.

(2) TSDM eliminates granularity in the reconstructed video. It performs this function without degrading rise or fall times, compared with a bistate delta-modulation system.



ORIGINAL PAGE IS
OF POOR QUALITY

Figure 13.12. Run-Length Decoder (Receiver Side)

(3) The high-speed, tri-state transmitter described herein, when used to handle the luminance information in a color link, employs about 97 chips. The R/L encoder, including the FIFO, uses about 170 chips. About 47 chips each are employed by the I and Q slow-speed transmitters. The complete system of two slow-speed receivers and a time compensator utilizes about 193 chips. The R/L decoder utilizes 187 chips, while the high-speed receiver uses about 79 chips.